Department of Energy Enegineering
School of Engineering - ETSI
University of Seville

Thermo-Economic Assessment of Supercritical CO_2 Power Cycles for Concentrated Solar Power Plants

Francesco Crespi

Seville, October 2019

Research work submitted in partial fulfillment of
the requirements for the degree of Doctor of Philosophy

PhD programme in Energy, Chemical and Environmental Engineering
Department of Energy Enegineering
School of Engineering - ETSI
University of Seville

Thermo-Economic Assessment of Supercritical CO_2 Power Cycles for Concentrated Solar Power Plants

Author: Francesco Crespi
Supervisor: Prof. David Sánchez Martínez, University of Seville
Co-Supervisor: Prof. Tomás Sánchez Lencero, University of Seville

Seville, October 2019

Research work submitted to the Department of Energy Engineering, School of Engineering, of the University of Seville in partial fulfillment of the requirements for the degree of Doctor of Philosophy

Non al denaro,
non all'amore né al cielo...
...ma ai miei genitori.
Senza di voi tutto questo non sarebbe stato possibile.

Acknowledgements

I wish to acknowledge the main supervisor of this thesis, Prof. David Sánchez, for the long time motivation, guidance and help throughout the course of my doctoral studies. I am also grateful to Prof. Tomás Sánchez, second supervisor of this thesis, for his support from the very beginning of my research.

I would also like to express my gratitude for the academic support received at the University of Seville and to sincerely thank my colleagues (and friends) at the Thermal Power Group (GMTS).

I am also grateful to all the people I've worked with at TU Delft, in particular to Sebastian Bahamonde, for his precious help and advice during my short visit to The Netherlands.

Above all, I am grateful to my family for their continuous support and confidence. Last but not least, I sincerely thank my friends here in Seville and in Italy. This would have not been possible without their help, support and understanding.

Seville, 23th October 2019 F. C.

Resumen

Los sistemas de concentración solar basados en campos de heliostatos y receptor central (comúnmente denominados sistemas de torre) permiten alcanzar grandes relaciones de concentración, asociadas a elevadas temperaturas del fluido de trabajo empleado en el receptor. La utilización de este tipo de sistemas de concentración en combinación con ciclos de potencia basados en dióxido de carbono (CO_2) en condiciones supercríticas es una forma realmente prometedora de maximizar la eficiencia total de una planta termosolar de concentración (*solar-to-thermal-to-electricity*), reduciendo al mismo tiempo su tamaño y el coste de la electricidad (*Levelized Cost of Electricity*).

A la vista de semejante interés, en los últimos quince años, se han publicado gran cantidad de artículos científicos sobre este tema, se han organizado varios congresos internacionales y se ha construido un número significativo de instalaciones experimentales en todo el mundo, hasta el punto de que el ciclo de potencia de sCO_2, se considera hoy en día como una de las alternativas más interesantes para un producir potencia eléctrica a partir de un buen número de fuentes de energía, entre ellas la energía solar. No obstante, el rápido crecimiento del interés de la comunidad científica e industrial alrededor de los ciclos de sCO_2 se ha basado inevitablemente en una búsqueda no estructurada de ciclos más eficientes y técnicamente viables, más allá de los propuestos originalmente por los precursores de la tecnología: Gianfranco Angelino y Edward Feher.

Observando este escenario, la presente tesis se centra en el análisis de los fundamentos termodinámicos del ciclo de potencia de CO_2 supercrítico, con el objetivo de proporcionar una vía estructurada para el estudio de viabilidad termo-económica de este último aplicado a centrales termosolares de concentración. De este modo, se pretende responder a la pregunta de si la tecnología termosolar para producción de energía eléctrica puede llegar a ser competitiva con otras tecnologías convencionales a medio y largo plazo, en un mercado carente de subsidios e incentivos. Con estas consideraciones, este documento se estructura en cuatro secciones claramente definidas. En primer lugar, se realiza una revisión exhaustiva del estado del arte de la tecnología de ciclos de potencia de CO_2 supercrítico, no solamente revisando la información disponible en la literatura científica sino, también, proponiendo una nueva categorización basada en las características termodinámicas intrínsecas de estos ciclos, con el objetivo de detectar su potencial real y descartar aquellos ciclos que no resultan de interés para la aplicación considerada. De esta revisión se obtiene una preselección de doce ciclos de potencia.

En segundo lugar, se presenta una comparación puramente termodinámica de los ciclos preseleccionados, tomando como parámetros de comparación (*key performance indicators*) el

trabajo específico y los rendimientos energético y exergético en un rango significativamente amplio de temperatura y presión de operación. Después de esta primera comparación, los ciclos *Matiant* y *Quasi-Combined* quedan descartados de la lista anterior de doce ciclos debido a su pobre rendimiento en aplicaciones termosolares.

En la tercera sección se propone una comparación económica de los diez ciclos restantes integrados en una planta CSP, añadiendo una central basada en turbina de vapor representativa del actual estado del arte de la tecnología; para ello, se tienen en cuenta todos los equipos de este tipo de instalaciones. La comparación se realiza en entorno SAM (*System Advisor Model*, desarrollado por el Laboratorio de Energías Renovables de Estados Unidos) si bien las simulaciones de los ciclos de sCO_2 se realizan en entorno Matlab, empleando código de diseño para intercambiadores de calor de ciruito impreso (*Printed Circuit Heat Exchangers*), basado en trabajos ya existentes en la literatura. Además, se desarrolla un análisis de incertidumbre basado en la metodología de Montecarlo, a fin de tener en cuenta la incertidumbre introducida en el proceso de estimación de costes. Como resultado de esta comparación económica, los ciclos *Partial Cooling*, *Allam* y *Transcritical* CO_2 se confirman como las opciones más interesantes. Este último ciclo, no obstante, se descarta en el último paso del análisis, debido a que requiere unas condiciones ambientales poco realistas en localizaciones de plantas termosolares (es necesaria una temperatura ambiente muy baja para permitir el proceso de condensación del fluido de trabajo).

En la última parte del documento se estudia el funcionamiento de los ciclos *Partial Cooling* y *Allam* en condiciones fuera de diseño, con el objetivo de evaluar el coste de electricidad de una planta termosolar basada en esta tecnología. Para ello se presenta una nueva metodología de caracterización del comportamiento fuera de diseño de los intercambiadores, denominada *Conductance Ratio Method*, junto con un modelo de orden reducido basado en la identificación de *Sub-espacios Activos*, destinado a reducir drásticamente el coste computacional del código. El software comercial *AxStream* se emplea para crear mapas de funcionamiento de los compresores y bombas de los ciclos, mientras que la turbina se considera operando mediante presión deslizante. Además, se consideran tres estrategias de control diferentes (por *Inventory*, *By-pass* y *Temperatura de Entrada a Turbina*) y se determina que una combinación entre las dos primeras opciones conduce al mejor rendimiento a carga parcial para ambos ciclos. La información obtenida se incorpora a *SAM* para obtener los valores de coste de electricidad de la planta.

El principal hallazgo de la presente tesis es que los ciclos de potencia sCO_2 son capaces de proporcionar valores de coste de electricidad (*Levelized Cost of Electricity* comparables a los de las plantas termosolares basadas en turbina de vapor, o incluso ligeramente menores. Esta circunstancia, teniendo en cuenta del enfoque conservador empleado a lo largo del presente trabajo (especialmente en términos de estimaciones económicas), confirma que los ciclos de sCO_2 son una alternativa interesante para mejorar la competitividad de las plantas CSP-STE a medio-largo plazo, si bien no parece que permitan reducciones drásticas del coste de electricidad como anuncian algunos autores.

Key words: *Energía renovable, Energía termosolar de concentración, Dióxido de carbono supercrítico, Ciclo de potencia con* sCO_2

Abstract

Concentrated Solar Power based on central receiver systems (i.e., solar towers) enable very high concentration ratios, which translate into very high temperatures of the working fluid in the receiver. Utilizing these concentration technology in combination with power cycles based Carbon Dioxide (CO_2) in supercritical conditions is a promising means to maximize total efficiency of Concentrated Solar Power plants (solar-thermal-electricity STE), whilst reducing both footprint and cost of electricity (Levelized Cost of Electricity).

In the light of these positive features, In the last fifteen years, a large number of papers researching this topic have been published in literature, several dedicated technical meetings have been organized and a significant number of experimental facilities have been developed worldwide. As a consequence, the sCO_2 power cycle is nowadays considered as one of the most interesting technologies for electric power generation based on different primary energy sources, amongst which solar energy. Nevertheless, the rapidly growing interest in sCO_2 shown by the scientific and industrial communities has inevitably given way to an often unstructured search for more efficient and technically feasible cycles beyond those originally proposed by the fathers of the technology: Gianfranco Angelino and Edward Feher.

In this scenario, this work is focused on the analysis of the thermodynamic principles of sCO_2 power cycles, with the aim to provide a structured pathway for the thermo-economic feasibility study of the latter when applied to CSP power plants. Thus, the work aims to find out whether or not Solar Thermal Electricity has the potential to become competitive against conventional power generation technologies (relying on fossil fuels or renewable energy sources) in the mid and long terms, in subsidy/incentive-free market conditions. With this is mind, the thesis is organized in four sections. Firstly, a thorough review of the state-of-the-art of sCO_2 power cycles is done, not only reviewing the information available in the public domain, but also proposing a new categorization based on the thermodynamic features inherent to these cycles. This review is aimed at identifying the actual potential of the cycles and, therefore, discard those layouts which are not interesting for the application considered. Based on this review, twelve cycles are shortlisted.

Secondly, a purely thermodynamic comparison of these cycles is developed, based on specific work and 1^{st} and 2^{nd} Law efficiencies for a wide range of operating pressure and temperature. After this analysis, the *Matiant* and *Quasi-Combined* layouts are discarded due to their poor thermodynamic performance overall.

The third section proposes an economic comparison of the ten remaining cycles integrated into a CSP plant, in addition to a conventional CSP-STE plant using steam turbine technology

for reference; to this aim, all the equipment that is needed in such power plants is taken into account. The comparison is performed in *SAM* environment (*System Advisor Model* developed by the US National Renewable Energy Laboratory) even though sCO_2 performance simulation is done with proprietary, in-house codes running in Matlab and using a specific off-design performance code of Printed Circuit Heat Exchangers. Additionally, an uncertainty analysis based on the Montecarlo methodology is developed in order to take into account the uncertainty incurred in the cost estimation process. As a result of this economic comparison, the *Partial Cooling, Allam* and *Transcritical* CO_2 layouts are found to be the most feasible solutions. Nevertheless, the latter cycle is eventually discarded for the unrealistic ambient temperature that is needed to enable condensation of the working fluid.

Finally, the last section of the thesis investigates the off-design performance of the *Partial Cooling* and *Allam* cycles with the aim to assess the Levelized Cost of Electricity of CSP-STE plants employing these cycles. A novel methodology to predict the off-design performance of heat exchangers, namely the *Conductance Ratio Method*, is presented along with a reduced-order model based on the *Active Sub-spaces* method and meant to drastically reduce the computational cost of the code. The commercial software *AxStream* is employed to produce performance maps of compressors and pumps and the turbine is assumed to operate in sliding-pressure mode. Also, three different control strategies are considered (*Inventory*, *By-pass* and *Turbine Inlet Temperature*) and a combination between the two former options is found to lead to the best part-load performance of both cycles. The information obtained is then incorporated into *SAM* to obtain the cost of electricity of the power plant.

The main finding of the present dissertation is that sCO_2 power cycles are capable of providing LCoE values comparable to those of CSP-STE plants based on steam turbines, or even slightly lower. Taking into account the conservative approach employed throughout the present work, especially in terms of economic estimations, this comes to confirm that sCO_2 power cycles are an interesting alternative to enhance the competitiveness of CSP-STE plants in the mid to long term, even if they do not seem to enable the drastic cost reductions claimed by some authors.

Key words: *Renewable energy, Concentrated Solar Power, Supercritical Carbon Dioxide,* sCO_2 *power cycle*

Contents

List of Figures

List of Tables

Nomenclature

Introduction - symbols

α	Absorptance	[−]
$\dot{Q}$	Thermal radiation	[W]
ϵ	Emissivity	[−]
η	Efficiency	[%]
λ	Reflectance	[−]
$ASME$	American Society of Mechanical Engineers	[−]
BP	British Petroleum	[−]
CO_2	Carbon dioxide	[−]
COP	Conference of the Parties	[−]
CR	Concentration Ratio	[−]
CSP	Concentrated Solar Power	[−]
DOE	US Department of Energy	[−]
GDP	Gross Domestic Product	[$]
I	Solar radiation	[W]
IEA	International Energy Agency	[−]
$KAERI$	Korea Atomic Energy Research Institute	[−]
$KAIST$	Korea Advanced Institute of Science and Technology	[−]
$LCoE$	Levelized Cost of Energy	$[\frac{¢}{kWh}]$
LFR	Linear Fresnel Reflector	[−]
$NETL$	National Energy Technology Laboratory	[−]
$NREL$	National Renewable Energy Laboratory	[−]
$PCHE$	Printed Circuit Heat Exchangers	[−]

PTC Parabolic Trough Collector [−]

PV Photovoltaic [−]

SAM System Advisor Model [−]

$SCARABEUS$ Supercritical Carbon dioxide Alternative fluids Blends for Efficiency Upgrade of Solar power plants [−]

sCO_2Flex Supercritical CO_2 Cycle for Flexible & sustainable support to the electricity system [−]

sCO_2Hero Supercritical CO_2 Heat Removal system [−]

sCO_2 Supercritical carbon dioxide [−]

SPD Solar Parabolic Dish [−]

SPT Solar Power Tower [−]

$STEP$ Supercritical Transformational Electric Power Project [−]

$SwRI$ Southwest Research Institute [−]

T Temperature [K]

TES Thermal Energy Storage [−]

TRL Technology Readiness Level [−]

$UNFCCC$ United Nations Framework Convention on Climate Change [−]

USD United States Dollars [$]

Introduction - subscripts

abs Absorbed [−]

amb Ambient [−]

b beam [−]

$conv$ Convective [−]

el Electric generator [−]

n normal [−]

$overall$ Overall CSP plant, solar to electric [−]

rad Radiative [−]

rec Solar receiver [−]

$refl$ Reflective [−]

sf	Solar field	[−]
th	Thermal cycle	[−]
$trans$	Transferred	[−]

Literature Review - symbols

$\dot{m}$	Mass flow	$[\frac{kg}{s}]$
$Bott.$	Bottoming	[−]
C_p	Heat capacity	$[\frac{W}{K}]$
c_p	Specific heat	$[\frac{J}{kgK}]$
$CPOC$	Cryogenic Pressurised Oxy-Combustion	[−]
GT	Gas Turbine	[−]
IC	Intercooled compression process	[−]
$MC-EJ$	Main Compression intercooled recompression with ejector	[−]
$MCFC$	Molten Carbonate Fuel Cell	[−]
$n.d.$	not declared	[−]
$Nes.$	Nested	[−]
ORC	Organic Rankine Cycle	[−]
$Preh.$	Preheating	[−]
R	Regeneration process	[−]
$RC-EJ$	Recompression with ejector	[−]
$Recompr.$	Recompression	[−]
RH	Reheated expansion process	[−]
$S-EJ$	Simple Recuperated with ejector	[−]
SFC	Split-flow before Compression process	[−]
SFE	Split-flow before Expansion process	[−]
SFH	Split-flow before Heating process	[−]
$SFHE$	Split-flow before Heating and Expansion process	[−]
ST	Steam Turbine	[−]
TCO	Texas Cryogenic Oxy-fuel	[−]

$TEES$	Thermo-Electric Energy Storage	[−]
TIT	Turbine Inlet Temperature	[K]
$Topp.$	Topping	[−]
$w/$	with	[−]
WHR	Waste Heat Recovery	[−]
LNG	Liquified Natural Gas	[−]
R134-a	Haloalkane Refrigerant, Norflurane	[−]

Literature Review - subscripts

WHR	Waste Heat Recovery	[−]

Thermodynamic Analysis - symbols

$\Delta\%$	Percentage Deviation	[%]
ΔP	Percentage Pressure drop	[%]
ΔT_i	Temperature difference at HX section i (pinch-point)	[°C]
ΔT_{min}	Minimum temperature difference (pinch-point)	[°C]
ϵ	Heat exchanger efficiency	[%]
ϕ	Split-flow (Recompression) factor	[−]
CF	Carnot Factor	[%]
i	Heat exchanger sub-section	[−]
NTU	Number of Thermal Units	[−]
P	Pressure	[MPa]
PR	Pressure Ratio	[−]
T	Temperature	[°C]
W_s	Specific Work	[$\frac{kJ}{kg}$]

Thermodynamic Analysis - subscripts

C	Carnot	[−]
$compr$	Compressor	[−]
$GMTS$	Grupo de Máquinas y Motores Térmicos (in-house result)	[−]
H	High	[−]

HX	Heat Exchanger	$[-]$
i	Heat exchanger sub-section	$[-]$
in	Inlet	$[-]$
L	Low	$[-]$
min	Minimum	$[-]$
O	Literature Reference	$[-]$
pol	Polytropic	$[-]$
rec	Recuperator	$[-]$
$turb$	Turbine	$[-]$

Economic Analysis - symbols

α	Flow angle with respect to the axial direction	$[°]$
$\bar{c}_p$	Mean specific heat	$[\frac{J}{kgK}]$
Δh_{steam}	Isentropic enthalpy change across the steam turbine	$[\frac{J}{kg}]$
ΔT	Temperature Difference	$[°C]$
ΔT_{range}	Cooling Tower temperature range	$[°C]$
ΔT_{solar}	Temperature rise across solar receiver	$[°C]$
$\dot{V}$	Volumetric flow	$[\frac{m^3}{s}]$
$\dot{W}_{el}$	Compressor Electric Power	$[HP]$
ϵ_{HX}	Porosity or Void Fraction	$[-]$
γ	Heat capacity ratio	$[-]$
Ψ	Stage loading coefficient	$[-]$
ρ	Density	$[\frac{kg}{m^3}]$
ρ_m	Metal density	$[\frac{kg}{m^3}]$
b	Cascade pitch	$[m]$
BoP	Balance of Plant	$[-]$
c_x	Axial velocity	$[\frac{m}{s}]$
C_{compr}	Compressor cost	$[k\$]$
C_{CT}	Cooling Tower cost provided by Thermoflex	$[k\$]$

C_{HX}	Heat Exchanger cost	[$]
C_{pump}	Pump cost	[$]
C_{raw}	Raw material cost	[$]
C_R	Solar Receiver cost	[$]
C_{SF}	Solar field cost	[$]
C_{TES}	Thermal Energy Storage cost	[$]
C_{TFX}	Turbine cost provided by Thermoflex	[k]
$C_{tot,BoP}$	Balance of Plant contribution to total installed cost	[$]
C_{tot}	Total installed cost without Balance of Plant contribution	[$]
C_{turb}	Turbine cost	[k]
D_c	Channel diameter	$[mm]$
EPC	Engineering, Procurement and Construction	[−]
f_m	HX density factor	[−]
F_x	Normal Force	$[N]$
F_y	Tangential Force	$[N]$
f_{rec}	Receiver cost correction factor	[−]
H	Pump head	$[ft]$
HTF	Heat Transfer Fluid	[−]
M	Heat exchanger Mass	$[kg]$
m_W	Cooling water mass flow	$[\frac{kg}{s}]$
N	Number of stages	[−]
OCC	Overnight Capital Cost	$[\frac{\$}{kW}]$
p	Static pressure	$[Pa]$
P_c	Channel pitch	$[mm]$
PB	Power Block	[−]
Q	Volumetric flow	$[\frac{gal}{min}]$
SM	Solar Multiple	[−]
t_c	Plate thickness	$[mm]$

u	Velocity	$[\frac{m}{s}]$
V	Heat exchanger Volume	$[m^3]$
VPE	Vacuum Process Engineering	$[-]$
W_{stage}	Expansion work	$[J]$

Economic Analysis - subscripts

el	Electric	$[-]$
ref	Reference case: standard solar salt	$[-]$
s	Molten salt	$[-]$

Partial Load Analysis - symbols

$(hA)^*$	Conductance ratio	$[-]$
$[A]$	Normalized sampled values AS matrix	$[-]$
$\bar{T}$	Mean Temperature	$[K]$
$\bar{x}$	Normalized sampled AS variable	$[-]$
ΔH	Compressor isentropic enthalpy variation	$[\frac{J}{kg}]$
ΔH_{corr}	Corrected compressor isentropic enthalpy variation	$[-]$
ΔT	Temperature difference	$[K]$
ΔT_{lm}	Log Mean Temperature Difference	$[K]$
δ	Percentage variation between two consecutive iteration steps	[%]
$\dot{m}$	Mass flow	$[\frac{kg}{s}]$
$\dot{m}_{corr}$	Corrected mass flow	$[m^2]$
$\dot{q}$	Heat duty	$[W]$
λ	Thermal conductivity	$[\frac{W}{Km}]$
μ	Dynamic viscosity	$[Pa \cdot s]$
Ψ	Flow coefficient	$[\frac{\sqrt{m^3 \cdot kg}}{s \cdot \sqrt{Pa}}]$
A	Area	$[m^2]$
a	Sound speed	$[\frac{m}{s}]$
AS	Active Subspaces	$[-]$
BC	Boundary Conditions	$[-]$

$BMPC$	Bechtel Marine Propulsion Corp	[−]
CF	Capacity factor	[%]
CIP	Compressor Inlet Pressure	$[Pa]$
CRM	Conductance Ratio Method	[−]
DNI	Direct Normal Irradiance	$[\frac{W}{m^2}]$
E_{year}	Annual Energy Production	$[GWh]$
f	Function	[−]
F_d	Thermal properties contribution term	[−]
Δh	Enthalpy	$[\frac{J}{kg}]$
h	Heat transfer coefficient	$[\frac{W}{Km^2}]$
$Inv.$	Inventory	[−]
IRR	Internal Rate of Return	[%]
IST	Integrated System Test	[−]
k	Heat exchanger sub-division	[−]
LHS	Latin Hypercube Sampling	[−]
N	Rotational speed	$[rpm]$
N_{corr}	Corrected rotational speed	$[\frac{rpm \cdot s}{m}]$
NPV	Net Present Value	[$]
Nu	Nusselt number	[−]
PD	Percentage Deviation	[%]
PPA	Purchase Price Allocations	[$]
Pr	Prandtl number	[−]
q	AS object function	[−]
R	Ideal Gas Constant	$[\frac{J}{K \cdot mol}]$
R_{tot}	Total thermal resistance	$[\frac{Km^2}{W}]$
R_{wall}	Wall thermal resistance	$[\frac{Km^2}{W}]$
Re	Reynolds number	[−]
TD	Mean temperature difference	$[K]$

TIP	Turbine Inlet Pressure	$[Pa]$
TOD	Time-of-delivery factors	$[-]$
tol	Tolerance	$[-]$
U	Thermal transmittance	$[\frac{W}{Km^2}]$
V	Volume	$[m^3]$
x	Reynolds scaling exponent	$[-]$
x_{AC}	Active variables	$[-]$
y	Prandtl scaling exponent	$[-]$

Partial Load Analysis - subscripts

$'$	Calculated in off-design conditions	$[-]$
AC	Active	$[-]$
Al	Allam cycle	$[-]$
$Cooler1$	First cooler after LT Rec	$[-]$
$corr$	Corrected parameter	$[-]$
d	Dominant	$[-]$
$HTRec$	High Temperature Recuperator	$[-]$
in	Inlet	$[-]$
k	Heat exchanger sub-division	$[-]$
$LTRec$	Low Temperature Recuperator	$[-]$
off	Off-design	$[-]$
on	On-design	$[-]$
PC	Partial Cooling cycle	$[-]$
s	Secondary	$[-]$
T	Turbine	$[-]$
tot	Total	$[-]$
TT	Total-to-total	$[-]$
$wall$	Wall surface	$[-]$
$x \hookrightarrow y$	HX side between point x to y	$[-]$

Appendix - symbols

ΔL_i	Length of sub-HX	$[m]$
$\dot{C}$	Heat capacity	$[\frac{W}{K}]$
$\dot{C}^*$	Ratio between minimum and maximum heat capacity	$[-]$
$\dot{Q}$	Heat duty	$[\frac{W}{m^2}]$
ϵ	Heat exchanger efficiency	[%]
σ_{MAX}	Maximum allowable mechanical stress	$[MPa]$
A	Area	$[m^2]$
D_c	Channel Diameter	$[mm]$
D_{hyd}	Hydraulic diameter	$[m]$
f_c	Friction factor	$[-]$
H	PCHE cross sectional area height	$[mm]$
N	Number of sub-HX divisions	$[-]$
N_{ch}	Number of channels	$[-]$
NTU	Number of Thermal Units	$[-]$
P_c	Channel Pitch	$[mm]$
p_c	Difference between Channel Pitch and diameter	$[mm]$
t_c	Plate thickness	$[mm]$
U	Thermal transmittance	$[\frac{W}{Km^2}]$
W	PCHE cross sectional area width	$[mm]$

Appendix - subscripts

C	HX cold side	$[-]$
$cond$	Conductive	$[-]$
$conv$	Convective	$[-]$
H	HX hot side	$[-]$
hor	Horizontal	$[-]$
i	Refers to i sub-HX division	$[-]$
tot	Total	$[-]$
ver	Vertical	$[-]$

1 Introduction

*This first chapter presents the **general background** of the thesis -in terms of sustainable development and energy utilization- and a **justification** of its research topic, along with a discussion of the specific **objectives** and associated **general methodology**. Also in this chapter, a brief description of the **structure** of the document and of the **original contribution to knowledge** provided by the thesis are presented.*

1.1 Background

The themes of sustainable energy and climate change are gaining increasing importance in the international, scientific debate in recent years, thanks also to the creation of several summits and conferences focused on these topics. Among these, the *Earth Summits*, consisting in decennial meetings of world leaders organized since 1972 with help of the United Nations, and the *United Nations Climate Change Conferences* (COP, Conference of the Parties), a series of yearly conferences developed by the United Nations Framework Convention on Climate Change (UNFCCC), are worth noting. The main accomplishment of these conferences, started in 1995, was the signature of the world-widely known Kyoto Protocol in 1997. This managed to move the public opinion, attracting the interest of a great majority of the scientific community and mass media, converting climate change and sustainable development into a worldwide topic of debate. All of a sudden, concepts like *greenhouse gas emissions* and *global warming* were on everyone's lips and several campaigns to raise awareness were initiated. This process continued during the past twenty years and is still ongoing nowadays, as demonstrated by the recent signing *Paris Agreement* in March 2019, where the climate change was universally recognized as a concrete threat to our planet. The agreement, proposed in 2015 during the COP17, focuses on mitigating global warming and establishes a long-term goal that is as necessary as it is challenging: on one hand, keeping the global average temperature raise to well below 2°C above pre-industrial levels; on the other, limiting this increase to 1.5°C, since this would substantially reduce the risks and effects of climate change. Figure 1.1 represents potential future emissions pathways of global greenhouse gas emissions in the case of no climate policies, with the currently implemented policies, with the national pledges set forth in the Paris Agreement and with the aforediscussed 2ºC and 1.5ºC consistent pathways. Values are expressed in gigatonnes of equivalent CO_2, while high, intermediate an low pathways represent ranges for a given scenario. The temperatures quoted to the right of the chart report the estimated average global temperature rise by 2100 (from pre-industrial levels). As claimed by several environmental organizations, an increase of only 2ºC would cause a tremendous damage to the ecosystem (extreme heat, water scarcity, extinction of the coral reef and of

several vegetal and animal species [14]), while a 3°C rise would be able to initialize an irreversible process as a consequence of which areas inhabited by more than 275 million people worldwide would potentially be flooded [15]. Observing such a destructive scenario from an engineering standpoint, it seems to be mandatory to seriously question ourselves about what sustainable development really means and, above all, what pragmatic actions could possibly give solutions to this looming problem.

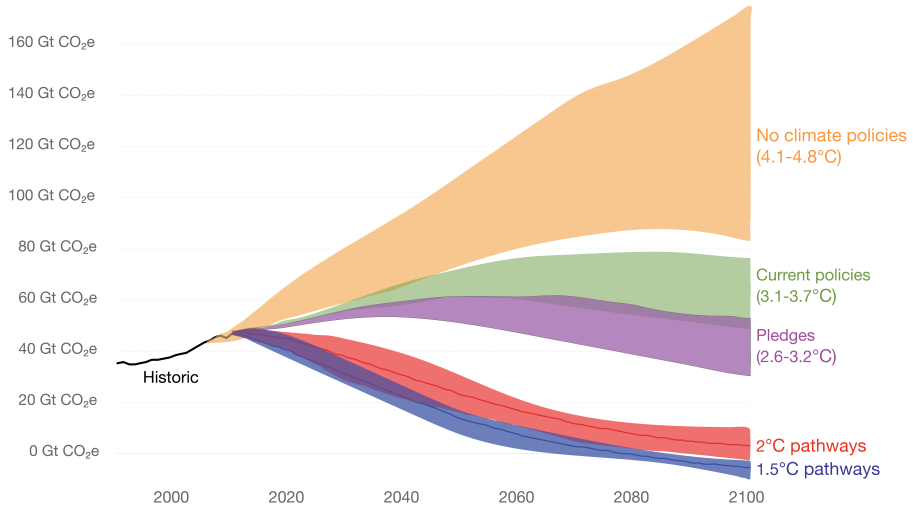

Figure 1.1: Global greenhouse gas emissions scenarios (adapted from [1]).

It is widely acknowledged that sustainable energy is a principle whereby the human use of energy "*meets the needs of the present without compromising the ability of future generations to meet their own needs*" [16]. In this definition, the *needs of the present* must be thoroughly discussed in order to completely understand the real extent of the problem. The population of the world has been growing steadily in the last centuries, increasing from 0.9 billion in 1800 to 7.4 billion in 2015 as reported in Figure 1.2, and there is no evidence of a decline in the near future. In fact, according to the last projections provided by [1], the world population will be increasing in the next decades, even if at a lower annual growth rate, at least until 2100. Interestingly, the steep increase in world population has translated into a parallel economic growth in the last century, in particular after World War II, as shown in Figure 1.3.

The World Gross Domestic Product (GDP) is usually employed as a figure of merit for the world's wealth, calculated as the total output of the world economy, adjusted for inflation and expressed in 2011 international dollars. From 1850 to 1950, world population doubled (from 1.26 to 2.52 billion) while GDP experienced an almost five-fold increase, reaching 9,250 billion dollars (USD). Nevertheless, the exponential growth was yet to come: from 1950 to nowadays, the world population tripled, while GDP experienced a tremendous twelve-fold increase, reaching 110,000 billion dollars (USD).

Such worldwide economic growth has, nonetheless, not been distributed evenly throughout the world. This is shown in Figure 1.4(a) where inequalities between the wealthiest and underdeveloped regions is very visible. Interestingly, there is a very clear parallelism between wealth

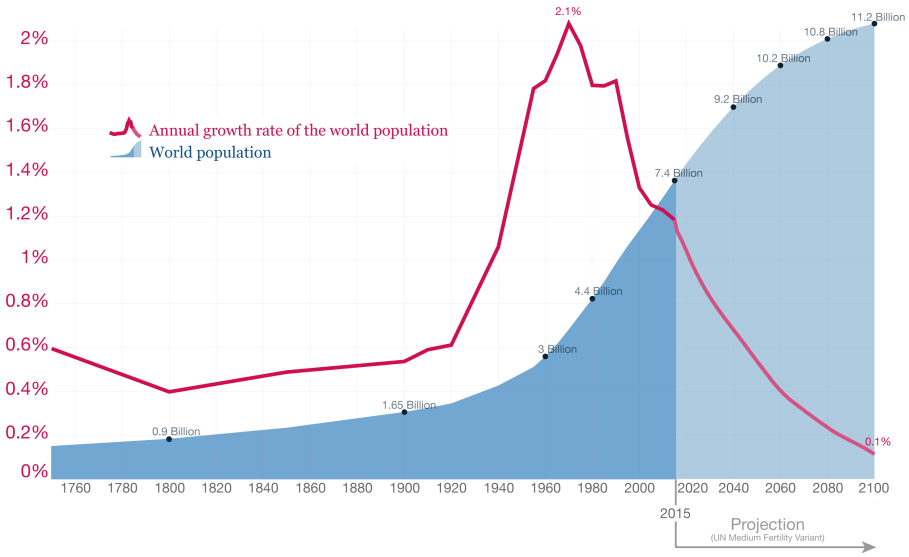

Figure 1.2: World population growth, 1750-2100 (adapted from [1]).

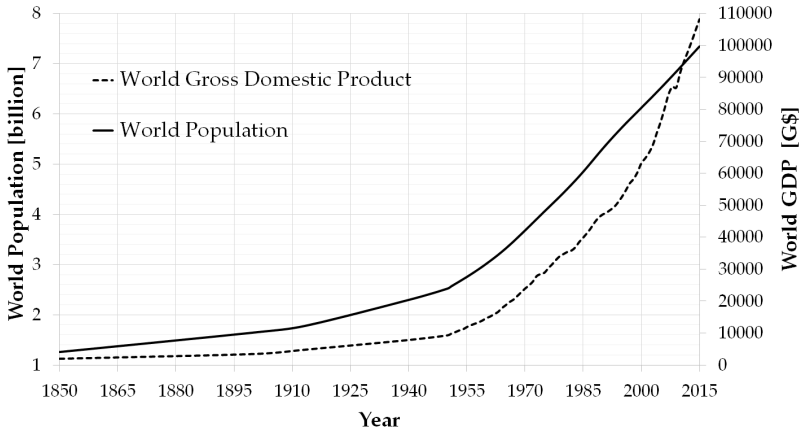

Figure 1.3: Evolution of World population and World Gross Domestic Product from 1850 to 2015 (based on data from [1]).

and consumption of energy (electricity), as observed in Figure 1.4(b), and the same can be claimed for other goods like the number of motor vehicle ownership, connections to internet, etc. [1]

Further to the previous discussion, Figure 1.5 presents the evolution of world GDP and Primary Energy Consumption in the last forty years, showing an undeniable similarity between the two trends. The data, taken from the British Petroleum Statistical Review of World Energy [2], confirms that the Primary Energy Consumption has more than doubled in this period, exceeding 13,000 Mtoe in 2015, against an almost four-fold increase of GDP. Interestingly, the same plot shows a temporary decline of both figures or merit, due to the Global Financial

[1] A complete data-set can be found in [1], even if the author decided to not include the corresponding diagrams here to limit the extension of the present chapter.

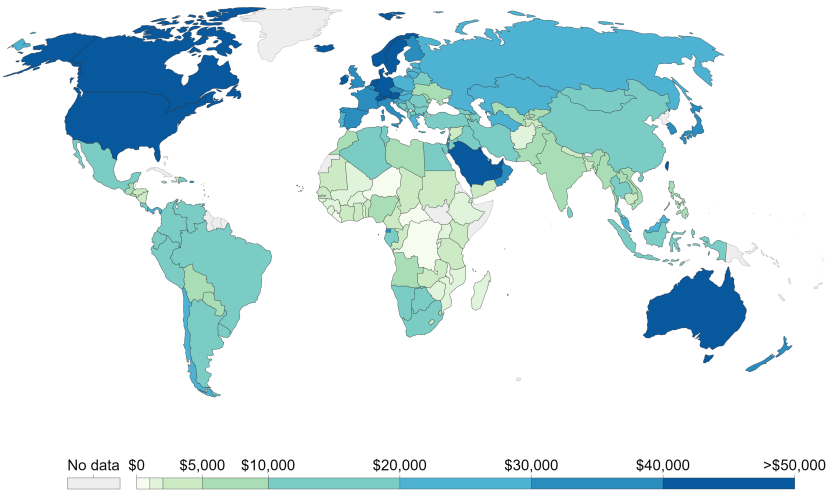

(a) World GDP per Capita in 2016 (adapted from [1]). Real GDP per capita is measured in USD, inflation adjusted to USD_{2011}.

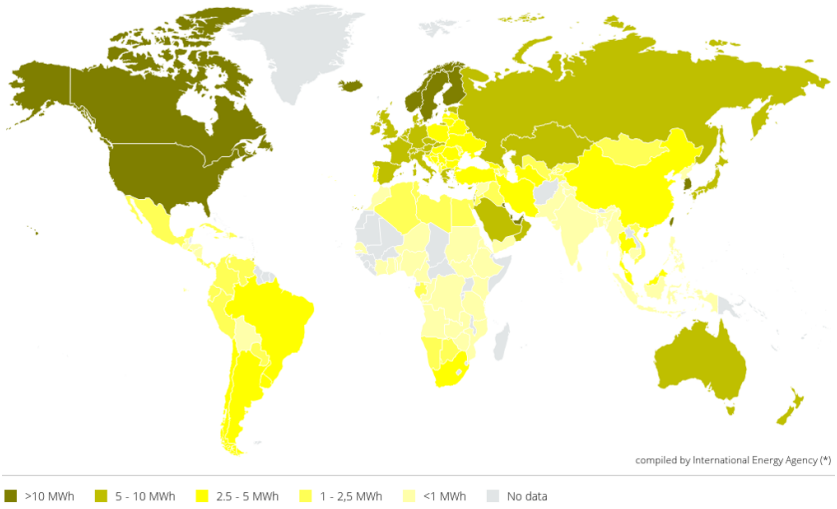

(b) World Electricity Consumption per capita in 2015 (adapted from [1]).

Figure 1.4: World distribution of GDP and Consumption of Electricity.

Crisis that took place around 2009.

In order to analyze possible strategies in the frame of sustainable development, it is mandatory to understand the contribution of each energy source to the cumulative consumption of primary energy and the extent to which this is affecting climate change. According to the technical report by BP, world energy consumption is characterized by the following scenario: fossil fuels provide the great majority of energy, reaching a total of 84.2 %, 34.2% of which obtained from Oil, 27.6% from Coal and 23.4% from Natural Gas; 10.4% of the total energy consumed is produced from renewable energies, and only 4.4% is provided by Nuclear. Figure 1.6 shows the evolution of this overall scenario in the last thirty years, and a possible projection to 2040, as declared by the International Energy Agency (IEA).

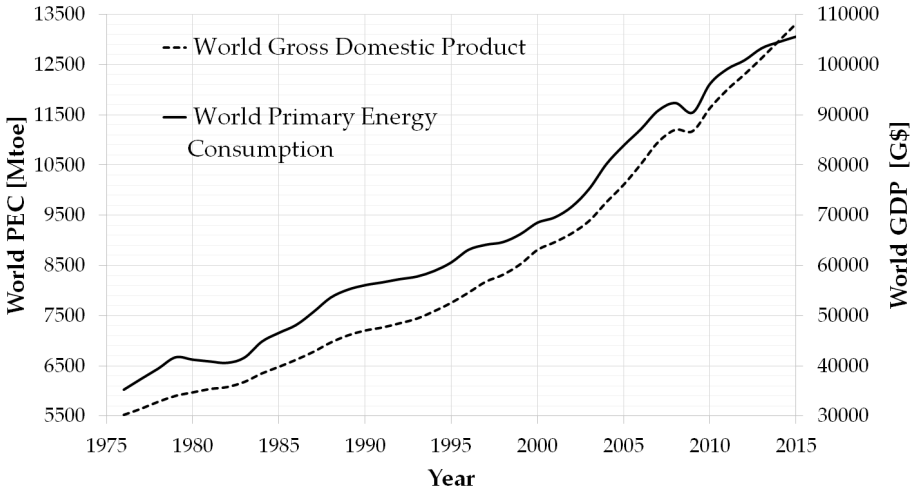

Figure 1.5: World Primary Energy Consumption in Mtoe (obtained from [2]).

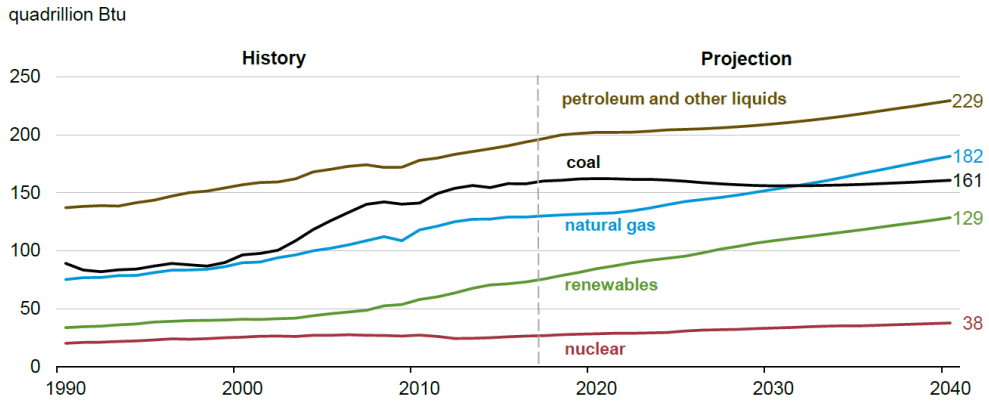

Figure 1.6: World Energy Consumption by fuel in Btu (obtained from [3]).

According to the data provided in this section, it becomes clear that even if renewable energies will increase their share of the World energy consumption significantly, fossil fuels still represent more than 75% of the primary energy consumption worldwide (at least according to IEA studies), which continues to increase carbon dioxide and other greenhouse gas emissions rate as previously discussed in Figure 1.1. This puts forward a need to de-carbonize the world energy consumption through the use of effective carbon abatement technologies in fossil fuel power plants and the deployment of renewable energy generation capacity at a faster rate. To this end, a balanced approach is needed, far from biased or simplistic statements like that set forth in the *Energy [R]Evolution* report by Greenpeace[4], which claims that "*there are no major economic or technical barriers to moving towards 100% renewable energy by 2050*". Such declarations are warmly welcomed by the general public and certainly work at a macroeconomic level, but energy supply is a very local task for which many hurdles and challenges remain unsolved[2]. Nevertheless, this being said, there is consensus in the urgent need to

[2]The discussion held between the scientific groups led by Prof. M.Z. Jacobson and Dr. C.T.M. Clack in regards to

find and develop new technologies to help deploy renewable electricity at the highest possible pace and to the largest possible extent, and this is the stage in which this thesis is presented.

1.2 Motivation for this research

Solar energy is acknowledged as the most abundant and competitive alternative amongst renewable energy sources, due to its characteristic features such as low-cost and large availability and the extremely low greenhouse gas emissions (from a Life Cycle Analysis perspective). Nowadays, photovoltaic panels are the technology of choice for the large majority of solar power generation facilities, in terms of installed capacity and energy produced [3]. Nevertheless, this technology also presents weaknesses, among which low dispatchability is without a doubt one of the most salient. Comparing the scenario proposed by Greenpeace [4] and the projections by IEA [3], Figure 1.7, it looks clear that Concentrated Solar Power (CSP) is also called to play a leading role along with PV in the intent to partially (or fully, in the most optimistic projection) replace fossil fuels. CSP presents all the features that PV is currently lacking in order to enhance the performance of Solar energy technology, both individually [19, 20] or in hybrid-configurations [21]. CSP is much more dispatchable than PV, thanks to a mature Thermal Energy Storage technology that allows Solar Tower plants to work really close to nominal conditions 24 h per day [22]. Moreover, CSP power plants can be designed for much larger power ratings, comparable to steam or gas turbine power plants; such is the case of like *Ouarzazate Solar Power Station* [23] and *Ivanpah Solar Power facility* [24], with outputs of 510 and 392 MW respectively (gross electric power) and using parabolic trough and solar tower technologies (Ouarzazate also employs thermal energy storage).

Among all the CSP technologies -Linear Fresnel Reflectors (LFR), Solar Parabolic Dishes (SPD), Parabolic Trough Collectors (PTC) and Solar Power Tower (SPT)- parabolic trough and central receiver systems have the largest share of installed capacity and also the largest potential for future development and mass deployment [19]. Among the two, this thesis focuses on central receiver systems (Solar Towers) because of their inherent thermodynamic potential enabling higher efficiency and the utilization of innovative power cycles. As a downside, it is acknowledged that the costs of central receiver systems are currently higher than those of parabolic trough power plants.

A typical commercial SPT with TES is presented in Figure 1.8. A solar field composed by a large number of heliostats concentrates solar radiation onto the external receiver surface, located in the upper part of the tower. In a standard configuration with TES enabled, molten salts flowing inside the receiver (usually referred to as *Solar Salts*, NaNO3-KNO3) absorb this energy in the form of sensible heat, increasing their temperature up to 565ºC. The high temperature salts are then stored in a hot tank from which they are then sent to a steam generator. Energy is transferred from the molten salts to the feed-water stream. The low temperature salts are sent to storage in a cold tank at 290ºC and the high pressure, high temperature live steam is used to drive the turbine in a >40% efficient *Rankine* power cycle. The installation cost and Levelized Cost of Energy (LCoE) of these plants is in the order of 5800 $/kW and 13-15 ¢/kWh [25] respectively, values that are not really appealing if compared to 3800 $/kW [26]

the potential electrification of United States based on renewable energy only [17, 18] is another recent example of this.

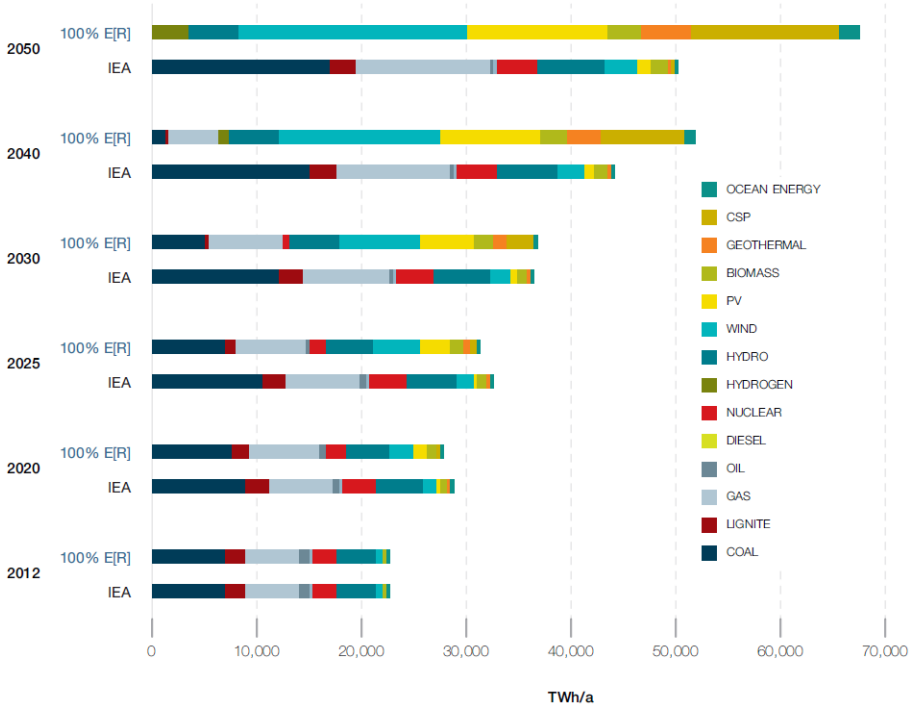

Figure 1.7: Foreseen development of electricity generation under the IEA "Current Policies" and the Energy [r]evolution case (obtained from [4]).

and 6-7 ¢/kWh [27, 3] for a coal power plant or 1600-1800 $/kW [25] and 8-9 ¢/kWh [28] for a photovoltaic farm. Moreover, these figures of merit can be drastically increased in unfavorable locations with a low availability of solar irradiation.

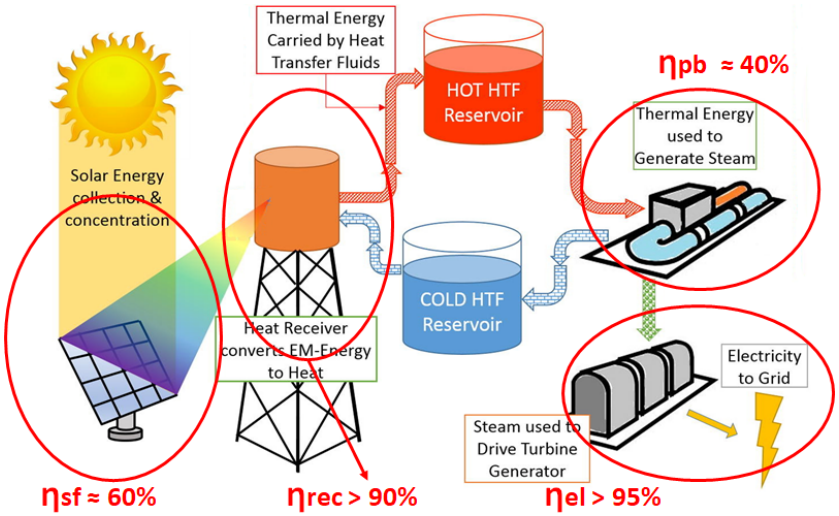

Figure 1.8: Schematic representation of a typical SPT plant with TES (obtained from [5]).

In order to tackle their potentially unfavorable economics, several solutions to reduce the

installation costs and LCoE of SPT technology have been studied in the last years. For example, a large number of different receiver geometries have been considered to enhance the solar Concentration Ratio (CR) (capacity to concentrate solar energy on the receiver, hence achieving high temperature and efficiency) [29] and receiver efficiency [30], solid particles receivers enabling fairly high temperatures have been explored. These receivers lead to higher thermal efficiencies [31] and enable the utilization of alternative fluids in the TES [5]. Moreover, a particularly interesting option is the employment of alternatives fluids in the power cycle, substituting steam in an attempt to achieve higher thermal efficiencies of the power block. It is to note that this is of critical importance considering the fact that the thermal efficiency of the power cycle is the weakest step in the overall energy conversion process. This is shown in Figure 1.8 and in Eq. (1.1), where the overall efficiency of the plant is expressed as the product of the the efficiency of the individual energy conversion steps.

$$\eta_{overall} = \eta_{sf} * \eta_{rec} * \eta_{th} * \eta_{el} \tag{1.1}$$

In Eq. (1.1), the efficiency of the solar field represents the ratio from the concentrated solar radiation that is effectively captured by the heliostats and reflected on the aperture plane of the receiver to the solar irradiance on the field times the total aperture area of the heliostats (maximum amount of solar energy that can be captured by the heliostats). The definition of receiver efficiency η_{rec} is clarified in Figure 1.9 where $\dot{Q}_{abs}$ is the the amount of concentrated radiation striking the aperture plane of the receiver.

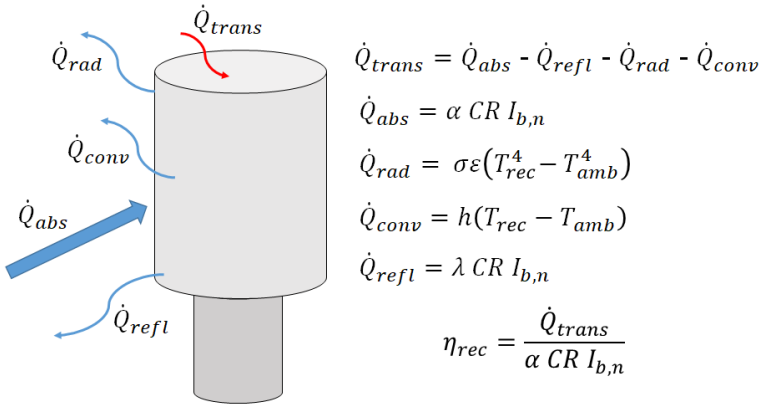

Figure 1.9: Heat balance of a solar receiver.

This value is then reduced to $\dot{Q}_{trans}$, which is the heat flux actually transferred to the receiver once the radiative ($\dot{Q}_{rad}$), convective ($\dot{Q}_{conv}$) and reflective ($\dot{Q}_{refl}$) losses are subtracted. All the formulations regarding these parameters, along with the definition of η_{rec}, are provided in Figure 1.9. The efficiency of the receiver η_{rec} is hence the ration from the thermal energy transferred to the working fluid to the the total incoming heat flux on the aperture plane. It usually takes high values, above 90% and it has little margin for further improvement [19]. The standard value of optical efficiency (η_{sf}) is in the order of 60%, considering an external cylindrical receiver. Again, several solutions have been proposed in literature to improve these values, such as the use of optimized novel fin-like receivers [32] or the use of innovative cavity

receivers [29, 33], but despite of small improvements in the order of 2-3% in η_{sf} [32], these are not able to overcome the major optical losses experienced by the system, in particular cosine, shadowing and spillage [34]. Finally, ηel is the electric generator efficiency, taking values that are usually above 95% due to its high TRL.

The remaining term in Eq. (1.1) is the thermal efficiency of the power cycle (η_{th}) which is currently in the order of 40% for standard Rankine cycles using steam turbine. This is a lower value than that of the former terms, and it has the potential to grow significantly if alternative fluids and cycle configurations are considered (note that raising this value to 50% brings about a 20% improvement in overall performance). One of the potential routes to achieving such higher efficiencies is the utilization of sCO_2 power cycles, due to a series of features that are thoroughly discussed in this thesis: much higher thermal efficiency, adaptability to high ambient temperature locations and small footprint.

Further to the foregoing discussion, and in order to better understand the real potential of sCO_2 power cycle technology to enhance SPT performance, the interactions between η_{rec} and η_{th} are now analyzed. To this end, let an "ideal" receiver (i.e. neglecting conductive, convective and other major optical losses and assuming $\alpha = \epsilon = 1$ and $\lambda = 0$). For this case, η_{rec} results to be strongly dependent on receiver temperature (T_{rec}) and on Concentration Ratio (CR), as shown in Figure 1.10(a) where the dependence of η_{rec} on the fourth power of receiver temperature and on the inverse CR, Eq. (1.2), becomes visible.

$$\eta_{rec} \approx 1 - \sigma\epsilon \frac{T_{rec}^4 - T_{amb}^4}{I_{b,n} CR} \tag{1.2}$$

Let now an ideal power cycle be considered. This ideal cycle would be a Carnot cycle, achieving highest thermal efficiency η_{th} for given receiver and ambient temperatures.The product of receiver and cycle efficiencies for this ideal case, herein called "system efficiency", is presented in Figure 1.10(b), representing the best possible power plant for a given solar field and electric generator. This parameter is extremely important since it credits the existence of an optimal receiver temperature T_{rec} yielding the most leveraged power plant design for each solar field technology (CR). Thus, considering concentration ratios ranging 400 to 1000 (standard values for SPT technology [35]), the optimum T_{rec} falls between 950 and 1200 K approximately, which is an intermediate/high temperature that results favorable for sCO_2 power cycles in comparison with conventional steam Rankine ones. This is shown graphically in Figure 1.11 where it becomes evident that Brayton-like sCO_2 power cycles achieve highest thermal efficiency in the temperature range of interest (obviously disregarding the Carnot cycle)[3]. Based on these results, this technology can be regarded as the best option to maximize the performance of next generation Solar Power Tower plants as expressed in Eq. (1.1).

The discussion presented so far in this section has credited an undeniable thermodynamic potential of sCO_2 power cycles applied to CSP plants. Nevertheless, several questions still re-

[3] It is acknowledged that the horizontal axis in Figures 1.10 and 1.11 do not represent the same parameter, but since turbine inlet temperature and receiver temperature are close to one another and they run in parallel, this does not preclude the conclusion reported in the text.

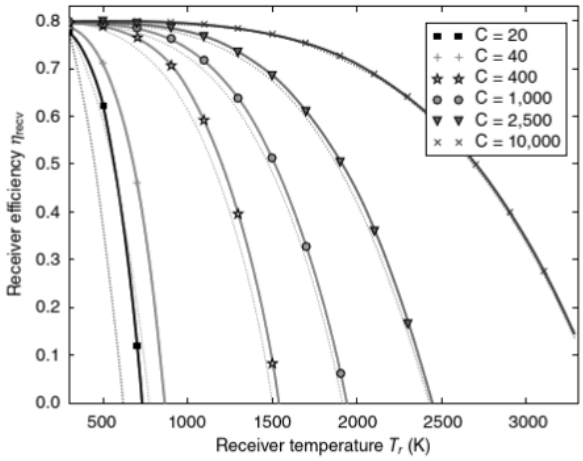

(a) η_{rec} as a function of T_{rec} and concentration ratio [36].

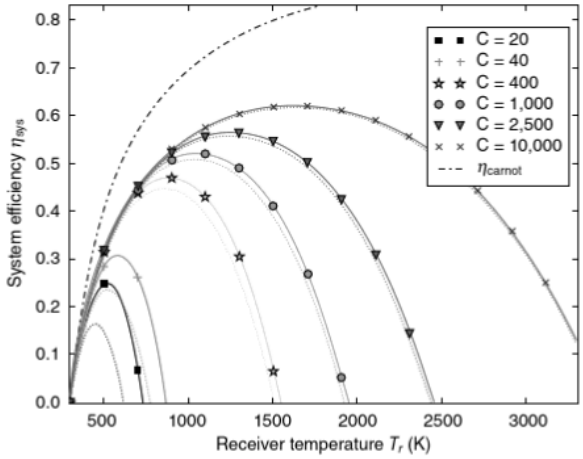

(b) System efficiency as a function of T_{rec} and CR [36].

Figure 1.10: Receiver and Carnot cycle efficiencies (η_{rec} and η_{Carnot}) and their combined effect as a function of receiver temperature and CR.

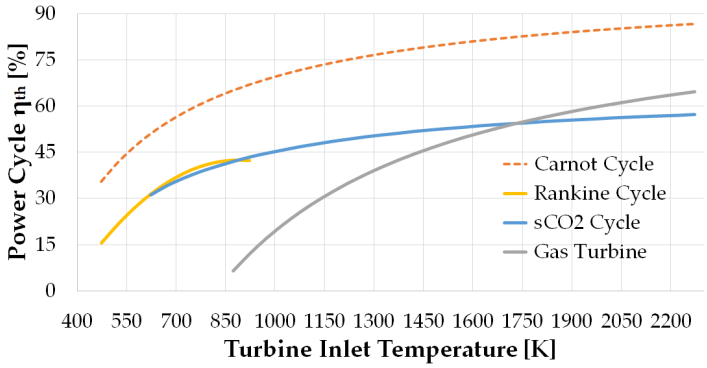

Figure 1.11: Dependence of cycle thermal efficiency (η_{th}) on turbine Inlet temperature, taking into account four different cycles. Minimum cycle temperature is set to 35ºC in all cases.

main unanswered and must be thoroughly discussed in order to fully understand its technical feasibility:

- For an actual power cycle, which is the operating temperature (receiver temperature) from which sCO_2 power cycles actually present better thermodynamic performance than current-state-of-technology steam cycles? Is this temperature achievable by the current or foreseen receiver technology?

- Even at a temperature range for which sCO_2 power cycles exhibit a clear thermodynamic advantage over contemporary steam technology, will they enable lower installation costs than state-of-the-art SPT plants?

- Will sCO_2 power cycles allow to significantly reduce LCoE of a CSP plant, making this technology competitive against steam driven SPT and fossil-driven gas or steam turbines? In particular, will sCO_2 power cycles serve to achieve the 6 ¢/kWh target cost of energy pursued by the Sunshot Program [37]?

1.3 An introduction to the current state of the art

In order to provide answers to these questions, a thorough review of the state of the art of the supercritical Carbon Cioxide (sCO_2) power cycle technology is mandatory. A brief introduction into it is provided in this section, aimed at helping the reader better understand the focus of this dissertation. Later on, Chapter 2 will present a longer and more detailed review of sCO_2 power cycles.

- **Fundamentals of the technology:** initially proposed by Feher [12] and Angelino [38] in the late 1960s, one of the very interesting features of this cycle is its ability to achieve high efficiency in a variety of applications operating at intermediate temperature: Concentrated Solar Power [39, 40], Waste Heat Recovery [41] and Gen IV nuclear reactors [42] amongst others. In his work [6], Angelino identified a certain range of turbine inlet temperatures (maximum cycle temperature) within which sCO_2 cycles were able to outperform both steam Rankine cycles (with preheating and reheat) and conventional Brayton cycles with state-of-the-art technology. Below the lower limit of this range, steam cycles would yield better performance whereas, above the upper level, conventional gas turbines (Brayton cycles) would be a more efficient choice.

  The limits of the temperature range for which sCO_2 is of interest depend also on turbine inlet pressure. Hence, considering intermediate pressures of about 130 atm (arond 13 MPa), the lower temperature limit turns out to be in the order of 550ºC whilst, if a higher pressure is considered (300 atm or about 30 MPa), this temperature increases to about 640 ºC, as shown in Figure 1.12. In this plot, it is easily observed that the sCO_2 cycles proposed by Angelino achieve thermal efficiencies higher than 53% at 700 ºC, as opposed to the 51% of double reheated steam cycles and 38.5% of an inter-cooled, non-recuperated Brayton cycle. This is very interesting information for CSP technology because, with the operating temperatures (550ºC) and pressures (15 to 30 MPa) of contemporary plants, there is virtually no advantage in using sCO_2 instead of steam. Therefore, higher temperatures are mandatory in order to substantially raise the efficiency of sCO_2-based CSP

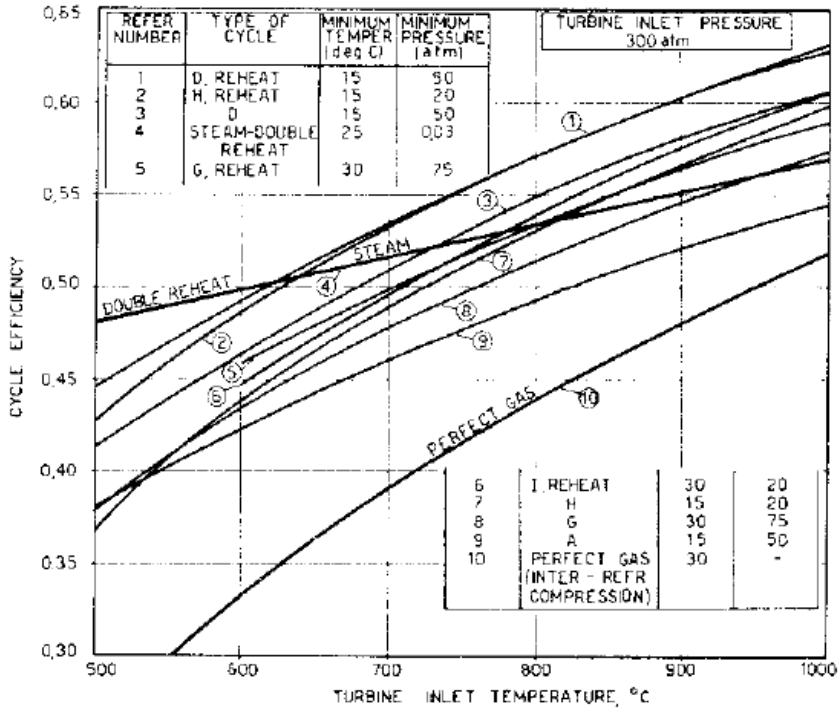

Figure 1.12: Performance of different carbon dioxide cycles in comparison with double reheat steam cycles and inter-cooled Brayton cycles at high turbine inlet pressure (300 atm) [6].

power generation with respect to state-of-the-art power plants.

A number of projects to develop sCO_2 technology are currently in progress worldwide, tackling different applications and exploring both fundamental aspects as well as other features related to commercialization. One of such initiatives is *NET Power's Clean Energy Demonstration Plant* [43], located in La Porte (Texas), which is the first large-scale power plant in the world operating with an sCO_2 cycle. This cycle is a semi-closed cycle, known as *Allam* cycle after its inventor, and it is based on the oxy-combustion of natural gas for efficient power generation and capture of pipeline-ready carbon dioxide. This plant presents a gross output of 25 MWe, although NET Power is currently working on a larger 295 MWe commercial facility. In addition to this project, the U.S. Department of Energy (DOE) is currently funding several projects through different programmes [39, 44], among which the *Supercritical Transformational Electric Power Project* (STEP Demo [45]) must be highlighted. This project, funded by DOE with $84 million, is lead by the Gas Technology Institute in collaboration with Southwest Research Institute, General Electric and the National Energy Technology Laboratory with the aim to design, build and operate a fully functional, integrated, pilot-scale power plant with 10 MW electric output, located in San Antonio (Texas). As the official site claims, "*STEP Demo will be among the largest demonstration facilities for sCO_2 technology in the world*".

Moreover, the Directorate General for Research and Development of the European Commission is also funding a number of projects. The *Supercritical CO_2 Heat Removal*

System (sCO_2 Hero [46]) is a project funded by the Horizon 2020 Research and Innovation programme, aimed at nuclear applications and marked in the Horizon 2020 programme. The *Supercritical CO_2 Cycle for Flexible & Sustainable Support to the Electricity System* (sCO2-Flex [47]) is funded by the same programme, with the aim to adapt a coal-fired power plant employing a 25 MW power block based on sCO_2 technology. Finally, the *Supercritical CARbon dioxide Alternative fluids Blends for Efficiency Upgrade of Solar power plants* (SCARABEUS [48]), funded by the Horizon 2020 programme, is the last European project to be started. With a strong participation by the University of Seville, the project is at developing sCO_2 blends with the ultimate objective of enabling condensation of the working fluid at very high ambient temperatures, thus increasing the efficiency and largely improving the economics of sCO_2-based CSP power plants.

In addition to these recent developments, the contribution of other smaller facilities to the development of sCO_2 technology in the past must also be acknowledged. Most of these facilities, at the micro (<500 kWe) or mini scale (<1 MWe), are located in USA (SANDIA National Laboratories [49, 50, 51, 52] , Bechtel Marine Propulsion Corporation [53, 54, 55, 56, 57], but there are also other systems in operation in Asia (KAERI and KAIST in South Korea [58, 59], Tokyo Institute of Technology in Japan [60] and the Nuclear Power Institute of China [61]), Europe (Research Centre Rez in Prague, Czech Republic [62]) and Australia (University of Queensland, [63]). Finally, a note on the single commercial available in the market must be made; this is an 8 MWe unit for Waste Heat Recovery developed by Echogen and currently commercialized by Siemens through Dresser-Rand [64, 65, 66].

The main topics for research and publication spread nowadays among turbomachinery, heat exchangers, off-design operation and further thermodynamic developments. This latter area is precisely the topic of the present thesis which aims to contribute a thorough and systematic theoretical analysis of the thermodynamic principles of the sCO_2 power cycle and on the economics of a potential for application to CSP. This has been identified by the author as a gap of the recent literature in the topic, which has mostly relied on the seminal works by Angelino and Feher. Indeed, the general approach followed by these authors got somehow lost in the last years when new layouts have continuously been proposed without providing a solid thermodynamic justification, hence leaving the aforelisted questions unanswered. This is thoroughly discussed in Chapter 2.

- **Installation Costs:** there are numerous technical analyses of sCO_2 power cycles, either from a thermodynamic standpoint or integrated into particular applications or energy sources, as commented in the previous paragraph. In contrast, there is still a great deal of uncertainty when it comes to the economic competitiveness of the technology. Some authors have tried to estimate the cost of sCO2 power cycles, from the fundamental work by Dostal [67] to contemporary works by NETL [68], SuperCritical Technologies Inc. [41], and the Massachusetts Institute of Technology [69]. More specifically, super-alloys for advanced power systems are studied by De Barbadillo et al. [70] and Cich et al. [71], while the cost of printed circuit heat exchangers (PCHE) is assessed by Hinze et al. [72] and Kim et al. [73]. The very recent work by Weiland et al. [74] is the last contribution to this task, providing cost estimation correlations for all the major components of

a sCO_2 power cycle, obtained from DOE data as obtained from vendors. Regarding concentrated solar power, NREL's System Advisor Model (SAM) [75] is the most common tool employed in literature for techno-economic analysis, also when using sCO2 cycles [76].

Further to the works cited above, it is worth noting that the vast majority of references in literature use cost estimates adapted to current-state-of-the-art CSP technology, with temperatures around 550 ºC and standard solar salts. When a sCO_2 power cycle is used, turbine inlet temperature must be increased in order to attain a significant thermodynamic gain (Fig. 1.12), and therefore alternative molten salts must also be employed. These features are loosely studied in literature, which raises the complexity of providing an accurate estimate of the installation costs of sCO_2-based CSP power plants. This is why, in the present dissertation, the cost estimation of all the major equipment, based on standard CSP technology and performed with SAM or with an in-house models, has been upgraded with a series of correction factors and uncertainty quantification to account for the singularities of sCO_2 blocks as opposed to those using steam turbines. This is considered an original contribution of this thesis.

- **Off-design Conditions:** as it can be deduced from the current state of development of the technology, the information about control of sCO_2 power cycles in partial load and transient conditions available in literature is limited. A number of publications have been produced in the last years, providing a small amount of test data coming from either theoretical analyses [77] or from the main experimental facilities mentioned earlier in this section. Amongst them, the contributions by SANDIA [78, 79, 80], Bechtel Marine Propulsion Corporation [57], Echogen [81] and KAIST [82] are worth noting. Moreover, a few dynamic models have been developed with the aim to predict off-design performance, such as the work presented by Direby et al. [80], using SANDIA's data for the compressors, and by Moyssetsev et al. [83], from Argonne National Laboratory. Other authors presented more specific studies as, for example, the transient characteristics during startup of one of the 100 kW class loops available in USA [84]. More recently, other publications have proposed other partial or complete dynamic models: Mahapatra et al [85] developed a software-based dynamic model of the STEP facility [45]; similarly, Zhang presented a dynamic model of a *Recompression* cycle employed in a CSP plant with thermal storage in Modelica Language [86]; finally, Wright et al. [87] also proposed a model to predict off-design performance of sCO_2 cycles for waste heat recovery applications. A very recent work that is worth noting has been developed by Allison et al. [88] using experimental data from the 1 MWe-scale sCO_2 test loop at SwRI, for which the design/control requirements of the facility are discussed.

  A final comment in regards to off-design performance prediction is to highlight that very little data or ready-to-use information is actually available. Most of the experimental data are confidential and most models make very case-specific simplifying assumptions which are not applicable to a different case or set of boundary conditions. For this reason, the author decided to develop a series of in-house models to predict off-design performance of heat exchangers and turbomachinery, along with some general assumptions about cycle control in CSP applications. This original work is thoroughly presented in Chapter 5 of the thesis.

In the light of this brief review of the current state of the art of sCO_2 technology, it becomes evident that no certain and univocal answers can be provided to the questions posed in the previous section. A deeper analysis of these three aspects (cycle configuration, cost estimation and off-design performance) seems therefore mandatory in order to understand the real potential and feasibility of Supercritical CO_2 power cycles for CSP power plants. This is the actual topic of the dissertation.

1.4 Structure of the dissertation

This thesis is divided into six chapters, each one of which corresponds to the different stages of the research:

- **Chapter 2 - State of the art**. This chapter presents a literature review focused on the sCO_2 power cycle technology. All the cycle layouts found in literature are described and categorized, providing a comprehensive classification with the aim to facilitate the comparison between different layouts. Both stand-alone and combined cycles configurations are taken into account.

- **Chapter 3 - Thermodynamic comparison**. The most interesting cycles amongst those reviewed in Chapter 2 are compared from a purely thermodynamic standpoint, considering steady-state conditions. First and Second Law efficiencies are used as figures of merit of this analysis, along with specific work. The aim of this study is to isolate the thermodynamic potential of each cycle from the inherent technical constraints brought about by the realization of the technology, hence providing a clear insight into the true potential of each cycle, regardless of the application.

- **Chapter 4 - Thermo-economic comparison**. In this chapter, the sCO_2 power cycle is integrated in a CSP plant with Thermal Energy Storage and a new thermo-economic comparison is carried out. On one hand, the installation costs for all the major equipment are assessed, calculating the Overnight Capital Cost per kW installed; on the other hand, the analysis is enriched with a new figure of merit, found to be extremely important both for the thermodynamic performance of the cycles and for their installation cost: the temperature rise experimented by molten salts in the solar receiver.

- **Chapter 5 - Partial Load Analysis and LCoE Assessment**. Among all the cycles considered in the previous chapters, two configurations are selected and their performance in off-design conditions are analyzed. This chapter presents off-design performance models of both heat exchangers and turbomachinery and different control strategies of the power cycle are discussed. Finally, the Levelized Cost of Electricity of a CSP power plant employing a sCO_2 power cycle is assessed using the free software SAM.

- **Chapter 6 - Conclusions**. The main findings of the research are discussed. Suggestions for future work are also given.

- **Appendix A - Heat Exchangers model**. Design and performance models of Printed Circuit Heat Exchanger are described in detail in this Appendix.

- **Appendix B - Off-design performance of the *Partial Cooling* cycle**. This Appendix provides all the results corresponding to the off-design performance of the *Partial*

Cooling cycle that are not included in Chapter 5. Providing these results in an appendix is aimed at reducing the overall length of the main report.

- **Appendix C - Off-design performance of the *Allam* cycle**. Akin to Appendix B, this annex provides the results corresponding to the *Allam* cycle.

- **Appendix D - Input Parameters to the System Advisor Model**. This appendix provides all the input parameters of the software used to perform techno-economic simulations in Chapter 5, in order not to increase the length of this part of the report.

1.5 Original contribution to knowledge

The core work of the present doctoral research is almost entirely original, even if some already-existing simulation tools have been adapted to be used in the parallel cycle analysis. For instance, the design model of Printed Circuit Heat Exchangers is developed with an in-house code based on an already existing model found in literature (see Appendix A). Nonetheless, the non-original content is explicitly highlighted throughout the dissertation, in order to separate original and non-original contents of the research.

The author would like to emphasize that the most salient original feature of this work is the approach used. Indeed, from the beginning, the dissertation tries to avoid preconceived ideas and to follow the mainstream research path defined by literature. Thus, in each step of the research, scientific questions are genuinely outlined, sometime even naively, and the answers obtained constantly shape the actual strategy and direction of the research, not vice-versa. As said, the result of this unconstrained thinking is a novel approach to the analysis of sCO_2 power cycle technology, which is thought to provide a clear insight into the most interesting layouts from a thermodynamical point of view, regardless of the application, and also into the actual techno-economic feasibility of the most suitable ones for CSP plants.

Finally, it is also to note that the content of this dissertation has partially been presented in several scientific papers, published in either high-caliber journals such as *Applied Energy*, *Renewable Energy* and the ASME *Journal of Engineering for Gas Turbines and Power* or presented at leading conferences, as commented in the introduction of each chapter. This is regarded as an indirect (or maybe direct) measurement of the originality and archival value of the research.

1.6 List of publications

Parts of this work have already been published in scientific journals and presented at technical conferences, as indicated at the beginning of each chapter. The following five publications have been produced by the author with assistance by the supervisors of the thesis and other peers at the University of Seville, plus a collaboration with SwRI and Alpha Laval (paper presented at ASME Turbo Expo 2017):

- F. Crespi, G. Gavagnin, D. Sánchez, G.S. Martínez, *Supercritical carbon dioxide cycles for power generation: A review*, **Applied Energy** 195, 152–183 (2017).

- F. Crespi, D. Sánchez, J.M. Rodríguez, G. Gavagnin, *Fundamental Thermo-Economic*

Approach to Selecting sCO2 Power Cycles for CSP Applications, **Proceedings of 4th International Seminar on ORC Power Systems**, Milan, IT, (2017).

- F. Crespi, D. Sánchez, K. Hoopes, B. Choi, N. Kuek *The Conductance Ratio method for off-design heat exchanger modeling and its impact on an sCO2 Recompression cycle*, **Proceedings of ASME Turbo Expo 2017**: Turbomachinery Technical Conference and Exposition, Charlotte, NC, (2017).

- F. Crespi, D. Sánchez, J.M. Rodríguez, G. Gavagnin, *A Thermo-Economic Methodology to Select sCO2 Power Cycles for CSP Applications*, **Renewable Energy**, (2018). (This paper is an extended version of the one included in the Proceedings of 4th International Seminar on ORC Power Systems in 2017)

- F. Crespi, G. Gavagnin, D. Sánchez, G.S. Martínez, *Analysis of the Thermodynamic Potential of Supercritical Carbon Dioxide Cycles: a Systematic Approach*, **Journal of Engineering for Gas Turbines and Power** 140, 051701-1–10 (2018).

- F. Crespi, D. Sánchez, T. Sánchez, G.S. Martínez, *Capital Cost Assessment of Concentrated Solar Power Plants Based on Supercritical Carbon Dioxide Power Cycles*, **Journal of Engineering for Gas Turbines and Power** 141, 071011-1–9 (2019).

The author would also like to highlight another work produced by the author himself in collaboration with other peers of Politecnico di Milano after his M.Sc. thesis, that, in spite of not being directly connected with the main topic of the present dissertation, helped the author to better understand construction and operation issues of CSP technology:

- F. Crespi, A. Toscani, P. Zani, D. Sánchez, G. Manzolini, *Effect of passing clouds on the dynamic performance of a CSP tower receiver with molten salt heat storage*, **Applied Energy** 229, 224–235 (2018).

2 Thermodynamics of Supercritical CO_2 Cycles. Literature Review

*This second chapter presents the review of the **state of the art** of **sCO_2 power cycles**. Firstly, the pathway from closed cycle gas turbines to sCO_2 cycle is discussed, along with an analysis of the seminal works of **Angelino and Feher**. Secondly, a total of **forty two stand-alone layouts** and **thirty eight combined cycles** resulting from a thorough literature search are categorized following original criteria aimed to unambiguously describe the configurations based on their thermodynamic characteristics. Finally, a quantitative and qualitative comparison between all the cycles taken into account is made, based on the data available in literature.*

The contents of this chapter are partially available in:

F. Crespi, G. Gavagnin, D. Sánchez, G.S. Martínez, 2017, *Supercritical carbon dioxide cycles for power generation: A review*, Applied Energy 195, pp. 152–183.

2.1 Historical approach to the closed cycle gas turbine

Closed cycle gas turbines were proposed some seventy five years ago by Dr. Curt Keller from Escher-Wyss, Switzerland, as a means to increase efficiency beyond the values achieved by contemporary steam turbines [89]. Numerous advantages over steam and open cycle gas turbines were claimed: high part load efficiency, efficient fuel utilization, reduced environmental impact, modular small-scale design, high efficiency over a wide range of power-to-heat ratios and compressor/turbine isolated from combustion products and environmental contamination.

The closed cycle gas turbine technology was nevertheless obscured in the late 1960s by a step improvement of open cycle combustion turbines thanks to the introduction of new materials and blade-cooling technologies, which enabled higher firing temperatures. All of a sudden, conventional gas turbines reached comparable and even higher efficiencies with much lower installation costs, and superseded the formerly leading technology, also due to the low prices of natural gas.

A new technology based on the closed cycle gas turbine was however proposed in this period: the supercritical CO_2 power cycle. It was actually an update of the already existing closed cycle engines with the introduction of this novel working fluid,carbon dioxide, which presented dense (real) gas behavior throughout the compression process due to the vicinity of the critical point. This particular feature enabled large reductions in compression work, therefore

increasing the overall thermal efficiency even at moderate turbine inlet temperatures. Even if the first sCO_2 cycle ever proposed was a partial condensation Brayton cycle patented by Sulzer in the late 1940s [90], the first landmark in the development of the supercritical CO_2 power cycle was set by the original works by Gianfranco Angelino (1968) [38, 6] and Edward Feher (1967-1969)[12, 91]. These authors, working in Europe (Politecnico di Milano, Italy) and United States (Douglas Aircraft Co.) respectively, presented the theoretical fundamentals of this innovative technology and proposed a series of possible configurations of the working cycle. They drew attention to the great potential of carbon dioxide used as working fluid in supercritical and transcritical power cycles, thanks to its advantageous thermodynamic properties. Soon after Angelino and Feher's seminal works, a few studies were developed by Strub and Frieder [92], a team at General Electric [93] and others but after little time the interest decayed and the technology was almost abandoned. It was not until forty years later that Vaclav Dostal revived the interest in the sCO_2 power cycle with the publication of his doctoral thesis in 2004 [67]. Dostal did a thorough review of the works by Angelino and Feher, both thermodynamically and technologically, and proposed some modifications in the cycle layouts. Starting from this publication, aimed at finding alternative technologies for nuclear reactors of a new generation, the sCO_2 Brayton power cycle has captured increasing attention by the scientific and industrial communities. As of today, this cycle is acknowledged as one of the most promising technologies for the next generation of power systems, provided that the technical challenges inherent to the high pressures and temperatures are successfully overcome.

2.2 The sCO_2 power cycle

2.2.1 Original works by Angelino and Feher

Most of the thermodynamic cycles studied by the scientific community today and those implemented in the few experimental loops available derive from the initial proposals of Angelino and Feher [38, 12]. For this reason, and in order to better understand the evolution of sCO_2 technology, it is worth starting from a comprehensive review of their work.

Several configurations of condensation (transcritical) cycles were set forth by Angelino in [38], with the main argument that standard Brayton cycles (gas turbines) yielded lower efficiency than Rankine cycles (steam turbines) when considering similar turbine inlet temperatures. As opposed to these though, the utilization of carbon dioxide at supercritical pressures was claimed to be able to provide the same or even higher efficiency than steam turbines whilst still retaining the simplicity of closed cycle gas turbines. Initially, Angelino considered a simple transcritical condensing cycle with a recuperative layout for which it was observed that the main contribution to inefficiency (irreversibility) came from the recuperative heat exchanger. For this reason, a series of layout modifications were devised by Angelino, aimed at reducing these losses and increasing cycle efficiency. To this end, a *Partial Condensation* cycle was proposed, with a reduced mass flow in the low temperature recuperator that managed to largely reduce the losses in this equipment. This cycle was actually the forerunner of the modern *Recompression* cycle where the low pressure carbon dioxide stream is split into parallel compression processes in order to achieve the same effect on the irreversibility of the low temperature recuperator.

The main shortcoming of the previous cycle was that turbine exhaust pressure was imposed by condenser pressure. Therefore, in order to make these two pressures independent from one another, a modification of the cycle layout was proposed whereby an additional compressor ensured pressure flexibility and convergence at the same time. This modified layout can be named *Partial condensation with precompression*[1] cycle and its modern evolution is the *Partial Cooling* cycle. Moreover, in order to attenuate sthe effects of high temperatures and pressures at turbine inlet, Angelino proposed a modification whereby the high pressure carbon dioxide flowing out from the high temperature recuperator was expanded (before entering the heat adder) in a high pressure, moderate temperature turbine. Thanks to this, turbine inlet pressure was reduced and hence the mechanical design of this component was made easier. This cycle can be named *Partial condensation with pre-expansion* cycle. Finally, the last modification of the base cycle layout in Angelino's work is the *Total condensation with precompression* cycle, very similar to the *Partial condensation with precompression* though, in this case, without the low pressure flow-split before compression. The advantage of the *Total condensation with precompression* cycle is the reduction in the number of components; on the negative side, the condensation section operates with all the mass flow rate and therefore the equipment have larger size and duty.

Contemporary to Angelino, Feher studied alternative power cycles which could potentially improve the performance of state-of-the-art Rankine and Brayton cycles [12]. The proposal of this author was built upon a purely supercritical cycle (halfway from Rankine to Brayton cycles) which could be implemented with either water-steam or carbon dioxide. The advantages of this cycle, as claimed by the author, were twofold. On one hand, the capability to overcome some of the limitations inherent to Rankine cycles such as temperature restrictions, turbine exhaust in saturated steam/vapor conditions and a large number of turbine stages (due to the large expansion ratios). On the other, the possibility to solve restrictions of Brayton cycles such as large compression work (fluid in gaseous state), high sensitivity of cycle performance to pressure drops and compressor efficiency and large heat transfer areas due to the low density at the usual operating pressures. A modified version of this cycle was also mentioned by the author, wherein pump inlet is below the critical pressure. This cycle, termed *pseudo-Supercritical* cycle by Feher, resembles the condensation cycle presented by Angelino in [38].

The final conclusions drawn by Feher are similar to those presented by Angelino. Both authors agree that the supercritical cycle enables higher efficiencies (ca. 50%) than conventional Brayton cycles with moderate turbine inlet temperatures. Also, with respect to Rankine cycles, supercritical carbon dioxide cycles offer potentially higher efficiencies at temperatures higher than some 600ºC but, more interestingly, with much smaller footprint. The main flaw of both analyses is nevertheless the oversimplification of the thermodynamic calculations as some of the assumptions are far from reality and yield misleading results. For instance, it is not realistic to neglect pressure drops in a system operating at 200 bar, or to consider ideal compression and expansion processes (both in Feher). This concern about the results obtained by Angelino is shared by Dostal et al. in [67] where it is stated that the assumptions made by the former author regarding turbomachinery efficiency must be updated (mainly for the compressor and pump) and the same applies to the pinch point differences in the high and low temperature

[1] Note that this name was not given in the original work by Angelino. It is a term proposed by the author of this work to better track the different layouts.

recuperators. The same authors indicate that the pressure losses considered by Angelino are too optimistic and thus the efficiency of the more complex cycles would have to be corrected to a lower value. In any case, these observations are valid for thermal efficiency only as nothing is said about auxiliary power or mechanical losses. With all this in mind, it is concluded that the figures obtained by Angelino and Feher in their fundamental contribution provide a very good initial approach to the topic even if they cannot be extrapolated to a practical case.

2.2.2 Categorization criteria

The sCO_2 power cycles taken into account in this work present a great variety of thermodynamic features. They can be fully supercritical or transcritical, with total/partial condensation or without it, simple or combined cycles, recuperative or not, etc. In order to properly analyze the differences between the various configurations, a categorization of the proposed layouts is required. The basic idea of the present work is therefore to organize the massive amount of information collected in literature, allowing a more comprehensive approach to sCO_2 cycles. To this end, the following assumptions have been made:

- **Fundamental division between simple and combined cycles.** Firstly, the cycle proposals found in literature are divided in two main groups: simple and combined cycles. It is nonetheless possible that the same cycle layout (for instance *Recompression*) appears in both categories, depending on whether that layout is used as a stand-alone power system or if, on the contrary, it is used in combination with other systems in a combined cycle application. In the former, the objective is to achieve highest cycle efficiency whilst, in the latter, the aim is to achieve the best combined performance of the waste heat recovery unit and the bottoming cycle [94]. This will be further explained later.

- **No discrimination between purely supercritical and transcritical cycles.** This means that, considering the same cycle layout, in the present categorization there is no difference between a Rankine or a Brayton cycle. Although it is acknowledged that from a component design standpoint this assumption is misleading, it is still valid conceptually. It enables a substantial reduction of the number of cycles taken into account and is based on two considerations:

  - The layouts used in a pseudo-Brayton or in a pseudo-Rankine sCO_2 cycle can be identical, except for the particular compression device (pump or compressor) and lowest temperature heat exchanger (cooler or condenser). This also makes it theoretically possible to shift from a transcritical to a supercritical cycle by merely changing the temperature and/or pressure at the inlet to the compressor [6, 95].
  - The thermodynamic features that characterize a given layout remain essentially unaltered when changing from transcritical to supercritical working conditions [6, 96].

- **No discrimination between cycles with or without condensation.** Akin to the previous assumption, the proposed categorization remains focused on the layout of the cycle, neglecting whether or not there is condensation of CO_2 during the heat rejection process. This assumption is even more important in the context of the cycle being supercritical or transcritical. Transcritical and condensing are not synonyms [97] even if they are sometimes considered equivalent. A supercritical cycle, whose reduced pressures and

temperatures are always higher than one, might feature condensation (supercritical condensation) whilst a transcritical cycle (reduced pressures and temperatures higher/lower than one depending on cycle station) might either present total/partial condensation (pseudo-Rankine) or just cooling without condensation (pseudo-Brayton). Thus, the same cycle layout can theoretically belong to either category, transcritical or supercritical, without this meaning that condensation is automatically implemented/discarded.

- **No discrimination based on the type of heat source.** An important characteristic of the sCO_2 power cycle is its applicability to a large number of different heat sources, due to its high efficiency in a wide temperature range. As further explained in section 2.6 (Table 2.4), the applications already considered range from nuclear power to concentrated solar power, and also combined cycles with gas turbines or fuel cells. The result is that the same cycle layout is found several times in literature with different temperature and pressure levels, even if the associated thermodynamic fundamentals remain the same. For the sake of generality, and in order to avoid repetition, the cycles in this work are not categorized according to their application/heat source but focusing on the layout and thermodynamic fundamentals. A direct consequence of this assumption is that cycles presenting oxy-combustion (internal combustion) and others that are externally fired might fall in the same category. This means that cycles operating on gas mixtures (typically 92—96% CO_2 and 4—8% of H_2O , N_2 and other combustion products) or CO_2 only are treated as a single cycle if they share the same layout.

- **Cycles labeled with a code based on thermodynamic features, excluding condensation.** This last assumption is the main argument to assign a certain category. Taking inspiration from [98], a system of labels is set up by the authors in order to unambiguously describe the cycle layout based on its thermodynamic characteristics. The features considered are: internal heat recovery (and number of recuperators), reheat, intercooling, flow-split before compression, flow-split before expansion, flow-split before heating and flow-split before heating-expansion (Table 2.1). Using this system, a *Simple Recuperated Brayton* cycle comprising compressor, heater, turbine, recuperator and cooler would be termed "R1". Adding reheat would change the code to "R1-RH" and considering intercooled compression and a two-stage internal heat recovery (low and high temperature recuperators) would yield "R2-RH-IC".

Symbol	Thermodynamic Feature
R	Internal heat recovery (recuperator)
IC	Intercooled Compression
RH	Reheated expansion
SFC	Split-flow before compression
SFE	Split-flow before expansion
SFH	Split-flow before heating
SFHE	Split-flow before heating and expansion

Table 2.1: Categorization criteria.

2.3 Stand-alone cycles

The different configurations found in literature are summarized in Table 2.2 and described in the following subsections.

Cycle Number	Cycle Name	Category Label	References
1	*Simple Recuperated*	*R*1	[12, 50, 53, 58, 61, 67, 91, 99-124]
2	*Transcritical* CO_2	*R*1	[6, 38, 125-129]
3	*Hot day*	$R1-IC$	[130, 109]
4	*Allam*	$R1-IC$	[131-135]
5	*Intercooling II*	$R1-IC$	[101, 113]
6	*Brayton* CO_2 *GT*	$R1-IC$	[136]
7	*Reheating II*	$R1-RH$	[101, 113]
8	*Split – Expansion*	$R1-RH$	[101, 113, 110]
9	*Matiant*	$R1-IC-RH$	[137, 138, 139]
10	*Allam + RH*	$R1-IC-RH$	[132]
11	*Forced Cooler*	$R1-IC-RH$	[140]
12	*DEMO*	$R1-IC-RH$	[141, 142]
13	*Preheating*	$R1-SFH$	[101, 113]
14	$S-EJ$	$R1-SFE$	[143]
15	*Inter – Recuperated*	*R*2	[101, 113]
16	*Recompression*	$R2-SFC$	[6, 8, 11, 38, 58, 61, 67, 96-107, 109-118, 120-123, 129, 144-158]
17	*BAS*	$R2-SFC$	[159, 160]
18	*Precompression*	$R2-IC$	[38, 6, 67, 99, 103, 111, 113, 11]
19	*Recuperated CPOC*	$R2-IC$	[161]
20	*Partial Cooling*	$R2-IC-SFC$	[38, 6, 99, 100, 67, 103, 109, 111, 115, 116, 146, 11, 122, 129]
21	*Intercooling I*	$R2-IC-SFC$	[97, 116, 136, 120, 129]
22	*Reheating I*	$R2-RH-SFC$	[97, 99, 103, 116, 108, 120, 123]
23	*Double Reheated Recompr.*	$R2-RH-SFC$	[121]
24	*Driscoll*	$R2-SFH$	[162]
25	*REC*2	$R2-SFC-SFH$	[150, 163]
26	*Turbine Split Flow I*	$R2-SFHE$	[101, 113]
27	*Turbine Split Flow II*	$R2-SFHE$	[101, 113]
28	*Turbine Split Flow III*	$R2-SFHE$	[101, 113]
29	$RC-EJ$	$R2-SFC-SFE$	[143]
30	*Recompression + IC + RH*	$R2-IC-RH-SFC$	[116, 108, 120, 164]
31	*Partial Cooling + RH*	$R2-IC-RH-SFC$	[116, 108, 164]
32	$MC-EJ$	$R2-IC-SFC-SFE$	[143]
33	*Double Recompression*	$R3-SFC$	[97]
34	*Partial Cooling w/ Impr. Recup.*	$R3-IC-SFC$	[6, 67, 111, 99]
35	*Cascade*	$R3-SFC-SFHE$	[105]
36	*REC*3	$R3-SFC-SFH$	[159, 150, 163, 160, 165]
37	*Schroder – Turner*	$R3-IC-RH-SFC-SFE$	[166, 167]
38	*Quasi – combined*	$R3-IC-RH-SFC-SFHE$	[168]
39	*Rankine w/ Reheat*	RH	[169, 110]
40	*Rankine w/ ejector*	$SFC-SFH$	[170, 110]
41	*CPOC*	IC	[161, 149]
42	*TCO*	$IC-RH$	[171]

Table 2.2: Summary list of stand-alone cycles.

2.3.1 R1

The *Supercritical Simple Recuperated* cycle (Figure 2.1) is a simple recuperated Brayton cycle adapted to the supercritical region. It is aimed at overcoming (to the extent possible) the inherent limitations presented by a standard/classic Brayton cycle, such as the very high compression work and large heat transfer areas due to a low specific volume. Taking advantage of the thermo-physical properties of carbon dioxide in the supercritical region, not only is compression work drastically reduced, but the resulting system is also much more compact and less sensitive to pressure drops. The reduction of compressor work brings about a lower compressor delivery temperature which, in combination with the low pressure ratio and recuperative nature of the cycle, brings about a substantial rise of thermal efficiencies.
This process is nonetheless more complex than in a standard Brayton cycle, due to the large variations of CO_2 properties near the critical point, and it also has technological implications

on the design of turbomachinery and heat exchangers. Indeed, the aerodynamic design of the compressor is halfway from hydraulic to thermal machinery theory [172] and the occurrence of an internal pinch point in the low temperature recuperator or in the cooler is also likely. The latter circumstance is caused by the strong influence of temperature and pressure on specific heat (c_{p,sCO_2}) and adds up to the dissimilar heat capacity ($C_{p,sCO_2} = \dot{m} \cdot c_{p,sCO_2}$) of the hot and cold sides of the recuperator. The cumulative effect is a twofold restriction on heat exchanger effectiveness, as clearly discussed in [67], which poses a limitation on the attainable efficiency of the cycle (reduced recuperative capacity) [173]. As an example of how this limitation could be overcome, Manente and Lazzaretto [174] propose a cascaded cycle composed by two separated *Supercritical Simple Recuperated* cycles to recover waste heat from a biomass combustion process. This configuration is termed *Simple Cascaded sCO_2 power cycle*, the term *cascaded* indicating that the two *Simple Recuperated* systems are actually two stand-alone cycles that collect waste heat at different temperature levels.

The *Transcritical CO_2* cycle in Figure 2.1 presents the same conceptual configuration as the *Supercritical Simple Recuperated* but turns out to be a pseudo-Rankine cycle. Recurrently proposed in [125, 126, 127, 119], this cycle fits in with low-temperature waste heat recovery applications and its use is also proposed in combined cycle applications (see Section 2.4.2).

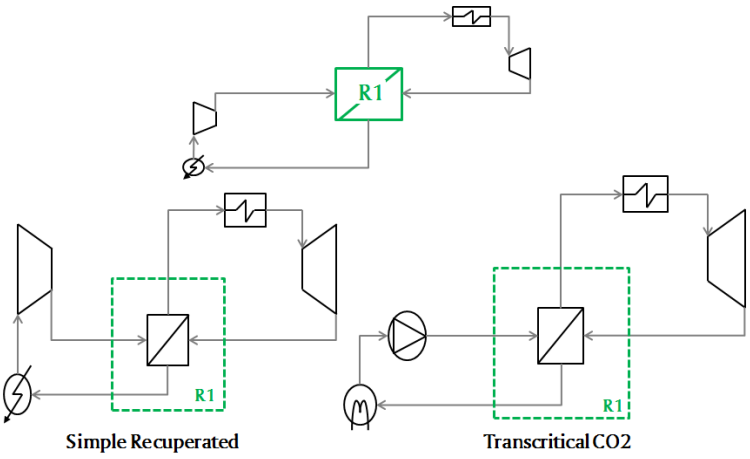

Figure 2.1: Stand-alone R1 cycles.

2.3.2 R1-IC

The *Hot Day* cycle, the *Allam* cycle, the *Intercooling II* cycle and the *Brayton CO_2 gas turbine cycle with two intercoolings* fall into the same category (Figure 2.2). They are all single-flow recuperative cycles with intercooled, multistage compression.

The *Hot Day* cycle is named after US Patent 8,783,034 [130]. It is a transcritical cycle developed by ECHOGEN and specifically designed for waste heat applications [109]. It is actually an evolution of the *Simple Recuperated* cycle that incorporates a three-step compression process with two compressors and a pump separated by an intercooler and a condenser respectively (or three compressors with two intercoolers in a different embodiment). The stream leaving

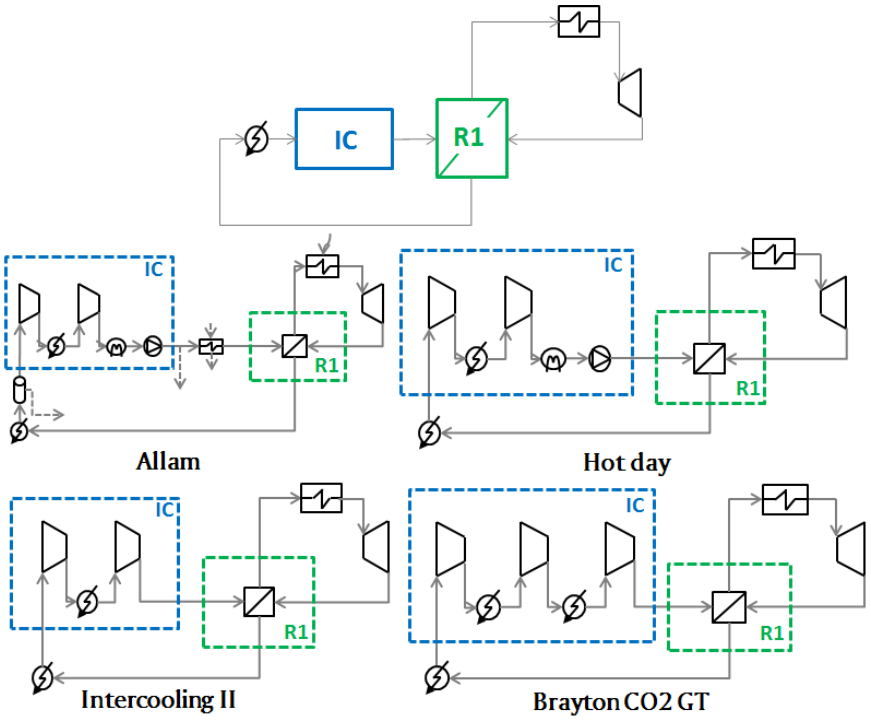

Figure 2.2: Stand- alone R1-IC cycles. General layout (top) and particular embodiments (center and bottom).

the pump flows into the recuperator and follows the standard layout of the *Simple Recuperated* cycle.

The *Allam* cycle (named after its lead inventor) is an oxy-fired cycle, combusting natural or synthetic gas with pure oxygen produced by an Air Separation Unit. The main features of this cycle are the very high efficiency and the capability to capture pipeline ready CO_2 without any auxiliary physical/chemical absorption system [131]. The *Allam* cycle results to be a highly recuperative cycle due to the internal recuperators and the thermal integration between the power cycle and the Air Separation Unit (needed of substantial cooling to reduce compression work of the various streams). The CO_2 cycle is of the semi-closed type. The CO_2-rich combustion gases are expanded in a turbine downstream of which they are cooled down in a staged recuperator. Then, water separation takes place before intercooled compression (gas compression first and then liquid compression in a pump). A fraction of this high pressure carbon dioxide is sent to storage (pipeline ready) whilst the rest flows towards the recuperator and combustor. Further optimization of this cycle with the integration of a coal gasification system is discussed in [134].

The *Intercooling II* cycle (or simply "Intercooling" in [101]) is an evolution of the *Supercritical Simple Recuperated* cycle, with the addition of intercooled compression, originally proposed for nuclear applications. The same applies to the *Brayton CO_2 gas turbine cycle with two intercoolings*, proposed by Muto in [136], which is also a variation of the basic *Supercritical Simple Recuperated* layout. The main difference between these two is that the *Brayton CO_2 gas*

turbine cycle with two intercoolings presents two intercoolers and it is specifically designed for solar thermal power plants.

2.3.3 R1-RH

The introduction of reheating enables a twofold improvement of cycle performance: expansion work increases and the thermal stresses due to the high pressures and temperatures at turbine inlet are largely reduced. Two cycles proposed by Ahn and Lee [101] result when reheating is implemented in the *Supercritical Simple Recuperated* cycle: the *Reheating II* cycle and the *Split Expansion* cycle (also proposed in [110]), Figure 2.3. The only difference between these two cycles is found in the heat addition process. In the first one, heat is added to the cycle in two steps (heater and reheater). In the second one, the high pressure outlet flow of the recuperator flows directly into the first turbine stage, without any addition of external heat, and is then reheated (external heat addition) before entering the low pressure turbine.

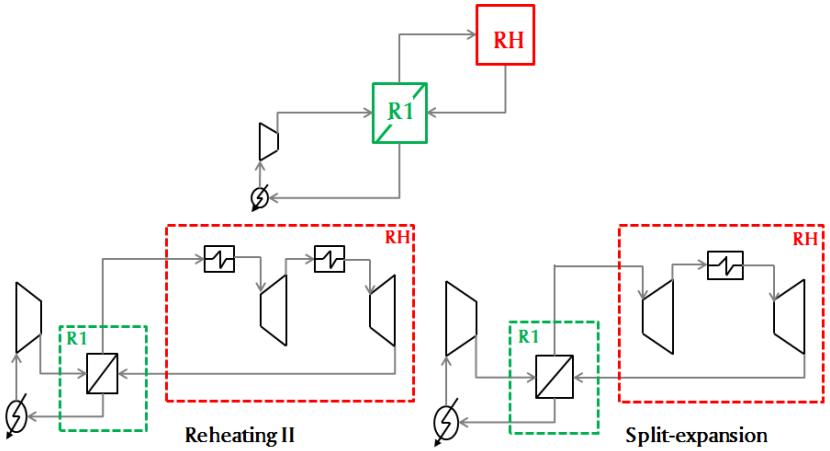

Figure 2.3: Stand-alone R1-RH cycles. General layout (top) and particular embodiments (bottom).

2.3.4 R1-IC-RH

This section includes those recuperative cycles that are characterized by a multi-stage intercooled compression and a reheated (therefore two-stage) expansion (Figure 2.4). The first cycle presented is the *Matiant* cycle, named after its inventors Mathieu and Iantovski [137, 138, 139]. It is an oxy-combustion cycle whose original feature is the presence of three expanders, one of them located in the middle of the heating process. As already seen for the *Allam* cycle, the *Matiant* cycle has the capability to capture and deliver pipeline-ready CO_2 produced during the oxy-combustion process.

The *Allam cycle with reheating* also falls in this category. It is just a basic *Allam* cycle incorporating a second turbine after reheat [132]. The *Forced Cooler* cycle [140] is an evolution of the *Supercritical Simple Recuperated* cycle with the addition of intercooling and reheat. The name of this configuration is due to the addition of an extra-cooler (namely *Forced cooler*) between

the standard cooler and the first compressor. The *Forced cooler* consists of a heat exchanger connected to a two-stage vapor-compression refrigeration cycle with a flash chamber, using R134-a as working fluid [140]. A series of different embodiments of this cycle are proposed in literature, with two or three compression stages, all of which belong to the present category. Therefore, the authors have decided to cite the one with two-stage intercooled compression only for the sake of simplicity.

The *DEMO* cycle, proposed by Yantovsky [141, 142] is almost identical to the *Allam cycle with reheating* with the addition of a high pressure turbine right after the recuperator. Therefore, this cycle presents a double reheat process with a sort of sequential oxy-combustion, three intercooled compressors in series and a pump for the last compression stage. A variant of the *DEMO* cycle is herein termed the *ALSTOM* cycle, devised by H.U. Frutschi and patented by ALSTOM technology Ltd. [175]. This incorporates one single compressor before the liquid compression stage (pump) and a single reheat.

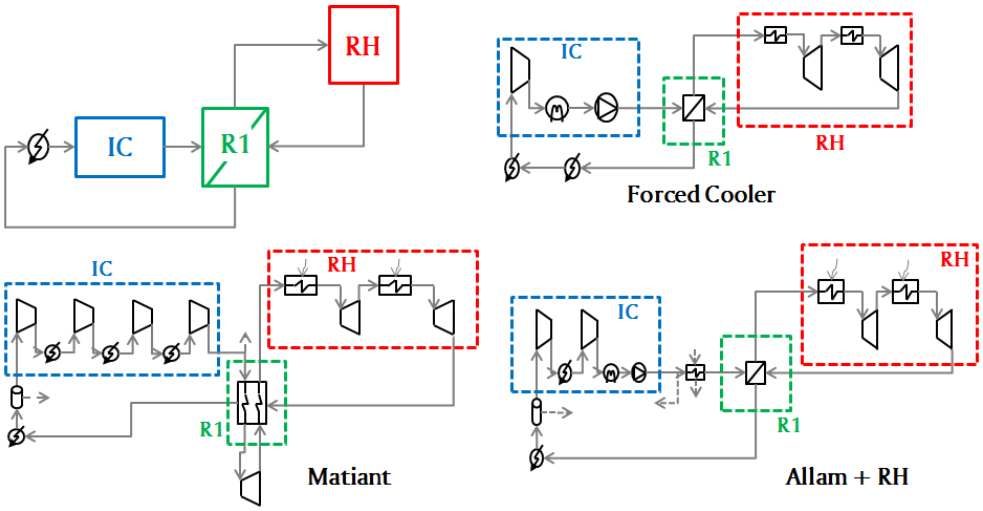

Figure 2.4: Stand-alone R1-IC-RH cycles. General layout (top) and particular embodiments (center and bottom).

2.3.5 R1-SFH

In the *Preheating* cycle [101], Figure 2.5, the supercritical CO_2 flow is split in two streams downstream of the compressor. One stream flows into the recuperator whilst the other flows into a first heater. Both flows are then mixed into a single stream and heated up in a second heater, downstream of which the turbine is located. Proposed for nuclear applications, this layout tries to better fit with the configuration of the heat source.

2.3.6 R1-SFE

The *S-EJ* cycle, proposed by Vasquez in [143], is a *Supercritical Simple Recuperated* cycle assisted by an ejector located upstream of the heater, Figure 2.5. The high-temperature CO_2 leaving the heater is split in two streams. One fraction is expanded in a turbine and then follows the standard Brayton cycle flowing into the recuperator. The remaining fraction enters

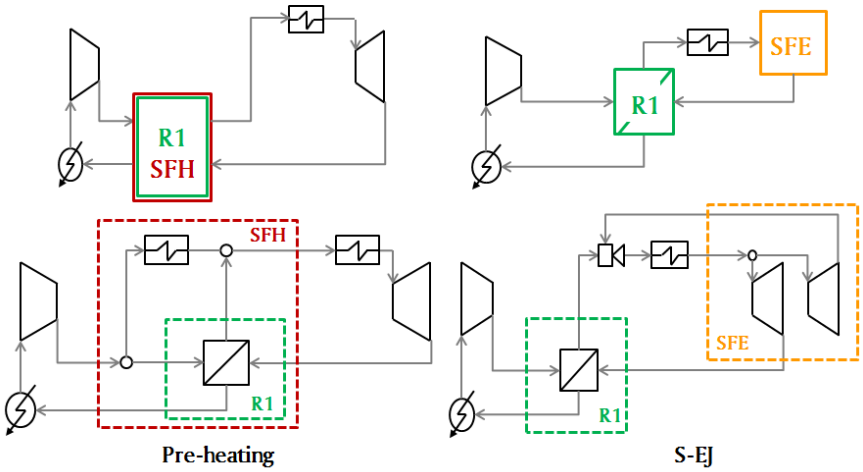

Figure 2.5: Stand-alone R1-SFH and R1-SFE cycles. General layouts (top) and particular embodiments (bottom).

a second turbine downstream of which it is directed to an ejector for mechanical compression. The addition of an ejector can result in a significant increase of thermal efficiency according to Vasquez, due to the compression brought about by the different velocities of the injected gas and the jet gas (motive fluid) [176].

2.3.7 R2

Label *R2* stands for a single-flow, highly recuperative cycle characterized by the presence of two recuperators, Figure 2.6. The *Inter-recuperated* cycle [101] is based on the *Supercritical Simple Recuperated* but incorporates a different configuration of the recuperation process. Thus, the latter is divided in two different heat exchangers, one of them located between the compressors.

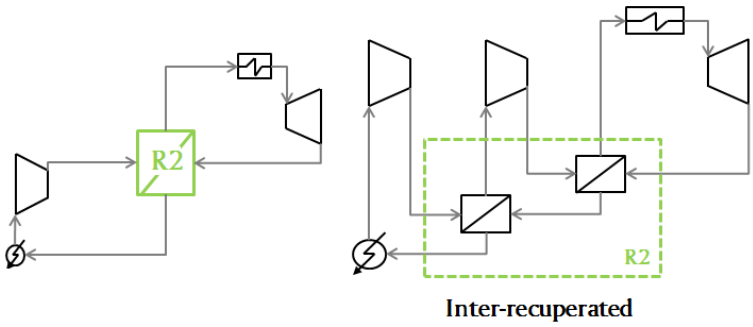

Figure 2.6: Stand-alone R2 cycles. General layout (top) and particular embodiment (bottom).

2.3.8 R2-SFC

The *Supercritical Recompression* cycle (Figure 2.7) is the evolution of the previous configuration proposed by Angelino [38, 6] and has evident connections with Feher's work [12]. The cycle is named after the re-compressor located in parallel with the main compressor, which

means that the flow is split in two for the compression process. The first stream flows into the cooler where its temperature is reduced to a value close to the critical temperature. The second stream is not cooled but compressed directly in the re-compressor. The benefits of this layout are twofold. First, the pinch point problem in the low temperature recuperator is attenuated due to the change in heat capacity that is brought about by the dissimilar mass flow rates on the high (reduced flow) and low pressure (full flow) sides of the equipment. Second, the thermal duty of the cooler is also reduced, hence reducing the size of this equipment. The *Supercritical Recompression* layout is the most extensively researched cycle in literature along with the *Supercritical Simple Recuperated*, as credited by the references in Table 2.2. Finally, the *Supercritical Recompression* configuration is used by Manente and Lazzaretto in the *Part-flow cascaded sCO_2 power cycle* [174], followed by a *Supercritical Simple Recuperated* cycle, and by Johnson and McDowell [177], followed by another *Supercritical Recompression* cycle.

The *BAS* cycle [159, 160] is essentially a *Recompression* cycle adapted to nuclear applications, Figure 2.7. The heating process is distributed in four different heat exchangers to better fit with the temperature limits imposed by the reactor layout.

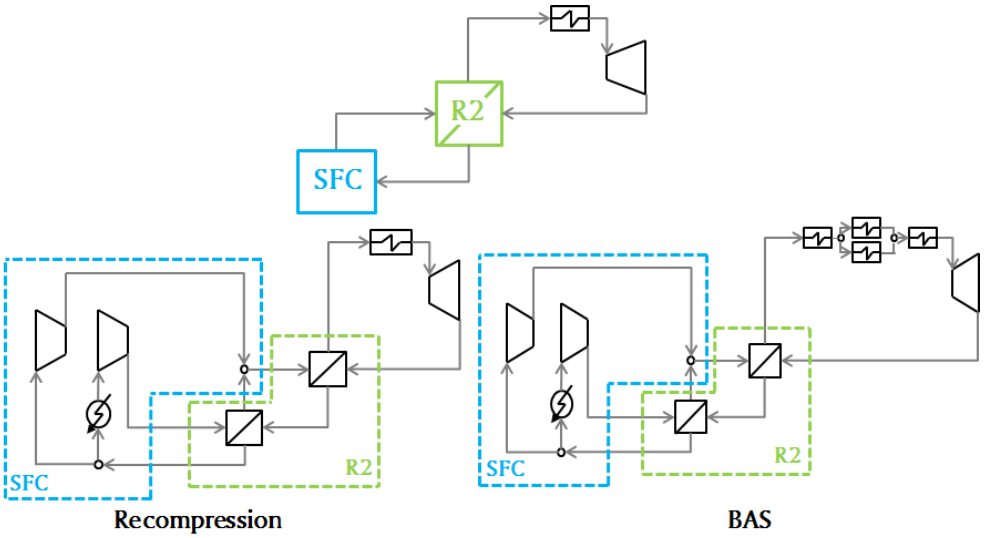

Figure 2.7: Stand-alone R2-SFC cycles. General layout (top) and particular embodiments (bottom).

2.3.9 R2-IC

The *Supercritical Precompression* cycle [67], Figure 2.8, is a further development of the *Partial condensation with precompression* cycle proposed by Angelino. It is a fully supercritical cycle that overcomes the restriction imposed by the compression process on turbine exhaust pressure. In effect, when the compressor inlet pressure is increased to supercritical values, either the expansion ratio is reduced or the turbine inlet pressure increases to prohibitive values. The outcome in the first case is a reduction in cycle specific work whereas, in the second case, the mechanical design of the components gets much more complex.

The *Recuperated CPOC* cycle [149], where CPOC stands for Cryogenic Pressurized Oxy-Combustion, is another oxy-fuel based power cycle with integrated carbon capture, which combines the supercritical *Recompression* cycle concept with an advanced oxy-combustion process. The basic sCO_2 cycle is only slightly modified with the addition of a cyclone downstream of the combustor (for ash removal) and a water separator between the low temperature recuperator and the cooler. The cycle is fully supercritical and the bleed valve for carbon dioxide sequestration is located between the re-compressor and the high temperature recuperator, Figure 2.8.

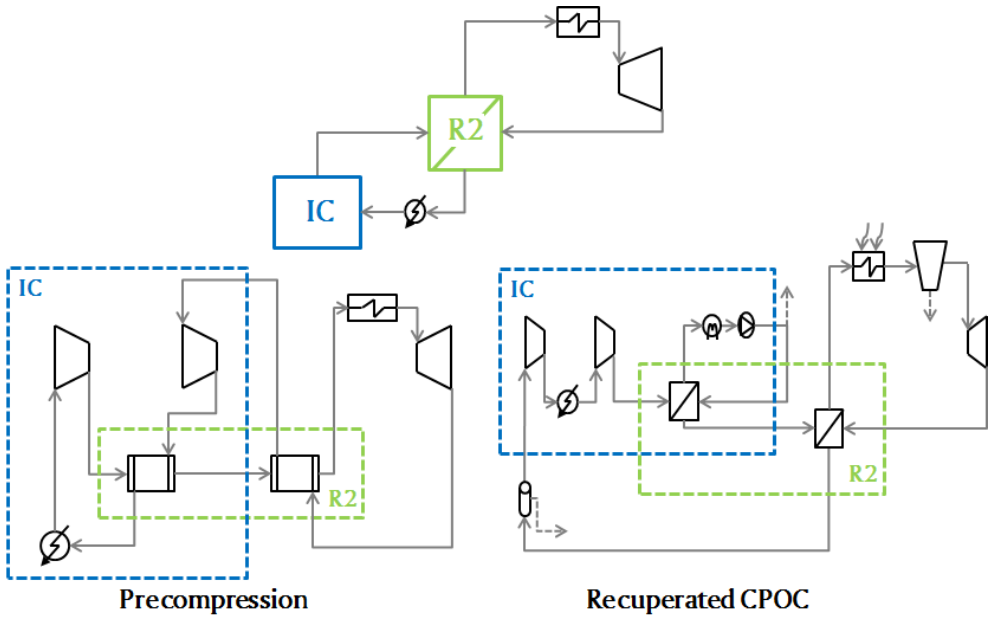

Figure 2.8: Stand-alone R2-IC cycles. General layout (top) and particular embodiments (bottom).

2.3.10 R2-IC-SFC

The *Supercritical Partial Cooling* cycle [67] derives, again, directly from Angelino's work. It is a modification of the *Partial condensation with precompression* cycle, very similar to the *Supercritical Recompression* layout but with the addition of a cooler and a pre-compressor before the flow-split, Figure 2.9. For this reason, this cycle can also be found in literature under the name *Modified Recompression* cycle [113]. The interest of the *Partial Cooling* cycle is a higher specific work [11] and a very low sensitivity of global efficiency to deviations of pressure ratio from the optimum value [115].

The *Intercooling I* layout proposed by Moisseytsev [97] is another split-flow, highly-recuperative cycle characterized by a multi-stage compression process. This configuration is very similar to the *Recompression* cycle but with the addition of intercooling in the main compression line, Figure 2.9. Originally investigated by Moisseytsev to better fit with sodium-cooled fast reactor applications, this cycle has also been considered for solar thermal power plants (*Supercritical CO_2 Gas Turbine with intercooling* [136]).

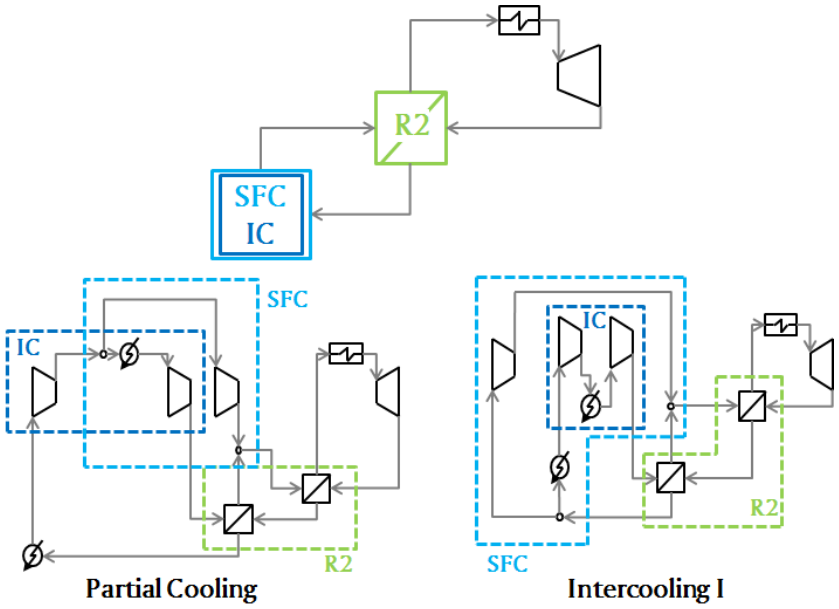

Figure 2.9: Stand-alone R2-IC-SFC cycles. General layout (top) and particular embodiments (bottom).

2.3.11 R2-RH-SFC

The *Reheating I* cycle proposed by Moisseytsev [97] is a mere evolution of the *Recompression* cycle, characterized by the addition of a single reheat as shown in Figure 2.10. As already mentioned for the *Intercooling I*, this cycle is specifically designed for sodium-cooled fast reactor applications where reheating takes place in a Na-to-CO_2 heat exchanger. Dostal and Kulhanek also proposed a cycle identical to *Reheating I*, under the name of *Split expansion* cycle [111, 99], and Padilla presented a comparison of *Recompression* cycles with and without reheating [154]. For the sake of simplicity, only the configuration proposed by Moisseytsev is considered in the present work.

The *Double Reheat Recompression* cycle [121] adds a second reheat to the configuration originally proposed by Moisseytsev, Figure 2.10. Additionally, Mecheri and Le Moullec propose a by-pass valve before the low-temperature recuperator, which results in a secondary stream of CO_2. This fraction of the main flow is split after the main compressor, heated up in another heater and re-injected before the high-temperature recuperator. The aim of this flow-split is to overcome the usual pinch-point problems and associated irreversibility in the internal heat recovery process, and it is also proposed in other cycles such as the *Simple Recuperated*, the *Recompression* and the *Double Recompression* [121] layouts.

2.3.12 R2-SFH

The *Driscoll* cycle, proposed by Dostal et al. [162], is a modification of the *Recompression* layout with a single compressor. The sCO_2 flow is split into two streams downstream of the compression process and merged later between the two recuperators, Figure 2.11. The aim is to prevent the development of an internal pinch-point in the low temperature recuperator,

but it results in a significant decrease of the thermal efficiency of the cycle [162].

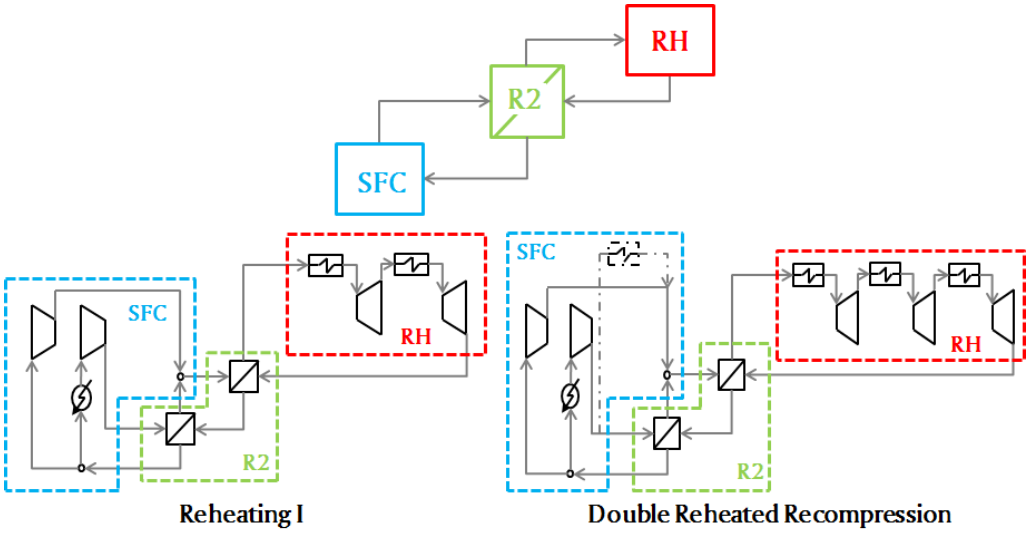

Figure 2.10: Stand-alone R2-RH-SFC cycles. General layout (top) and particular embodiments (bottom).

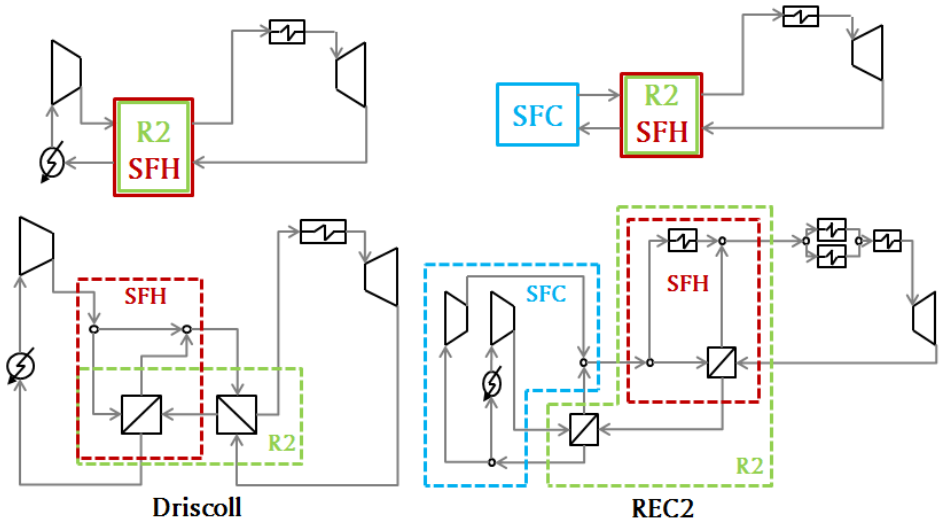

Figure 2.11: Stand-alone R2-SFH and R2-SFC-SFH cycles. General layouts (top) and particular embodiments (bottom).

2.3.13 R2-SFC-SFH

As already explained for the *Preheating* cycle, the *SFH* is usually employed to better fit with the temperature range imposed by the thermal source. In the case of the *REC2* cycle designed for fusion reactors [150, 163], a standard *Recompression* configuration is modified with the addition of four heaters, one of them in parallel with the second recuperator. This is shown in

Figure 2.11.

2.3.14 R2-SFHE

The *Turbine Split Flow I, II and III* cycles are three highly-recuperative configurations characterized by a flow-split situated between compressor and recuperator [101]. The sCO_2 flow is divided in two different streams that are then heated up and expanded separately, before being finally mixed together before the cooler, Figure 2.12. These layouts increase the expansion work (a second turbine is added) but this does not result in an increase in thermal efficiency [101]. The three cycles differ from one another in the layout of the recuperation/expansion process.

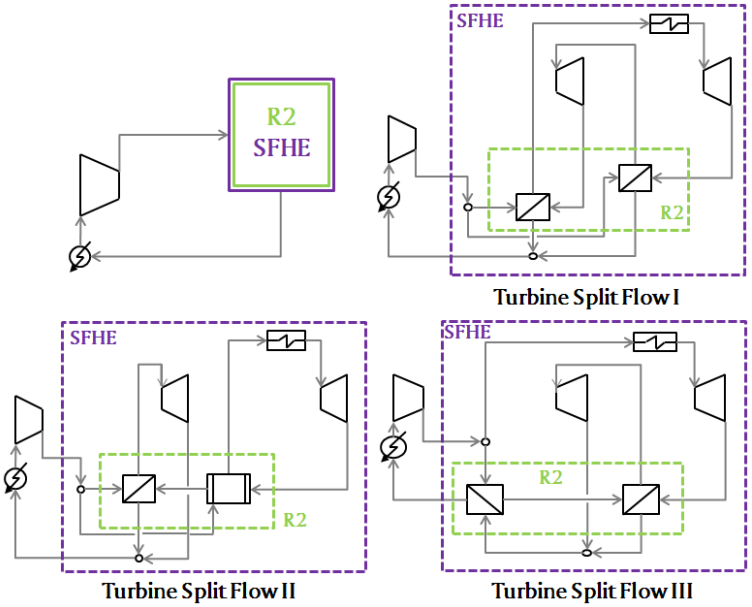

Figure 2.12: Stand-alone R2-SFHE cycles. General layout (top left) and particular embodiments (top right and bottom).

2.3.15 R2-SFC-SFE

The *RC-EJ* cycle is another configuration proposed by Vasquez in [143], consisting in a *Recompression* cycle assisted by an ejector. This configuration, shown in Figure 2.13, is characterized by the same features as the *S-EJ* (ejector) and *Recompression* (split-flow) cycles.

2.3.16 R2-IC-RH-SFC

This category contains two layouts proposed by Turchi [116] initially and then also by Padilla et al. [108] and Shelton et al. [120]. The general layout is aimed at enhancing the performance of the *Recompression* and *Partial Cooling* cycles by merely adding multi-stage intercooled compression and reheated expansion processes (Figure 2.14). The benefits provided by these configurations, named *Recompression with IC and RH* and *Partial Cooling with RH* respec-

tively, are the same as those previously discussed for their standard configurations without reheat.

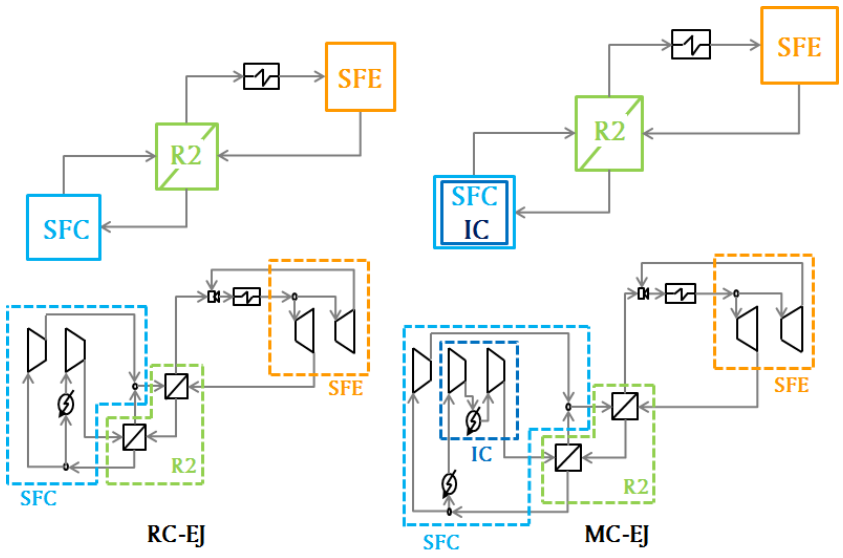

Figure 2.13: Stand-alone R2-SFC-SFE and R2-IC-SFC-SFE cycles. General layouts (top) and particular embodiments (bottom).

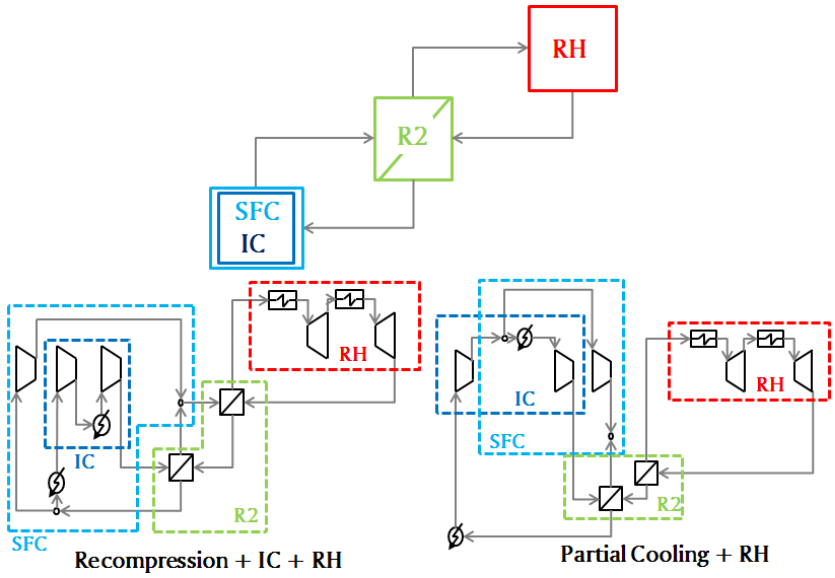

Figure 2.14: Stand-alone R2-IC-RH-SFC cycles. General layout (top) and particular embodiments (bottom).

2.3.17 R2-IC-SFC-SFE

The *MC-EJ* cycle is the third configuration proposed by Vasquez [143] and consists in a *Recompression* cycle assisted by an ejector with the addition of intercooling in the main compression

line, Figure 2.13. It presents essentially the same characteristics as the *RC-EJ* cycle plus a reduction of compression work thanks to intercooling.

2.3.18 R3-SFC

The *Double Recompression* cycle is a highly recuperative configuration proposed by Moisseytsev [97] where the standard high-temperature recuperator cycle is divided in two heat exchangers (intermediate and high temperature) in order to improve its effectiveness, Figure 2.15. In this layout, the stream of CO_2 is split twice, downstream of the intermediate and low temperature recuperators respectively, following the same idea as in the *Recompression* cycle. Nevertheless, this configuration does not have any beneficial impact on thermal efficiency (other than the enhanced heat transfer in the recuperator) [97].

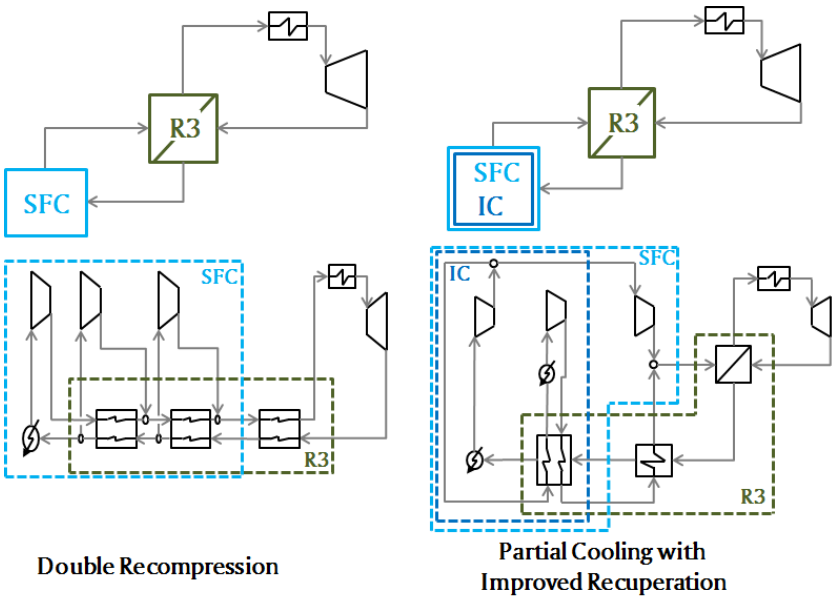

Figure 2.15: Stand-alone R3-SFC (left) and R3-IC-SFC (right) cycles. General layouts (top) and particular embodiments (bottom).

2.3.19 R3-IC-SFC

The *Partial cooling with improved recuperation* cycle [67] is again a further development of a configuration proposed by Angelino in [6]. Starting from a standard *Partial Cooling* layout, an additional three-stream recuperator is located between the second recuperator (now working at intermediate temperature) and the cooler. The aim of this configuration shown in Figure 2.15 is to attain higher thermal efficiency thanks to the recovery of the heat available at the outlet of the pre-compressor [111]. This is only possible if the outlet temperature of the latter is higher than the outlet temperature of the main compressor. In an alternative layout, the three-stream recuperator can be replaced by two recuperators connected in parallel [111].

2.3.20 R3-SFC-SFHE

The *Cascade Supercritical CO_2* cycle proposed by Johnson et al. [105] was included in the sCO_2 cycle development programme at Pratt & Whitney Rocketdyne for solar thermal applications. It is a further development of the *Supercritical Recompression* cycle with the addition of a flow-split valve downstream of the low temperature recuperator (cold side). As shown in Figure 2.16, this valve divides the flow into two streams, both of which follow the layout of a *Supercritical Simple recuperated* cycle independently (i.e., recuperator, heater and turbine) rejoining upstream of the low temperature recuperator (low pressure, high temperature side). The aim of this configuration is to recover heat from the solar plant with two heaters, in order to better fit with the large ΔT that is typical of this technology.

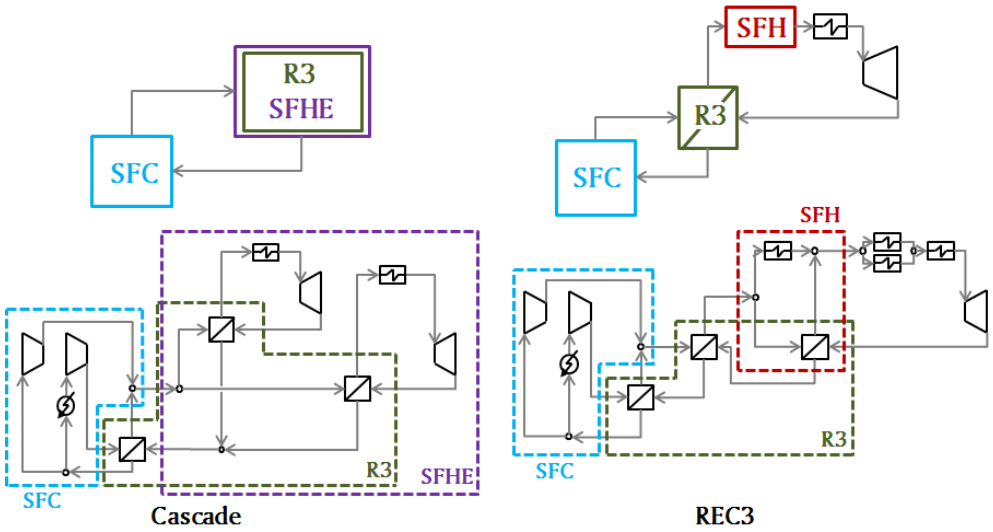

Figure 2.16: Stand-alone R3-SFC-SFHE (left) and R3-SFC-SFH (right) cycles. General layouts (top) and particular embodiments (bottom).

2.3.21 R3-SFC-SFH

The *REC3* cycle is the second configuration proposed in [150]. It is very similar to the *REC2* layout but incorporates a third recuperator at intermediate temperature. Differently from the *Double Recompression* cycle, the *REC3* configuration presents two compressors only and can be considered a development of the *Recompression* cycle with a more complex layout of the recuperation process, Figure 2.16.

2.3.22 R3-IC-RH-SFC-SFE

The *Schroder-Turner* cycle is an evolution of the *Partial cooling with improved recuperation* system, the main difference being the presence of three compressors and one power turbine only as shown in Figure 2.17. It is an extremely recuperative cycle, capable of taking advantage of the specific heat mismatch between the various streams in the recuperators thanks to several flow-splits [166, 167]. In an alternative embodiment, the *Schroder-Turner* cycle can be simplified by removing the low-temperature recuperator [167]. This latter configuration is the

one considered in Table 4.

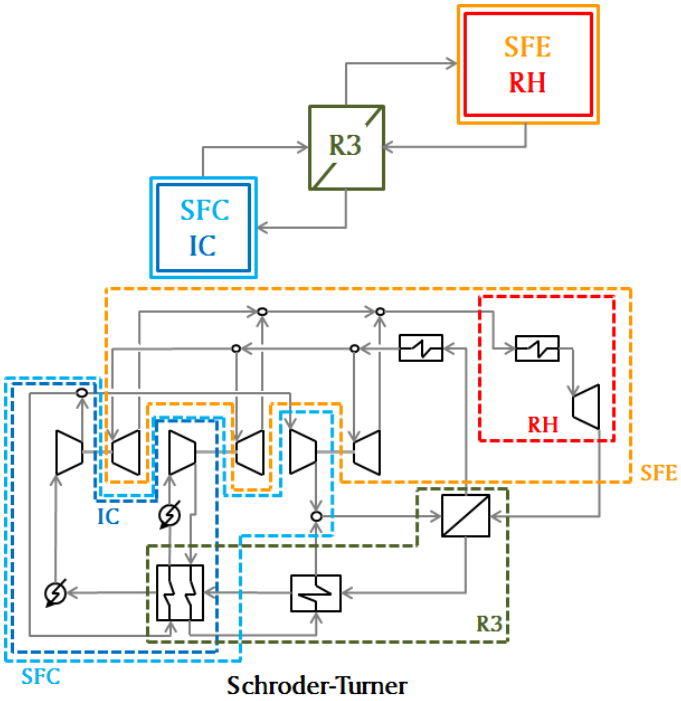

Figure 2.17: Stand-alone R3-IC-RH-SFC-SFE cycles. General layout (top) and particular embodiment (bottom).

2.3.23 R3-IC-RH-SFC-SFHE

The *Quasi-combined* system is an oxy-combustion cycle proposed by Zhang and Lior [168] whose complex layout incorporates several components as shown in Figure 2.18. The compression process is similar to the *Partial Cooling* cycle where the flow is split into two streams after a first compressor. The first stream is condensed thanks to the heat absorbed by an LNG evaporator, and then pumped and heated in the low and intermediate temperature recuperators. Then, this stream is expanded in a high-pressure turbine and heated in the high-temperature recuperator before rejoining the second stream (as in the *Matiant* cycle). This second stream is compressed after the flow-split valve, heated up in the intermediate temperature recuperator and finally mixed with the first stream. Once mixed, the entire flow enters the oxy-combustion chamber along with methane and pure oxygen (from an Air Separation Unit) and the resulting combustion gases are expanded across the low pressure turbine. After this, the working fluid is used (as if it were a *pseudo-topping-cycle*) to heat up the low temperature, high pressure flow in three recuperators before being finally directed to the water separator, cooler (again working with evaporating LNG) and first compressor. The name *Quasi-combined* derives from the fact that the mixed flow of sCO_2 and H_2O coming from low pressure turbine and flowing towards the water separator acts as a sort of Brayton-like "topping cycle", heating the pure sCO_2 flow that acts as the corresponding Rankine-like "bottoming cycle" [168].

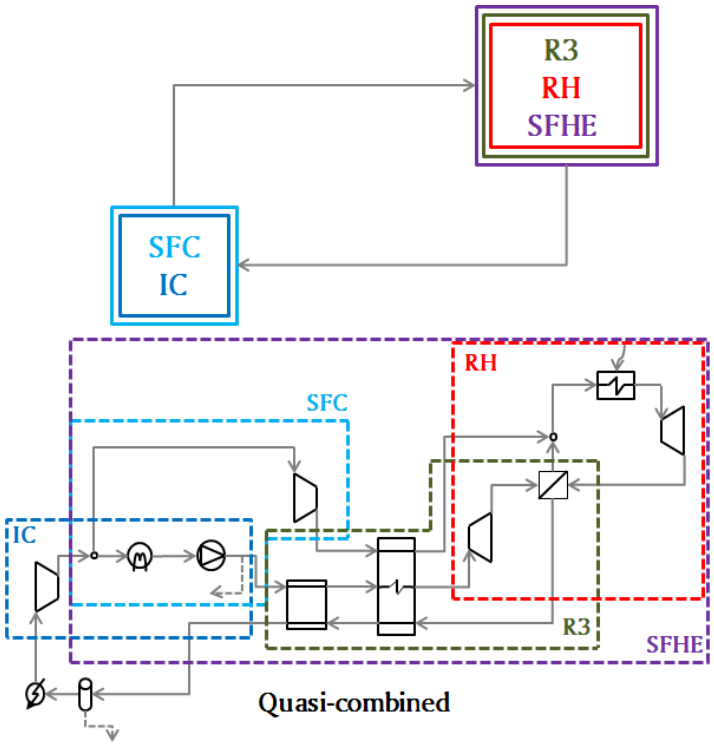

Figure 2.18: Stand-alone R3-IC-RH-SFC-SFHE cycles. General layout (top) and particular embodiment (bottom).

2.3.24 RH

Tuo proposes the *Rankine with Reheat* cycle for low-temperature waste heat recovery applications as a sort of evolution of the *Transcritical* CO_2 layout with the addition of a single reheat [169], Figure 2.19.

2.3.25 SFC-SFH

The *Rankine with ejector* cycle was proposed by Li et al. for low-grade heat applications (ca. 100 °C) [170]. It consists of a simple non-recuperative Rankine cycle where the flow is split before the compression process: one stream is compressed, heated, expanded in the turbine and directed to the ejector whereas the other is compressed, heated in a second heater working at lower temperature and then sent to the ejector. This is shown in Figure 2.19. The two streams are mixed in the ejector and the cycle is closed by a cooling process that can either be implemented in a cooler or a condenser (Supercritical or Transcritical layouts respectively).

2.3.26 IC

The *Cryogenic Pressurised Oxy-Combustion* cycle [149, 161] is the ancestor of the *Recuperative CPOC* cycle presented earlier, Figure 2.20. It is a non-recuperative cycle and, in spite of a possible utilization in combined cycle applications, it does not bring about further benefits than the recuperative configuration.

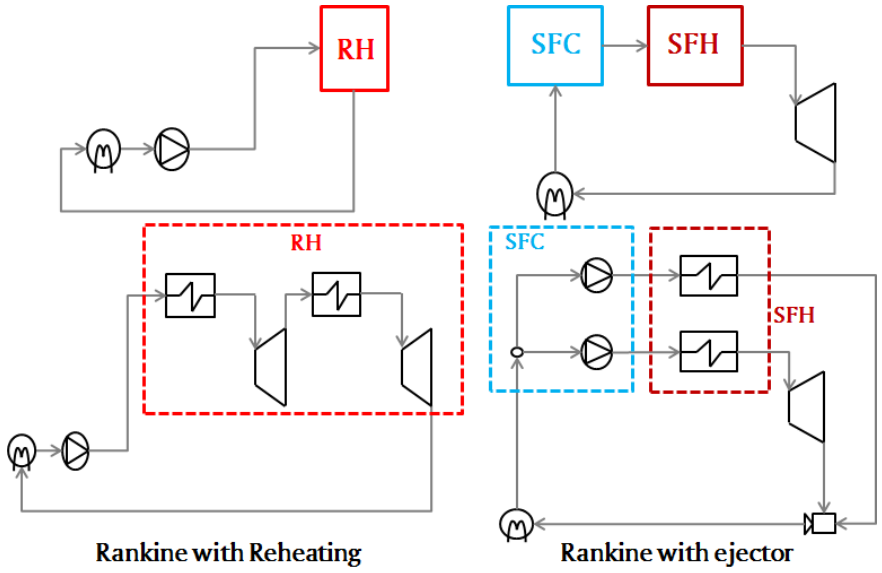

Figure 2.19: Stand-alone RH and SFC-SFH cycles. General layouts (top) and particular embodiments (bottom).

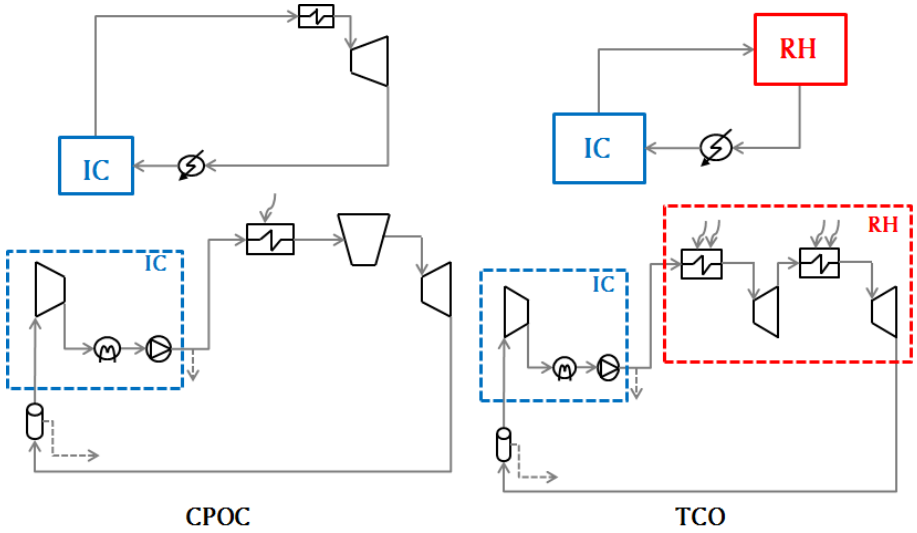

Figure 2.20: Stand-alone IC and IC-RH cycles. General layouts (top) and particular embodiments (bottom).

2.3.27 IC-RH

The *Texas Cryogenic Oxy-fuel (TCO)* cycle proposed by the Southwest Research Institute [171] is another oxy-combustion non-recuperative power cycle with reheat, Figure 2.20. Thanks to the novel oxy-fuel combustor geometry and to the high pressure ratio, this configuration is claimed to be able to reach significant thermal efficiency gains even if important technological challenges such as the high temperature and extremely high pressure at turbine inlet are faced.

2.4 Combined cycles

Combined cycles are usually made up of two thermally integrated cycles operating at different temperature levels. High temperature heat is supplied to the topping cycle which converts a fraction of it into mechanical work and rejects (all or part of) the remaining to the bottoming cycle. This lower temperature heat is again partially converted into mechanical work by this second system. The fraction of heat that is not converted into work is rejected to the environment at very low temperature [178].

Amongst the several cycles quoted below, some incorporate the supercritical/transcritical CO_2 cycle in the topping system, the bottoming system or both. For those cases with a bottoming CO_2 cycle, the topping system is usually a combustion gas turbine. For those where the CO_2 cycle is the topping system, the bottoming system has to operate at a fairly low temperature and hence an Organic Rankine Cycle (ORC) is almost universally adopted. In this case, it is also usual that the performances of the topping sCO_2 system are slightly penalized in order to maximize the global performance of the combined cycle plant [165]. The different configurations found in literature are summarized in Table 2.3.

Number	Cycle Name	Category Label	Locus of sCO_2 cycle	References
1	[*Simple Recuperated*	*R*1	*Topping*]	[102, 179-181]
2	*Simple Recuperated* + *RH* + *IC*	*R*1 – *IC* – *RH*	*Topping*	[102]
3	*Recompression*	*R*2 – *SFC*	*Topping*	[165, 179-184]
4	*Partial Cooling*	*R*2 – *IC* – *SFC*	*Topping*	[179]
5	*Partial Cooling* + *RH*	*R*2 – *IC* – *RH* – *SFC*	*Topping*	[102]
6	sCO_2–*ORC II*	*R*3 – *SFC*	*Topping*	[165]
7	sCO_2–*ORC III*	*R*3 – *SFC*	*Topping*	[165]
8	sCO_2–*ORC IV*	*R*3 – *IC* – *SFC* – *SFH*	*Topping*	[165]
9	*Brayton*	*Simple*	*Bottoming*	[185, 186]
10	*iso* – *Brayton*	*Simple*	*Bottoming*	[187]
11	*Simple Recuperated*	*R*1	*Bottoming*	[186-193]
12	*Hot Day*	*R*1 – *IC*	*Bottoming*	[109]
13	*Preheating*	*R*1 – *SFH*	*Bottoming*	[41, 190]
14	*Triple Heating*	*R*1 – *SFH*	*Bottoming*	[190]
15	*Dual Expansion*	*R*1 – *SFHE*	*Bottoming*	[190]
16	*Combined Recompr. and Preheat.*	*R*1 – *SFC* – *SFH*	*Bottoming*	[190]
17	*Precompression*	*R*2 – *IC*	*Bottoming*	[190]
18	*Recompression*	*R*2 – *SFC*	*Bottoming*	[188, 190, 194, 195]
19	*Partial Recuperation*	*R*2 – *SFHE*	*Bottoming*	[190]
20	*Cascade I*	*R*2 – *SFHE*	*Bottoming*	[94, 196, 41, 190]
21	*Cascade II*	*R*2 – *SFHE*	*Bottoming*	[94, 196, 190]
22	*Dual Stage*	*R*2 – *SFHE*	*Bottoming*	[189, 41]
23	*Cascade I* + *IC*	*R*2 – *IC* – *SFHE*	*Bottoming*	[94, 196, 190]
24	*Cascade II* + *IC*	*R*2 – *IC* – *SFHE*	*Bottoming*	[94, 196, 190]
25	*Composite Bottoming II*	*R*2 – *SFC* – *SFHE*	*Bottoming*	[188]
26	*Composite Bottoming III*	*R*2 – *SFC* – *SFHE*	*Bottoming*	[188]
27	*Cascade III*	*R*2 – *IC* – *SFH* – *SFHE*	*Bottoming*	[94, 196, 197, 190]
28	*Three* – *Stage*	*R*3 – *SFHE*	*Bottoming*	[181]
29	*Bottoming recompr. with Reheat*	*R*3 – *RH* – *SFC*	*Bottoming*	[188]
30	*Composite Bottoming I*	*R*3 – *SFC* – *SFHE*	*Bottoming*	[188]
31	*Composite Bottoming IV*	*R*3 – *RH* – *SFC* – *SFHE*	*Bottoming*	[188]
32	*Simple Recuperated* + *Recompr.*	*R*1 + (*R*2 – *SFC*)	*Bottoming*	[188]
33	*Recompression* + *Preheating*	(*R*2 – *SFC*) + (*R*1 – *SFH*)	*Bottoming*	[196]
34	*Precompression* + *Preheating*	(*R*2 – *IC*) + (*R*1 – *SFH*)	*Bottoming*	[196]
35	$sCO_2 + TCO_2$	*R*1 + *Simple*	*Bottoming*	[194, 195, 180]
36	*RCO*2 + *TCO*2	(*R*2 – *SFC*) + *Simple*	*Topping* + *Bottoming*	[107, 183, 180]
37	*Peregrine Turbine*	*Simple*	*Nested*	[198]
38	*Recuperated Peregrine Turbine*	*R*1 – *SFH*	*Nested*	[198]

Table 2.3: Summary list of combined cycles.

2.4.1 Topping cycles

Some of the stand-alone cycles presented in the first part of this work have also been proposed for combined cycle applications. For instance, the *Supercritical Simple Recuperated* cycle is used in the *L1XRY* system in [102, 179, 180] and in [102] again with the addition of reheat and intercooling, *L2XRY* in [102]. Moreover, combined cycles making use of the *Supercritical Recompression* layout are proposed in [165] (*sCO_2-ORC I*) and successively in [179, 182, 183, 180, 184]. Finally, the *Supercritical Partial Cooling* cycle is considered in [179] and the *Supercritical Partial Cooling* cycle with reheat is used in the *L3XRY* system in [102] again. All this information about the possible combinations are reflected in Table 2.3[2].

Further to the cycles in the paragraph above, three novel topping cycle configurations are proposed by Pichel et al. [165]. These are categorized and presented in the following sections.

R3-SFC

The *sCO_2-ORC II* is based on the *Supercritical Recompression* cycle as shown in Figure 2.21. The sCO_2 flow directed to the main compressor is firstly heated in an additional recuperator (called ORC Regenerator), then used as heat source for the ORC bottoming cycle and finally sent to the cooler and the main compressor. The hot fluid employed in the ORC Regenerator is a high-temperature sCO_2 stream obtained from a flow-split valve at the inlet to the heater, which is later re-injected into the re-compressor flow stream between the two standard recuperators. The aim of this layout is to increase the temperature level of the thermal energy provided to the bottoming cycle. Nevertheless, the efficiency of the sCO2 cycle results to be affected negatively, a circumstance that must be more than compensated for by the ORC system if this combined configuration is to be of any interest [165].

The *sCO_2-ORC III* is almost identical to the previous configuration, with the difference that the additional flow-split is made at the turbine inlet in order to obtain a stream at higher temperature for the bottoming cycle, Figure 2.21. According to the authors, and for the afore-cited reasons, this flow configuration has an even more detrimental effect on the performance of the sCO_2 cycle performance [165]. Therefore, the fraction of CO_2 directed to the ORC regenerator must be small enough to limit this effect but, at the same time, it must enable a good performance and substantial contribution of the bottoming cycle.

R3-IC-SFC-SFH

The *sCO_2-ORC IV* cycle makes use of the sCO_2 flow at the outlet from the recompressor, which is at a higher temperature than the outlet from the main compressor, as heat source for the bottoming cycle, Figure 2.22. The standard low-temperature recuperator is divided in two steps and the first flow-split, determining the fraction of CO_2 going to the main-compressor and the re-compressor, is performed between these two heat exchangers. The fraction going to the main-compressor is then split in two cold fluid streams for the new low temperature recuperators. On the other hand, the fraction going to the re-compressor is initially compressed and part of its sensible heat is then transferred to the bottoming ORC cycle. This flow is later cooled down in an intercooler, compressed in a second re-compressor and finally mixed with

[2] The main features of these cycles were already presented before and are therefore not repeated here again.

the main stream before the high temperature recuperator [165].

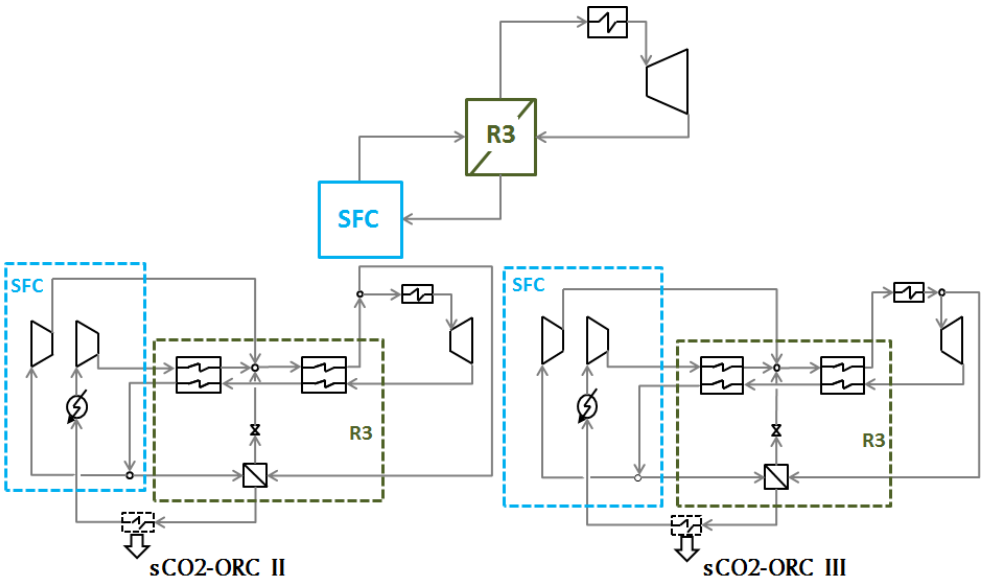

Figure 2.21: Topping R3-SFC cycle. General layout (top) and particular embodiments (bottom).

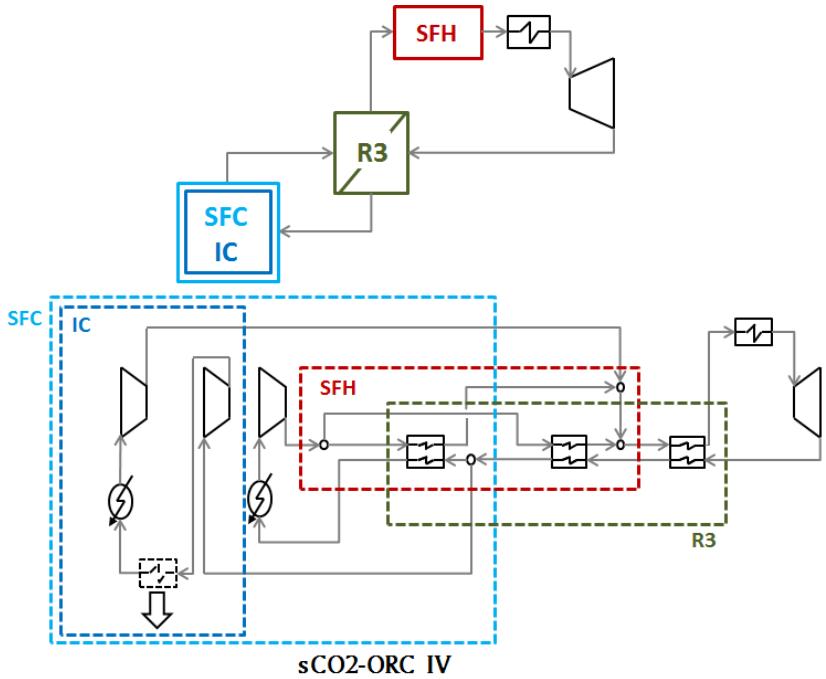

Figure 2.22: R3-IC-SFC-SFH Topping cycles. General layout (top) and particular embodiment (bottom).

2.4.2 Bottoming cycles

The aim of the bottoming cycle of a combined system is slightly different from that of a standard stand-alone cycle. Akin to waste heat recovery, not only has the bottoming system to achieve a high thermal efficiency but it also has to ensure that the amount of heat recuperated from the topping cycle is as high as possible. This is common-place in gas and steam combined cycle applications [178] and, even if it is not directly applicable to all sCO_2-based combined cycles, it remains a crucial design feature if the overall efficiency is to be maximized [94].

As already seen for the topping cycles, section 2.4.1, some of the stand-alone cycles presented in section 2.3 have also been proposed as part of combined systems in literature. For instance, Tahmasebipour et al. present a simple non-recuperative sCO_2 Brayton cycle to enhance the thermal efficiency of the *Shazand* steam power station [185] and Shu et al. present both a recuperative and a non-recuperative Brayton cycle for a waste heat recovery application downstream of an internal combustion engine [186]. A bottoming *Supercritical Simple Recuperated* cycle is proposed for integration with a gas turbine in [188, 189, 199] along with a *Supercritical Recompression* system in [188, 199]. The *Hot day* cycle is proposed by Nassar et al. [109], the *Preheating* cycle by Wright et al. [41] and the *Precompression* cycle in [190, 199], all of them integrated downstream of a gas turbine exhaust. A combined cycle composed entirely by sCO_2 cycles is proposed by Wang et al. for nuclear applications [107]. This is formed by a topping *Supercritical Recompression* cycle and a bottoming *Transcritical Rankine* cycle, both running on carbon dioxide and adopting the name *RCO2+TCO2* in this work.

In a less conventional application, sCO_2 cycles have also been proposed to bottom Molten Carbonate Fuel Cells (MCFC) in hybrid systems. These systems use a topping high temperature fuel cell and a bottoming heat engine to combine the production of electrochemical and mechanical work (hence the name hybrid). The CO_2 cycles that are most frequently considered in these applications are the *Supercritical Simple Recuperated* layout [191, 192, 194, 195, 193] and the *Recompression* cycle [194, 195] even if other configurations are also possible. For instance, Bae et al. introduce a hybrid system composed by a bottoming combined cycle formed by two CO_2 cycles, *Supercritical Simple Recuperated* and *Transcritical Rankine*, coupled to a MCFC [194, 195]; this layout is here referred to as sCO_2+TCO_2. The fuel cell is the heat source of the *Supercritical Simple Recuperated* cycle, which results to be the topping unit of the bottoming combined cycle, and is also connected with the *Transcritical Rankine* cycle working as the corresponding bottoming system. The latter presents high thermal efficiency in the low temperature range and is able to exploit the waste heat of the topping cycle better than an ORC. Moreover, if a lower efficiency of the sCO_2 recuperator is accepted, a more compact and flexible system can be obtained thanks to the good performance of the *Transcritical Rankine* system [194].

Cascaded configurations composed by one or more of the already presented stand-alone cycles are proposed by Cho et al [196] and Moroz et al. [188]. The former presents two configurations. The first one consists of a *Recompression* cycle that exploits a stream of high temperature flue gases, followed by a *Preheating* cycle working at lower temperatures. A second proposal follows the same approach to combine the *Precompression* and *Preheating* cycles. Moroz et al., on the other hand, present a combination of a *Recompression* cycle followed by a *Simple*

Recuperated system.

Simple bottoming cycles

The *iso-Brayton* cycle was recently proposed by Heo et al. [187] for waste heat recovery applications downstream of gas turbines. It presents a non-recuperative configuration characterized by an iso-thermal compression process. The fluid is compressed at constant temperature, then heated up and finally expanded in a turbine as shown in Figure 2.23. It is worth noting that this cycle does not include a cooler, so the fluid exiting the turbine flows directly into the iso-thermal compressor whose inlet temperature is therefore the same as the turbine exhaust temperature. This can significantly simplify the cycle layout, even if the technology needed to compress at constant temperature is still under development.

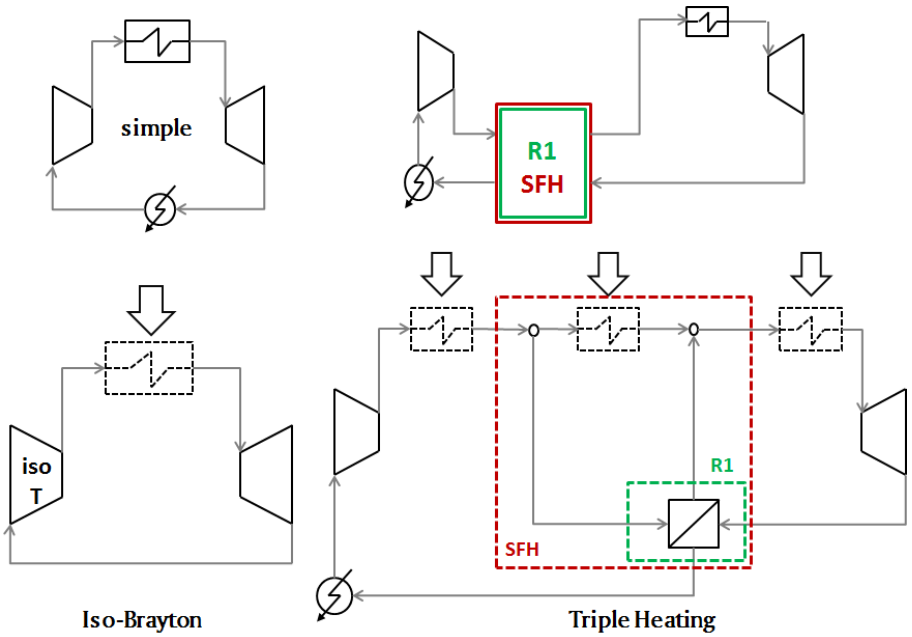

Figure 2.23: Simple and R1-SFH bottoming cycles. General layouts (top) and particular embodiments (bottom).

R1-SFH

The *Triple Heating* cycle proposed by Kim et al. [190] is almost identical to the *Preheating* cycle. The difference is just the addition of a heater right after the compressor and before the usual flow-split valve in the reference configuration, Figure 2.23. The main aim of this cycle is to enhance the recovery of waste heat.

R1-SFHE

Another cycle proposed in [190] is the *Dual Expansion* layout. It is an evolution of the *Supercritical Simple Recuperated* cycle obtained by simply adding a new heater-turbine line, Figure

2.24. A flow-split valve divides the main flow in two downstream of the compressor. The first stream flows into the recuperator, is heated up in the heater and then expanded in a turbine before it finally returns to the recuperator. The other fraction of the flow follows a similar path but without the first step (recuperator): it is heated up and then expanded in a second turbine before rejoining the first stream upstream of the recuperator.

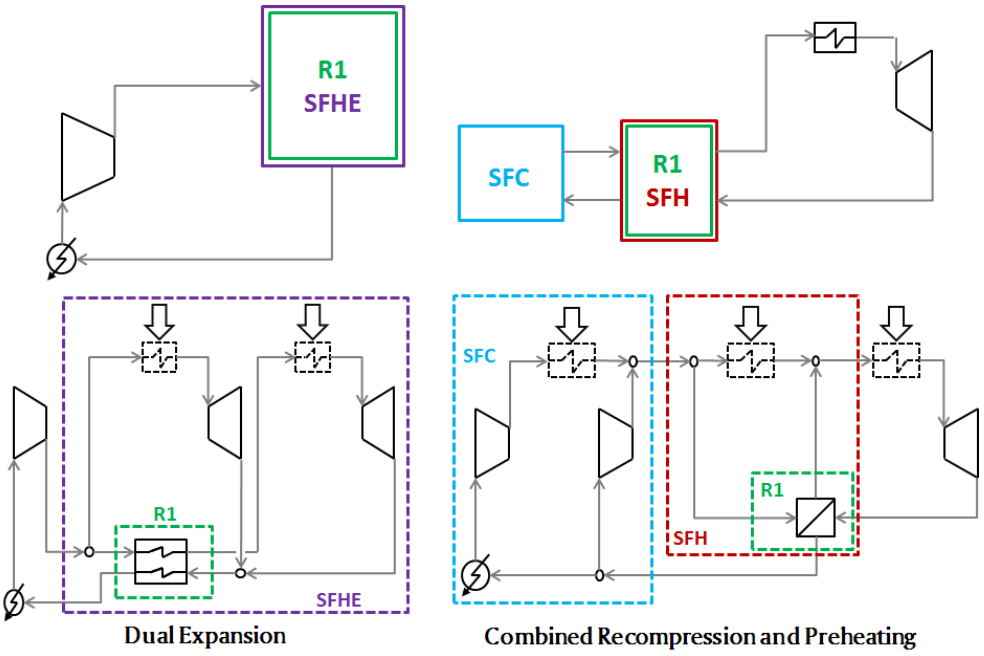

Figure 2.24: R1-SFHE and R1-SFC-SFH Bottoming cycles. General layouts (top) and particular embodiments (bottom).

R1-SFC-SFH

The *Combined Recompression and Preheating* cycle is another proposal made by Kim et al. [190]. This configuration, as suggested by its name, results from the combination of the stand-alone cycles that are contained in the name, Figure 2.24. The compression process is taken from the *Recompression* cycle, retaining the flow-split valve that divides the main stream before the compression stage. One fraction is cooled, compressed and then heated up with the exhaust of the topping cycle (not in a low temperature recuperator as in the *Recompression* cycle). The second fraction is compressed only (not heated) before it rejoins the first stream downstream of the heater. After compression, the flow is divided again in two streams, closing the cycle with the known configuration of a *Preheating* cycle.

R2-SFHE

The *Cascade I* cycle in [94] presents a flow-split after the compressor, where the sCO_2 flow is divided in two streams. The first stream is heated up thanks to the recovery of waste heat from the topping cycle, and then expanded in a turbine downstream of which it is sent to two recuperators in series. The second stream raises its temperature across the cited recuperators

and is then expanded in a second turbine before being mixed with the first stream downstream of the high temperature recuperator, Figure 2.25. The main benefit of this configuration is that the waste heat recovery process is strongly enhanced thanks to the absence of recuperation in the first sCO_2 stream. On the negative side, the main shortcoming is the lower efficiency of the low temperature recuperator, which is negatively affected by the different mass flow rates on each side (hot and cold) [94].

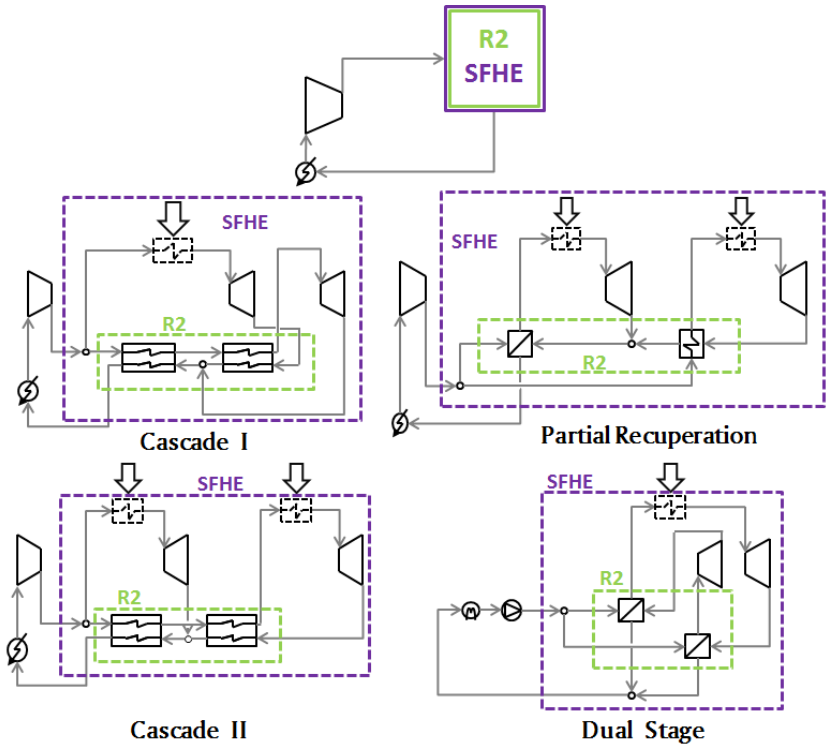

Figure 2.25: R2-SFHE Bottoming cycles. General layout (top) and particular embodiments (center and bottom).

Another configuration proposed by Kimzey is the *Cascade II* cycle [94]. This is an evolution of the previous *Cascade I* cycle with the addition of another heat exchanger connected with the topping cycle. This second heat exchanger is located just upstream of the second turbine (downstream of the recuperator in the second sCO_2 stream), Figure 2.25.

The layout of the *Dual Stage* cycle presented in [189, 41] is very similar to that of the *Cascade I* layout. The only difference is the existence of a recuperator in both sCO_2 streams rather than just one, Figure 2.25. Therefore, the temperature of sCO_2 at the inlet of the waste heat recovery process is higher than in the *Cascade I* configuration.

The *Partial Recuperation* cycle is the last proposal made by Kim et al. in [190]. The flow is divided in two after the compressor. The first stream flows into the high pressure side of the high temperature recuperator, is heated up in a heater, expanded in a turbine and, finally, it flows across the low pressure side of the high temperature recuperator. The second stream

enters the low temperature recuperator (high pressure side), then the heater and, finally, the second turbine. The two streams mix before flowing into the low temperature recuperator, Figure 2.25.

R2-IC-SFHE

The *Cascade I with intercooling* and the *Cascade II with intercooling* cycles are two configurations proposed by Kimzey, identical to the ones presented previously with the simple addition of intercooling, Figure 2.26. The benefits of this layout are twofold. On one hand, the total compression work decreases, with a consequent increase of net power output. On the other, the temperature of the sCO_2 flow after compression is lower so the waste heat recovery from exhaust gases of the topping cycle is enhanced [94].

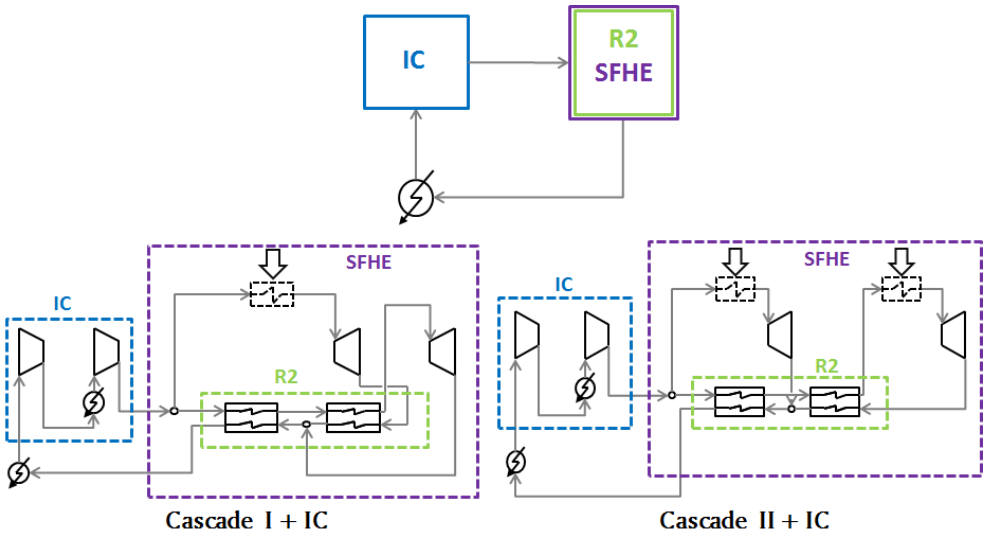

Figure 2.26: R2-IC-SFHE Bottoming cycles. General layout (top) and particular embodiments (bottom).

R2-SFC-SFHE

Moroz et al. propose a series of novel configurations for the bottoming cycle of a combined system in [188]. The main idea is to combine different stand-alone cycles in a unique layout by using several flow-splits, Figure 2.27. In the *Composite bottoming II* configuration, the standard layout of a *Recompression* cycle is used and a second turbine is then inserted in the main-compressor line by splitting the flow in two streams. Therefore, the resulting configuration is a combination of a *Recompression* cycle and a simple non-recuperative Brayton cycle. Both heaters (each one specific to the main and secondary turbines) are both thermally connected to the topping cycle, thus enhancing waste heat recovery. The *Composite bottoming III* cycle is an evolution of the previous configuration, with the addition of another flow-split valve downstream of the low-temperature recuperator. This enables splitting the expansion process in two turbines whilst also increasing the recovery of heat from the flue gases of the topping system.

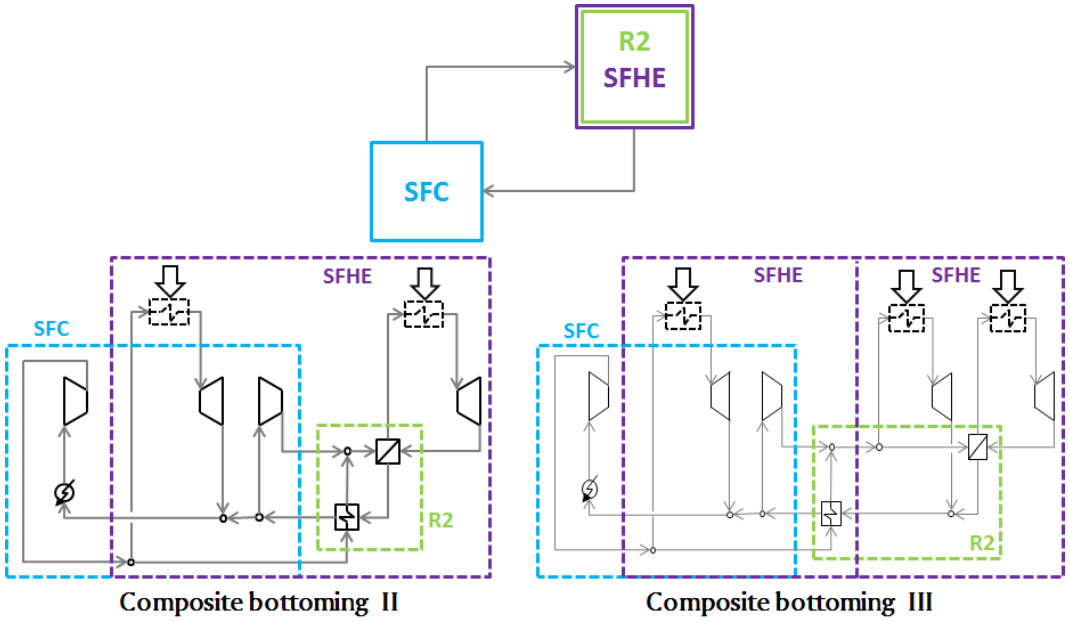

Figure 2.27: R2-SFC-SFHE Bottoming cycles. General layout (top) and particular embodiments (bottom).

R2-IC-SFH-SFHE

The last configuration proposed by Kimzey is the *Cascade III* cycle, also reconsidered by Huck in [197]. The latter is similar to the *Cascade I with intercooling* layout due to the flow-split after the compression process and the fact that only one of the two sCO_2 streams recovers heat from the topping cycle. The novel feature of this configuration is the division of the heat recovery process in two heat exchangers, in between which the two sCO_2 streams are mixed, Figure 2.28. This allows to control the temperature profiles of the recuperators by varying the mass flow rates of the two streams, hence reducing the irreversibility of the internal heat exchange process [94].

R3-SFHE

The *Three stage* configuration presented in [181] is a modification of the *Dual Stage* layout. In this configuration, the sCO_2 flow that does not receive thermal energy from the topping cycle is divided in two streams, each one expanded in a different turbine and sent to a different recuperative heat exchanger. These two secondary streams are finally mixed together with the main stream before flowing into the condenser, Figure 2.28.

R3-RH-SFC

Another configuration proposed by Moroz et al. is the *Bottoming recompression with reheat* cycle [188]. Contrary to the proposals presented previously, the latter does not result from the combination of different cycles but from the modification of the standard *Recompression*

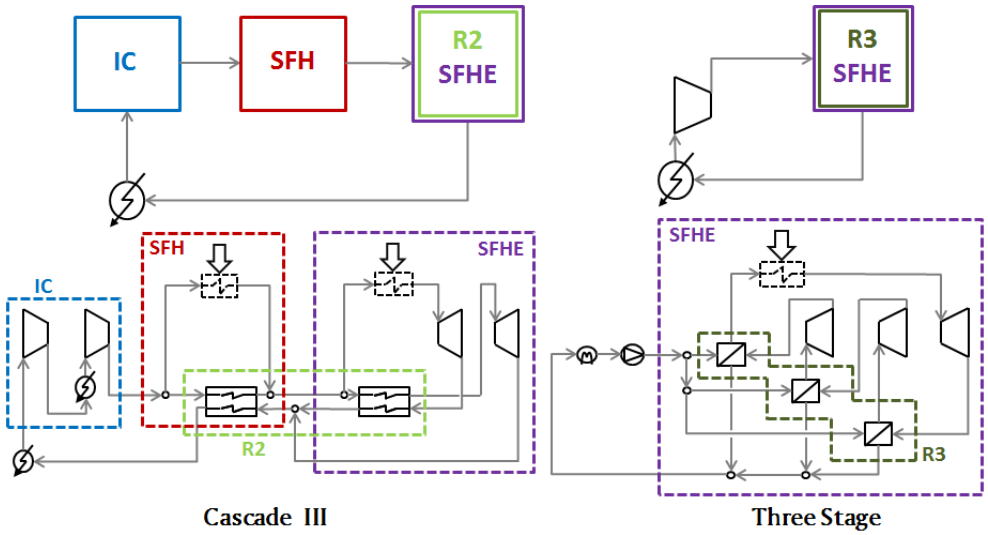

Figure 2.28: R2-IC-SFH-SFHE and R3-SFHE Bottoming cycles. General layouts (top) and particular embodiments (bottom).

cycle. A reheating process is enabled by merely adding a high temperature recuperator, a new heat exchanger connected to the topping cycle and a second turbine, Figure 2.29.

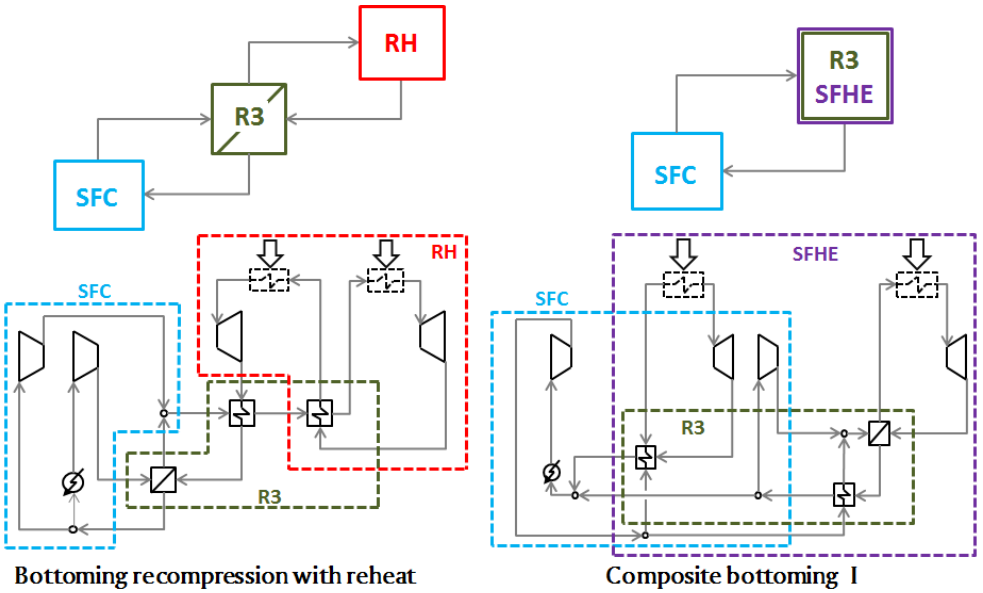

Figure 2.29: R3-RH-SFC and R3-SFC-SFHE Bottoming cycles. General layouts (top) and particular embodiments (bottom).

R3-SFC-SFHE

The *Composite bottoming I* cycle in [188] is essentially the same as the *Composite bottoming II*, with the addition of a recuperator before the secondary turbine, Figure 2.29. Therefore, it results from the combination of the *Recompression* and *Simple Recuperated* cycles.

R3-RH-SFC-SFHE

The *Composite bottoming IV* cycle is the last configuration proposed by Moroz et al. in [188]. It is obtained by adding a reheating process to the *Composite bottoming III* layout in Figure 2.30. The flow at the outlet of the last turbine flows through a new recuperator, after which it is heated up by the flue gas stream of the topping cycle and then expanded in a new turbine. This increases the waste heat recovery potential and the net power output of the combined cycle.

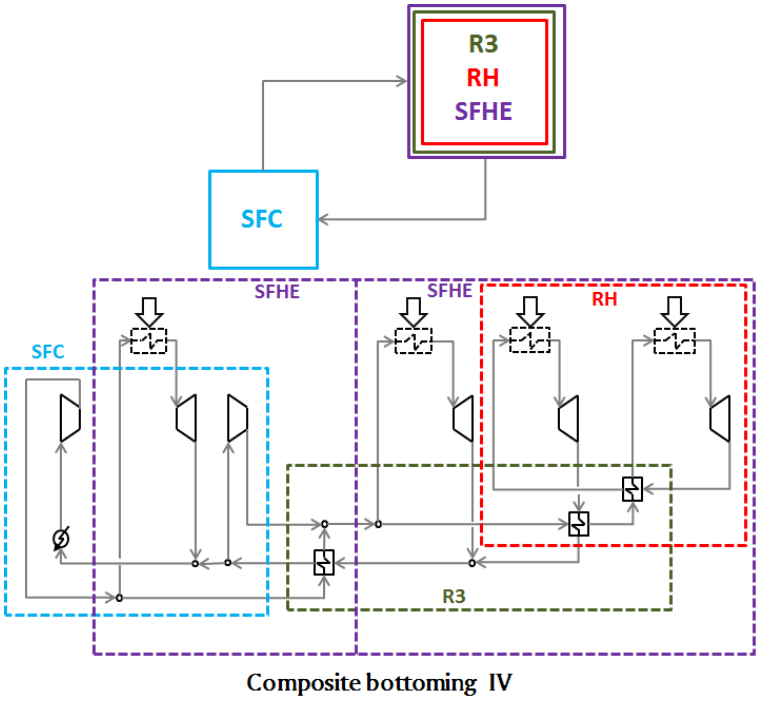

Figure 2.30: R3-RH-SFC-SFHE Bottoming cycles. General layout (top) and particular embodiment (bottom).

2.4.3 Nested cycles

The previous sections have presented several configurations for topping and bottoming sCO_2 cycles in combined cycle applications with somewhat standard integration layouts: heat is supplied to a topping system which produces work and rejects heat to a bottoming system that further converts a fraction of this into useful work. Alternative proposals can be found in literature though. For instance, Stapp proposes two *nested* configurations where a sCO_2 cycle is combined with a gas turbine in such a way that a standard topping/bottoming cycle structure cannot be defined, Figure 2.31.

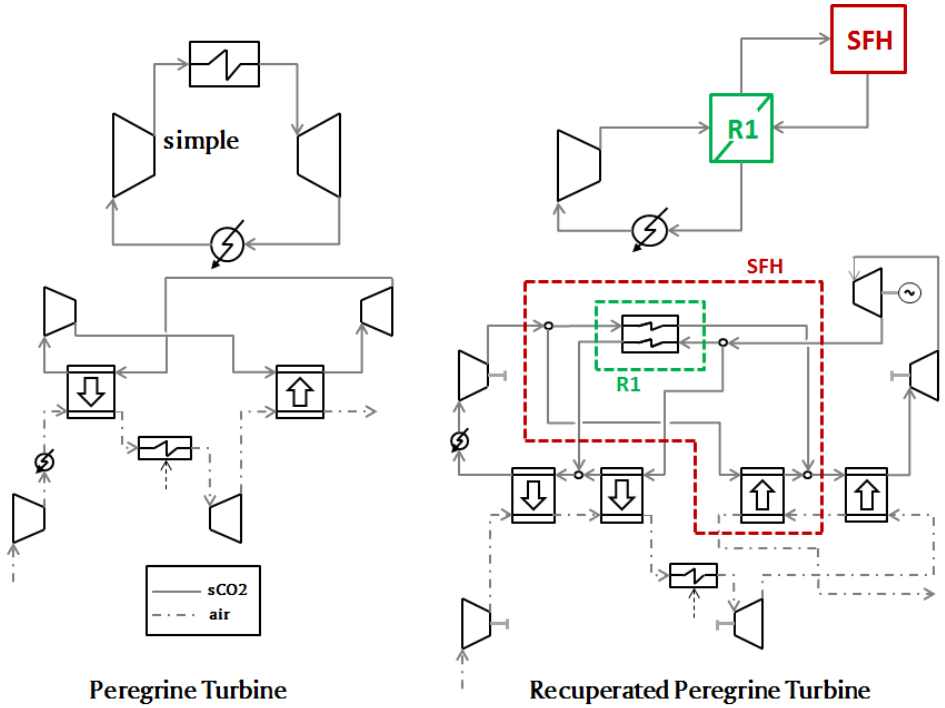

Figure 2.31: Nested simple (left) and R1-SFH (right) cycles. General layouts (top) and particular embodiments (bottom).

The combined system proposed by *Peregrine Turbine* is formed by two Brayton cycles: the topping cycle is a low pressure ratio gas turbine whilst the bottoming system presents a closed sCO_2 Brayton layout. Although none of the cycles is recuperative, they are nested into one another to yield a "globally recuperative" cycle [198]. In fact, this could be seen as a cross-recuperative layout in the sense that there are two recuperators where the working fluids of different cycles exchange heat to increase the global system efficiency. Thanks to this smart integration, the *Peregrine Turbine* system is able to achieve high thermal efficiencies. An evolution of this configuration is the *Recuperated Peregrine Turbine* cycle which presents the same fundamentals but is based on a *Simple Recuperated* sCO_2 cycle and makes use of four heat exchangers (rather than two) to connect the CO_2 system to the gas turbine.

2.5 Other cycles

Besides power production, sCO_2 systems have been investigated for several alternative applications. For instance, various systems have been proposed to store energy in different ways: thermal energy storage (TES) [200, 201], bulk energy storage [41], heat-pump based energy storage [202, 203] and thermo-electric energy storage (TEES) [204]. Also, a number of sCO_2 combined systems have been looked into for mobile applications (cooling and power production [205], fuel savings [206]), ship propulsion [207] and waste heat recovery in the aero and naval industries [208, 209]. The feasibility of less conventional power plants based on sCO_2 cycles has been studied in [210, 155, 211, 212, 213] for co-generation, [214] for geother-

mal power and [215] for combined heating, cooling and hot water production. Finally, other applications under investigation are hydrogen production [216], refrigeration [217] and novel dual-evaporator systems [218].

2.6 Comparison

2.6.1 Thermal performance

The review presented in this chapter confirms that sCO_2 power cycles have been proposed in literature for a number of different applications. From Nuclear power plants to Waste Heat Recovery, from Concentrated Solar Power to oxy-combustion plants, this technology always shows great potential in comparison to the default technologies employed in those fields. Tables 2.4 and 2.5 summarize the boundary conditions (minimum and maximum temperatures and pressures of the cycle) and thermal efficiencies declared in the original papers for the stand-alone and combined cycles[3], along with the application proposed for each of them. In both cases, some standardization of the minimum cycle temperature is observed and there is also certain uniformity in the maximum pressure. For combined cycles, the minimum cycle pressure does not vary largely from one layout to another. Nevertheless, large discrepancies in turbine inlet temperature are observed; even if these are larger for stand-alone applications (Table 2.4), they also arise in combined cycle configuration (Table 2.5).

Figure 2.32 puts together the declared thermal efficiency of each stand-alone power cycle considered in this work. The large dispersion observed in the chart is interesting: even if most cycles exhibit efficiencies in the range from 40 to 50%, some reach 60% whilst others are well below 10%. This is due to the different layout of each cycle but, also, the very different boundary conditions considered by the authors, in particular turbine inlet temperature (TIT) but also other parameters like cooling medium available (sink temperature) isentropic efficiencies of turbomachinery and effectiveness (or terminal temperature difference) of heat exchangers. Actually, this is further assessed in Figure 2.33 where efficiency is plotted against turbine inlet temperature for all the cycles considered, showing the clear impact of this parameter on cycle performance. The aforecited dispersion is still visible (for the cited reasons) but it is attenuated to a very large extent.

Figure 2.34 presents the same information as Figure 2.32 for the combined cycle layouts considered, giving independent values for the sCO_2 and overall combined cycles whenever possible. Two aspects are worth noting. The efficiency of the sCO_2 cycles (in blue) is also not uniform, as it was the case for the stand-alone cycles. Also, regarding the global combined cycle efficiency, these combined systems using sCO_2 technology demonstrate that they are able to achieve comparable (but not substantially higher) efficiencies to state-of-the-art gas and steam combined cycle power plants.

[3] Note that, in this case, minimum and maximum pressure and temperature correspond to the sCO_2 cycle only

Num.	Cycle Name	P_{min}	T_{min}	P_{max}	T_{max}	η_{th}	Application	Ref.
1	*Simple Recuperated*	7.35	32.0	25.0	550	56.0	Not specified	[12]
2	*Transcritical CO2*	5.0	15.0	20.0	700	42.0	Nuclear	[38]
3	*Hot day*	6.5	28.0	25.0	510	37.3	WHR	[109]
4	*Allam*	3.0	20.0	30.0	1150	59.0	Oxy-combustion	[132]
5	*Intercooling II*	7.5	32.0	25.0	500	37.0	Nuclear	[101]
6	*Brayton CO2 GT*	1.8	35.0	10.2	650	45.0	CSP	[136]
7	*Reheating II*	7.5	32.0	25.0	500	37.5	Nuclear	[101]
8	*Split – Expansion*	7.5	32.0	25.0	500	34.0	Nuclear	[101]
9	*Matiant*	0.1	29.0	30.0	1300	44.3	Oxy-combustion	[137]
10	*Allam + RH*	0.1	20.0	30.0	1150	60.0	Oxy-combustion	[132]
11	*ForcedCooler*	6.7	-40.0	25.0	830	48.7	Nuclear/CSP	[140]
12	*DEMO*	0.4	20.0	24.0	1250	52.0	Oxy-combustion	[141]
13	*Preheating*	7.5	32.0	25.0	500	27.0	Nuclear	[101]
14	*S – EJ*	6.8	32.0	25.0	650	41.6	Nuclear/CSP	[143]
15	*Inter – Recuperated*	7.5	32.0	25.0	500	38.0	Nuclear	[101]
16	*Recompression*	7.8	32.0	25.0	550	46.5	Nuclear	[11]
17	*BAS*	8.5	30.0	25.0	458	42.0	Nuclear	[159]
18	*Precompression*	9.6	32.0	25.0	550	43.5	Nuclear	[11]
19	*Recuperated CPOC*	0.1	-62.0	17.5	1200	63.0	Oxy-combustion	[161]
20	*Partial Cooling*	5.0	32.0	25.0	550	46.1	Nuclear	[11]
21	*Intercooling I*	7.6	32.0	20.0	480	39.0	Nuclear	[97]
22	*Reheating I*	7.6	32.0	20.0	415	37.0	Nuclear	[97]
23	*Double Reheated Recompression*	7.5	32.0	30.0	620	52.4	Fossil Fuel (Coal)	[121]
24	*Driscoll*	7.6	32.0	25.0	550	40.0	Nuclear	[162]
25	*REC2*	8.5	30.0	25.0	550	45.7	Nuclear	[150]
26	*Turbine Split Flow I*	7.5	32.0	25.0	500	33.0	Nuclear	[101]
27	*Turbine Split Flow II*	7.5	32.0	25.0	500	30.5	Nuclear	[101]
28	*Turbine Split Flow III*	7.5	32.0	25.0	500	29.0	Nuclear	[101]
29	*RC – EJ*	14.7	32.0	25.0	650	41.6	Nuclear/CSP	[143]
30	*Recompression + IC + RH*	8.0	32.0	25.0	550	48.5	CSP	[116]
31	*Partial Cooling + RH*	5.0	32.0	25.0	550	48.0	CSP	[116]
32	*MC – EJ*	5.6	32.0	25.0	650	41.6	Nuclear/CSP	[143]
33	*Double Recompression*	7.6	32.0	20.0	466	39.0	Nuclear	[97]
34	*Partial Cooling w/ Improved Recup.*	4.4	32.0	15.0	550	45.0	Nuclear	[99]
35	*Cascade*		*not declared*			41.4	CSP	[105]
36	*REC3*	8.5	32.0	22.5	600	46.0	Nuclear	[159]
37	*Schroder – Turner*	6.6	47.0	34.9	650	49.6	Solar	[167]
38	*Quasi – combined*	0.1	-70.0	15.6	1300	65.6	Oxy-combustion	[168]
39	*Rankine w/ Reheat*	5.7	20	12	90	7.3	WHR	[169]
40	*Rankine w/ ejector*	7.2	30.0	12.5	72.0	6.4	WHR	[170]
41	*CPOC*	0.1	-17.7	15.2	530	30.0	Oxy-combustion	[161]
42	*TCO*	0.1	20.0	48.3	705	40.0	Oxy-combustion	[171]

Table 2.4: Stand-alone cycles. Original boundary conditions ($P[MPa]$, $T[°C]$).

Num.	Cycle Name	sCO_2	Other	P_{min}	T_{min}	P_{max}	T_{max}	η_{th,sCO_2}	$\eta_{th,overall}$	Ref.
1	*Simple Recuperated*	*Topp.*	*ORC*	4.0	35.0	30.0	727	32.5	42.8	[102]
2	*Simple Recuperated + RH + IC*	*Topp.*	*ORC*	3.0	35.0	27.0	727	*n.d.*	49.1	[102]
3	*Recompression*	*Topp.*	*ORC*	7.4	30.0	25.0	500	43.3	43.5	[165]
4	*Partial Cooling*	*Topp.*	*ORC*	3.8	55.0	25.0	800	49.7	52.3	[179]
5	*Partial Cooling + RH*	*Topp.*	*ORC*	3.5	35.0	29.5	727	*n.d.*	50.5	[102]
6	sCO_2 *−ORC II*	*Topp.*	*ORC*	7.4	30.0	25.0	500	36.9	38.0	[165]
7	sCO_2 *−ORC III*	*Topp.*	*ORC*	7.4	30.0	25.0	500	37.8	38.1	[165]
8	sCO_2 *−ORC IV*	*Topp.*	*ORC*	7.4	30.0	25.0	500	37.3	39.2	[165]
9	*Brayton*	*Bott.*	*ST*	7.8	32.0	20.0	300	*n.d.*	41	[185]
10	*iso − Brayton*	*Bott.*	*GT*	0.5	35.0	30.0	400	41.0	*n.d.*	[187]
11(*a*)	*Simple Recuperated*	*Bott.*	*GT*	5.8	20.0	20.0	365	*n.d.*	48.9	[189]
11(*b*)	*Simple Recuperated*	*Bott.*	*MCFC*	7.5	35.0	22.5	650	39.9	59.4	[192]
12	*Hot Day*	*Bott.*	*GT*	6.5	28.0	25.0	510	*n.d.*	37.3	[109]
13	*Preheating*	*Bott.*	*GT*	7.7	32.0	24.0	390	27.8	21.2	[41]
14	*Triple Heating*	*Bott.*	*GT*	8.9	36.9	27.6	346	26.9	*n.d.*	[190]
15	*Dual Expansion*	*Bott.*	*GT*	8.9	36.9	27.6	398	27.5	*n.d.*	[190]
16	*Combined Recompr. and Preh.*	*Bott.*	*GT*	8.9	36.9	27.6	346	*n.d.*	*n.d.*	[190]
17	*Precompression*	*Bott.*	*GT*	8.8	36.9	27.6	385	31.4	*n.d.*	[190]
18(*a*)	*Recompression*	*Bott.*	*GT*	8.4	30.0	32.0	450	33.9	51.7	[188]
18(*b*)	*Recompression*	*Bott.*	*MCFC*	7.4	35.0	22.5	650	45.1	61.1	[195]
19	*Partial Recuperation*	*Bott.*	*GT*	8.9	36.9	27.6	498	29.7	*n.d.*	[190]
20	*Cascade I*	*Bott.*	*GT*	8.5	36.9	27.6	604.9	28.4	*n.d.*	[94]
21	*Cascade II*	*Bott.*	*GT*	8.4	36.9	27.6	604.9	31.2	*n.d.*	[94]
22	*Dual Stage*	*Bott.*	*GT*	5.8	20.0	20.0	426	*n.d.*	50.0	[189]
23	*Cascade I + IC*	*Bott.*	*GT*	6.0	36.9	27.6	604.9	33.7	*n.d.*	[94]
24	*Cascade II + IC*	*Bott.*	*GT*	6.0	36.9	27.6	604.9	33.7	*n.d.*	[94]
25	*Composite Bott. II*	*Bott.*	*GT*	8.4	30.0	32.0	450	28.1	55.1	[188]
26	*Composite Bott. III*	*Bott.*	*GT*	8.4	30.0	32.0	450	28.4	55.4	[188]
27	*Cascade III*	*Bott.*	*GT*	5.0	36.9	27.6	604.9	35.2	*n.d.*	[94]
28	*Three − Stage*	*Bott.*	*GT*	6.4	20.0	20.0	480	26.0	23.7	[181]
29	*Bott. Recompr. w/ RH*	*Bott.*	*GT*	8.4	30.0	32.0	450	35.6	52.9	[188]
30	*Composite Bott. I*	*Bott.*	*GT*	8.4	30.0	32.0	450	31.5	55.4	[188]
31	*Composite Bott. IV*	*Bott.*	*GT*	8.4	30.0	32.0	450	29.5	55.8	[188]
32	*Simple Recuperated + Recompr.*	*Bott.*	*GT*	8.4	30.0	32.0	260|450	32.3	55.3	[188]
33	*Recompression + Preheating*	*Bott.*	*GT*	7.8	32.0	28.0	307|570	34.1	57.9	[196]
34	*Precompression + Preheating*	*Bott.*	*GT*	7.8	32.0	28.0	333|570	33.4	57.6	[196]
35	sCO_2+TCO_2	*Bott.*	*MCFC*	6.4|8.1	25.0|55.0	22.5	650	46.1	61.5	[195]
36	*RCO2 + TCO2*	*Topp. + Bott.*		6.4|7.4	25.0|32.0	10.0|20.0	230|550	44.3	45.9	[107]
37	*Peregrine Turbine*	*Nes.*	*GT*	7.5	32.0	25.4	750	*n.d.*	49.0	[198]
38	*Recuperated Peregrine Turbine*	*Nes.*	*GT*	7.8	32.0	26.7	750	*n.d.*	43.0	[198]

Table 2.5: Combined cycles. Original boundary conditions ($P[MPa]$, $T[°C]$).

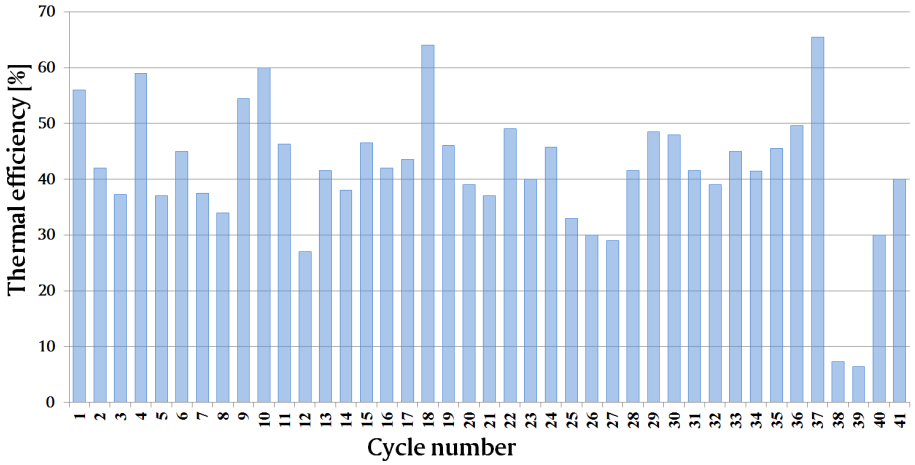

Figure 2.32: Stand-alone cycles. Summary of thermal efficiencies (Correspondence of cycle number in Table 2.4).

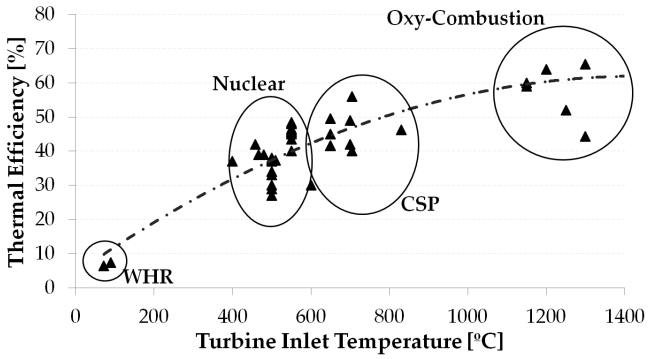

Figure 2.33: Influence of turbine inlet temperature on thermal efficiency for the stand-alone cycles considered.

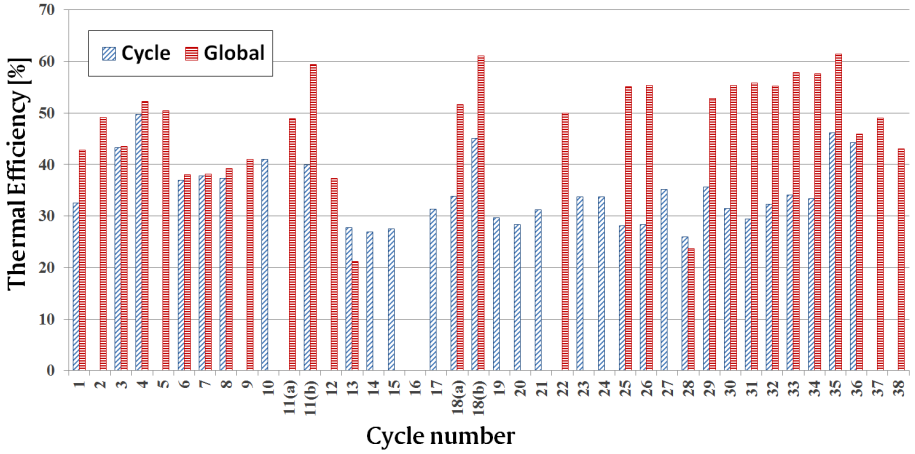

Figure 2.34: Combined cycles. Summary of sCO_2 and overall thermal efficiencies (Correspondence of cycle number in Table 2.5).

2.6.2 Qualitative comparison

Further to the comparison of thermal performance given in the previous section, a new assessment of the technology is presented below. With the objective of identifying the main advantages and shortcomings (flaws) of the numerous cycles proposed, their corresponding strengths and weaknesses (as identified by the author) have been listed in Tables 2.6 to 2.9. The first set of tables, Table 2.6 and 2.7, corresponds to stand-alone layouts whereas Tables 2.8 and 2.9 refer to combined cycle configurations.

Tables 2.6 and 2.7 do not aim to be exhaustive nor to provide a complete list of strengths and weaknesses to which no further items could be added. Also, given the fundamental description presented in this chapter, where emphasis has been put on the thermodynamic features of sCO_2 cycles, a complete SWOT (strengths, weaknesses, opportunities, threats) analysis has been considered arbitrary or likely to introduce large subjectivity.

For the cited reasons, Tables 2.6 and 2.7 focus on the following aspects:

- Layout: simple layouts are preferred over more complex configurations. Usually, the latter require a larger number of components which would arguably make off-design operation less flexible than in the former case. Nevertheless, complexity is in some cases linked to flow-split valves whose set point depends on the operating strategy of the cycle, and can therefore bring additional maneuverability to the power plant (i.e., the fraction of flow diverted depends on certain restrictions regarding the pressure and temperature at certain locations of the cycle, thus changing dynamically with the operating conditions).

- Thermal efficiency: further to the previous bullet point, thermal efficiency usually comes at the cost of a higher cycle complexity.

- Carbon capture: some cycles based on oxy-combustion enable carbon capture without chemical processes involved. Unfortunately, this is usually accompanied by the need to incorporate an Air Separation Unit to work in parallel with the sCO_2 cycle.

- Suitability for certain applications, in particular nuclear reactors.

- Cooling process: some cycles require very low temperatures at the beginning of the compression process which means wet or even cryogenic cooling systems.

- Footprint: there are some features related to the footprint of the system: specific/expansion work, effectiveness (pinch point) of heat exchangers...

The information in Tables 2.8 and 2.9 is based on similar principles but incorporates features that are specific to combined cycles. The most important amongst these is the temperature rise across the heater in cycles used to bottom higher temperature systems, according to the information in Table 2.3. In these cycles, this temperature rise is proportional to the efficiency of waste heat recovery. In other words, the larger ΔT_{heater}, the more energy is recovered from the exhaust of the topping cycle and the higher η_{WHR}. Another feature that is linked to the previous one is whether the heating process is split into more than one heat exchanger. This layout is usually aimed at enhancing the heat recovery process even if it brings about a higher

♯	Cycle Name	Strengths	Weaknesses
1	Simple recuperated	Simple layout Experimental facilities available	Internal pinch-point Moderate thermal efficiency
2	Transcritical CO_2	Simple layout High specific work	Wet cooling needed
3	Hot Day	Relatively simple layout Commercial	Moderate thermal efficiency
4	Allam	Very high thermal efficiency Integrated CO_2 capture Commercial	Very complex layout ASU needed High TIT
5	Intercooling II	Simple layout	Increased cooling load
6	Brayton CO_2 GT	Good thermal efficiency Specific for CSP	Lack of significantly positive features
7	Reheating II	Simple layout Higher expansion work	Lack of significantly positive features
8	Split-Expansion	Simple layout Higher expansion work	Low thermal efficiency
9	Matiant	High specific work Integrated CO_2 capture	Remarkably high TIT ASU needed Very complex layout
10	Allam+RH	Very high thermal efficiency Integrated CO_2 capture	Very complex layout ASU needed
11	Forced Cooler	High thermal efficiency	R134-a refrigeration cycle is needed
12	DEMO	High thermal efficiency Integrated CO_2 capture	Complex layout High rated TIT ASU needed
13	Preheating	Fits with ΔT of nuclear reactor	Low thermal efficiency
14	S-EJ	High thermal efficiency Lower pressure level	Complex layout Number of components
15	Inter-recuperated	Enhanced recuperation of heat	Modest thermal efficiency
16	Recompression	High thermal efficiency Internal pinch-point cleared Smaller cooler Experimental facilities available	Complex recuperator design
17	BAS	Fits with ΔT of nuclear reactor	Large number of HXs
18	Precompression	Unrestricted turbine exhaust pressure	Mechanical design of components
19	Recuperated CPOC	Very high thermal efficiency Integrated CO_2 capture	Complex layout High rated TIT Cryogenic cooling system ASU needed
20	Partial Cooling	High thermal efficiency High specific work Low sensitivity to PR deviations	Complex layout
21	Intercooling I	Fits with Na-cooled fast nuclear reactor	Complex layout

Table 2.6: Stand-alone cycles: Strengths-Weaknesses analysis (Part 1).

♯	Cycle Name	Strengths	Weaknesses
22	Reheating I	Fits with Na-cooled fast nuclear reactor	Complex layout
23	Double Reheated Recompression	High thermal efficiency Internal pinch-point cleared	Complex layout
24	Driscoll	Prevents pinch-point problems	Low thermal efficiency
25	REC2	Fits with ΔT of nuclear reactor	Large Number of HXs
26	Turbine Split Flow I	Higher expansion work	Low thermal efficiency
27	Turbine Split Flow II	Higher expansion work	Low thermal efficiency
28	Turbine Split Flow III	Higher expansion work	Low thermal efficiency
29	RC-EJ	High thermal efficiency Lower pressure level needed	Complex layout Number of components
30	Recompression+IC+RH	Same as Recompression cycle Specifically designed for CSP	Large number of HXs Number of components
31	Partial Cooling+RH	Same as Partial Cooling cycle Specifically designed for CSP	Large number of HXs Number of components
32	MC-EJ	High Thermal Efficiency Lower pressure level needed Reduced compression work	Complex Layout Number of components
33	Double Recompression	Highly recuperative Fits with Na-cooled fast nuclear reactor	Very complex layout No increase in thermal efficiency
34	Part. Cooling with Improved Recuperation	Highly recuperative Fits with Na-cooled fast Nuclear reactor	No increase in thermal efficiency
35	Cascade	Commercial interest Designed for CSP (high $\Delta T_{receiver}$)	Complex layout Number of components
36	REC3	Fits with ΔT of nuclear reactor Highly recuperative	Complex layout Large number of HXs
37	Schroder-Turner	High thermal efficiency Extremely recuperative	Very complex layout
38	Quasi-Combined	Remarkably high thermal efficiency Integrated CO_2 capture Remarkably high pressure ratio High specific work	Very complex layout Remarkably high rated TIT LNG cooling system ASU needed
39	Rankine with Reheat	Designed for low-T WHR Simple layout	Low thermal efficiency
40	Rankine with ejector	Designed for low-T WHR	Low thermal efficiency Ejector needed
41	CPOC	Integrated CO_2 capture	Low thermal efficiency Cryogenic cooling system ASU needed
42	TCO	High thermal efficiency Integrated CO_2 capture	Prohibitive pressure level ASU needed

Table 2.7: Stand-alone cycles: Strengths-Weaknesses analysis (Part 2).

♯	Cycle Name	Strengths	Weaknesses
1	Simple Recuperated	See cycle 1, Table 2.6	See cycle 1, Table 2.6
2	Simple Recuperated + IC + RH	See cycle 1, Table 2.6 High turbine exhaust temperature	See cycle 1, Table 2.6
3	Recompression	See cycle 16, Table 2.6	See cycle 16, Table 2.6
4	Partial Cooling	See cycle 20, Table 2.6 High combined cycle efficiency	See cycle 20, Table 2.6
5	Partial Cooling + RH	See cycle 20, Table 2.6 High combined cycle efficiency High turbine exhaust temperature	See cycle 31, Table 2.6
6	sCO2-ORC II	High specific work High turbine exhaust temperature	Complex layout Large number of HXs Low combined cycle efficiency
7	sCO2-ORC III	High specific work High turbine exhaust temperature	Complex layout Large number of HXs Low combined cycle efficiency
8	sCO2-ORC IV	High specific work High turbine exhaust temperature	Very complex layout Large number of HXs Low combined cycle efficiency
9	Brayton	Very simple layout Not recuperative High ΔT_{heater}	Low combined cycle efficiency
10	iso-Brayton	Very simple layout (no cooler) Not recuperative High ΔT_{heater}	Low combined cycle efficiency Isothermal compression process
11	Simple Recuperated	See cycle 1, Table 2.6	Highly recuperative Small ΔT_{heater}
12	Hot day	See cycle 3, Table 2.6 High ΔT_{heater}	See cycle 3, Table 2.6
13	Preheating	Heating process in two steps High $\Delta T_{heaters}$	Low combined cycle efficiency
14	Triple heating	Heating process in three steps High $\Delta T_{heaters}$ Excellent waste heat recovery	Large number of HXs
15	Dual Expansion	Heating process in two steps High waste heat recovery	Complex layout
16	Combined Recompression + Preheating	Heating process in three steps Very high $\Delta T_{heaters}$ Excellent waste heat recovery	Complex layout
17	Precompression	See cycle 18, Table 2.6 High combined cycle efficiency	See cycle 16, Table 2.6 Poor waste heat recovery
18	Recompression	See cycle 16, Table 2.6	Highly recuperative Poor waste heat recovery Low global specific work
19	Partial Recuperation	Heating process in two steps	Complex layout

Table 2.8: Combined cycles: Strengths-Weaknesses analysis (Part 1).

♯	Cycle Name	Strengths	Weaknesses
20	Cascade I	Good waste heat recovery	Low recuperator effectiveness Low net specific work
21	Cascade II	Heating process in two steps Good waste heat recovery High net specific work	Low thermal efficiency
22	Dual Stage	Same as cycle 20 in this table High specific work	Wet cooling needed
23	Cascade I + IC	High net specific work	Low recuperator effectiveness
24	Cascade II + IC	Heating process in two steps Very good waste heat recovery High thermal efficiency High net specific work	
25	Composite bottoming II	Heating process in two steps Very good waste heat recovery High combined cycle efficiency	Complex layout Number of components
26	Composite bottoming III	Heating process in three steps Very good waste heat recovery High combined cycle efficiency	Very complex layout Number of components
27	Cascade III	Heating process in two steps Remarkable waste heat recovery High thermal efficiency Remarkable net specific work	Complex layout
28	Three Stage	High specific work	Wet cooling needed Complex layout
29	Recompression bottomming + RH	See cycle 18, Table 2.8 High combined cycle efficiency Heating process in two steps	See cycle 18, Table 2.8
30	Composite bottoming I	Heating process in two steps High combined cycle efficiency	Complex layout Highly recuperative
31	Composite bottoming IV	Heating process in four steps Very good waste heat recovery High combined cycle efficiency	Very complex layout Number of components
32	Recompression + Simple Recuperative	See cycle 11 and 18, Table 2.8 Heating process in two steps High combined cycle efficiency	Number of components Very large number of HXs
33	Recompression + Preheating	See cycle 13 and 18, Table 2.8 Heating process in three steps High combined cycle efficiency	Number of components Very large number of HXs
34	Precompression + Preheating	See cycle 13 and 17, Table 2.8 Heating process in three steps High Combined Thermal Efficiency	Several Components Very large number of HXs
35	sCO2 + TCO2	See cycle 1,Table 2.8; cycle 2, Table 2.6 Simple layout High combined cycle efficiency	Wet cooling needed
36	RCO2 + TCO2	See cycle 3,Table 2.8; cycle 2, Table 2.6	Wet cooling needed
37	Peregrine Turbine	Simple Layout High combined cycle efficiency	
38	Recuperated Peregrine Turbine		Complex layout Large number of HXs

Table 2.9: Combined cycles: Strengths-Weaknesses analysis (Part 2).

costs due to the several high temperature heat exchangers that are needed.

Finally, even if some interesting works with a formal approach to project appraisal have recently been published [41], assessing the economics of sCO_2 cycles is still very uncertain due to the lack of experimental facilities and standardization. Therefore, most of the attempts to evaluate the cost of the technology are based on mere extrapolations from other power generation technologies. It is precisely in this scenario that the qualitative comparison presented in this section, in combination with the numerical information provided in Section 2.6.1, provides hints to screen potential layouts for specific applications. With this information, a pre-selection of cycles is possible. Then, a more rigorous assessment of the on-design and off-design thermal performance should give way to a complete techno-economic evaluation for which considering specific boundary conditions would be mandatory.

2.7 Selection of the best cycle layout

Reorganizing all the information discussed so far in chronological order, the lack of a clear development path of sCO_2 technologies from a thermodynamic performance standpoint becomes even more evident. Table 2.10, excerpted from Table 2.4, presents the following information for each cycle: name, most likely application, declared thermal efficiency, year of publication. Then, Figure 2.35 illustrates the chronological evolution of the thermal efficiency of the cycles, together with their corresponding peak temperatures. Thermal efficiencies are shown as blue bars and referring to the left axis, whilst turbine inlet temperatures are represented by markers whose values are given by the right axis. All these markers are then connected by a black dashed line[4].

#	Name	Application	η_{th}[%]	Year	Ref.	#	Name	Application	η_{th}[%]	Year	Ref.
1	Simple Recuperated	Not.spec.	40.4	1968	[12, 11]	22	Hot day	WHR	37.3	2013	[130, 109]
2	Transcritical CO2	Nuclear	42.0	1968	[38]	23	Intercooling II	Nuclear	37.0	2014	[101]
3	DEMO	Oxy-comb.	52.0	1995	[141]	24	BraytonCO2GT	CSP	45.0	2014	[136]
4	Matiant	Oxy-comb.	44.3	1999	[137]	25	Reheating II	Nuclear	37.5	2014	[101]
5	Quasi-Combined	Oxy-comb.	65.5	2006	[168]	26	Split-Expansion	Nuclear	34.0	2014	[101]
6	Intercooling I	Nuclear	39.0	2009	[97]	27	Allam + RH	Oxy-comb.	60.0	2014	[132]
7	Reheating I	Nuclear	37.0	2009	[97]	28	Pre-heating	Nuclear	27.0	2014	[101]
8	Double Recompression	Nuclear	39.0	2009	[97]	29	Inter-recuperated	Nuclear	38.0	2014	[101]
9	Recompression	Nuclear	46.5	2011	[38, 11]	30	Recuperated CPOC	Oxy-comb.	64.0	2014	[161]
10	Precompression	Nuclear	43.5	2011	[38, 11]	31	REC2	Nuclear	45.7	2014	[150]
11	Partial Cooling	Nuclear	46.1	2011	[38, 11]	32	Turbine Split Flow I	Nuclear	33.0	2014	[101]
12	Driscoll	Nuclear	40.0	2011	[162]	33	Turbine Split Flow II	Nuclear	30.0	2014	[101]
13	Part. Cool. w/ impr. rec.	Nuclear	45.0	2011	[6, 11]	34	Turbine Split Flow III	Nuclear	29.0	2014	[101]
14	Rankine w/ reheat	WHR	7.30	2011	[169]	35	Rankine w/ ejector	WHR	6.40	2014	[170]
15	Cascade	CSP	41.4	2012	[105]	36	CPOC	Oxy-comb.	30.0	2014	[161]
16	TCO	Oxy-comb.	40.0	2012	[171]	37	Forced Cooler	Nuclear/CSP	46.3	2016	[140]
17	Allam	Oxy-comb.	59.0	2013	[131]	38	S-EJ	Nuclear/CSP	41.6	2016	[143]
18	BAS	Nuclear	42.0	2013	[159]	39	RC-EJ	Nuclear/CSP	41.6	2016	[143]
19	Recompression + RH + IC	CSP	48.5	2013	[116]	40	MC-EJ	Nuclear/CSP	41.6	2016	[143]
20	Partial Cooling+ RH	CSP	48.0	2013	[116]	41	Double Reheated Recompr.	Fossil Fuel	52.4	2016	[121]
21	REC3	Nuclear	45.5	2013	[159]	42	Schroder-Turner	Solar	49.6	2016	[167]

Table 2.10: Survey of sCO_2 cycle layouts published in the public domain. Where two references are provided, the first one indicates the year of first publication whilst the reported thermal efficiency is taken from a more recent source.

The possible applications (i.e. energy source) of the cycles in Table 2.10 are easily deduced

[4] It is noted that turbine inlet temperature is not reported for the *Cascade* cycle, number 15 in Fig. 2.35. This is because values were not provided in the original work from [105]

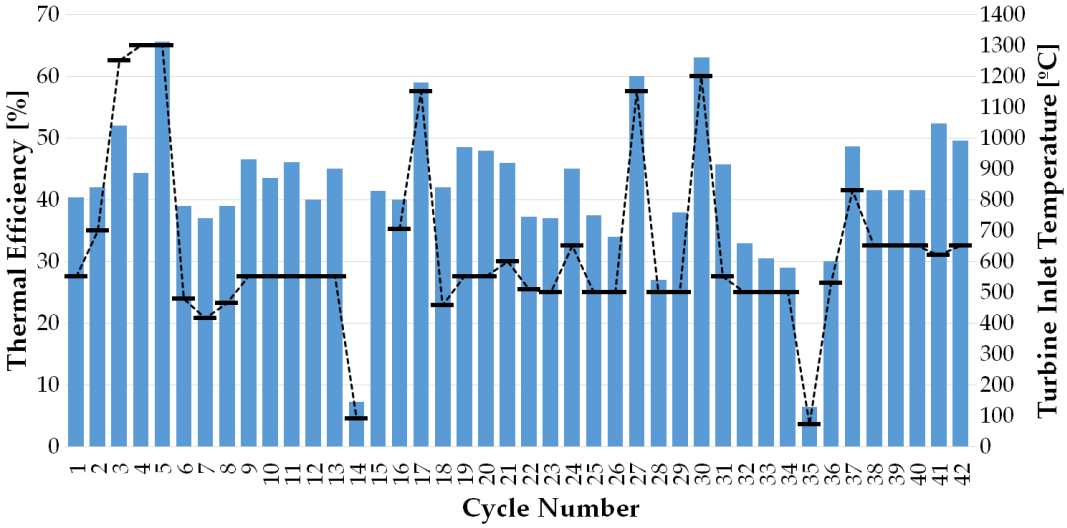

Figure 2.35: Chronological development of sCO_2 cycles: thermal efficiencies and Turbine Inlet Temperatures. Cycle numbers refer to Table 2.10, and are different from those in Table 2.4.

from their corresponding TIT by merely observing Fig.s 2.33 and 2.35: oxy-combustion and fossil-fuel driven cycles present exhibit really high temperatures (above 1000 ºC), Nuclear and CSP applications lie between 500 and 750 ºC, and WHR options operate at extremely low temperatures, lower than 100 ºC.

The scenario depicted in the foregoing tables and charts is certainly heterogeneous, and it pretty much looks as if each new cycle did not rely on the previously existing body of knowledge. This observation could arguably be explained by the absence of a thorough and rigorous analysis of the underlying thermodynamics principles of sCO_2 cycles. Indeed, even if a large number of works regarding cycle optimization have been published, virtually none has followed the path already set forth by Angelino and Feher [6, 12].

In spite of the comments set forth earlier in this section, the information contained in Table 2.10 and Figure 2.35, along with the qualitative comparison included in Tables 2.6 and 2.7, is now employed in the pre-selection of cycles, aimed at finding the best layouts that will be object of the thermodynamic and thermo-economic comparisons developed in the next chapters. Hence, those cycles with higher thermal efficiencies could easily be identified as the best candidates, but a selection based only on this figure of merit could turn out really misleading. In fact, configurations presenting high values of η_{th} are normally characterized by extremely high TIT, so choosing only amongst these cycles could limit the study to layouts specifically created for oxy-combustion applications. Moreover, keeping in mind that the actual topic of the present PhD dissertation is to analyze the feasibility of sCO_2 cycles applied to CSP plants with Thermal Energy Storage, extremely high temperatures might not be of interest. Based on this rationale, the author decided to select those cycles with highest thermal efficiency but trying *a)* to maintain in this portfolio representative cycles for the three main fields of application (oxy-combustion, CSP and Nuclear in Table 2.10), *b)* to take into account the real impact that the different configurations had in specific literature and *c)* to avoid extremely

complex layouts. The result is a set of twelve different cycles, as described in the following paragraphs.

Firstly, in order to retain the original works by Feher [12] and Angelino [38], the *Simple Recuperated* and the *Transcritical CO_2* are selected, cycles number 1 and 2 in Figure 2.35. As discussed previously, the former is a Brayton-like cycle, while the second is a Rankine-like one. They share the same simple layout, with the only difference that the cooler and compressor of the *Simple Recuperated* cycle are replaced by a condenser and pump in the *Transcritical CO_2*. Both cycles are reported to achieve intermediate thermal efficiency when operating with moderate turbine inlet temperature,so there may be margin for improvement of their thermodynamic performance. Moreover, these cycles have already been included in experimental facilities [50, 53, 54, 52] discussed in Chapter 1, which means that they are at a higher Technology Readiness Level (TRL), and they have strongly influenced all the research done in sCO_2 technology in the last forty years.

The *Recompression*, *Precompression* and *Partial Cooling* cycles (number 9, 10 and 11 in Figure 2.35) have been selected from the work by Kulhanek and Dostal [11]. Originally proposed by Angelino [38] with a transcritical configuration, these layouts are presented by Dostal in his PhD thesis as being the best candidates for Nuclear power plants [67]. If an intermediate turbine inlet temperature is considered (550ºC, [11]), these cycles have the potential to achieve fairly high thermal efficiency, 46.5, 43.5 and 46.1 % respectively. Together with the *Simple Recuperated* cycle, these layouts are the most referenced and studied ones in literature (see Table 2.2). In particular, the *Recompression* cycle is very likely the most famous configuration, and it has already been experimented several times by SANDIA [49, 51]. This provides the cycle with a high TRL.

For CSP applications, the following three cycles are selected: *Recompression+RH+IC*, *Partial Cooling+RH* and *Schroder-Turner*. The first two cycles are proposed by Turchi et al. [116]; they are mostly evolutions of the afore-described *Recompression* and *Partial Cooling* cycles, with the addition of intercooling and reheat. These features enhance their thermodynamic performance strongly, along with the fact that the double heater may be able to improve the performance of the solar receiver. On the other hand, the *Schroder-Turner* layout presents one of the best recuperator configurations among the cycles presented in literature, along with a high thermal efficiency, which may have a positive impact on its thermodynamic and thermo-economic features.

Akin to the *Recompression+RH+IC* layout, the *Double Reheated Recompression* cycle is an evolution of the *Recompression* configuration with an enhanced reheat process. In spite of its complexity, this layout results to be very interesting given the extremely high thermal efficiency claimed by Mecheri and La Moullec [121].

The *Allam*, *Matiant* and *Quasi-Combined* cycles are selected as representatives for oxy-combustion applications. These cycles are particularly interesting due to their high specific work which enables, along with the very high thermal efficiency, a significant footprint reduction. Moreover, it is worth noting that the *Allam* cycle is the only cycle that has already chieved the pre-commercial scale [133].

Finally, it must be highlighted that some cycles characterized by very high thermal efficiency ($\eta_{th} > 45\%$) have been excluded from the pre-selection process, mostly due to the complexity of their layouts or to the need for especial equipment what makes them less feasible than the selected configurations. In particular, the *DEMO*, *Allam+RH* and *Recuperated CPOC* layouts are very similar to the *Allam* cycle and share the same advantages but at the cost of a much more complex layout; therefore, the author has decided to consider the *Allam* cycle only. The same applies to the *REC2*, *REC3* and *Partial Cooling with improved recuperation* cycles, which are mere evolutions of the *Recompression* and *Partial Cooling* layouts, but with a larger number of heat exchangers which is not compensated for by the resulting performance gain.

2.8 Conclusions

This chapter has presented a thorough review of the state of the art of sCO_2 power cycles, covering forty two different stand-alone layouts and thirty eight combined cycle configurations. These cycles have also been categorized according to their main features, yielding twenty seven and thirty different categories respectively, Tables 2.2 and 2.3. The average thermal efficiency of the stand-alone power cycles is in the order of 40%, Table 2.4, even if values in the range from 60 to 65.5% are achieved by oxy-combustion cycles using very high turbine inlet temperatures, Figure 2.33. For combined cycle layouts, efficiencies in the range from 50 to 60% seem to be easily affordable.

From a global perspective, there is no doubt that the sCO_2 power cycle has captured the attention of the energy industry either for stationary power generation, combined heat and power or waste heat recovery. Its versatility in a wide range of applications and fuels, whether fossil, nuclear or renewable, and the remarkable performance at moderate temperatures set this technology apart from the competitors that currently dominate the market.

Based on this premise, the truth is that the rapid growth of the scientific and industrial communities around sCO_2 has inevitably relied on an unstructured search of more efficient and technically feasible cycles, sometimes lacking an underpinning thermodynamic rationale. This is in contrast with the seminal works by Angelino [38, 6] and Feher [12] which put forward a systematic approach to sCO_2 technology for different operating conditions. Along the same lines as the latter authors, the author of this research has humbly tried to review and categorize the vast amount of information produced around supercritical carbon dioxide in recent years. It has indeed been shown that this can be systematically organized in cycles sharing some basic features and, therefore, performances. Such categorization will hopefully yield a sort of road-map to be used by researchers in the field to screen the cycles that meet their interests best.

As a result of the this thorough literature review, twelve configurations have been selected as possible candidates for CSP power plants: *Simple Recuperated*, *Transcritical CO_2*, *Precompression*, *Recompression*, *Recompression+RH+IC*, *Partial Cooling*, *Partial Cooling+RH*, *Schroder-Turner*, *Double Reheated Recompression*, *Allam*, *Matiant* and *Quasi-Combined*. These configurations are thoroughly presented and analyzed from a thermodynamic standpoint in the following chapter.

3 Thermodynamic Analysis

This chapter presents a thermodynamic comparison between the twelve cycles selected in the previous chapter, without further economic or technological considerations. In the first part of the analysis, ***no technical restrictions*** *are considered with the aim to focus on the actual thermodynamic potential of each cycle. Then, in a second phase, restrictions are set on the maximum temperature achievable by the recuperator. In all cases,* ***common boundary conditions*** *are used, and various peak temperature levels are considered, theoretically corresponding to different potential applications. A brief description of the models employed to characterize the performance of heat exchangers is also provided.*

An adapted version of this chapter has been published in:

F. Crespi, G. Gavagnin, D. Sánchez, G.S. Martínez, 2018, *Analysis of the Thermodynamic Potential of Supercritical Carbon Dioxide Cycles: a Systematic Approach*, Journal of Engineering for Gas Turbines and Power 140, 051701.

3.1 Introduction

The objective of the present chapter is to set up and develop a systematic analysis of the different sCO_2 cycles proposed in literature in order to hopefully draw universal conclusions regarding the layouts that are most interesting. To this end, common boundary conditions must be fed into a thermodynamic model of performance along with a similar set of assumptions regarding where the technological limits (maximum pressure) lie.

After the thorough review provided in Chapter 2, a total of forty two different configurations are identified, amongst which twelve layouts of interest are chosen. The corresponding layouts are presented in Figure 3.1: *Simple Recuperated*, *Transcritical CO_2*, *Precompression*, *Recompression*, *Recompression+RH+IC*, *Partial Cooling*, *Partial Cooling+RH*, *Schroder-Turner*, *Double Reheated Recompression*, *Allam*, *Matiant* and *Quasi-Combined*. For these configurations, the dependence of specific work and thermal efficiency on pressure ratio and turbine inlet temperature has been explored. The results are then presented in the form of standard diagrams as those already employed by Angelino in [6], Figure 3.2, and other authors for open and closed cycle gas turbines [219, 98].

Angelino's original idea is developed a little further though and applied to the analysis of the twelve cycles at four temperature levels (550, 750, 950 and 1150 ^{o}C) and a significantly

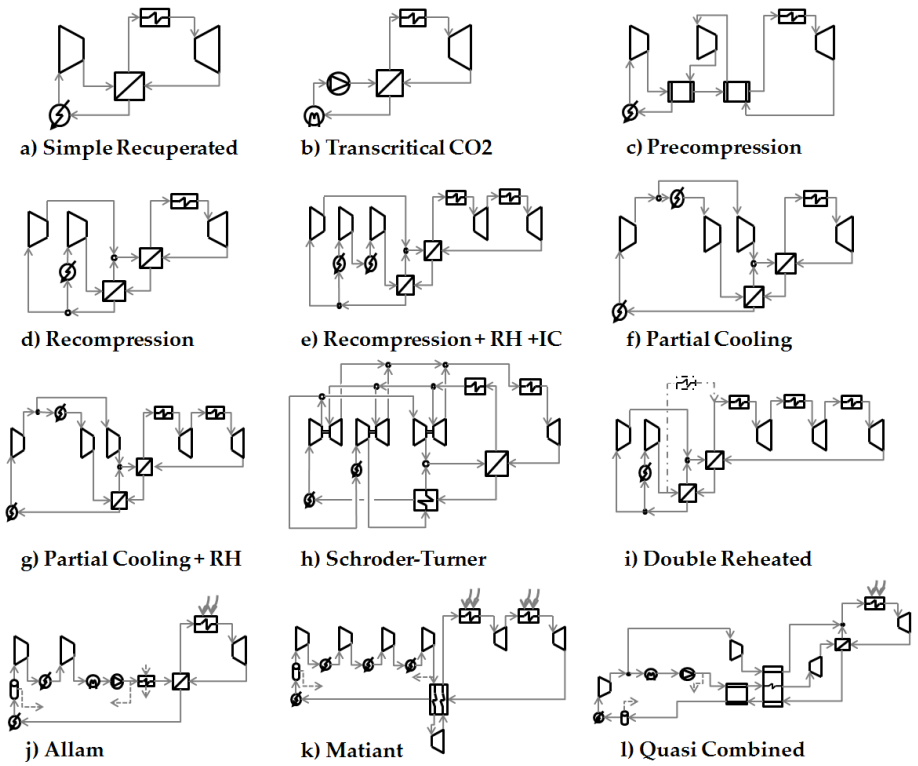

Figure 3.1: Layouts of selected cycles.

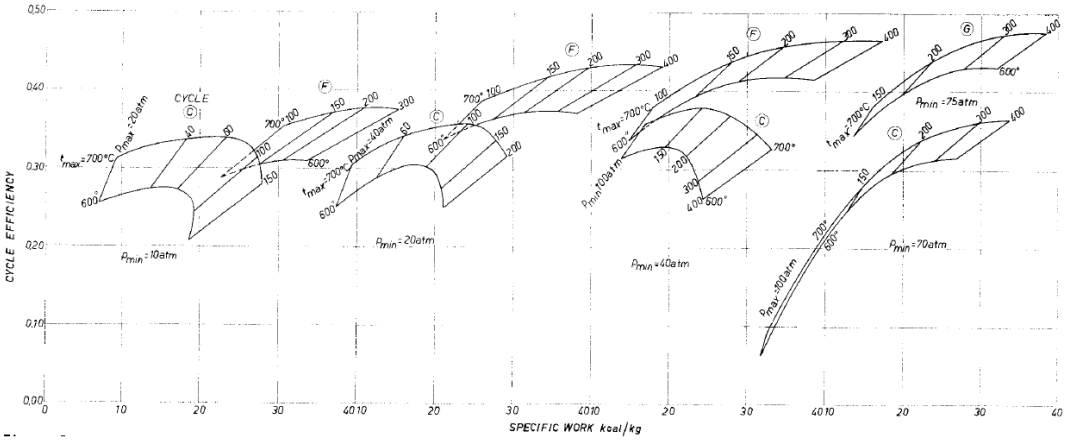

Figure 3.2: Diagrams of Thermal Efficiency vs. Specific Work, as originally proposed by Angelino [6].

larger range of pressures (in certain cases up to 600 MPa). The aim of this approach is to actually separate the thermodynamic potential of each cycle from the inherent technological constraints brought about by the very high operating pressures and temperatures. This is thought to provide a clearer insight into which cycles offer a larger margin for efficiency gain, should a parallel development of materials, manufacturing and auxiliary systems take place.

Moreover, the author decided not to consider temperatures lower than 550ºC for a twofold reason: on one hand, this is the current state-of-the-art temperature for a CSP plants with TES, and reducing this value would only lead to a reduction in terms of thermal efficiency without any evident benefit; on the other hand, even if no particular application is taken into account, Angelino [6] specifically claimed that the sCO_2 cycle is able to achieve efficiencies higher than a Rankine cycle only if its turbine inlet temperature is significantly higher than 550ºC, depending on the pressure level considered. Therefore, limiting the study to temperatures higher than 550 ºC, sCO_2 power cycles are analyzed for the conditions of interest only, those for which sCO_2 technology has the potential to yield better performance than standard Rankine cycles using water/steam.

Nevertheless, before starting the analysis of the selected cycles, a brief description of tools used during the simulations is provided in the next section.

3.2 Simulation tools

In order to analyze the cycles presented in the previous section, in-house Matlab models have been developed on the principal assumption that the working fluid is pure CO_2. This assumption is however not formally correct for oxy-fired cycles (cycles j, k and l in Figure 3.1), which typically work with a mixture of CO_2, H_2O and residuals in the turbine and low pressure side of the recuperator. Nevertheless, the corresponding inaccuracy (i.e., the impact of the modified composition on turbine work and heat exchanger performance) is considered to not have a strong influence on cycle performance whilst, at the same time, it simplifies the calculations and enables considering these cycles for externally fired applications also. The validation presented later in this chapter confirms that this approach is correct.

For the calculation of the thermodynamic properties of sCO_2, the open-source library *CoolProp* has been used [220]. Fyrthermore, since the comparison developed in the present chapter is based on (on-design) thermodynamic performance only, the major equipment of the cycle can be simulated with simple thermal models, without considering their actual geometry and design. In order to carry out the thermo-economic assessment contained in the next chapters, much more elaborated models have been specifically developed by the author.

3.2.1 Heat Exchangers

Heat exchangers have been modeled with a one-dimensional model whereby the equipment is divided into a suitable number of sub-heat exchangers, all with the seam heat duty, in order to consider small temperature changes and therefore constant sCO_2 properties in each of them [10]. This common expedient enables the application of simplified performance analysis methods like, for instance, the ϵ-NTU methodology in each division [221]. Other approaches used in literature are even simpler, assuming constant effectiveness or constant ΔT_{min} (pinch-point) at one end of the heat exchanger. In the present work, an initial value of $\epsilon = 95\%$ is assumed for all divisions and the corresponding temperature differences between hot and cold fluids (ΔT_i) are computed. The resulting minimum difference (pinch point of the heat exchanger ΔT_{min}) is checked to be not lower than 5 ºC. If this were not the case (i.e., $\Delta T_i < 5$ ºC for any given i), the corresponding ϵ_i would be reduced to achieve the target pinch point. A thorough explanation of the one-dimensional model has been published by the author and co-workers in the public domain [221].

3.2.2 Turbomachinery

Turbomachinery performance models are fairly simple given that, at this stage, the code is intended for on-design thermodynamic performance only, for which isentropic efficiencies or equivalent figures of merit of the compression/expansion process serve the purpose. Nevertheless, a survey of the isentropic compressor/turbine efficiencies reported in (or reverse-calculated from) the original references yields a very large variability (the actual values are provided in a later section) so it is decided in this work to use representative polytropic efficiencies for compressors (89%), turbines (90%) and pumps (83%). These then yield different isentropic efficiencies depending on the operating conditions of each turbomachine (mostly pressure ratio). It is worth noting that the choice of a constant polytropic in lieu of isentropic efficiency is made in order to better capture the influence of the very different pressure/temperature ratios of the cycles considered[1].

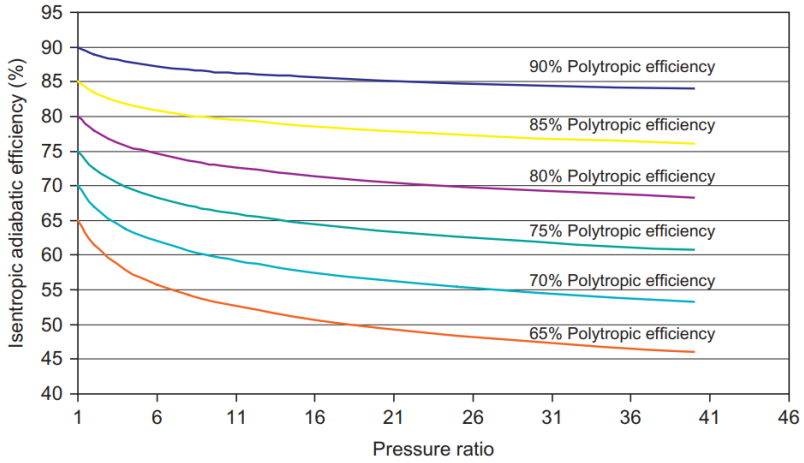

(a) Relationship between isentropic and polytropic efficiency of an air compressor.

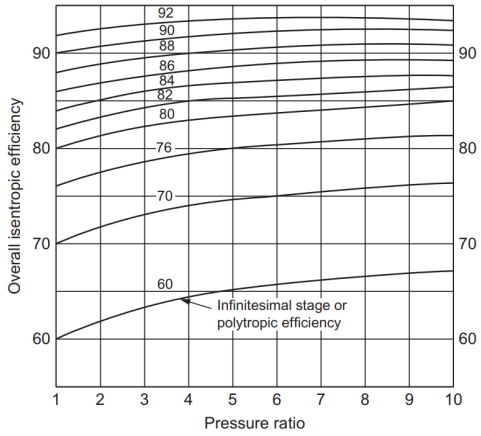

(b) Relationship between isentropic and polytropic efficiency of an air turbine.

Figure 3.3: Relationship between isentropic and polytropic efficiency in compressors and turbines (taken from [7]).

[1] Boyce claims that polytropic efficiency, also called *small stage* or *infinitesimal stage* efficiency, *"is the true aerodynamic efficiency exclusive of the pressure-ratio effect"* [7]

Figure 3.3 shows the correlation between polytropic and isentropic efficiencies of an air compressor and turbine with varying pressure ratio [7]. It becomes clearer that, considering a constant value of polytropic efficiency, the isentropic one varies as a consequence of the specific operating conditions.

3.2.3 Split-Flow Definition

As commented in the previous chapter, several sCO_2 cycles exhibit parallel streams during the compression and heat exchange processes (sometimes also during expansion) which are aimed at overcoming the known pinch point problem in low temperature heat exchangers, see Tables 2.6 and 2.7. This feature is usually referred to as a Split-Flow (or Part-Flow) compression process, and it is characterized by an additional parameter termed "Split-Flow" or "Recompression" fraction (ϕ). The latter represents the portion of fluid that, skipping the main compressor, is compressed in the recompressor without previous cooling, and then mixed with the main stream in between the low and high-T recuperators. In Figure 3.1, it is possible to see that the *Recompression* and *Partial Cooling* cycles and their respective evolutions incorporate this particular feature. Figure 3.4, taken from the work of Dyreby et al. at the University of Wisconsin-Madison [8] and showing results of a *Recompression* cycle operating at 550ºC and 20 MPa (TIT and cycle maximum pressure respectively) with different recuperator conductance values, shows the importance of a correct selection of ϕ. It is worth noting that an optimal ϕ, yielding the highest thermal efficiency, becomes very visible.

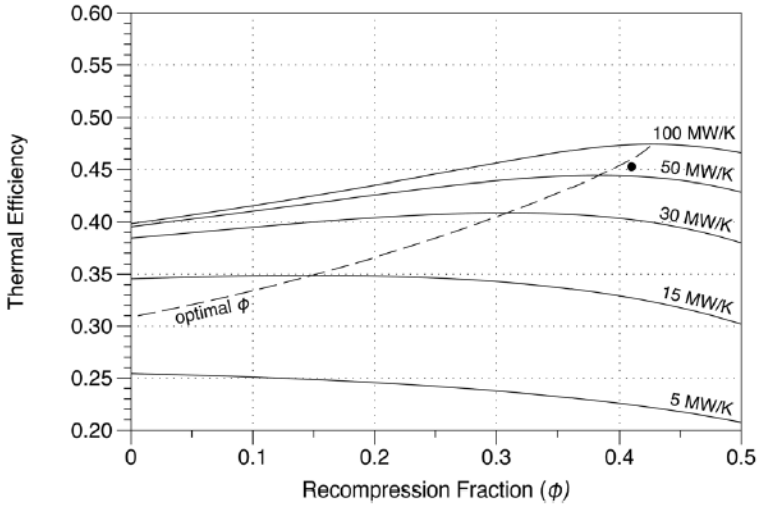

Figure 3.4: Dependence of thermal efficiency on split-flow Fraction, considering a *Recompression* cycle operating at 550ºC and 20 MPa (taken from [8]).

The definition of the optimum split-flow fraction, in literature, can nevertheless be defined either as the one that yields the highest thermal efficiency or, alternatively, that matches the temperatures of two streams that mix at a particular location (thus reducing thermal stresses of the components). The so defined fractions ϕ apply to a fixed set of boundary conditions and, when the latter change, they must change accordingly. Irrespective of this, in this dissertation, the values of ϕ are set to those reported in the original papers during verification of the code. Also, they do not remain constant but, on the contrary, they are continuously

adapted to yield highest thermal efficiency η_{th} for each set of boundary conditions considered.

In order to clarify this further, Figure 3.5 provides the trends presented by ϕ and η_{th} when the maximum cycle pressure is varied from 15 to 35 MPa, considering the *Recompression* and *Partial Cooling* layouts with turbine inlet temperature set to 750°C.

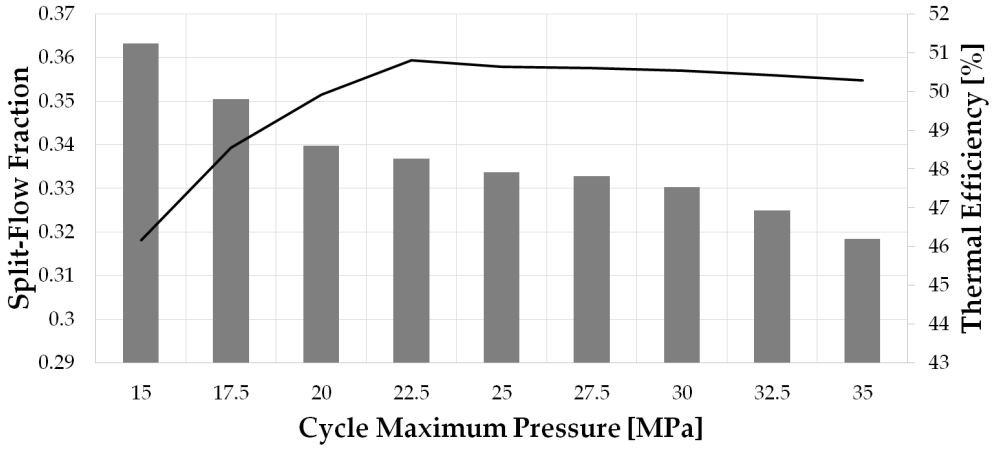

(a) Dependence of split-flow fraction and thermal efficiency on maximum pressure for the *Recompression* layout.

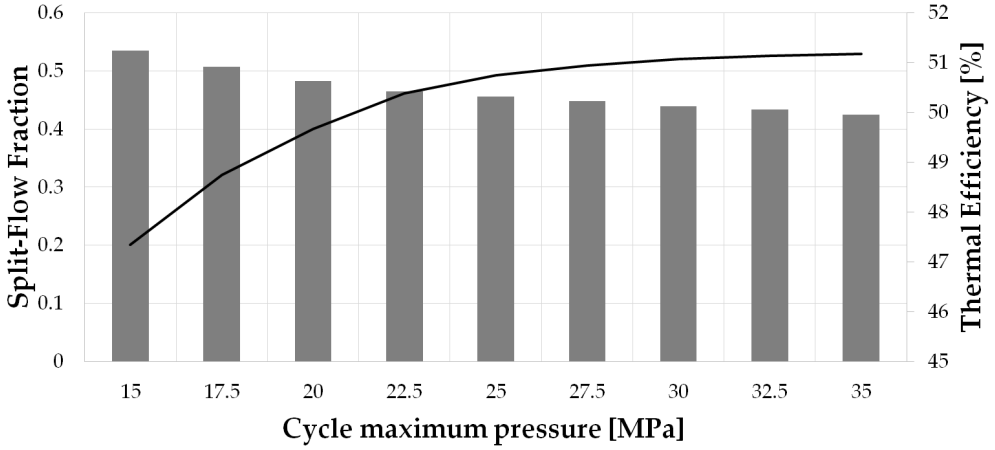

(b) Dependence of split-flow fraction and thermal efficiency on maximum pressure for the *Partial Cooling* layout.

Figure 3.5: Dependence of split-flow fraction and thermal efficiency on maximum pressure for different configurations. Turbine inlet temperature is set to 750°C.

The split-flow fraction is then represented by bars on the left axis, while thermal efficiency is presented by a black line whose values are reported by the right axis. Firstly, it is to note that ϕ decreases for increasing pressure in both configurations, and this means that the portion of low-T fluid flowing across the low-T recuperator increases. On the other hand, the trend of η_{th} results to be fairly different depending on which layout is taken into account. It is worth noting that the values of ϕ obtained for the former layout are very similar to those shown by Dyreby and shown in Figure 3.4. Considering a pressure of 20 MPa, for instance, the maximum thermal efficiency is achieved when 34% of the main sCO_2 stream is directed to the

recompressor, while the remaining 66% is sent to the low-T recuperator.

3.2.4 Verification

In order to validate the models, a comparison between the performances reported in the original references and those computed by the code is presented in Table 3.1 and Figure 3.6. It is observed that the calculated thermal efficiencies (η_{th}) are very similar to the original values ($\eta_{th,0}$) for cycles from *a* to *i*, for which deviations (Δ%) are smaller than 1%. For oxy-fired cycles though, the deviation is slightly larger, the reason being the cited assumption about the composition of the working fluid. Actually, as checked by the author, these deviations become negligible when specific simulations are run with corrected fluid compositions across the cycle, adjusted as per the corresponding oxy-combustion stoichiometry. This is confirmed by cases *j* and *j2* in Table 3.1 which correspond to the same *Allam* cycle with pure CO_2 and oxy-combustion products respectively; whereas the error in the later is negligible, the calculated efficiency in the former is 8% lower than in the reference case. This verification confirms that the code is accurate and it can hence be used in this fundamental analysis.

Cycle	η_{compr}	η_{turb}	η_{rec}	$\eta_{th,0}$	η_{th}	Δ%
a	89	93	95	40.44	40.45	0.02
b	85	90	95[1]	42.00	41.63	0.88
c	89	93	95	43.49	43.45	0.09
d	89	90	95/93	46.48	46.98	1.07
e	89	93	95	46.12	46.11	0.02
f	89	93	95	48.50	48.62	0.25
g	89	93	95	48.00	48.31	0.65
h	85/88	93/89	96/98	49.57	49.65	0.16
i	89	93	ΔT_{min} = 6 ºC	52.40	52.42	0.04
j	85	88	95[1]	59.00	54.22	8.10
j2	85	88	95[1]	59.00	59.40	0.68
k	75/85	87	95[1]	44.30	48.99	10.5
l	88	88	90[2]	65.60	66.42	1.25

Table 3.1: Verification of the simulation code employing the efficiencies reported in literature (η_{compr}, η_{turb} and η_{rec}). Note that, for the *Simple Recuperated* cycle *a*, reference [11] is used instead of [12] and that all the values in the table are displayed as percentages.

[1] Value not declared in the original papers. The author has assumed the standard value of 95% from literature.

[2] Heat exchanger effectiveness is not reported in [168] . The author has found that an effectiveness of 90 % provides the best fit with the values declared in this reference.

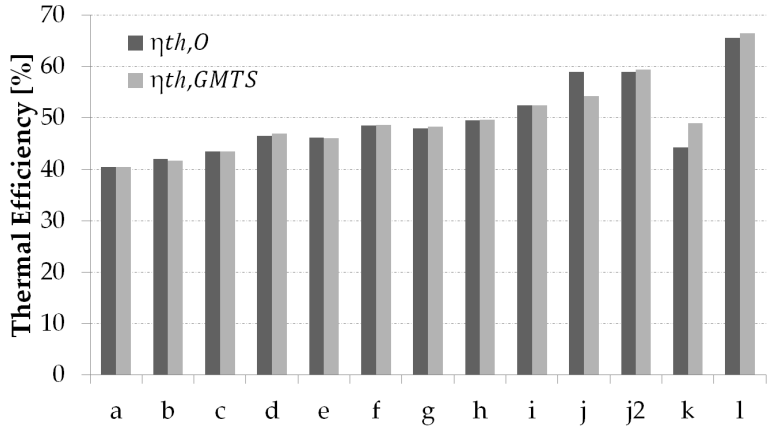

Figure 3.6: Verification of the code: comparison between original ($\eta_{th,0}$) and computed thermal efficiencies (η_{th}).

3.2.5 Boundary Conditions and Complementary Assumptions

In order to achieve comparable results, the selected cycles have been analyzed under the common set of boundary conditions reported in Table 3.2. Regarding compressor inlet conditions, the standard values in literature (32 ºC and 7.5 MPa) are used for the *Simple Recuperated*, *Precompression* and *Recompression* cycles (including the alternative embodiments *e* and *i*). The *Partial Cooling* and related cycles (*g* and *h*) show a lower minimum pressure due to the presence of a pre-compressor, whilst the *Transcritical* CO_2 (*b*) layout presents lower compressor inlet pressure and temperature to enable condensation. Finally, the original paper conditions are used for the oxy-fired cycles (*j*, *k* and *l*).

Cycle	$T_{in,compr}$ [ºC]	$P_{in,compr}$ [Mpa]	$\eta_{pol,turb}$ [%]	$\eta_{pol,compr}$ [%]	$\eta_{pol,pump}$ [%]	ΔP_{HX} [%]
a	32	7.5	90	89	83	1
b	15	5	90	89	83	1
c	32	7.5	90	89	83	1
d	32	7.5	90	89	83	1
e	32	7.5	90	89	83	1
f	32	5	90	89	83	1
g	32	5	90	89	83	1
h	32	5	90	89	83	1
i	32	7.5	90	89	83	1
j	20	3	90	89	83	1
k	29	0.1	90	89	83	1
l	-70	0.1	90	89	83	1

Table 3.2: Parameters used in the sensitivity analysis. Note that turbomachinery efficiency is polytropic.

The thermodynamic analysis presented in the following sections is simplified by assuming

that the inlet conditions to the compressor and pump remain constant whilst the pressure and temperature at turbine inlet change during the analysis. This assumption is based on numerous parametric studies about how compressor inlet conditions can impact thermal efficiency conclude that rising compressor inlet temperature and pressure (CIP and CIT) leads to a dramatic drop in cycle performance. Indeed, Figure 3.7, taken from the works by Turchi [103] and Dyreby [8], confirms that setting the inlet conditions of the compressor to as close as possible of the critical point of CO_2 is beneficial for cycle performance.

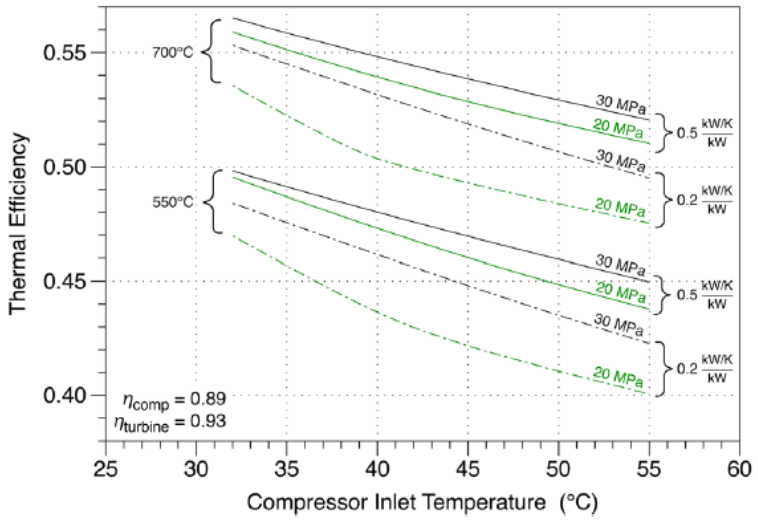

(a) Dependence of thermal efficiency upon compressor inlet temperature for the *Recompression* layout. Different turbine inlet temperature and pressure and recuperator conductance are considered. Taken from [8].

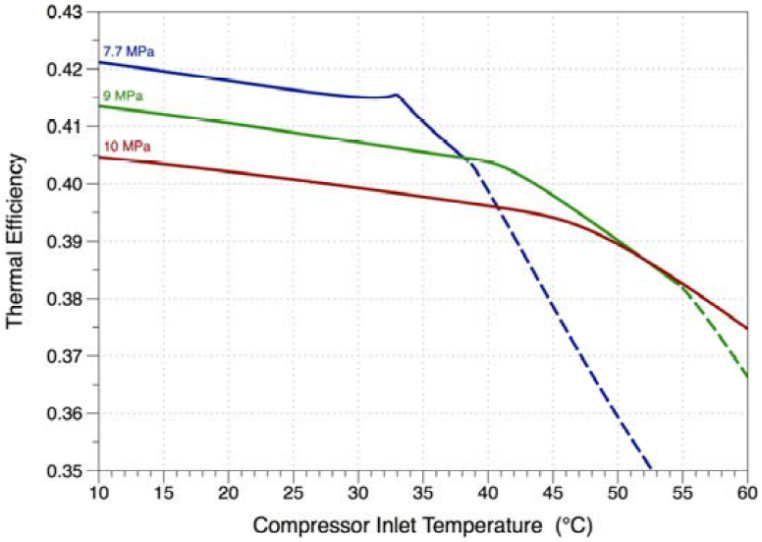

(b) Dependence of thermal efficiency upon compressor inlet temperature and pressure for the *Simple Recuperated* layout. Turbine inlet temperature is set to 550ºC. Taken from [103].

Figure 3.7: Dependence of thermal efficiency upon compressor inlet temperature and pressure for different cycle layouts.

Moreover, even if Figure 3.7(b) confirms that further reductions of compressor inlet temperature below the critical temperature might also bring about higher thermal efficiencies, this is usually limited by ambient temperature or by the components employed to implement the cycle. For instance, in order to obtain the left branch of the blue line for temperatures below the critical temperature, Bryant et al. change the layout from a *Simple Recuperated* to a *Transcritical CO2* one, thus enabling condensation. Of course, this change would not be feasible in practice due to the fact that it would request a pump/compressor system capable of working with a fluid characterized by a extremely wide range of compressibility factors. Still, the plot is useful to show the great potential of the *Transcritical CO2* cycle configuration when low temperatures can be achieved at the beginning of the compression process.

A final consideration in regards to compressor inlet temperature and pressure is the possibility to change the composition of the working fluids, as suggested by several authors [222, 223, 224]. This could potentially increase the pseudo-critical temperature of the mixture, with respect to the critical temperature of CO_2, thus enabling condensation cycles even with high ambient temperatures. This option is certainly promising and it is briefly discussed in the last chapter of this work.

Finally, pressure drops across heat exchangers are set to 1% on each side (recuperators, coolers and heaters) whereas piping pressure drops have been neglected. The effectiveness of heat exchanger takes the default value of 95% (90 % for the *Quasi-Combined* cycle) whenever the resulting pinch point is not lower than 5 ^{o}C; if this were the case, the corresponding effectiveness would be reduced to match this desired minimum pinch-point.

3.3 Results

3.3.1 Analysis of Individual Cycles

The performances of the aforedescribed cycles have been studied for four different turbine inlet temperatures -550, 750, 950 and 1150^{o}C- and variable pressure ratio. The lower boundary of the temperature range is taken after Angelino's statement that steam Rankine cycles are more efficient than their supercritical CO_2 counterpart for peak temperatures below 550^{o}C, whereas the upper boundary is set to a reasonable value that is well above what contemporary heat exchangers can achieve (note that these cycles are mostly intended for externally fired applications). Regarding pressure level, PR is varied from virtually no compression to its maximum thermodynamically consistent value (i.e., maximum pressure ratio that does not yield thermodynamically inconsistent results like, for instance, temperature crossing in heat exchangers), even if this turns out to be ridiculously high. The thermodynamic limits are therefore not fixed arbitrarily by the authors, but they are specific to each cycle configuration and come usually determined by the recuperation process. In most cases, the sensitivity analysis to PR is limited by the PR value for which heat transfer in the recuperators is feasible.

The curves plotted in Figures 3.8 to 3.19 result from the computation of thermal efficiency and specific work for each layout and set of operating conditions. As observed, the plots are made up of two segments with black (full) and white (empty) markers. Black markers correspond to cycles where peak pressure is not higher than 40 MPa whereas white markers indicate that the peak cycle pressure is above this value. This threshold value of maximum cycle pressure is higher than the values usually employed in literature, 25-30 MPa [101, 132], but it is still taken

as a representative technological limit for next generation power plants. This is based on the demonstrated operation of supercritical steam power stations at 35 MPa as early as 1960 [225] and on the foreseen increase in live steam pressures in the decades to come [226]. Therefore, the black markers stand for conditions that are currently feasible technology-wise whereas empty markers correspond to scenarios that are valid from a theoretical standpoint only.

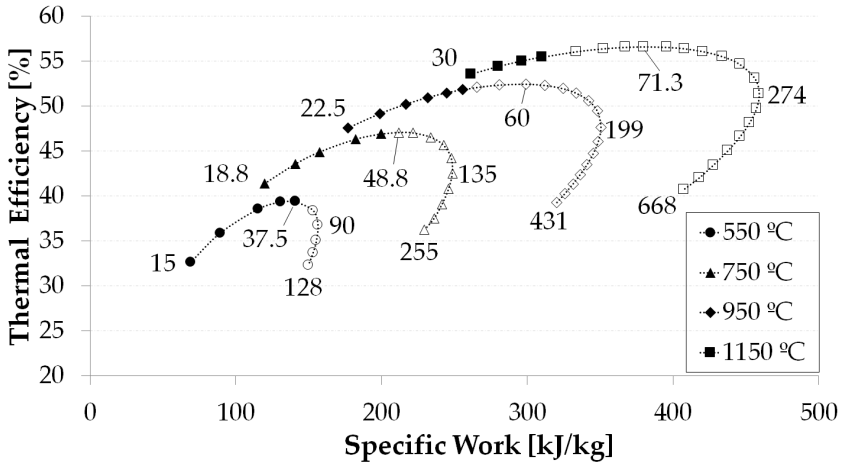

Figure 3.8: η_{th} vs W_s diagrams for the *Simple Recuperated* cycle.

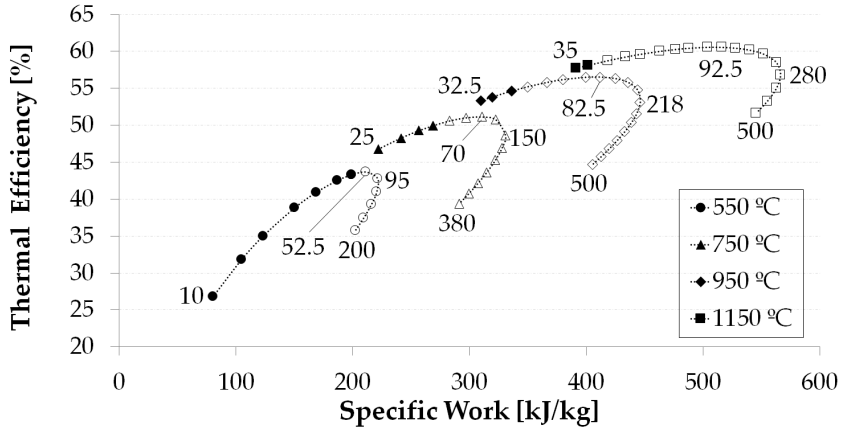

Figure 3.9: η_{th} vs W_s diagrams for the *Transcritical CO2* cycle.

Each plot in the diagram shows three or four labels indicating maximum cycle pressure for certain operating conditions. These values are reported for the first and last calculations (i.e., cycles with minimum and maximum peak pressure) and for the cases yielding highest thermal efficiency and specific work (even though this last value is not reported in cases where very high pressure ratios are not feasible). Quoting peak pressure has been preferred over pressure ratio as the latter value is not directly related to the mechanical capability of the system components (note that compressor inlet pressure might be different for different cycles and thus

there is no univocal correspondence between pressure ratio and peak cycle pressure). Also, it is worth noting that some curves present a relatively high first value, for instance 34.5 MPa for the *Recompression+IC+RH* layout in Figure 3.12) or 40.5 MPa the for *Partial Cooling* cycle in Figure 3.13. Even if this is partially due to the inherently higher compressor inlet pressures, the main reason is that the curves have been trimmed to avoid intersections between different lines.

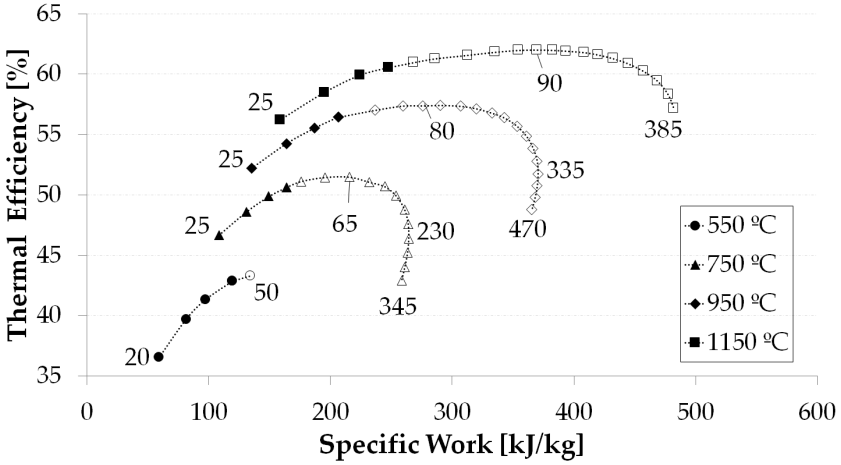

Figure 3.10: η_{th} vs. W_s diagrams for the *Precompression* cycle.

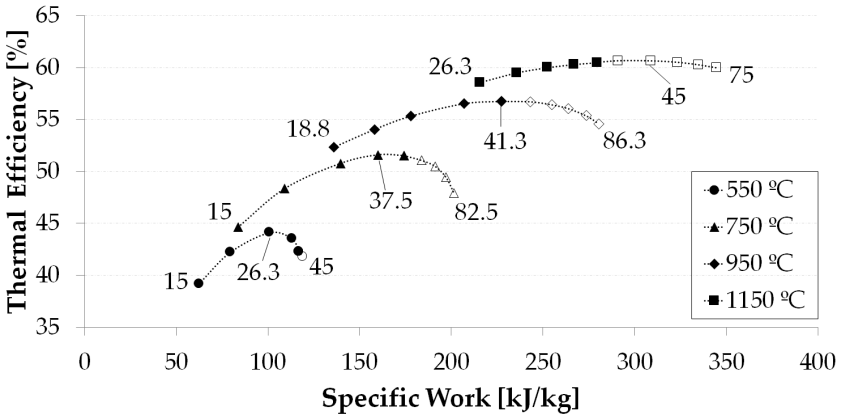

Figure 3.11: η_{th} vs. W_s diagrams for the *Recompression* cycle.

Interestingly, the shape of the η_{th} vs. W_s curves changes significantly depending on the configuration considered and the same happens to the maximum pressure of the. Yet, it is possible to observe several affinities between cycles characterized by similar layouts or thermodynamic features. For instance, the *Recompression+IC+RH* and *Double Reheated Recompression* layouts stem from the common root of the *Recompression* cycle, and this can easily be observed in the similar patterns presented in Figures 3.11, 3.12 and 3.16. The same consideration is applicable to the *Partial Cooling* and *Partial Cooling+RH* layouts, which

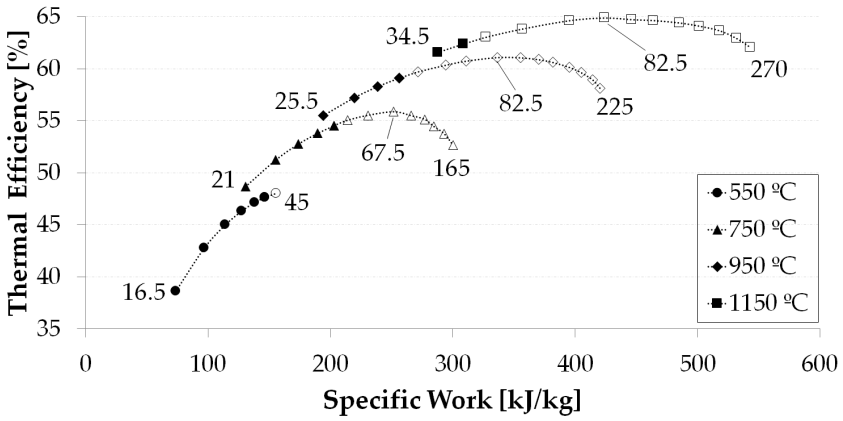

Figure 3.12: η_{th} vs. W_s diagrams for the *Recompression+RH+IC* cycle.

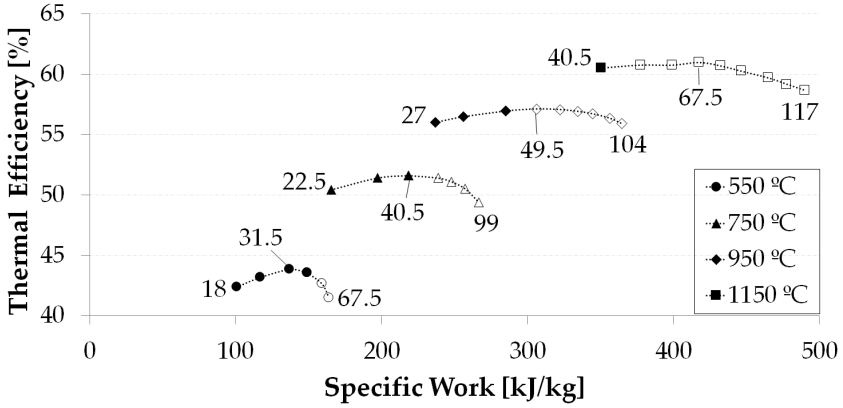

Figure 3.13: η_{th} vs. W_s diagrams for the *Partial Cooling* cycle.

are characterized by the same plateau-type trend, especially at high temperatures, or the oxy-fired *Matiant* and *Quasi-Combined* cycles, whose corresponding plots seem to fold back on themselves sharplier. Interestingly, most of these trends are in line with those already discussed by Frutschi in [98] for closed cycle hot-air turbines, demonstrating the common thermodynamic principles of both closed cycles.

Finally, some common features shared by all the cycles in the comparison are worth noting. For instance, the plots corresponding to lower turbine inlet temperatures seem to have a more circular shape and they turn elliptical and flatter when temperature increases. Regarding the technological limits, it is confirmed that most cycles reach their peak thermal efficiency and specific work at pressures higher than 40 MPa when turbine inlet temperature is higher than 550ºC. On the contrary, when this temperature is lower than 550ºC, some cycles achieve peak efficiency within the *feasible* pressure range whilst others do not; this is shown in Figures 3.8,3.10,3.11,3.13,3.15,3.16,3.19. Remarkably, the *Quasi-Combined* cycle is the only configuration presenting diagrams almost fully situated within the technological limitations (black markers), mainly due the relatively low pump inlet pressure, Figure 3.19.

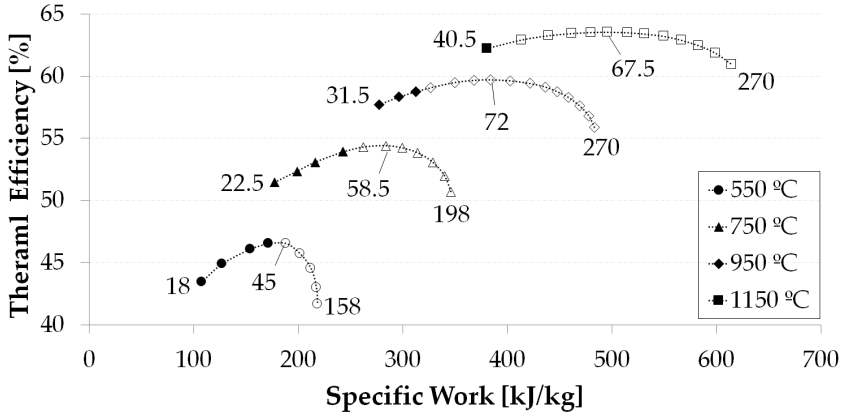

Figure 3.14: η_{th} vs. W_s diagrams for the *Partial Cooling + RH* cycle.

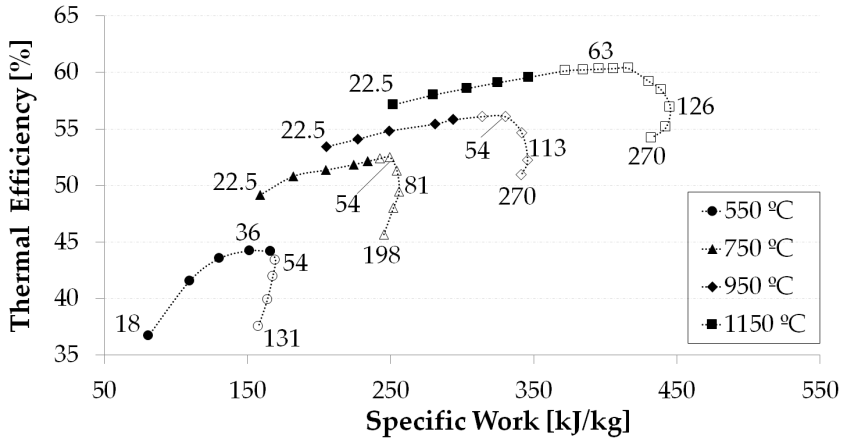

Figure 3.15: η_{th} vs. W_s diagrams for the *Schroder-Turner* cycle.

3.3.2 Compared Analysis

A global assessment of the individual plots shown in the foregoing section suggests that some of the cycles still hold a non-negligible potential for further efficiency increase (should higher pressures be attainable) whereas others seem to have already achieved the best performance possible for a given turbine inlet temperature (no further gains for higher pressures), all this for the current limits of technology. For instance, the *Transcritical* CO_2 cycle operating at 750ºC turbine inlet temperature would be able to attain efficiencies higher than 50% with a very high specific work, hence fuel and footprint savings simultaneously; such performance would set the thermodynamic road-map for further cycle development, notwithstanding the very high pressures that would be required (~75 MPa). At the same time, cycles acknowledged to be most efficient, like the *Recompression* layout, seem to have already achieved the highest efficiency for the current turbine inlet temperatures, thus holding no further gains coming from higher operating pressures.

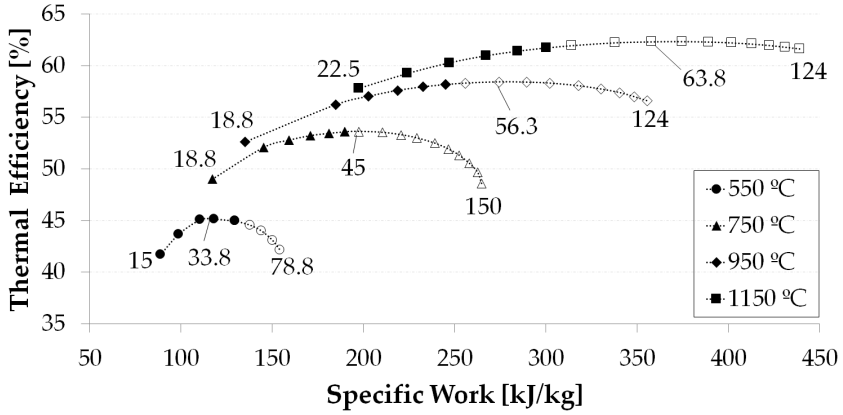

Figure 3.16: η_{th} vs. W_s diagrams for the *Double Reheated Recompression* cycle.

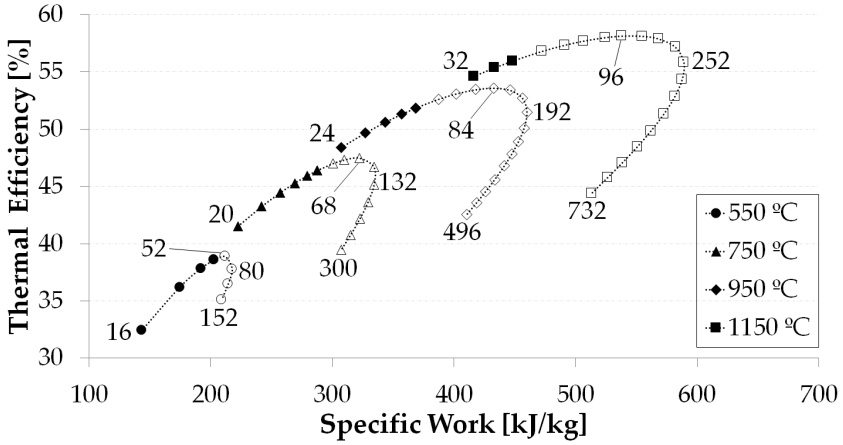

Figure 3.17: η_{th} vs. W_s diagrams for the *Allam* cycle.

Another interesting, not obvious question to answer is which the most efficient or most compact cycle is for a given turbine inlet temperature (energy source). In order to provide a sensible answer to this question, this section presents a comparison amongst the various layouts discussed earlier which are overlaid on one single chart for each temperature level. This is shown in Figures 3.20 to 3.21 where some plots have been trimmed to simplify the reading. The increasing ranges of the horizontal and vertical scales for increasing inlet temperature must be noted.

Let the chart corresponding to 550ºC be considered, Figure 3.20. Those cycles conceived for oxy-fired applications (if stable oxy-combustion at such temperature is possible at all) like the *Allam* and, especially, *Matiant* cycles are not of much interest as they exhibit fairly low thermal efficiency in spite of a very high specific work (small footprint). For this peak temperature, the highest specific work corresponds to the *Allam* cycle if mechanical limits are set on the operating pressure, and the *Transcritical* CO_2 if higher pressures are allowed.

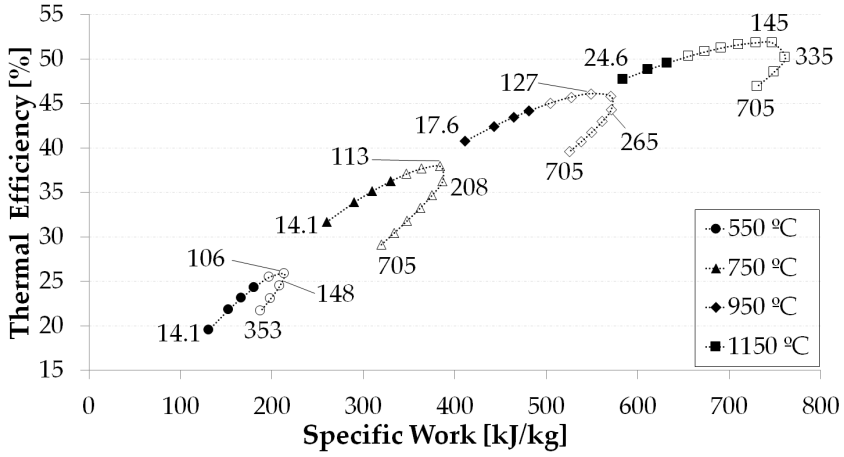

Figure 3.18: η_{th} vs. W_s diagrams for the *Matiant* cycle.

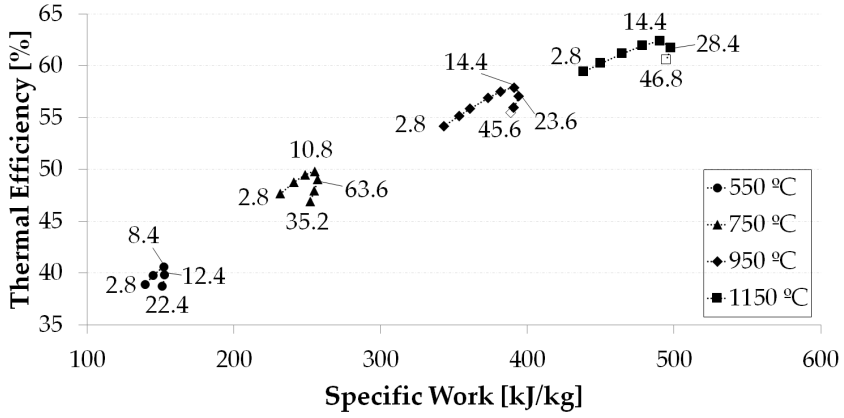

Figure 3.19: η_{th} vs. W_s diagrams for the *Quasi-Combined* cycle.

With respect to efficiency, the *Partial Cooling + RH* and *Recompression+IC+RH* layouts attain highest efficiencies (46.5 and 47.6% respectively) when pressure is limited to 40 MPa whereas efficiency rises to a higher value (48%) for the *Recompression+IC+RH* cycle if this limit is released. Moreover, from a global standpoint, the *Partial Cooling+RH* and *Transcritical* CO_2 cycles provide a good compromise between thermal efficiency and specific work. In summary, Figure 3.20 confirms that the most interesting cycles are the *Recompression*, *Double Reheated Recompression*, *Recompression+IC+RH*, *Partial Cooling+RH*, *Transcritical* CO_2 and, in terms of specific work only, *Allam* cycles.

Increasing turbine inlet temperature brings about changes in the absolute thermal efficiency and specific work achieved by each cycle and also in their relative position in the η_{th} vs. W_s diagram. This is easily observed by comparing the two graphs in Figure 3.20. In the plot on the right, corresponding to 750 ºC, the *Matiant* cycle exhibits highest specific work but this feature is offset by a very low thermal efficiency. The *Allam* cycle follows behind with a slightly lower specific work but higher thermal efficiency. Nevertheless, both oxy-fired cycles are still

burdened by a low turbine inlet temperature and cannot compete against most of the cycles in the comparison. Considering thermal efficiency only, the scenario remains the same as for 550ºC. The *Recompression+IC+RH* cycle achieves highest η_{th}, 54.5 or 55.8% depending on whether or not pressure limits are in place. The *Double Reheated Recompression* and *Partial Cooling + RH* layouts follow close behind, enabling efficiencies of almost 54%. Overall, the cycles indicated in the previous paragraph remain the most interesting options.

A turbine inlet temperature of 550 ºC would be typical of a WHR application, or even a state-of-the-art CSP plant using molten salts, whereas 750 ºC would represent nuclear applications in Gen IV High Temperature Gas Reactors. 950 ºC is a very interesting temperature level as this is currently foreseen for next generation CSP applications using central receiver technology. The resulting performances at this temperature are shown in Figure 3.21 where the corresponding plots for each cycle are observed to concentrate on a smaller region of the η_{th} vs. W_s diagram. Regarding oxy-fired cycles, the *Matiant* cycle shifts rightwards to attain very high specific work even if still with the lowest efficiency amongst the cycles considered. When pressure is limited to 40 MPa, the *Partial cooling+RH* layout stems as the most efficient although with moderate specific work, being later matched in efficiency by the *Recompression+IC+RH* cycle when no pressure limit exists; it is noteworthy that the latter cycles can achieve almost 60% efficiency at 950ºC only. Globally, the cycles of interest at this temperature are the *Recompression*, *Double Reheated Recompression*, *Recompression+IC+RH*, *Partial Cooling+RH*, *Transcritical* CO_2, *Quasi-Combined* and, again only in terms of specific work, *Allam* cycles.

The last chart is shown in Figure 3.21 and corresponds to 1150 ºC turbine inlet temperature. It shows similar patterns to Figure 3.21 but with higher efficiency and specific work, in particular the latter. The are two main takeaways in this chart. The first is that whilst the achievable efficiency for the given pressure limit of 40 MPa is just over 62%, some of the cycles have the potential to raise this value to almost 65%, which is remarkable for a somewhat moderate inlet temperature. The second is related to the *Quasi-Combined* cycle which shifts "north-east" from its initial position in Figure 3.20 to a relative position in Figure 3.21 where it begins to outperform all the other configurations. This modifies the overall scenario, as a result of which the most interesting cycles turn out to be the *Precompression*, *Recompression+IC+RH*, *Partial Cooling+RH*, *Transcritical* CO_2, *Allam* and *Quasi-Combined* layouts. Actually, the latter yields the best combination of thermal efficiency (63%) and specific work (~475 kJ/kg), amongst the portfolio of cycles in this work. This is a very interesting finding as one could have overlooked the true potential of this layout if having the information in Figure 3.20 only, which comes to highlight the interest of the parametric analysis shown in this chapter.

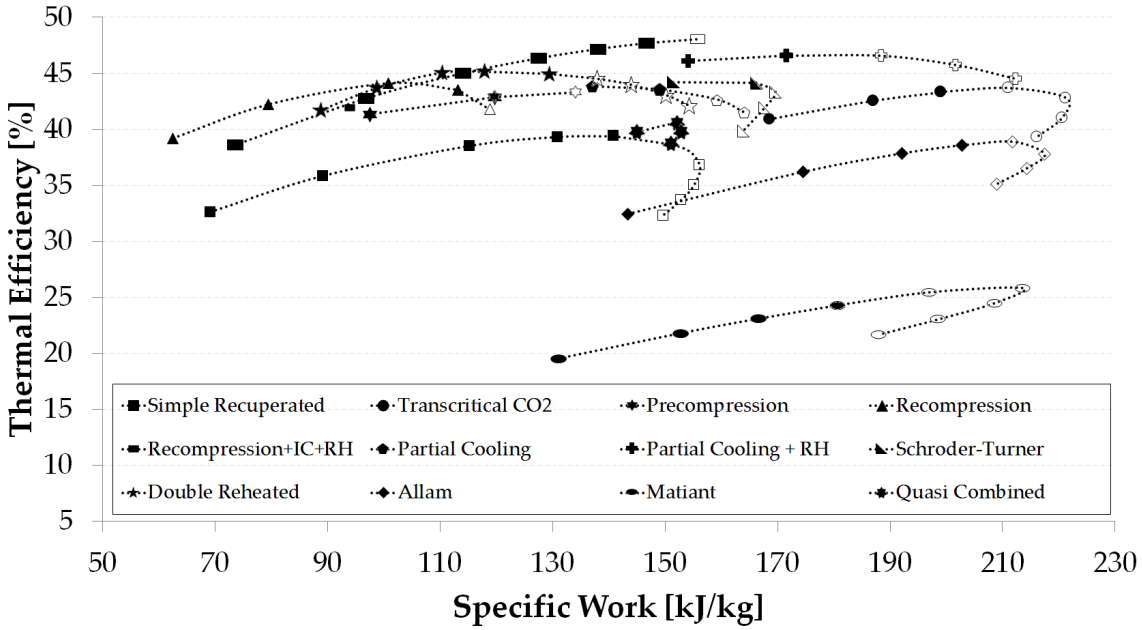

(a) Comparison of cycles operating at TIT=550ºC.

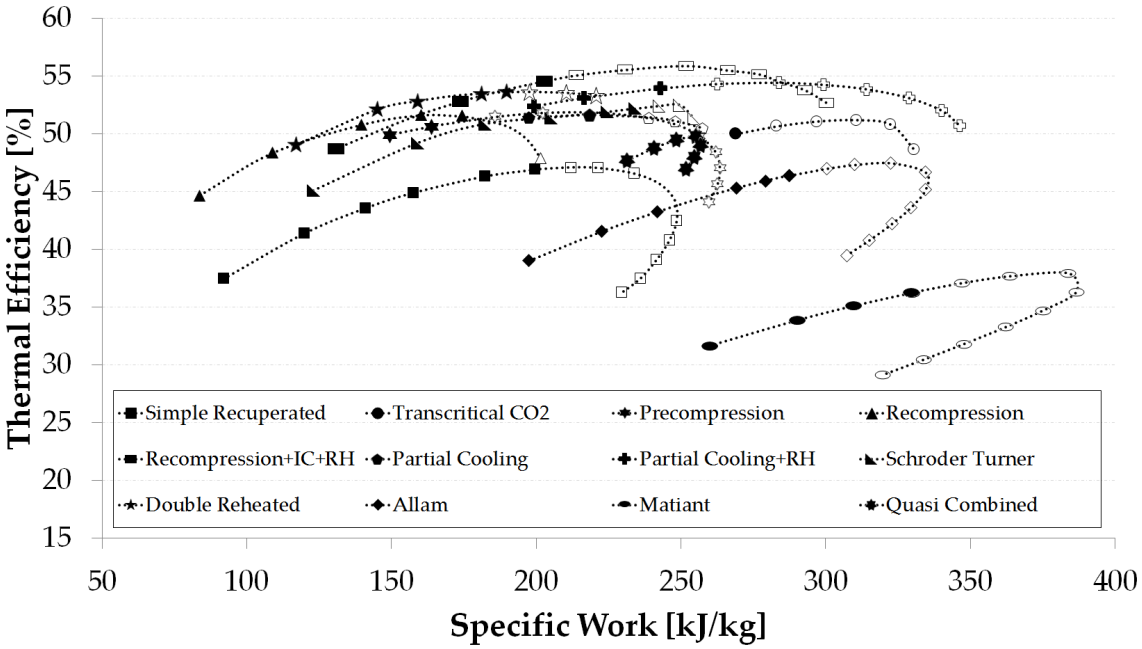

(b) Comparison of cycles operating at TIT=750ºC.

Figure 3.20: Comparison of cycles operating at TIT=550 ºC and TIT=750ºC.

3.3.3 Further Mechanical Limitations

An interesting analysis from a practical standpoint is to consider another mechanical constraint with regards to the hot inlet temperature of the high temperature recuperator. To assess this effect, the operating temperature of this equipment is limited to 800ºC which is higher than for state-of-the-art equipment made of stainless steel (675ºC) but still compatible with

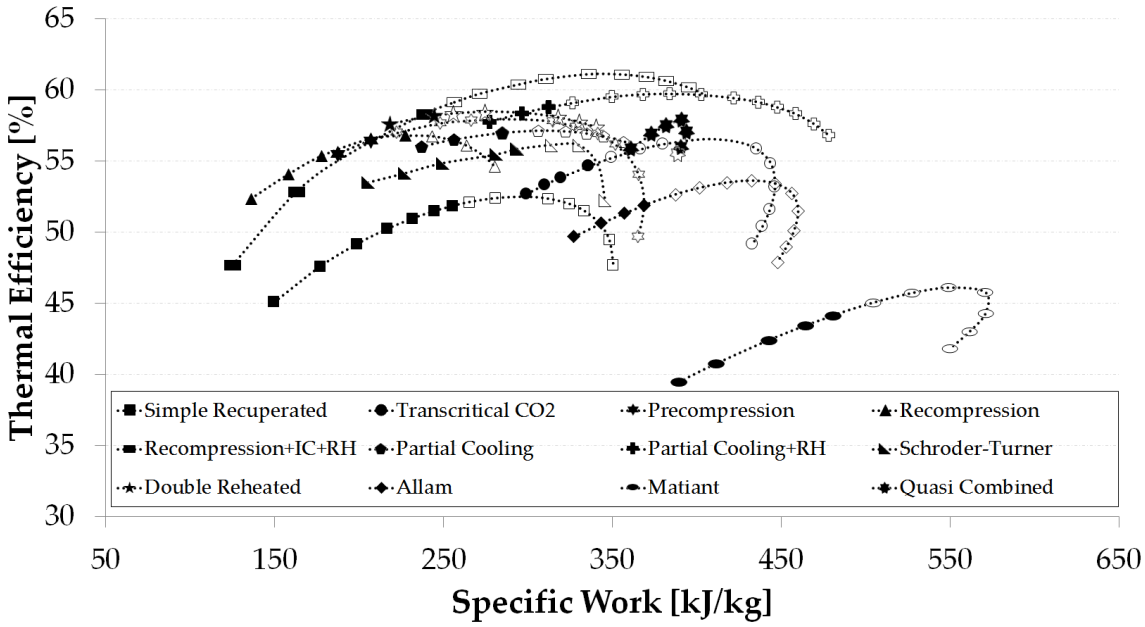

(a) Comparison of cycles operating at TIT=950°C.

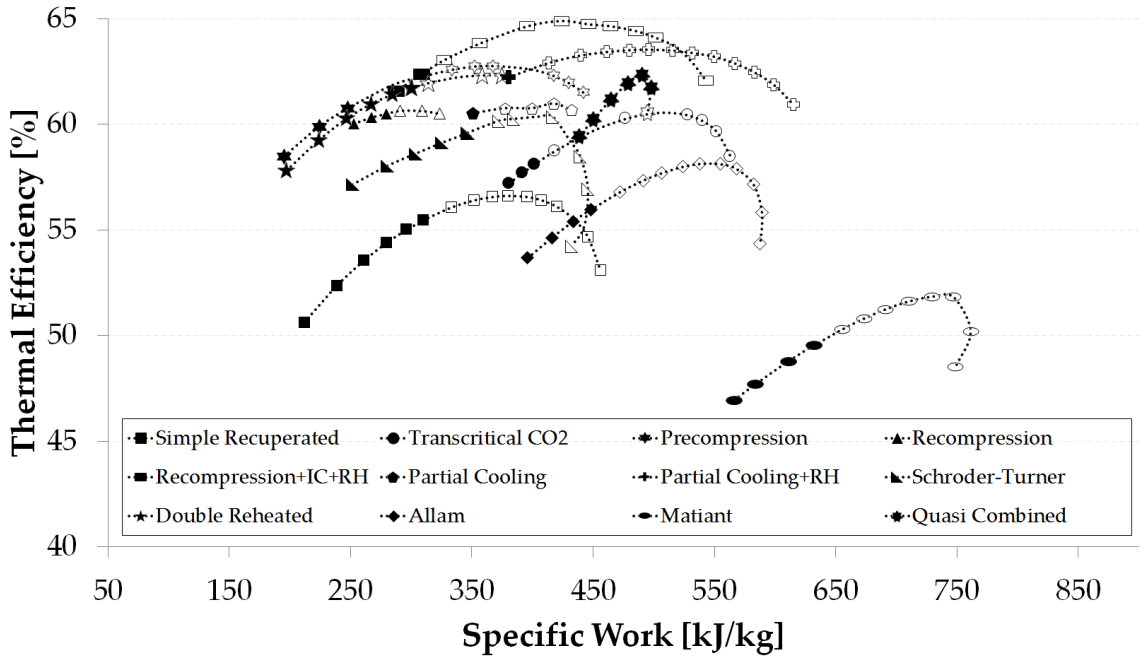

(b) Comparison of cycles operating at TIT=1150°C.

Figure 3.21: Comparison of cycles operating at TIT=950°C and TIT=1150°C.

more advanced materials such as Inconel 625 [227].

When this restriction is applied to a turbine inlet temperature of 950°C, Figure 3.21(a) transforms into Figure 3.22 where some of the formerly feasible pressure ratios are not feasible anymore. For instance, the *Recompression+IC+RH* and *Double Reheated Recompression* cycles

cannot satisfy the new requirement for any pressure ratio, due to the reduced expansion ratio of the last turbine, caused by the reheating process; therefore, the corresponding curves are removed from the chart. Also, the *Partial Cooling+RH* layout complies with the new constraint for pressures higher than 40.5 MPa only, which means that they are at the very end of what is considered technically feasible today (and most likely economically unfeasible). Considering 1150ºC, Figure 3.23 represents the new scenario and the dramatic difference is immediately observed by comparing the latter chart with Figure 3.21(b). At this high turbine inlet temperature, only three cycles comply with the new mechanical constraint: *Quasi-Combined*, *Transcritical* CO_2 and *Allam*.

These observations confirm the conclusion obtained in the previous section; i.e., that the *Quasi-Combined* and *Partial Cooling+RH* cycles are the most interesting cycles at intermediate to high turbine inlet temperature levels. The interest and versatility of the approach presented in this chapter is also highlighted further.

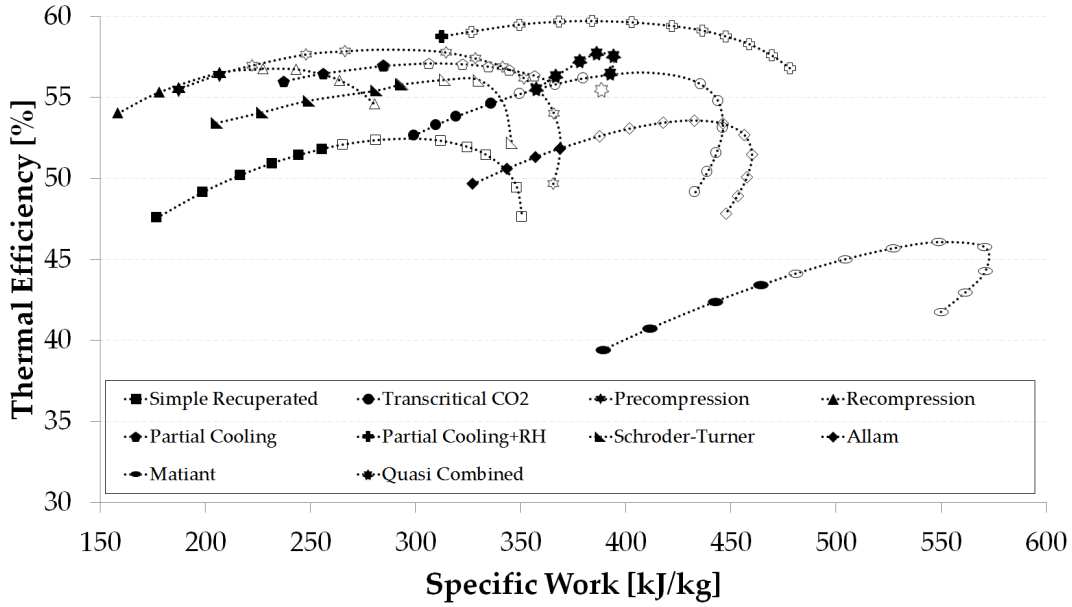

Figure 3.22: Comparison of cycles operating at TIT=950 ºC. Operating conditions yielding recuperators with hot inlet temperatures higher than 800ºC have been removed.

3.3.4 Second Law Analysis

Table 3.2 showed earlier that the boundary conditions applied to each cycle were not completely homogeneous. Such differences come from the need to model dissimilar cycles and become particularly evident for the compressor/pump inlet conditions in the *Transcritical* CO_2 and the *Quasi-Combined* layouts. Although this is inevitable to model the particular features of these cycles properly (condensation and cryogenic cooling respectively), it can also be misleading when the comparison relies on the First Law of Thermodynamics only, as in Figures 3.20 to 3.23.

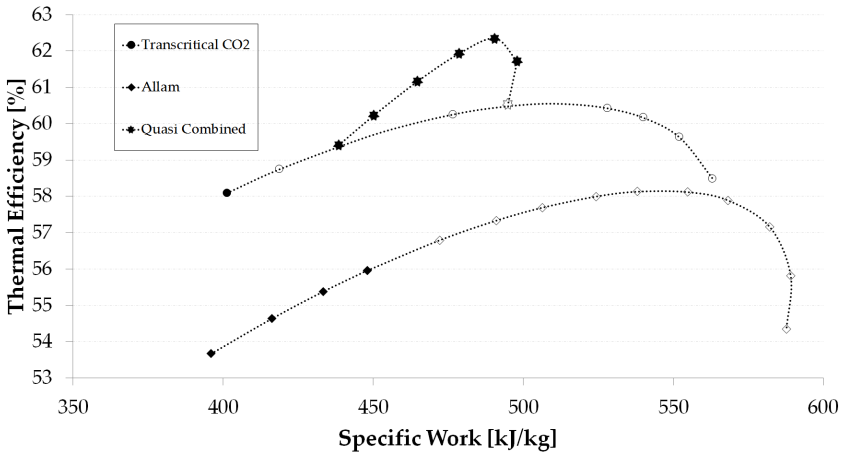

Figure 3.23: Comparison of cycles operating at TIT=1150 ºC. Operating conditions yielding recuperators with hot inlet temperatures higher than 800ºC have been removed.

Such limitation is easily overcome if the Second Law is also used, as it is the case in this section where the Carnot Factor (*CF*) is used as a metric of cycle performance. This factor is the ratio from the thermal efficiency of the cycle (η_{th}) to the thermal efficiency of the Carnot cycle operated between the same extreme temperatures (η_C), Eq. (3.1).

$$\eta_C = 1 - \frac{T_L}{T_H} \quad , \quad CF = \frac{\eta_{th}}{\eta_C} \tag{3.1}$$

Based on this figure of merit representing Second Law performance, a new plot of *efficiency* vs. specific work is presented in Figures 3.24 and 3.25. These new charts account for the dissimilar cold cycle temperatures, and they introduce significant changes in the results with respect to the previous analysis. It is immediately observed, in fact, that the *Quasi-Combined* layout, which stood out as one of the most promising cycles in Figure 3.22 and the best in Figure 3.23, is no longer interesting in Figure 3.25(a) and does not seem the most promising in Figure 3.25(b) either. Actually, the apparently very high thermal efficiency was due to an extremely low temperature at compressor inlet and not to a layout with unmatched thermodynamic potential. On the contrary, the *Partial Cooling + RH* configuration exhibits better performance than any other cycle in the comparison, which confirms the results based on First Law presented in earlier sections. In this case, the cycle has some inherent advantages over the alternative layouts whereas no significant changes are produced in the 550ºC and 750ºC scenarios.

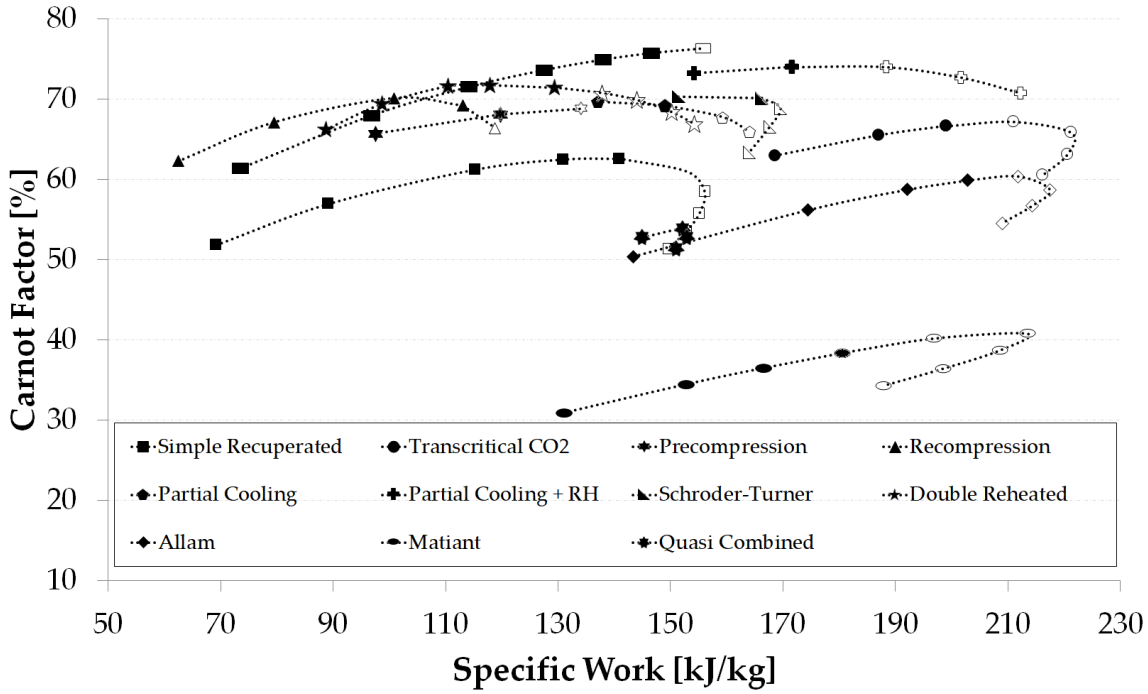

(a) Carnot Factor comparison of cycles operating at TIT=550ºC.

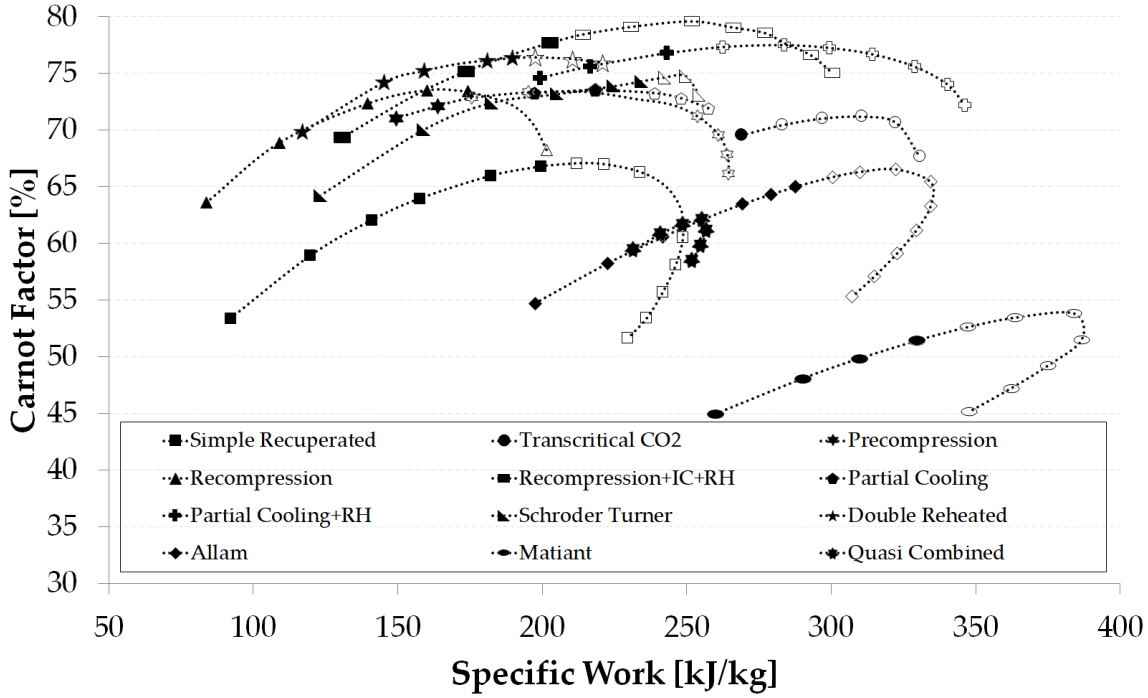

(b) Carnot Factor comparison of cycles operating at TIT=750ºC.

Figure 3.24: Carnot Factor comparison of cycles operating at TIT=550ºC and TIT=750ºC.

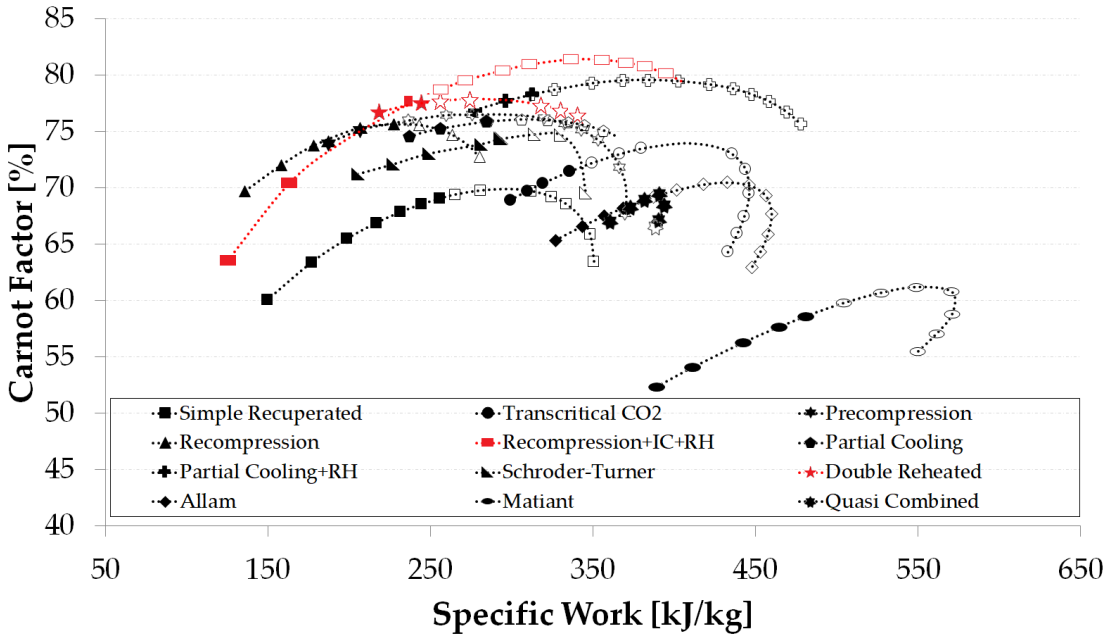

(a) Carnot Factor comparison of cycles operating at TIT=950ºC.

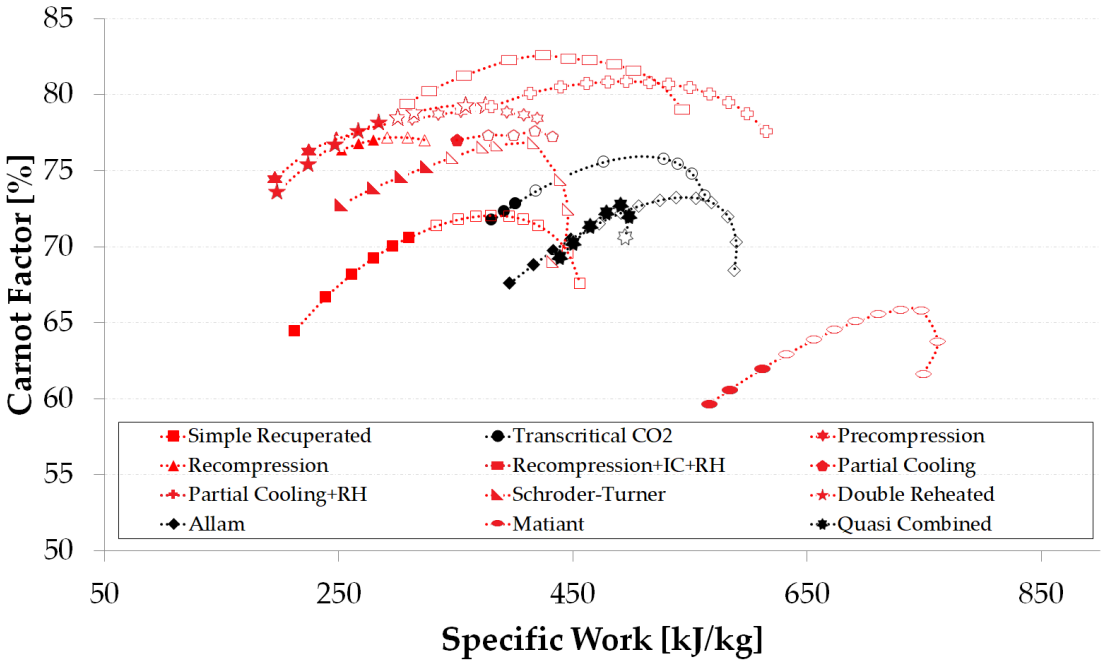

(b) Carnot Factor comparison of cycles operating at TIT=1150ºC.

Figure 3.25: Carnot Factor comparison of cycles operating at TIT=950ºC and TIT=1150ºC. Operating conditions yielding recuperators with hot inlet temperatures higher than 800ºC have been highlighted in red.

3.4 Conclusions

Some interesting conclusions can be drawn from the individual and compared analyses of the twelve sCO_2 cycles considered in this chapter. As a general observation, pressure ratio seems to have a weaker influence on thermal efficiency at lower turbine inlet temperatures, as deduced from the lower slope (flatter curves) of the η_{th} vs. W_s lines in Figure 3.20(a) in comparison with the same plots in Figure 3.21(b). Accordingly, increasing the pressure ratio in the latter set of plots brings about similar enhancements of thermal efficiency and specific work. This was to be expected from the recuperative layout of the cycles and is here confirmed and quantified.

Another important conclusion is that a number of cycles are of no interest at all, regardless of whether or not pressure limits are taken into account. These cycles would easily be identified if an envelope curve were plot by linking the rightmost black markers achieving highest efficiency and specific work. Those cycles falling to the left of this "border" would have no added value and should be disregarded for future analysis (except if there were noteworthy economic reasons that would compensate for a higher heat rate). On the contrary, those intersecting the envelope curve should be kept for further analysis. This is illustrated in Figure 3.26 where the grey area stands for the remaining potential to achieve higher efficiency and specific work, should higher operating pressures be enabled in the future.

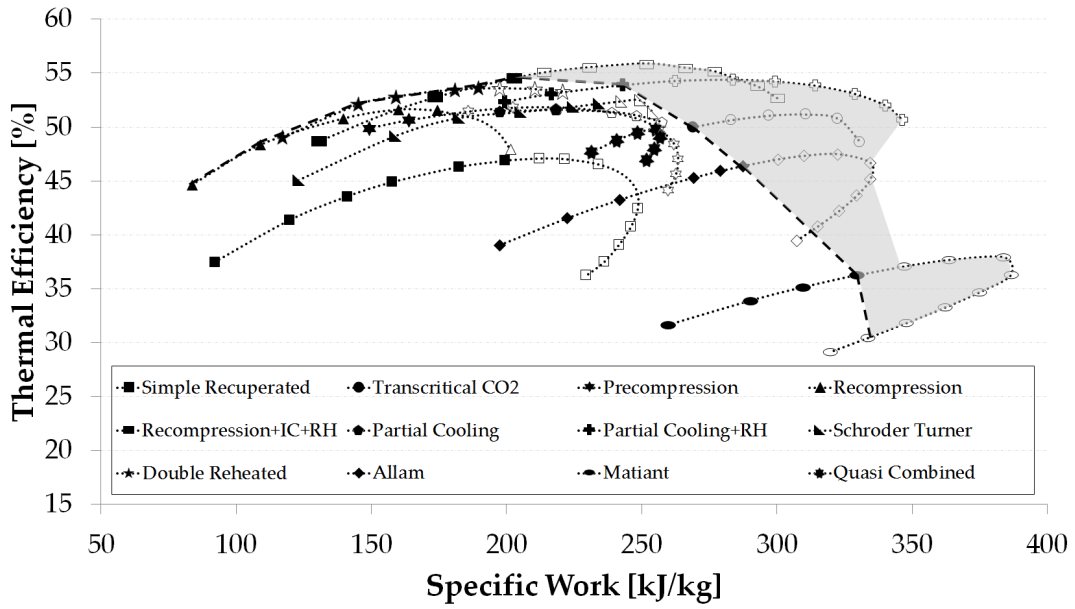

Figure 3.26: Comparison of cycles operating at TIT=750ºC, showing envelope curve for 40 MPa and margin for future performance enhancement.

The conclusions above are general but must be taken with care given that the relative positions of the cycles in Figures 3.20 and 3.21 change when turbine inlet pressure changes. Thus, according to the aforedescribed rationale, the *Quasi-Combined* cycle should have been discarded from an analysis at 550ºC. Nevertheless, as turbine inlet temperature increases, the

corresponding plot shifts northeast and, by the time this temperature reaches 950ºC, the cycle yields the most leveraged performance (i.e., combination of η_{th} and W_s).

Based on this remark, reporting the most interesting cycle must be accompanied by an indication of the operating and boundary conditions considered, including whether or not technological limits exist. Only with such a complete description, one can state that the *Quasi-Combined* and *Partial Cooling* + *RH* cycles are the most interesting for applications with turbine inlet temperatures in the range from 900 to 1200ºC, and peak cycle pressure and hot inlet temperature to the recuperator limited to 40 MPa and 800ºC respectively. Moreover, if cryogenic cooling is not available or if the minimum cycle temperature is limited to a minimum value regardless of the cycle layout, then the *Partial Cooling* + *RH* cycle must be acknowledged as the best choice based on the Carnot Factor analysis. Below 800ºC, the *Recompression* + *IC* + *RH* layout yields the best performance and complies with the maximum cycle pressure being lower than 40 MPa. These last two configurations are as well the best options for 550ºC and 750ºC, from the point of view of both the First and Second Laws of Thermodynamics, Figures 3.20 and 3.24).

Finally, when there are no restrictions to pressure and temperature, the analysis shows that the *Recompression* + *IC* + *RH* cycle yields highest thermal efficiency irrespective of turbine inlet temperature: 48% at 550ºC, 59% at 750ºC, 61% at 950ºC and 65% at 1150ºC.

4 Economic Analysis

*This chapter focuses on **estimating the capital cost of the system**, including all the major equipment such as the power block, the solar subsystem (field, tower and receiver) and the thermal energy storage. A **brief review of the current cost engineering techniques** is presented first, describing the existing methodologies (if available) in order to select the most suitable one for the objectives of this thesis, along with a description of the major equipment and the assumptions needed to model them. A summary of the **thermal design model of PCHEs** is also presented in this chapter, with a full description in the corresponding appendix. In the second part of the chapter, the costs of each equipment are estimated and **an uncertainty analysis is developed, based on the Montecarlo method**. Finally, the results of this cost estimation are provided, both in general terms and through a breakdown of specific costs.*

Parts of this chapter have been published in:

F. Crespi, D. Sánchez, J.M. Rodríguez, G. Gavagnin, 2017, *Fundamental Thermo-Economic Approach to Selecting sCO_2 Power Cycles for CSP Applications*, Energy Procedia 129, pp. 963-970.

F. Crespi, D. Sánchez, T. Sánchez, G.S. Martínez, 2019, *Capital Cost Assessment of Concentrated Solar Power Plants Based on Supercritical Carbon Dioxide Power Cycles*, Journal of Engineering for Gas Turbines and Power 141, 071011.

4.1 Introduction

The previous chapter presented a comparison between twelve different cycle configurations based on their thermodynamic features only. These power cycles were considered individually in order to discover their thermodynamic potential, without considering any specific applications *a priori*. Nevertheless, results were provided for four different turbine inlet temperatures which are representative of certain applications, as shown in Figure 2.33. Hence, 550ºC would be representative of Nuclear Power plants and standard steam turbine CSP plant, 750ºC would represent the next generation of CSP plants if new molten salts were developed adopted [116], 950ºC could be achieved in CSP using solid particles receivers in lieu of molten salts [31] and, finally, 1150ºC could refer to oxy-combustion power cycles.

In this chapter, the thermodynamic approach used in Chapter 3 is complemented with economic performance tools following the path set forth by other authors recently [116, 108, 228,

229], with the ultimate objective to estimate the Overnight Capital Costs (*OCC*) of the resulting sCO_2-based CSP plants employing the different cycle layouts presented in the foregoing chapter. Ten layouts are selected amongst the twelve cycles considered originally, with the boundary conditions and specifications presented in Table 4.1. In this selection, both the *Matiant* and *Quasi combined* cycles have been discarded, the former due to its poor thermal performance at 750°C (see Figure 3.20(b)) and the latter due to its low Second Law efficiency brought about by cryogenic cooling (see Figure 3.24(b)). Additionally, these two configurations present further complexity due to the presence of three-flow heat exchangers and cryogenic cooling system, whose higher costs are not compensated for by a high thermal performance.

Power Output [MW_{el}]	P_{max,sCO_2} [MPa]	TIT [°C]	$T_{s,min}$ [°C]	$T_{s,max}$ [°C]	$TES_{capacity}$ [hour]	SM [-]
50	30	750	480	770	10	2.4

Table 4.1: Specifications of the reference power plant.

4.2 Cost Estimation techniques and models

Estimating the cost of a Concentrated Solar Power plant can become an extremely complex task, depending on the level of detail required [230]. The difficulty lies on the lack of reliable data since these are mostly proprietary of the EPC companies acting in the CSP industry, especially when an emergent technology like sCO_2 in this work is involved. The only publication that is worth mentioning is the work developed by Weiland et al. [74], providing cost estimation correlations for all the major components of a sCO_2 power cycle, employing vendor component costs collected by U.S. DOE and presented in ASME Turbo Expo 2019, only a few weeks before the present manuscript was deposited.

In this section, cost estimation models developed for the entire power plant are reported and discussed. At this stage, the various equipment are considered are modeled individually since the chapter is meant only to assess the installation costs of the plant, for which transient and partial load conditions of the power plant (i.e., system integration) are not necessary.

4.2.1 Solar Subsystem

With the expression *Solar Subsystem*, the author refers to all the equipment, not included in the power block, that collect and concentrate solar radiation, transforming it into the final heat power input for the power block itself. Therefore, the *Solar Subsystem* is constituted by the field of heliostats, solar tower and receiver and thermal energy storage system. The intermediate heat exchanger that links the solar heat transfer fluid with the sCO_2 working fluid is not hereby considered but it is, instead, included in the *Power Block* section.

Before analyzing each one of these equipment though, the following assumption concerning the entire solar subsystem must be discussed. The high temperatures considered in this work are unattainable by the molten salts used in contemporary CSP plants, whose degradation temperature is in the order of 600°C [231]. Therefore, salts with a different composition and capable of enabling the turbine inlet temperature demanded by the present study needs to be taken into account. Amongst the different candidates, FLiNaK seems to be the most interesting

one, thanks to its good thermo-physical properties and its wide range of operability in terms of maximum and minim temperature allowed [232]. This fluid has been studied several times in literature, in particular for thermal and mechanical design of Printed Circuit Heat Exchanger [13, 73] and as coolant for nuclear reactor applications [233].

FLiNaK is a ternary eutectic alkaline metal fluoride salt mixture of Lithium, Sodium and Potassium (46.5% LiF, 11.5% NaF and 42% KF). It has a melting point of 454ºC and a boiling point of 1570ºC, yielding an operating temperature range that is compatible with the sCO_2 power blocks considered. A comparison between FLiNaK and the standard solar salt, along with their thermodynamic properties, is provided in Table 4.2 where a constant temperature difference of 20ºC between the hot (salt) and cold (carbon dioxide) fluids is adopted to model the heat transfer rate between FLiNaK and sCO_2 (note that CO_2 behaves close to ideally in this temperature and pressure region far from the critical point). This assumption considers that the heat transfer process between FLiNaK and sCO_2 is not far from ideal (constant, low temperature difference between hot and cold fluid) and yields a standard approach linking the temperature change of molten salts to the temperature change of sCO_2 without loss of generality. Accordingly, the fact that the ΔT experienced by both fluids are linked, implies that the inventory (or mass flow rate) of molten salts needed in the solar subsystem is a function of the inlet temperature of carbon dioxide to the heat addition process, which depends itself on cycle layout, turbine inlet temperature and pressure ratio.

Salt	Composition	Freezing Point [ºC]	Boiling Point [ºC]	Density [kg/m^3]	Specific heat J/kgK]	Price [$/kg]
Solar Salt	$NaNO_3$-KNO_3	220 [231]	600 [231]	$-0.636 \cdot T + 2090$ [75]	$0.172 \cdot T + 1443$ [75]	1.1 [234]
FLiNaK	LiF-NaF-KF	454 [235]	1570 [235]	$2408.9 - 0.624 \cdot T$ [13]	$1267.2 + 1.0634 \cdot T$ [13]	8.6

Table 4.2: Comparison between a standard molten salt and FLiNaK. Price of FLiNaK calculated from data available in [13].

Solar Power Towers are fully-developed commercially nowadays [19], as shown by the significant number of operating commercial-scale plants [230], and as such several software have added the capability to provide a design for all the major equipment of the plant, along with their cost estimations. Amongst these tools, the author decided to use SAM, an open-source software developed by NREL and used frequently by various works in literature, for instance Ho et al [236, 237] and Schmitt et al. [76]. This software provides a wide range of different CSP plant design and of their corresponding financial models, with default commercial values that can easily be customized. Moreover, a significant set of interesting locations worldwide is available, for which the solar subsystem equipment can automatically be optimized according to geographical coordinates.

Using these features, a conventional 50 MW Solar Power Tower with Thermal Energy storage based on molten salts is modeled, considering the reference location in Seville and employing the specifications provided in Table 4.1 [1]. The resulting costs of the solar subsystem are stored in a database to be used later in the power plants based on sCO_2 technology. This latter information is used in later sections.

[1] With the exception of minimum and maximum temperatures of the salts, which must be 290 and 574ºC given that standard solar salts are employed.

Of course, the change in composition of the heat transfer fluid affects the final cost of the solar subsystem in several ways. First of all, FLiNaK is significantly more expensive than the standard solar salts. Secondly, the higher temperature rise of molten salts enabled by FLiNak poses larger challenges to the design of the solar receiver and thermal energy storage. This is all discussed in the next section.

Solar Field

The cost of the solar field (C_{SF}) is very sensitive to the efficiency of the power block as this figure drastically affects the heat input required for the given power output. This is shown in Figure 4.1 where the inverse, non-linear dependence of C_{SF} upon η_{th} is observed. These results are obtained with SAM, considering a surrounding field composed by square heliostats with a unit surface of 144.4m^2. The total amount of mirrors, and therefore the total reflecting surface, obviously changes inversely to the thermal efficiency, and it is obtained by an automatic optimization process carried out by the software.

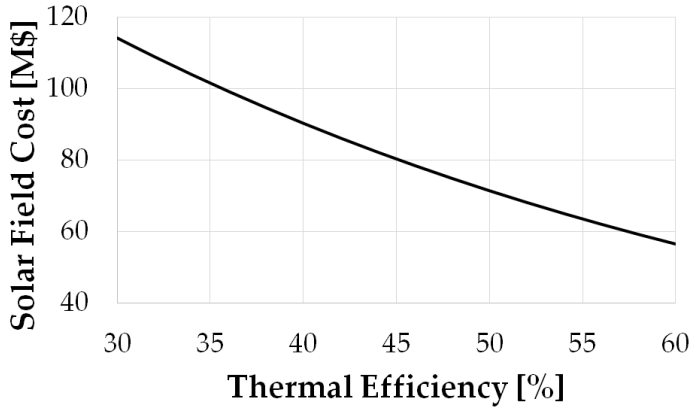

Figure 4.1: Solar Field Cost function as produced by SAM.

Solar Receiver and Tower

The cost of these components is again obtained with SAM based on the values given for a reference power plant using steam turbine technology. For the tower, the cost depends on height, which is itself dependent on the thermal efficiency of the power block through heat input [230], Figure 4.2. This is the only dependence of the solar tower cost function as no differences are expected between towers in power plants based on steam turbines or sCO$_2$ cycles.

With respect to the receiver, a cylindrical one similar to Gemasolar Power Plant [22] is taken into account, and two correction factors are then applied to the reference values calculated with SAM for state-of-the-art molten salts used in contemporary CSP plants. The first correction accounts for the different operating temperature of the receiver, which in this work is increased to 770ºC with respect to standard steam technology. In accordance to this, and in order to account for the higher technical risk, 30% higher costs are considered regardless of the size of the receiver. The second correction factor takes into account that the working

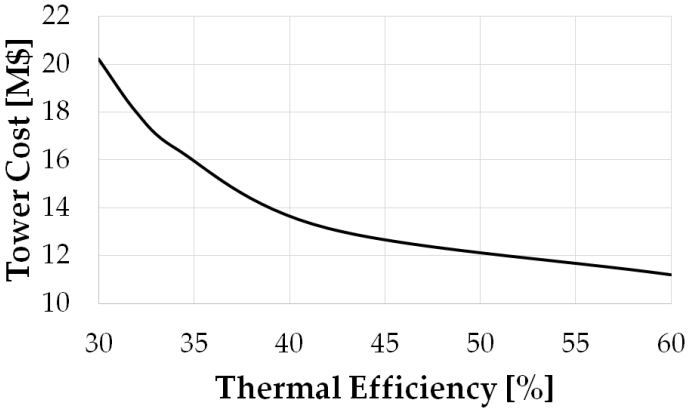

Figure 4.2: Solar Tower Cost function as produced by SAM.

fluid in a CSP plant based on steam turbines and in a plant based on sCO_2 technology are likely to exhibit a very different temperature rise across the receiver. This translates into an inversely proportional variation of molten salt flow rate and, therefore, receiver volume. The factor takes into account the different energy absorption capacity of state-of-the-art salts used in contemporary CSP plants with respect to a high temperature salt like FLiNaK, which is the working fluid of choice in this work.

The resulting global correction factor is shown in Eq.(4.1) where subscripts FLiNaK and ref refer to the said high temperature salt and the solar salt used by default in commercial CSP plants. The cost function of the reference receiver $C_{R,ref}$ is shown in Figure 4.3.

$$C_{R,FLiNaK} = f_{rec} \cdot C_{R,ref} = 1.3 \cdot \frac{\bar{c}_{p,ref} \cdot \Delta T_{ref}}{\bar{c}_{p,FLiNaK} \cdot \Delta T_{FLiNaK}} \cdot C_{R,ref} \tag{4.1}$$

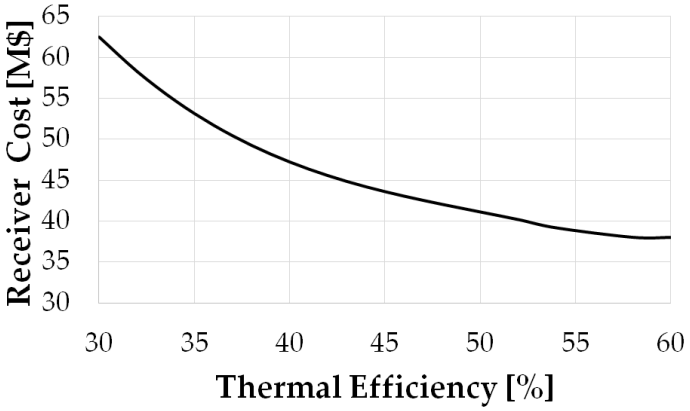

Figure 4.3: Solar Receiver Cost function as produced by SAM.

Thermal Energy Storage

The Thermal Energy Storage system is perhaps the equipment which is affected the most by the change in molten salts, due to the huge amount of HTF contained in it and for the greater temperature rise enabled by FLiNak. Its cost (C_{TES}) is calculated with an in-house code previously developed at the University of Seville. Originally, this model considered an 1 MWe parabolic trough plant based on steam turbines operating at 550ºC, with Delcoterm thermal oil employed in the TES system.The model, which was initially intended for small plants, was modified by Rodríguez to fit to larger scales and then modified again by the author of this thesis to incorporate FLiNak as HTF, both from the thermodynamic and economic standpoints. A complete description and validation of Rodriguez's model is provided in [238], including the cost of purchasing the major equipment as well as other costs related to installation, insulation, foundations and all the auxiliary equipment required for system operation.

The costs employed by the model are corrected with cost indexes available in the International Journal of Production Economics to account for the time value of money [239], and with exponential cost scaling factors taken from literature [240]. The cost of the individual components of the storage system are adapted from the detailed project budget reported in [234], which provides cost estimates of every single component of a real storage project. Additional information, like wages, labor hours and productivity is taken from [241].

In the present study, the maximum operating temperature of molten salts is set to 770ºC whereas the minimum temperature is dictated by the working sCO_2 cycle, meaning that it has a different value for each configuration. The gap between these two temperatures is the temperature rise across the solar receiver (ΔT_{solar}) which is found to affect the size and cost of the TES largely; this was also the case for the receiver in the previous section. It is to note that estimating the effect of this parameter combined with the one caused by thermal efficiency is not trivial, especially because the relation between the two is not known a priori. To this end, a sensitivity analysis of C_{TES} to variations of η_{th} and ΔT_{solar} is done by varying these parameters in the ranges 30-60 % and 90-300ºC respectively. The results of this study are presented in Figure 4.4, where it becomes evident that the size of the storage system is inversely proportional to ΔT_{solar}. Indeed, when ΔT_{solar} increases, the specific energy storage capacity (kJ/kg) of the storage material increases, thus reducing the inventory of molten salts for the same specifications (hours of extended operation at full load). On the other hand, η_{th} also contributes to reducing the size of the storage system since the heat input required for a given electric output is reduced proportionally to η_{th}.

Therefore, knowing the pattern of ΔT_{solar} for each cycle configuration turns out indispensable to complete the thermo-economic comparison, since the TES system is undoubtedly one of the most expensive equipment of a CSP plant. These trends are successively presented and discussed in Section 4.3 of this Chapter.

4.2.2 Heat Exchangers

Following the most usual approach, and even if the author acknowledges that it might not be the best option for a large scale-commercial power plant, Printed Circuit Heat Exchangers have been considered the technology of choice in this analysis, for their common acceptance and proven capability [67, 78, 242]. The name of this HXs derives from the procedure used to

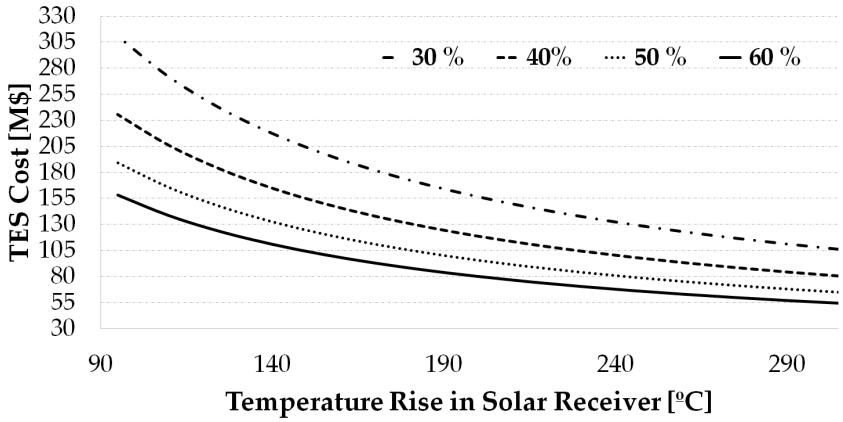

Figure 4.4: Cost of Thermal Energy Storage system.

manufacture the flat metal plates that form the core of the heat exchanger, done by chemical milling. The plates are then stacked, diffusion bonded and finally converted into a solid metal block, as shown in Figure 4.5 from [9]. This model of compact heat exchangers is particularly indicated for high pressure fluids, due to the fact that the plates are alternately joined by diffusion bonding, yielding a compact, extremely strong, all-metal heat exchanger core [242]. On the negative side, the resulting equipment is bulky and heavy and the manufacturing cost is very high. The main manufacturers of PCHEs today are Heatric [243], Vacuum Process Engineering VPE [244] and Alfa Laval [245], which declare different maximum design pressures and temperatures in the range from 650 to 1000 bar and from 800 to 900ºC. Any of these manufacturers provide equipment suitable for the operating conditions considered in the feasible range of the present study, Table 4.1.

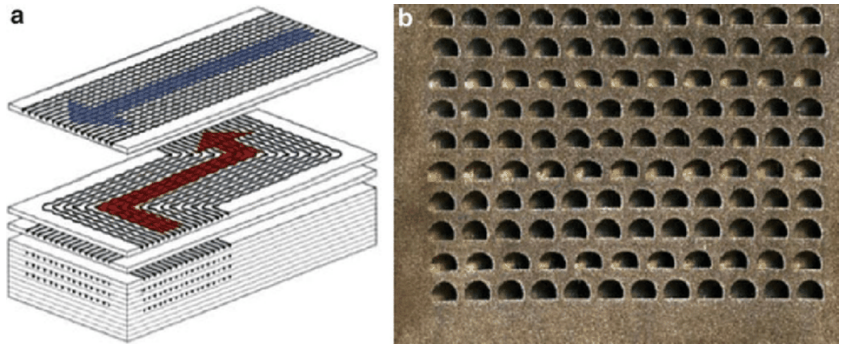

Figure 4.5: Section of a counter-flow PCHE. Taken from [9].

The thermal performance of the PCHE has been modeled with an in-house code whose description and validation are available in a series of joint publications by the author of this thesis and Kevin Hoopes, from Southwest Research Institute, TX [221, 246]. These works were originally presented at the 5^{th} International sCO_2 Power Cycles Symposium held in San Antonio in 2016 and the ASME Turbo Expo conference held in Charlotte, NC, in 2017. Reference to the second work is made in Chapter 5.

The model is based on the standard approach considering the heat exchanger as divided in N divisions with equal heat duty and with a low enough temperature rise/drop on each side so as to enable the application of the ϵ-NTU method in each division [2] [10]. In addition to this, as published in [221, 246], the code has recently been improved with new thermal correlations for wavy channels PCHE [73] and a mechanical stress analysis based on the work by Yoon [13]. To this latter aim, a maximum allowable mechanical stress must be set, which in this case corresponds to a maximum pressure difference between the hot and cold sides after which the geometry of the PCHE (channel pitch and wall thickness) is modified to ensure mechanical integrity at the working pressure and temperature of interest. This approach links the working pressure and void fraction of the equipment, yielding bulkier PCHEs at higher pressures. A complete description of the in-house model, along with the thermodynamic correlations employed, is provided in Annex A.

The default geometry of the PCHE design code is presented in Figure 4.6. This geometry makes use of a counter-flow layout with semi-cylindrical, zigzag channels whose dimensions take values usually employed in the industry [67]. In particular, the channel pitch and plate thickness take approximate values which must later be varied according to the pressure levels in order to ensure mechanical integrity (see Annex A).

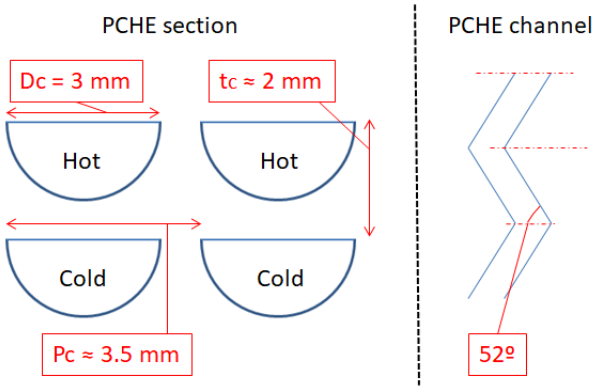

Figure 4.6: Section of the counter-flow PCHE taken into account in the in-house model. D_c, P_c and t_c are channel diameter, pitch and plate thickness.

The cost of the PCHEs is estimated with a methodology based on the works by Dostal [67] and Kim [73]. In these, the mass of the heat exchanger M is obtained from its volume V and void fraction -or porosity- ($\epsilon_{HX} = 1 - f_m$) which is given a reference value taken from literature. The latter parameter represents a sort of "density" of the HX, as defined in Eq.(4.2) where D_c, P_c and t_c are the channel diameter, pitch and plate thickness. The former is set to 3 mm whilst the other two parameters result from the mechanical analysis (typical values are 3.5 and 2 mm respectively). The total mass is finally obtained by merely multiplying V, f_m and ρ_m (density of the raw material considered). The cost of the PCHE is then calculated from the cost of the raw material (C_{raw}), expressed in \$/kg, Eq.(4.3).

[2] The ϵ-NTU method is based on the assumption that the fluid's properties are constant. Hence, it cannot be applied in a flange to flange simulation or with too few internal divisions, due to the strong real-gas-behavior of sCO_2.

$$f_m = 1 - \frac{\pi \cdot {D_c}^2}{8 \cdot P_c \cdot t_c} \quad ; \quad M = \rho_m \cdot V \cdot f_m \tag{4.2}$$

$$C_{HX}[\$] = M \cdot C_{raw} \tag{4.3}$$

Two different alloys are considered depending on the operating temperature. *Stainless Steel 316L* is used for the coolers, which do not have to withstand high temperatures, and the recuperators whose maximum temperature does not exceed 475 ºC. *Inconel 617* is employed in those HXs operating at higher temperatures, including the heaters. The maximum allowable mechanical stresses of these alloys, taken from [247, 248], are represented as a function of temperature in Figure 4.7.

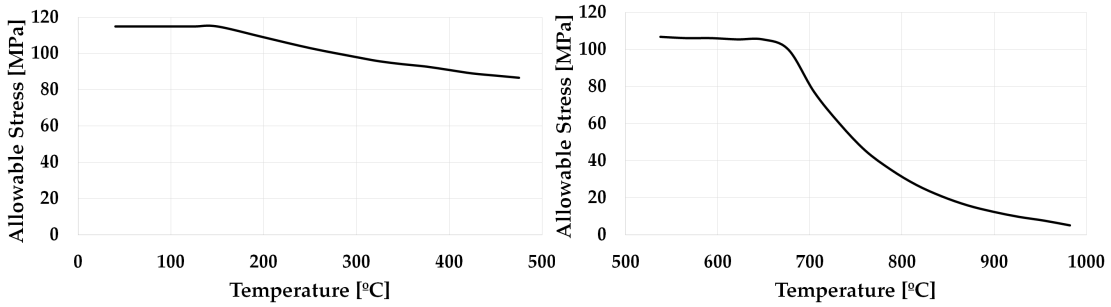

(a) Allowable stress for *Stainless Steel 316L*. [247]

(b) Allowable stress for *Inconel617* [248].

Figure 4.7: Maximum allowable mechanical stresses of materials employed in HX design, as a function of temperature.

Estimating the manufacturing/processing cost to be added to the raw material (usually supplied in bars) to calculate C_{raw} in PCHEs is a challenging task, inasmuch as this information is proprietary of the original equipment manufacturers. This is why the approach presented by Kim et al. to produce a correction factor that could be applied to the un-processed (raw material) cost is used, in the absence of a better approach [73]. These authors consider a cost of 150 \$/kg for the processed *Alloy 800 HT*, which is six times higher than the cost of the un-processed material in the market (ca. 25 \$/kg). Applying this correction factor to the afore-listed alloys yields the following cost ranges: *Stainless Steel 316L* from 20 to 25 \$/kg, *Inconel 617* from 120 to 180 \$/kg.

4.2.3 Turbomachinery

Turbomachinery components are simulated with simple lumped volume models given that these are intended for on-design performance only, the same way already discussed in Chapter 3. Then, due to the lack of reliable cost data for sCO_2 turbomachinery, standard cost estimates for air compressors and centrifugal pumps are employed, as presented in [249]. The cost of centrifugal compressors is obtained as a function of the required electric power in Horse Power, Eq.(4.4), whereas the cost of the pumps is calculated as a function of their volumetric

flow Q and head H in gal/min and ft, Eq.(4.5).

$$C_{compr}[k\$] = 7.90 \cdot \dot{W}_{el}{}^{0.62}, \quad 200 < \dot{W}_{el}[HP] < 30000 \tag{4.4}$$

$$\begin{cases} C_{pump}[\$] = 2 \cdot F_T \cdot C_b \\ F_T = exp(9.8849 - 1.6164 \cdot ln(Q \cdot \sqrt{H}) + 0.083 \cdot (ln(Q \cdot \sqrt{H}))^2) \\ C_b = 3 \cdot exp(8.833 - 0.6019 \cdot ln(Q \cdot \sqrt{H}) + 0.0519(ln(Q \cdot \sqrt{H}))^2) \end{cases} \tag{4.5}$$

Supercritical CO_2 turbines are expected to be less costly than steam turbines of similar output due to the lower footprint brought about by the lower specific volume of the working fluid and the lower pressure ratio of the working cycle (fewer stages) [67]. Based on this rationale, the cost of sCO_2 turbines is extrapolated from the cost of supercritical steam turbines without steam bleeds, as produced by Thermoflex software [250]. Two correction factors are then applied, the first of which is the ratio of volume flow rate between the reference and sCO_2 turbines. The second correction factor is based on the assumption that, due to material strength limitations, stage loading in a sCO_2 turbine is roughly 25-30% lower than in a steam turbine, Eq.(4.6),

$$\Psi_{sCO_2} = \frac{W_{stage,sCO_2}}{u^2_{sCO_2}} = 0.75 \cdot \Psi_{steam} = 0.75 \cdot \frac{W_{stage,steam}}{u^2_{steam}} \tag{4.6}$$

where Ψ is the stage loading coefficient, $W_{stage,steam}$ is the expansion work and u is the peripheral blade speed at mean turbine radius. Such a statement can be easily deduced from the following expression of the forces exerted by turbine blades on an incompressible, inviscid flow expanding across a bi-dimensional cascade, given by mass and momentum conservation:

$$\begin{cases} F_x = (p_1 - p_2) \cdot b \\ F_y = \rho \cdot b \cdot c_x^2 \cdot (\tan\alpha_1 - \tan\alpha_2) \end{cases} \tag{4.7}$$

where ρ is density, b is pitch of the cascade, c_x is axial velocity and α is flow angle with respect to the axial direction. The boundary conditions and forces are illustrated in Figure 4.8.

Should the steam and carbon dioxide flows turn a similar angle across the cascade (deflection) in Figure 4.8, the tangential force F_y exerted on the blade would increase proportionally to the change in density and axial velocity squared, Eq.(4.7). With this in mind, the following observations are noteworthy:

- Turbine inlet density almost doubles when using supercritical carbon dioxide in a CSP application at 750°C versus a similar plant using supercritical steam turbines at the standard temperature of 560°C[3].

[3]The approximate density of steam at 250 bar and 560°C is 75 kg/m^3 whilst carbon dioxide at 300 bar and 750°C has a density of 145 kg/m^3.

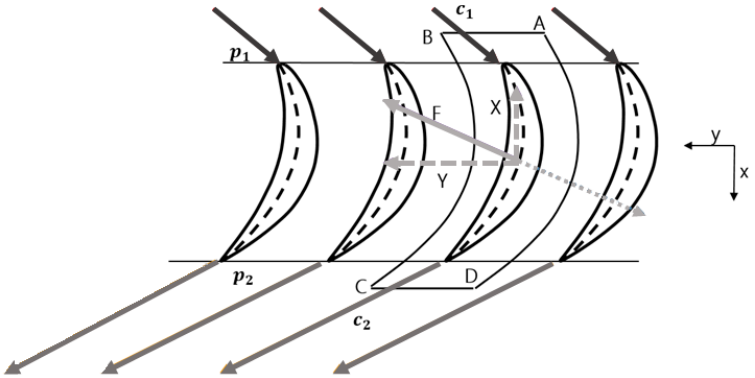

Figure 4.8: Forces on a cascade of turbine blades.

- In addition, the density drop along the expansion line in a supercritical steam cycle is much larger than in a supercritical CO_2 cycle due to (i) the much larger expansion ratio of the former cycle and (ii) the higher isentropic exponent of steam. As a result, the average densities of steam and carbon dioxide in these turbines are 40 and 90 kg/m^3,[4]. The cumulative effect on tangential force, based on these average densities, would be a double F_y for CO_2.
- On the other hand, the change in axial velocity can be correlated to the change in speed of sound, which is in the order of 20% (525 m/s for CO_2 and 650 m/s for steam at turbine inlet). This means a 35% lower axial velocity squared, hence tangential force, for CO_2.

Nevertheless, this last contribution is not able to counteract the significant increase in F_y produced by the difference in fluid density, and the tangential force in the sCO_2 case can be roughly considered as 165% higher than the supercritical steam one. In the light of these results, F_y in a sCO_2 turbine could be reduced by simply reducing the pitch/chord ratio of the blade row. Nevertheless, it is unrealistic to think that the twofold difference between F_{y,CO_2} and F_{y,H_2O} can completely be offset through this effect as this would drastically increase profile losses (friction on the blade passage walls). This is why a 15-25% lower load coefficient for sCO_2 is assumed in Eq.(4.6), the remainder reduction of F_{y,CO_2} (if any) relying on a higher solidity. The resulting difference in tangential force F_y between sCO_2 and supercritical steam turbines turns out to be in the order of 150%, as indicated in Eq. 4.8 later.

If expansion work in the Rankine steam cycle and in each sCO_2 cycle is then expressed as a function of expansion ratio, turbine inlet conditions and properties of the working fluid, the following correction factor can be devised under the assumption that all stages in the turbine exchange equal work

$$\frac{N_{sCO_2}}{N_{steam}} = 1.5 \cdot \frac{\bar{c}_{p,sCO_2} \cdot TIT \cdot (1 - PR^{\frac{1-\gamma}{\gamma}})}{\Delta h_{steam}} \tag{4.8}$$

where N is the number of stages, TIT and PR are the turbine inlet temperature and pressure ratio of the sCO_2 cycle and Δh_{steam} is the isentropic enthalpy change across the steam turbine.

[4]These densities are based on isentropic expansions from the conditions in footnote [1] to 0.080 and 75 bar for steam and carbon dioxide respectively.

With this information, the resulting cost function of the sCO_2 turbine is

$$C_{turb}[k\$] = C_{TFX} \cdot \frac{\dot{V}_{sCO_2}}{\dot{V}_{steam}} \cdot \frac{N_{sCO_2}}{N_{steam}} \tag{4.9}$$

where C_{TFX} is the cost estimate of a supercritical steam turbine of given volumetric flow rate $\dot{V}_{steam}$ as provided by Thermoflex.

4.2.4 Cooling Towers

The cost of this equipment is also obtained with Thermoflex, considering a standard natural draft wet cooling tower with horizontal fill. To this aim, the inlet temperature of hot water entering the cooling tower and the tower range (ΔT_{range}) are set to 26.8 ºC and 10 ºC respectively. With this information, the water mass flow rate of the cooling tower is easily calculated by merely applying energy conservation under ISO ambient conditions: 15 ºC, 1 atm and 60% RH. The correlation estimating the cost of the cooling tower as a function of the water mass flow rate $\dot{m}_w$ is presented in Eq.(4.10).

$$\begin{cases} C_{CT}[k\$] = a \cdot \dot{m}_w^6 - b \cdot \dot{m}_w^5 + c \cdot \dot{m}_w^4 + d \cdot \dot{m}_w^3 + e \cdot \dot{m}_w^2 + f \cdot \dot{m}_w + g \\ a = 2.45 \cdot 10^{-15} \quad b = -1.1 \cdot 10^{-11} \quad c = 1.9 \cdot 10^{-9} \\ d = -1.52 \cdot 10^{-5} \quad e = 0.0046 \quad f = 1.17 \quad g = 26.62 \end{cases} \tag{4.10}$$

For the case of the *Transcritical CO_2* cycle, which has a minimum cycle temperature of 15ºC to enable condensation [251], the water temperature at the inlet to the cooler is set to 10 ºC whereas the range ΔT_{range} remains the same as in the other cycles.

4.2.5 Balance of plant and other assumptions

Balance of Plant (BoP) is the last contribution to the total installed cost. This cost $C_{tot,BoP}$ is assumed to be in the range from 10 to 20% of the total installed cost. Other owner's costs or costs related to engineering, procurement and construction are not included in the calculations.

4.3 Sensitivity Analysis to Pressure Ratio

A series of specifications for the reference power plant considered in the economic analysis were presented in Table 4.1 at the beginning of this chapter. Amongst them, turbine inlet temperature comes usually determined by the energy source or application, as discussed earlier, whilst the appropriate value of peak pressure is less easily fixed, due to the lack of sCO_2-based commercial power plants and of specific references in literature. Nevertheless, from Chapter 3, it results evident that the thermodynamic performance of all the cycles generally improve when higher pressures are considered. Therefore, a starting point to assess the best turbine inlet pressure would be to consider the highest feasible value from the thermodynamic and economic standpoints. To this end, a parametric study is developed whereby this pressure varies from 15 to 40 MPa, on the assumption that the latter value sets the current limit in turbine inlet pressure (as drawn from the experience with ultrasupercritical steam turbines).

The figures of merit considered in the parametric analysis are thermal efficiency, temperature rise across the solar receiver ΔT_{solar}, whose importance is remarked in Section 4.2.1, Overnight Capital cost (OCC) and Power Block (PB) cost. Figure 4.9 presents the trends of η_{th} and ΔT_{solar},

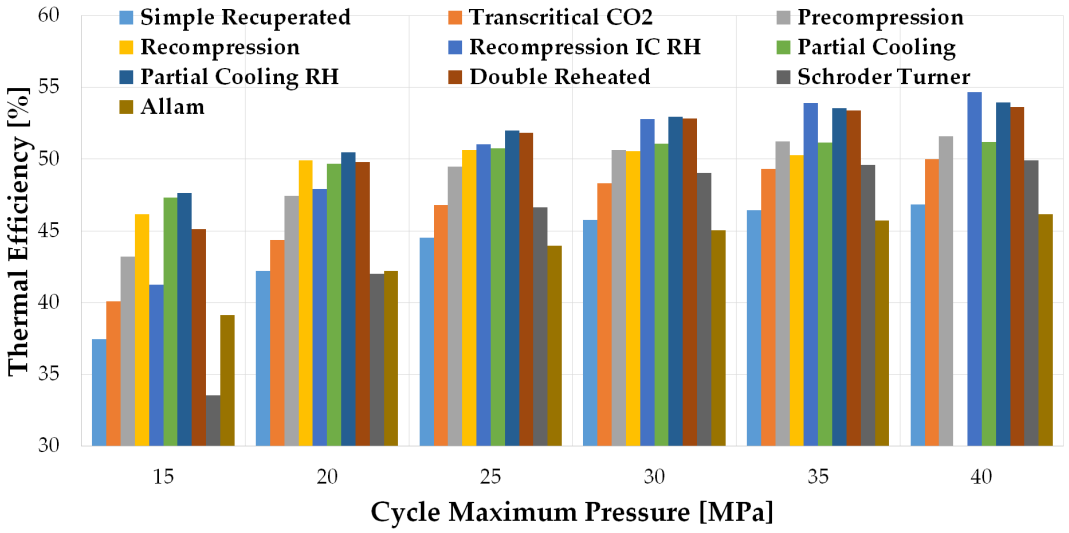

(a) Thermal efficiency as a function of peak cycle pressure. TIT is set to 750ºC in all cycles.

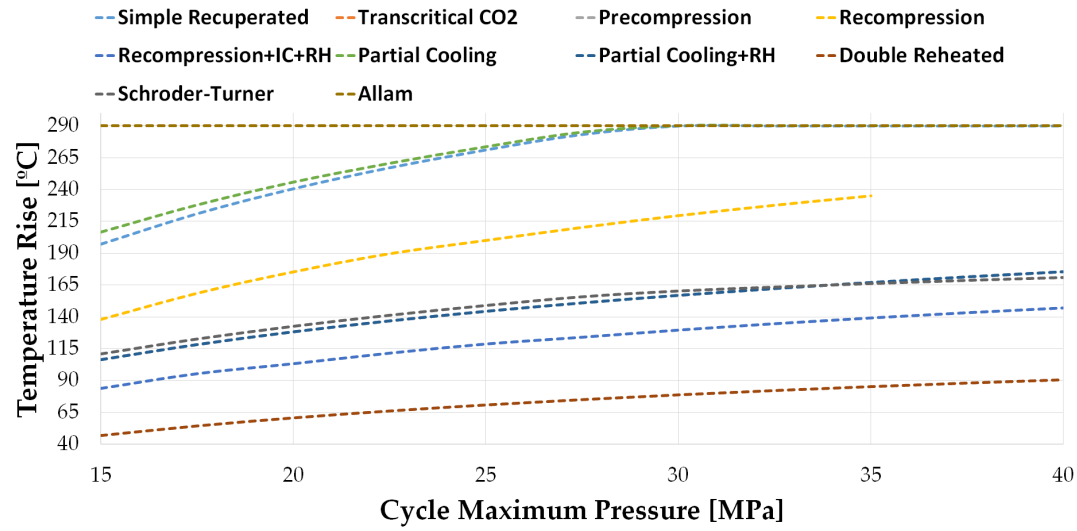

(b) Temperature rise across solar receiver as a function of peak cycle pressure. TIT is set to 750ºC in all cycles. The *Transcritical CO_2 Allam* cycles show the same trend, constant and equal to 290ºC.

Figure 4.9: η_{th} and ΔT_{solar} as a function of peak cycle pressure.

the former of which was already discussed in the previous chapter with a different graph, Figure 3.20.

Interestingly, ΔT_{solar} and η_{th} show similar trends since both of them increase monotonically, even if ΔT_{solar} for *Transcritical CO2*, *Allam*, *Simple Recuperated* and *Recompression* remains constant at 290ºC for pressures higher than 30 MPa, in order to avoid solidification of the molten salt. Theoretically, if lower FLiNaK temperatures were possible, the trend of ΔT_{solar} would be a true monotonic increase. As expected, those layouts presenting highest η_{th} (*Partial Cooling + RH*, *Recompression+IC+RH* and *Double Reheated*) are also those with lowest ΔT_{solar}. From a thermodynamic standpoint, this is explained by the recuperative nature of the cycle: indeed, those cycles with the highest potential for internal heat recovery (preheating of the

receiver inlet stream with heat available in the turbine exhaust flow) reducing the need for external heat addition, leading to a higher average temperature of the heat addition process (hence ΔT_{solar}). The large importance of this observation is found in the very strong an counteracting impacts of these two parameters on the costs of the solar subsystem and the power block.

Figure 4.10 shows the Overnight Capital Cost and Power Block Cost. It becomes very visible that all configurations exhibit similar features. The Overnight Capital Cost decreases as the peak pressure gets higher and then, once a minimum value *OCC* is reached, it rises again as pressure continues to grow.

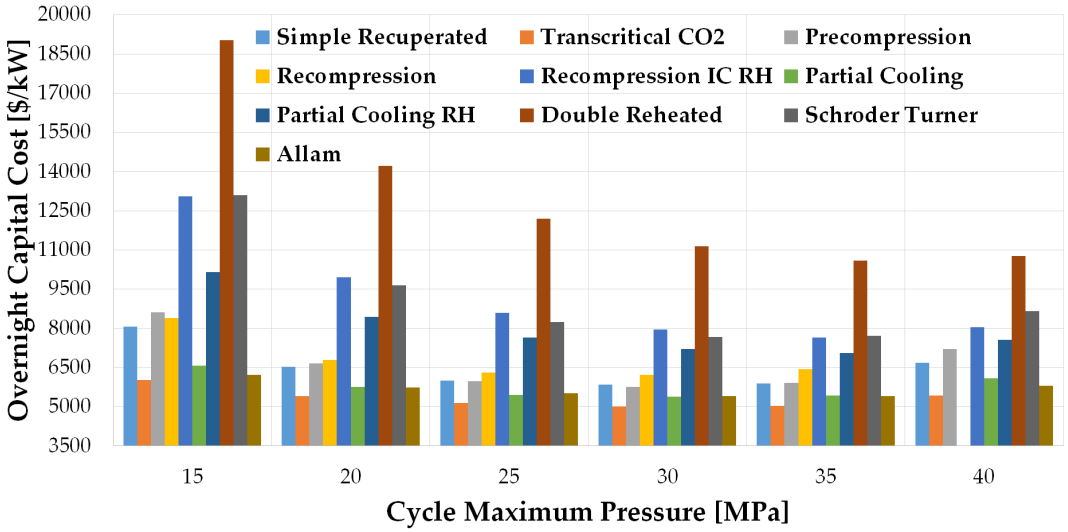

(a) Overnight Capital Costs per kilowatt as a function of peak cycle pressure.

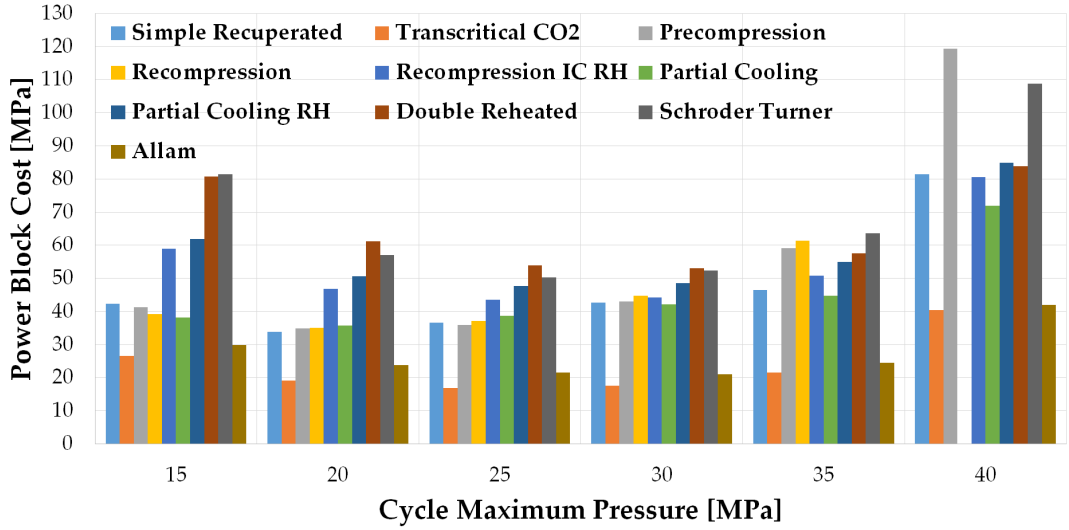

(b) Power Block Costs as a function of peak cycle pressure.

Figure 4.10: OCC and PB costs as a function of peak cycle pressure.

The initial decay is mostly thanks to a higher thermal efficiency, Figure 4.9(a), whilst the

subsequent rise is due to the very high operating pressures. The Power Block cost presents a somewhat mirrored trend, with highest costs at very high pressures and also high costs when pressure is very low. In this case, it is also observed that the pressure at which the PB cost is lowest depends on cycle configuration. This becomes particularly evident for the *Schroder-Turner* and *Precompression* cycles which reach very high *PB* costs (higher than 100 M$) for pressures around 40 MPa due to two counteracting effects. At low to intermediate pressures, the rise of thermal efficiency is dominant and brings about a PB cost reduction. On the other hand, at high pressure, the equipment get bulkier to endure the extremely high mechanical stresses, and this has a large impact on the cost of major components. Generally speaking, it is worth noting that almost all the configurations exhibit a minimum *PB* and *OCC* at around 25 MPa and 35 MPa.

Based on the information obtained from Figures 4.9 and 4.10, the assumption to consider a 30 MPa peak pressure for the reference power plant is validated. Among the feasible pressures, either mechanically or thermodynamically speaking, this value ensures a significant reduction of the Overnight Capital cost from which it can be inferred that the PB cost has a smaller effect on OCC as compared to other subsystems, in particular the solar field and thermal energy storage system. This conclusion also increases the interest in ΔT_{solar}, which has a very strong influence on the cost of the TES itself, since it is found to achieve its maximum value (for four of the ten cycles considered) when a pressure of 30 MPa is adopted.

4.4 Uncertainty Analysis

As it is common to any cost analysis [252], the foregoing discussion on how to estimate the costs of the different components in a supercritical CO_2 power plant holds an inevitable degree of uncertainty. In order to address it, a probabilistic approach to uncertainty quantification based on the Montecarlo methodology is incorporated into the assessment. This tool is highly recommended to take into account the uncertainty encountered in the cost estimation process, especially if an innovative technology like sCO_2 is considered.

Based on a similar analysis by Ho et al. [236, 237], uniform probability distributions are assigned to each main parameter in the cost functions presented before. This means constant probability between the maximum and minimum values that each parameter can take, as reported in Table 4.3. The limits are wider for those parameters which bring in larger uncertainty whereas the range is lower for the most mature technology, for instance the solar field. With these boundary conditions, and setting the number of samples to 10000, the Overnight Capital Cost (*OCC*) is calculated.

The uniform probability distribution used in [236, 237] has been selected for its capacity to define the boundary conditions more clearly and for its low computational duty [5]. Nonetheless, calculations with a normal distribution have also been performed in order to double check potential errors (larger uncertainty) coming from the selection of a wrong probability function. The results obtained with both distributions are almost identical, but with a significant computational cost saving for the uniform distribution, which is used in the remainder of this work.

[5] Personal communication with Craig Turchi, NREL.

The criteria used to define the possible ranges of values for all the costs employed in the uncertainty analysis, resumed in Table 4.3, are as follows:

- For turbomachinery, the uniform distribution considers that a 40% higher cost than in Eqs.(4.4-4.9) is possible, whilst the possibility to have a lower cost is considered negligible. This assumption is made principally to take into account the extreme lack of information available about cost estimation techniques for sCO_2 turbomachinery, with the intent to provide results close to the worst case scenario instead of more optimistic ones.

- Something similar applies to the cost of the cooling tower for which potential changes of ±30% are foreseen due to large variations in relative humidity at the selected plant site.

- Regarding the heat exchangers, the range of values discussed and provided in Section 4.2.2 is used in the uncertainty analysis. It is worth highlighting that these costs include both raw material and manufacturing/processing costs.

- The solar field and tower are already mature technologies and thus only a 10% deviation towards higher costs is considered, possibly brought about by unforeseen local constraints.

- The range shown in Table 4.3 for the thermal energy storage system is wider, accounting for potential changes between -20% and +30% with respect to the cost estimated by the in-house code, Figure 4.4. This range is intended to leave room for a new generation of less costly molten salts being introduced in the market in the near to mid future.

- The cost of the receiver C_R is thought to potentially be up to 50% higher than the value provided by Figure 4.3, due to unforeseen material-related issues encountered when operating the system at very high temperatures.

- Finally, $C_{tot,BoP}$ is assumed to be in the range from 10 to 20% of the total installed cost.

Cost [k$]	Min Value	Max Value	Distribution
Compressor	C_{compr}	$1.4 \cdot C_{compr}$	Uniform
Pump	C_{pump}	$1.4 \cdot C_{pump}$	Uniform
Turbine	C_{turb}	$1.4 \cdot C_{turb}$	Uniform
SS 316L [$/kg]	20	25	Uniform
Inconel 617 [$/kg]	120	180	Uniform
Cooling Tower	$0.7 \cdot C_{CT}$	$1.3 \cdot C_{CT}$	Uniform
Solar Field	C_{SF}	$1.1 \cdot C_{SF}$	Uniform
TES	$0.8 \cdot C_{TES}$	$1.3 \cdot C_{TES}$	Uniform
Receiver	$1.3\ C_R$	$1.8 \cdot C_R$	Uniform
Tower	C_{tower}	$1.1 \cdot C_{tower}$	Uniform
BoP	$0.1 \cdot C_{tot}$	$0.2 \cdot C_{tot}$	Uniform

Table 4.3: Uncertainty analysis: limits of the uniform probability distributions.

4.5 Economic Results

This section presents the results provided by the uncertainty analysis using the Montecarlo method. To this aim, the probability density functions of OCC-per-kW are presented first, providing an overall scenario of configurations considered. Secondly, a comparison between these configurations is developed, considering the 85% percentile and analyzing the individual contributions to OCC.

A summary of all the figures of merit obtained for all the cycles considered and the operating conditions in Table 4.1 (750ºC and 30 MPa) is provided in Table 4.4. The information shown contains the main performance parameters such as η_{th}, W_s, ΔT_{solar}. This is later employed to estimate the cost of all major equipment with the correlations and assumptions discussed at the beginning of this Chapter.

Cycle	$T_{in,compr}$ [ºC]	$P_{in,compr}$ [MPa]	η_{th} [%]	W_s [kJ/kg]	ΔT_{solar} [ºC]
a	32	7.5	45.8	171	290
b	15	5	48.3	242	290
c	32	7.5	50.6	164	254
d	32	7.5	50.5	142	220
e	32	7.5	52.8	174	130
f	32	5	51.1	192	290
g	32	5	53.0	210	157
h	32	5	52.8	159	80
i	32	7.5	49.0	200	160
j	32	3	45.0	252	290

Table 4.4: Parameters used in the economic analysis.

4.5.1 Total Costs

The specific Overnight Capital Costs (per installed electric kilowatt) of the cycles presented in Figure 3.1 are presented in Figure 4.11[6]. Three regions are identified in this chart. On the right hand side, the *Double Reheated* cycle is identified as having the highest OCC-per-kW with up to 14000 $/kW. In the central region, the *Recompression+IC+RH, Schroder-Turner* and *Partial Cooling+RH* cycles exhibit high OCC-per-kW with up to 10000 $/kW. Finally, the other six layouts are on the left hand side of the chart with installed costs in the range from 5000 to 7000 $/kW.

The first interesting observation is related to the impact of uncertainty. It is worth noting that those cycles with higher costs also experience larger uncertainty, manifested as a less steep slope which broadens the range of possible installed cost values. For instance, for the *Double Reheated* layout, this range increases to more than 4000 $/kW between the least and most probable costs. This is symptomatic of a larger data dispersion in the Montecarlo simulation, due to the higher relative importance of the thermal energy storage system and the tower/receiver. Such behavior could have been deduced from the values given in Table 4.3 for the latter

[6]Note that the *Matiant* and *Quasi Combined* layouts, k and l in Figure 3.1, are excluded from the economic analysis as discussed at the beginning of the Chapter.

component.

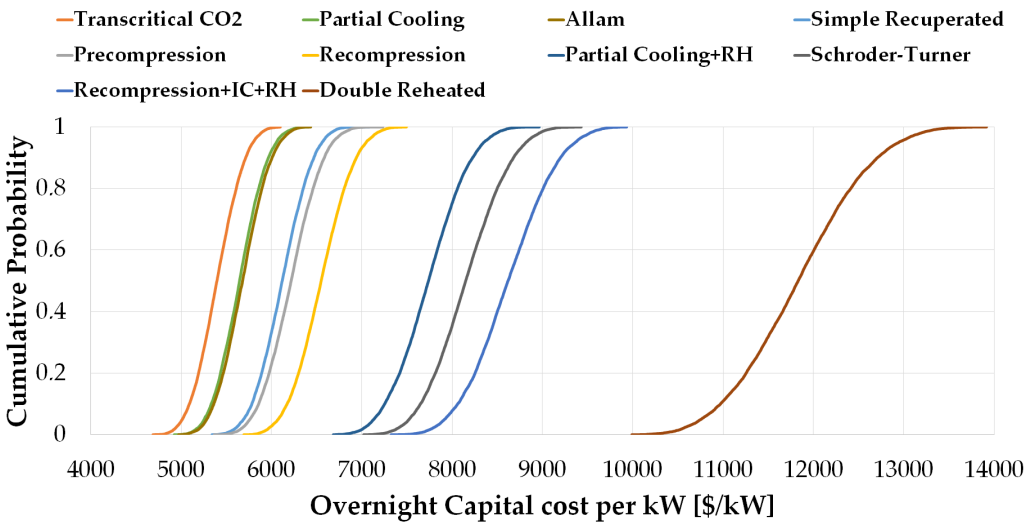

Figure 4.11: Cumulative probability distribution of Overnight Capital Costs per kilowatt. All cycles (see Figure 3.1 to identify labels).

The physical explanation of the foregoing discussion has to do with the fact that these cycles with higher costs are extremely recuperative, leading to significantly smaller values of ΔT_{solar} (smaller temperature rise in the heaters) and an exponential rise of the size of receiver and TES; this confirms what was already observed in Section 4.2.1. On the other end, heat recovery in the *Transcritical* CO_2 layout is not particularly enhanced, yielding a larger ΔT_{solar} and a more vertical slope in Figure 4.11. This is also observed in the close-up of those cycles with lowest capital cost presented in Figure 4.12. In the light of these results, it is easily concluded that the *Transcritical* CO_2 cycle is the only layout likely to yield an *OCC* lower than 6000 $/kW whilst the *Partial Cooling* and *Allam* cycles yield the same value but with 90% confidence only.

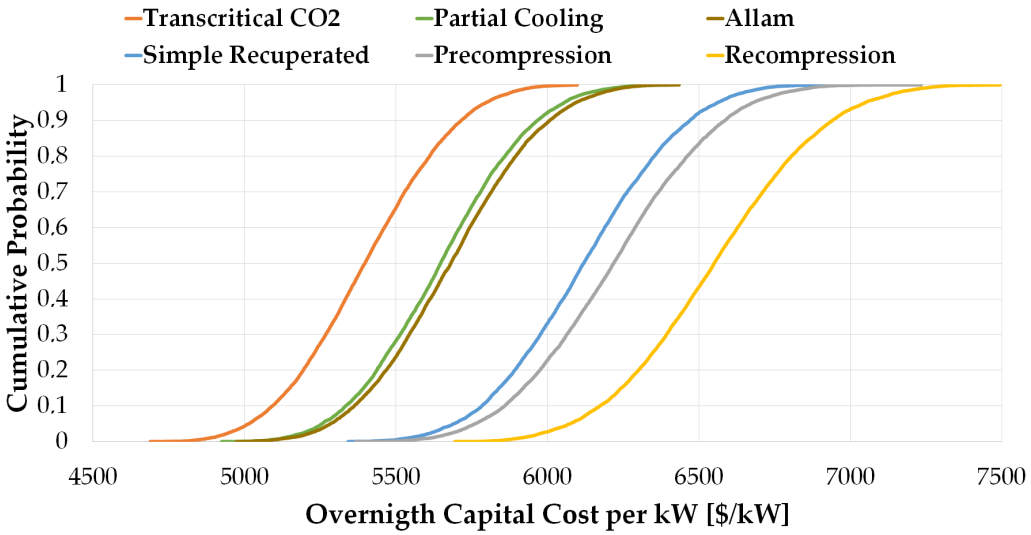

Figure 4.12: Cumulative probability distribution of Overnight Capital Costs per kilowatt. Close-up of Figure 4.11.

4.5.2 Cost Breakdown

Upon evaluation of the impact of uncertainty, the 85% percentiles are used to perform a capital cost comparison of the ten cycles considered in the analysis. The comparison is presented in Figure 4.13 with the labels already presented in Figure 3.1.

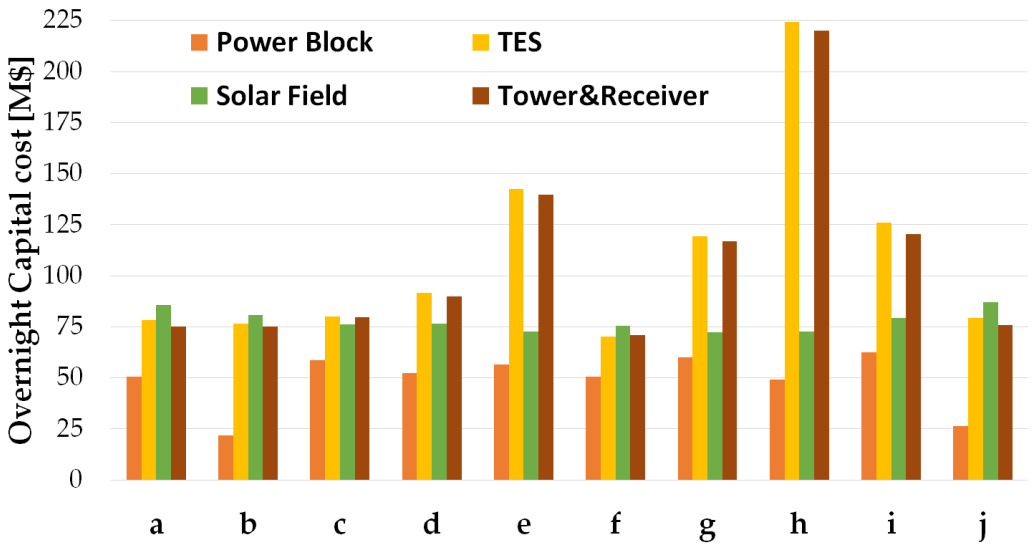

Figure 4.13: Breakdown of Capital Costs. Labels refer to Figure 3.1.

At first glance, the *Recompression+IC+RH* and *Double Reheated* layouts (*e* and *h* in Figure 4.13) exhibit unusual results. Indeed, the costs of thermal energy storage and tower/receiver are significantly higher than that of the solar field, which is usually the most expensive subsystem in a CSP plant. A similar though slightly attenuated pattern is presented by other layouts:

Recompression, Schroder-Turner and *Partial Cooling+RH* (d, i and g respectively). This is due to the very low ΔT_{solar}, which is actually much lower than ΔT_{ref} and leads to a dramatic increase in the size of these components. In particular, the *Double Reheated* layout presents a ΔT_{solar} of 80ºC, a value three times lower than ΔT_{ref} (284ºC) and the maximum ΔT_{solar} achieved by some of the configurations considered (290ºC, see Table 4.4). The conclusion already reported in [253] with regards to the capital importance of ΔT_{solar} is confirmed here again.

Another interesting observation in Figure 4.13 is the share of the solar field in those cycles with more complex layouts (e, g, h, i) which is indeed lower thanks to a higher efficiency η_{th}. Unfortunately, this lower cost is outweighed by the much higher cost of the remaining components in the plant. And for the same reasons, the cost of the power block is significantly lower than that of the solar subsystem in those cycles characterized by simpler configurations (b and j, for instance). Also due to this relationship between efficiency and size of solar field, the costs of power block and solar field are comparable in those cycles incorporating reheating and intercooling (e, g), due to the higher thermal efficiencies achieved. Nevertheless, on the negative side, these cycles typically exhibit low ΔT_{solar}, see Table 4.4, which leads to extremely high C_{TES}, C_R and C_{tower}. This can be better observed in Figure 4.14 where a breakdown of the power block cost is provided.

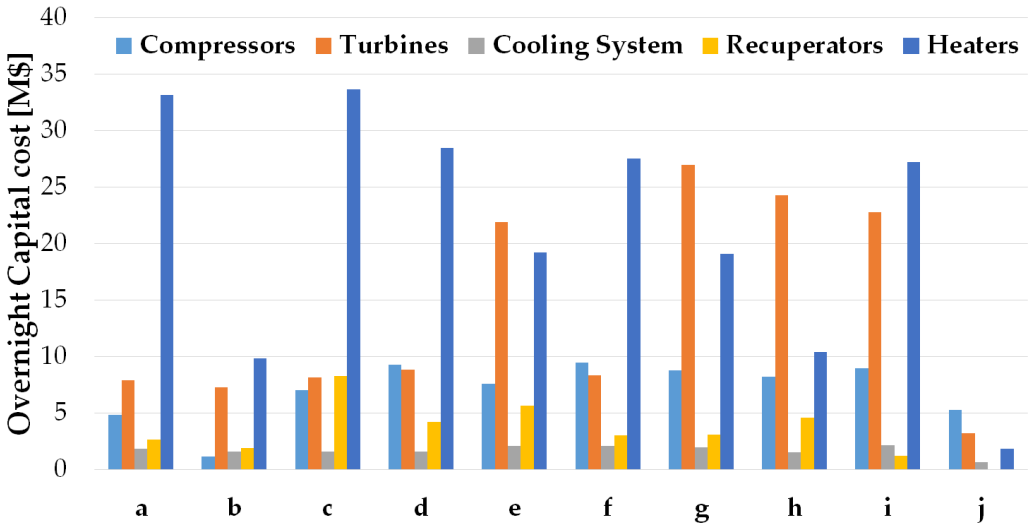

Figure 4.14: Breakdown of Power Block Costs. Labels refer to Figure 3.1.

The *Recompression+IC+RH, Partial Cooling + RH, Double Reheated* and *Schroder-Turner* layouts in Figure 4.14 (e, g, h and i) show a high turbine cost, due to the larger number of turbomachineries required by the reheating configuration. Yet, the costliest items turn out to be the heaters, owing to the more expensive materials that must be used to withstand the extremely high temperatures at the inlet. Furthermore, the cost of the heaters is directly affected by ΔT_{solar} given that, for a given output, a larger temperature rise across the heater implies a lower ΔT across the solar receiver, which also implies a smaller temperature difference between the hot and cold tanks of the thermal energy storage system. This can be inferred from the parallel trends of TES and heaters costs, yellow bars in Figures 4.13 and 4.14

respectively.

The thermodynamic information presented in Chapter 3 and the cost analysis in the previous section are integrated in Figure 4.15. This chart presents a comparison between the ten cycles considered in terms of First and Second Law efficiencies and *OCC*, allowing to better understand the foregoing discussion. It is easily observed that the *Transcritical* CO_2 (*b*), *Allam* (*j*) and *Partial Cooling* (*f*) cycles are the least expensive options. Nevertheless, while the first two configurations do not exhibit particularly good thermodynamic features, the *Partial Cooling* system seems to provide a better compromise. This is further assessed in Figure 4.16, where the trade-offs between the key figures of merit of each cycle are presented. These metrics are thermal efficiency η_{th}, Carnot Factor CF, temperature rise across the receiver ΔT_{solar} and installed cost (expressed as 1-$/kW).

Thermal efficiency has a direct impact on the size of the solar field and, accordingly, the tower and receiver. The Carnot Factor is a measure of the overall irreversibility of the cycle, hence the temperature gap (between the hot and cold reservoirs) needed to achieve a given thermal efficiency; i.e., a combination of thermal efficiency and compressor inlet temperature for cycles operating at constant turbine inlet temperature. The temperature rise is an indirect measure of the inventory of molten salts that is needed to run the cycle and store thermal energy in the Thermal Energy Storage system. Finally, the complementary relative cost 1-$/kW is self-explanatory.

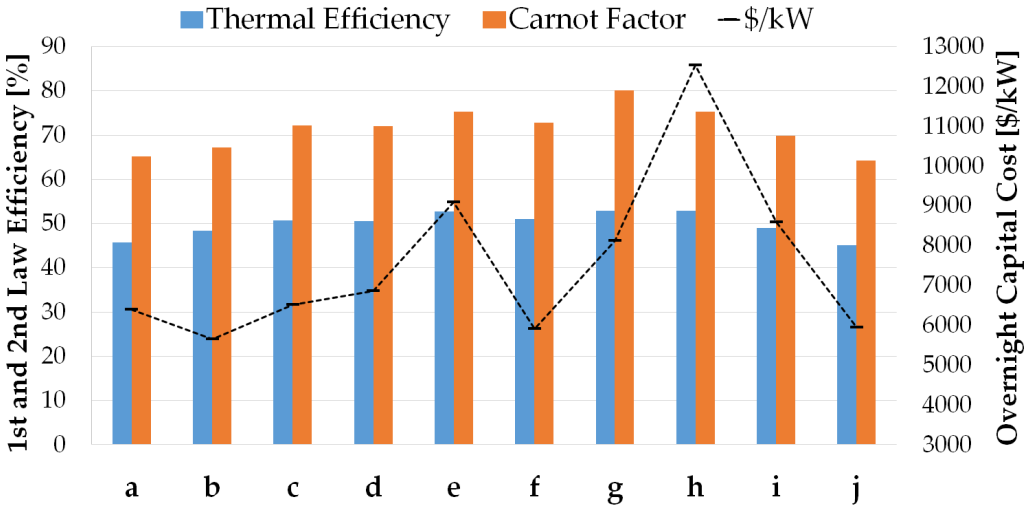

Figure 4.15: Thermo-economic comparison of supercritical CO_2 cycles.

The aim of Figure 4.16 is to provide a graphical comparison of the overall performance of the cycles, both thermally and economically. Accordingly, the layout achieving highest value in each axis (note that each metric is expressed in relative terms for the sake of the comparison) stems as the best option since it provides highest production of energy at the minimum cost. With this in mind, it becomes clear that the *Double Reheated* layout cannot be considered the best choice because it exhibits an extremely high *OCC* (1-$/kW→0) in spite of its high thermal efficiency. The other three cycles, on the other hand, present very similar areas.

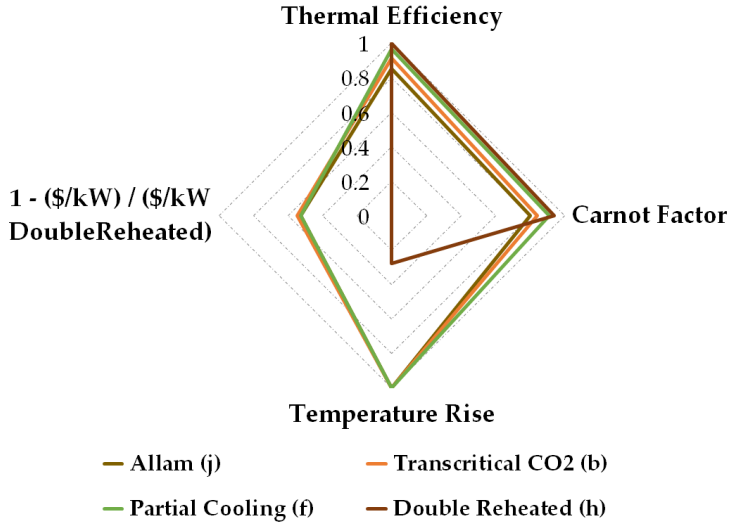

Figure 4.16: Thermo-economic comparison of supercritical CO_2 cycles. Trade-offs between key figures of merit.

The economic results of the uncertainty analysis, Figure 4.12, suggest that whilst the *Transcritical CO_2* cycle could be the layout of choice for the CSP application considered, the *Partial Cooling* cycle also presents significantly higher thermal efficiency and Carnot factor, Figure 4.15, even if with slightly higher $/kW, Figure 4.16. For these reasons, the *Partial Cooling* cycle would potentially step forth as a shorter-term, slightly more feasible option whereby a balanced techno-economic performance would be attained with less demanding design constraints for the solar receiver. On the negative side, this would be at the cost of a larger inventory of salts as shown in Figure 4.16.

4.6 Conclusions

This chapter presented an assessment of the Overnight Capital Cost of a 50 MW_e CSP power plant with a 10 hour Thermal Energy Storage system, operating at high temperature and employing a sCO_2 power cycle. The major equipment of the plant have been modeled either with validated in-house codes (Thermal Energy Storage, heat exchangers) or using software accepted by the industry (SAM for the solar field, tower and receiver, and Thermoflex for the turbomachinery and cooling tower). The commercial software has also been employed to calculate reference costs of a steam-based CSP plant with a TES of similar capacity using state-of-the-art molten salts. Then, a series of correction factors have been developed in order to account for the difference between the high temperature salt $FLiNaK$ and the reference salt, thus adapting the cost estimates to plants based on sCO_2 technology.

The integral thermo-economic analysis applied to the cycles explored in Chapter 3 has been based on the Overnight Capital Cost per kilowatt and on efficiency according to the First and Second Laws of Thermodynamics. A first conclusion is that only the *Transcritical CO_2* cycle seems to be likely to enable installation costs lower than 6000 $/kW with a 100% probability. If the 85% confidence interval is considered, the capital cost of this cycle is 5657 $/kW,

which seems to be competitive against some 3800 $/kW for a coal power plant [254] or 5800 $/kW for a state-of-the-art CSP plant using tower technology [255]. Interestingly, this configuration does not present a remarkably high η_{th} (lower than 48.5%) or a very high Carnot Factor.

The *Partial Cooling* and the *Allam* layouts follow close behind with 5907 and 5943 $/kW respectively. Considering the former cycle, the relatively low *OCC* is combined with very good thermodynamic features. This cycle provides a thermal efficiency higher than 51%, and apparently the best compromise between thermodynamic and economic features. Finally, very complex layouts seem to be not advisable, even if they are characterized by really high thermal efficiencies η_{th}. The *Double Reheating*, *Recompression+IC+RH* and *Partial Cooling+RH* cycles are actually able to exceed 53% thermal efficiency but suffer from a much larger number of components, some of them operating at high temperature. As a consequence, their capital costs per kilowatt increase to 12538, 9096 and 8130 $/kW respectively.

The work in this chapter suggests that sCO_2 can potentially be installed at a cost that is comparable with current steam turbine technology. Bearing in mind that the latter technology does not hold the potential to become much more efficient than it currently is, this is a promising result that has now to be confirmed by the calculation of the corresponding Levelized Cost of Electricity in the next Chapter.

5 Partial Load Analysis and LCoE Assessment

This chapter focuses on the analysis of the **off-design operation of the power block** caused by variations in either temperature or load, in order to **estimate the Levelised Cost of Electricity of the plant**, therefore concluding the thermo-economic analysis started in Chapter 4. In the first part of this chapter, a quasi steady-state model of the power block is developed, including a series of in-house codes meant to predict the off-design performances of turbomachinery and heat exchangers. The performance maps of the compressors are obtained with **AxSTREAM** software whilst an original methodology called **Conductance Ratio Method** is used for the PCHEs. In the second part of the chapter, the results obtained are implemented in the **System Advisor Model (SAM)** software in order to assess the LCoE of the plant, considering the two best sCO_2 cycles (Partial Cooling and Allam) in four different geographical locations. Finally, a standard steam-turbine CSP plant is studied, and an overall comparison between these three plant layouts is presented.

Sections of this chapter can be found in:

F. Crespi, D. Sánchez, K. Hoopes, B. Choi, N. Kuek, 2017, *The Conductance Ratio method for off-design heat exchanger modeling and its impact on an sCO2 Recompression cycle*, Proceedings of ASME Turbo Expo 2017: Turbomachinery Technical Conference and Exposition, Charlotte, NC.

5.1 Introduction

In the previous chapter, three configurations were highlighted for their particularly good thermo-economic features: *Transcritical CO_2*, *Allam* and *Partial Cooling* cycle. Although the former has the lowest installation costs, it is as well the one requiring the most restricting boundary conditions from a technological and environmental point of view. In order to enable the condensation process, in fact, the inlet temperature to the *Transcritical CO_2* pump must be set to 15°C, which means an extremely low ambient temperature, in the order of 8°C if evaporative cooling is considered or less than 5°C if air coolers are used. Such values are really difficult to achieve in a CSP plant, due to the fact they are typically located in arid (even desertic) areas, characterized by extremely high values of solar irradiation and therefore with intermediate-high ambient temperatures. This unlikely feasibility of the *Transcritical CO_2* cycles is the reasons why the author decided to limit the partial load analysis to the *Allam* and *Partial Cooling* layouts only, given that they are more easily implemented in a CSP plant. Nevertheless, the thermal and economic features of the *Transcritical CO_2* cycle are still ac-

knowledged and hence this layout should be considered by the sCO_2 research community for other applications.

As previously commented in Chapter 1, the information about off-design performance of sCO_2 cycles found in literature is scarce and not readily available. The great majority of experimental data are kept confidential by the major producers and research institutes and, in the best cases, they are published partially. Nevertheless, some works are worth to be mentioned, such as those presented by Wright [78] and Dyreby [79, 80] employing data from SANDIA, Clementoni [57] (Bechtel Marine Propulsion Corporation), Avadhanula et al. [81] (Echogen), Gao et al.[82] (KAIST) and Allison et al. [88]. The latter uses experimental data from the 1 MWe-scale sCO_2 test loop at SwRI and discusses a few design/control requirements of the facility; unfortunately, the very recent presentation at ASME Turbo Expo 2019 (only a few weeks before the deposit of this work) has not enabled implementing the results in this thesis. Moreover, Clementoni et al. also presented a study about thermal transients during loop startup observed in the IST experimental facility at Bechtel Marine [84], and Avadhanula et al. provided a transient model using an implicit 1-D Navier Stokes solver [81]. Other interesting works presenting dynamic models have been published by Moisseytsev et al. [83], Mahapatra et al. [85], Zhang et al. [86] and Wright et al. [87]. As said, most of these models are not easily reproducible, since a lot of parameters are kept confidential, or they make overly optimistic assumptions (for instance, the work presented by Muto et al. [256]).

According to the situation depicted in the foregoing discussion, the author of this thesis decided to create a series of in-house models in order to study the most problematic components of the power block, namely compressors and PCHEs, and these are presented in the following sections. Moreover, all the auxiliary information needed to develop a quasi steady-state model of the power block are taken from research elaborated previously at the Thermal Power Group of the University of Seville by other PhD students, as duly acknowledged in the present Chapter.

5.2 Turbomachinery

5.2.1 Compressors

Predicting the off-design performance of a centrifugal compressors is not trivial, in particular if sCO_2 is the working fluid and the rated conditions of the turbomachinery lie in the vicinity of the critical point, as in the *Allam* and *Partial Cooling* cycles. Therefore, a detailed analysis of these equipment falls beyond the scope and aim of the present doctoral work and it would, indeed, constitute a doctoral research on its own. Nevertheless, in order to provide a model capable of predicting the part-load performance of the cycle, which is needed to assess the LCoE of the CSP plants of interest, a somewhat simplified (still physics-based) model of performance of turbomachinery is developed in this chapter, trying to maintain the best possible compromise between computational cost and accuracy of results.

In spite of the large circulating mass flow in the cycles (around 200 kg/s in the *Allam* cycle and up to 260 kg/s if the *Partial Cooling* layout is considered), the corresponding volumetric flows at the inlet to the compressor are fairly small, 0.4 and of 3 m^3/s respectivelys, due to the very high density of sCO_2 in the proximity of the critical point. This flow rates are suitable for centrifugal compressors [257], as confirmed by literature where this type of machinery are the

choice by default for sCO_2 power cycles [172, 79, 80].

In order to model the off-design performance of turbomachinery a series of corrected parameters are chosen as suggested in [258]. These parameters, whose formulation is provided in Eq.(5.1), are the corrected mass flow rate $\dot{m}_{corr}$ (mass flow divided by compressor inlet density ρ_{in} and sound speed a_{in}), corrected rotational speed N_{corr} (shaft speed divided by sound speed at compressor inlet a_{in}) and isentropic enthalpy change ΔH_{corr} (compressor isentropic enthalpy rise divided by sound speed squared a_{in}^2). Finally, pressure ratio PR and total-to-total efficiency (η_{TT}) are also used as figures of merit of performance.

$$\dot{m}_{corr} = \frac{\dot{m}}{\rho_{in} \cdot a_{in}}; \qquad N_{corr} = \frac{N}{a_{in}}; \qquad \Delta H_{corr} = \frac{\Delta H_{is}}{a_{in}^2} \tag{5.1}$$

The performance maps of the compressors modelled in this chapter have been produced with AxSTREAM [259] and they are taken from the work by Del Pozo [260]. These maps have then been integrated by the author of this thesis into the general simulation platform. For a sake of simplicity, the compressors are designed without inlet guide vanes, assuming that these equipment can operate at variable speed in order to accommodate the variable operating conditions in off-design. This operating strategy enables flexibility with acceptable values of η_{TT} and does not preclude other operating strategies from being used in the future. An example of such performance maps is provided in Figure 5.1, while the entire set of results is provided in Section 5.6 and in Annex B.

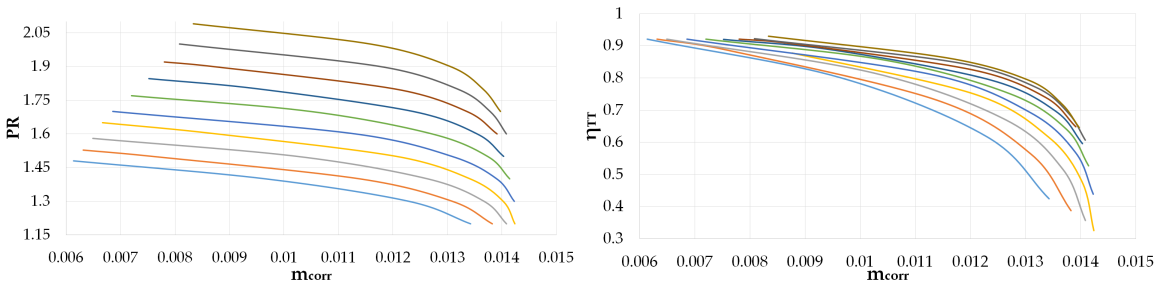

(a) Example of PR-$\dot{m}_{corr}$ performance maps obtained with AxSTREAM.

(b) Example of η_{TT}-$\dot{m}_{corr}$ performance maps obtained with AxSTREAM.

Figure 5.1: Example of compressor performance maps obtained with AxSTREAM. Results correspond to the first compressor in the *Partial Cooling* cycle.

The design and analysis methodology to model the pump in the *Allam* cycle is similar. The only change is that volumetric flow and hydraulic head are used in lieu of corrected mass flow rate $\dot{m}_{corr}$ and Pressure Ratio.

5.2.2 Turbine

The model used to estimate the off-design performance of the turbine is much simpler than that of the compressor. First, regardless of the cycle configuration, the reduced pressure and temperature at turbine inlet suggest that the working fluid behaves as an ideal gas with constant properties (specific heat at constant pressure and isentropic exponent). Then, the

turbine is assumed to operate in sliding pressure mode whereby turbine inlet pressure changes according to the variations in inlet mass flow rate and temperature. Under sliding pressure operation, the polytropic efficiency of the turbine is assumed to remain constant whereas the correlation between turbine inlet pressure, density ($\rho_{in,T}$) and mass flow rate is characterized by Eq.(5.2). In other words, a constant value of the inlet flow factor of the turbine (Ψ) is assumed as suggested by Cotton[261]:

$$\Psi = \frac{\dot{m}_T}{\sqrt{TIP * \rho_{in,T}}} = constant \tag{5.2}$$

5.2.3 Further Assumptions Regarding Partial Load

Once the Turbine inlet pressure is set by means of Eq. 5.2, the thermodynamic state at the other high-pressure stations of the cycle are completely characterized thanks to the off-design model of Printed Circuit Heat Exchangers presented and discussed in the next Section. It is worth noting, therefore, that the pressure drops across heat exchangers are calculated for the specific partial load conditions, not remaining constant at the on-design values.

With respect to the low-pressure section, starting at turbine outlet and ending at the inlet to the first compressor, other assumptions must be made in order to fully characterize the off-design performance. For instance, the minimum cycle pressure varies at partial load, it usually decreases, in particular when the circulating mass flow is reduced for certain operating strategies (*Inventory* or *By-pass*), as shown in Section 5.5. As said, pressure drops in HXs can be easily obtained with in-house codes so it is sufficient to provide an approximation of pressure at turbine outlet (or compressor inlet) in order to fully determine the entire low-pressure line. To this end, the correlations provided in Eqs.(5.3-5.6) are employed, taken from the doctoral dissertation of Muñoz de Escalona [262] and adapted to the *Partial Cooling* and *Allam* cycle layouts respectively (See Fig. 5.2). A first equation intended to calculate the volume of the heat exchangers in the low-pressure section of the power cycle is provided (V_T in Eqs.(5.3,5.5)), using ideal gas equations and disregarding the volume of interconnections. Given that V_T does not depend on off-design conditions and considering two different loads (nominal and a generic partial load), the second correlation provided in Eqs.(5.4,5.6) is finally obtained. The latter of these equations provides the inlet pressure to the compressor at partial load conditions, thus defining the low-pressure section conditions of both configurations and completing the required assumptions to model the part-load performance of the cycles.

$$V_{T,PC} = V_{HTRec} + V_{LTRec} + V_{Cooler1} = \frac{\dot{m}_{10\hookrightarrow 11} \cdot R \cdot \bar{T}_{10\hookrightarrow 11} + \dot{m}_{11\hookrightarrow 12} \cdot R \cdot \bar{T}_{11\hookrightarrow 12} + \dot{m}_{12\hookrightarrow 1} \cdot R \cdot \bar{T}_{12\hookrightarrow 1}}{P_{min}} \tag{5.3}$$

$$P^{off}_{1,PC} = \frac{\dot{m}^{off}_{10\hookrightarrow 11} \cdot (T^{off}_{10} + T^{off}_{11}) + \dot{m}^{off}_{11\hookrightarrow 12} \cdot (T^{off}_{11} + T^{off}_{12}) + \dot{m}^{off}_{12\hookrightarrow 1} \cdot (T^{off}_{12} + T^{off}_{1})}{\dot{m}^{on}_{10\hookrightarrow 11} \cdot (T^{on}_{10} + T^{on}_{11}) + \dot{m}^{on}_{11\hookrightarrow 12} \cdot (T^{on}_{11} + T^{on}_{12}) + \dot{m}^{on}_{12\hookrightarrow 1} \cdot (T^{on}_{12} + T^{on}_{1})} \cdot P^{on}_{1} \tag{5.4}$$

$$V_{T,Al} = V_{LTRec} + V_{Cooler1} = \frac{\dot{m}_{9\hookrightarrow 10} \cdot R \cdot \bar{T}_{9\hookrightarrow 10} + \dot{m}_{10\hookrightarrow 1} \cdot R \cdot \bar{T}_{10\hookrightarrow 1}}{P_{min}} \tag{5.5}$$

$$P_{1,Al}^{off} = \frac{\dot{m}_{10\hookrightarrow 1}^{off} \cdot (T_{10}^{off} + T_{1}^{off}) + \dot{m}_{9\hookrightarrow 10}^{off} \cdot (T_{9}^{off} + T_{10}^{off})}{\dot{m}_{10\hookrightarrow 1}^{on} \cdot (T_{10}^{on} + T_{1}^{on}) + \dot{m}_{9\hookrightarrow 10}^{on} \cdot (T_{9}^{on} + T_{10}^{on})} \cdot P_{1}^{on} \tag{5.6}$$

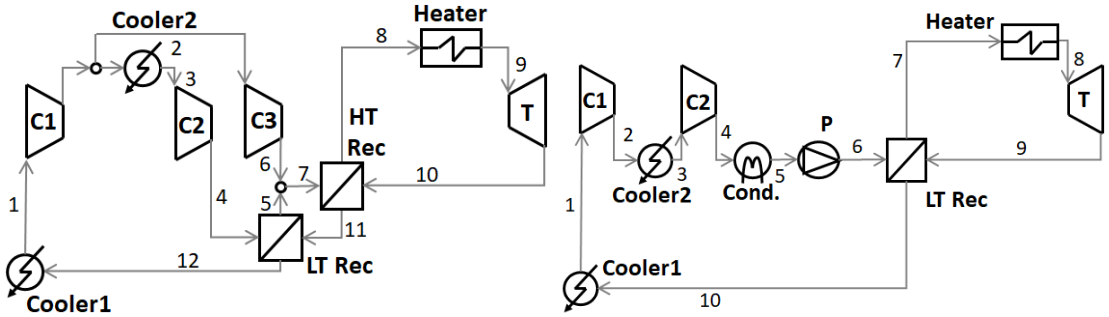

(a) *Partial Cooling* cycle layout.

(b) *Allam* cycle layout.

Figure 5.2: Layouts of the *Partial Cooling* and *Allam* cycles.

5.3 Heat Exchangers: the Conductance Ratio Method

The most common methods to model the performance of heat exchangers are the Log Mean Temperature Difference (ΔT_{lm}) and the effectiveness vs. number of heat transfer units ($\varepsilon - NTU$). They share the same theoretical background to relate the duty of a heat exchanger, $\dot{q}$ in Eq.(5.7), to the actual heat exchanger geometry by way of the overall heat transfer coefficient, or UA term shown in Eq.(5.8) [10]. This UA term is actually the inverse of the total thermal resistance and can be calculated as the simple summation of the individual contributions of the convective resistances of the fluids on each side of the heat exchanger, plus the conductive resistance across the separating wall, Eq.(5.8). Making use of the latter equation and of the Log Mean Temperature difference (ΔT_{lm}), Eq.(5.7) can be reformulated as Eq.(5.9).

$$\dot{q} = \dot{m}_{hot} * (\Delta h_{hot}) = \dot{m}_{cold} * (\Delta h_{cold}) \tag{5.7}$$

$$\frac{1}{UA} = R_{tot} \approx \frac{1}{hA_{hot}} + R_{wall} + \frac{1}{hA_{cold}} \tag{5.8}$$

$$a) \qquad \dot{q} = UA * f(\Delta T) \qquad , \qquad b) \qquad f(\Delta T) = \Delta T_{lm} \tag{5.9}$$

As shown in the foregoing equations, the on-design performance of a heat exchanger is only a function of the overall UA term and not the constituent hA terms. The same overall UA term could potentially be made up from many different combinations of individual hA terms. Each one of these combinations could correspond to a different heat exchanger geometry and therefore have different off-design performance, given that dissimilar geometries will react to the same off-design conditions differently.

Therefore, estimating the off-design performance of a HX turns out fundamental for a coherent cycle analysis in partial load, hence for LCoE assessment. The following approaches to simulate the off-design performance of heat exchangers in power systems are found in literature:

(a) UA is assumed to be constant;
(b) The terminal temperature difference, if applicable, is assumed to be constant;
(c) When the $\varepsilon - NTU$ method is used, the effectiveness, or $\varepsilon - NTU$ correlation $\varepsilon = f(NTU)$, is assumed to be constant;
(d) A detailed geometry of the heat exchanger is drafted which complies with the rated thermo-mechanical specifications of the component. Then, the off-design performance is obtained using one of the afore-cited methods [10];
(e) The UA term is scaled from on-design to off-design conditions using a scaling correlation -for instance, Eq. (5.10)- based on the off-design mass-flow rates of the participating fluids and a correction for the properties of the dominant[1] fluid in the heat transfer process [263, 264].

$$(UA)_{off} = (UA)_{on} * \left(\frac{\dot{m}_{d,off}}{\dot{m}_{d,on}}\right)^{0.65} * \left(\frac{F_{d,off}}{F_{d,on}}\right) * \left(\frac{\dot{m}_{s,off}}{\dot{m}_{s,on}}\right)^{0.15} \tag{5.10}$$

$$F_d = \frac{c_p^{0.33} \cdot k^{0.67}}{\mu^{0.32}} \tag{5.11}$$

The ΔT_{lm} and $\varepsilon - NTU$ methods can be used with all the five categories but neither of them is valid with variable thermodynamic properties. This problem can nevertheless be solved by dividing the heat exchanger in a series of sub-heat exchangers with small enough ΔT's where the properties can be well approximated by their average value [10]. Methods *a)* and *b)* are often used in the preliminary analysis of feed-water heaters in steam power plants but they are not reliable if accurate results are sought, and the same comments apply to method *c)*.

Method *d)* yields better results but it needs the additional effort to design the detailed geometry of the heat exchanger, which implies deciding the type of heat exchanger to use. Also, in most cases, this calculation is done considering thermal performance only whilst the mechanical design ensuring integrity is overlooked. This is a common deficiency to all methods but it becomes more relevant for method *d*) given the additional effort of calculating a detailed geometry whose mechanical performance is uncertain, in particular when supercritical fluids at very high pressures are considered. Another disadvantage of this method is that when the draft geometry is chosen the off-design performance of the heat exchanger is also fixed. This is especially disadvantageous during cycle design and analysis as it is possible that the draft geometry chosen yields sub-optimal off-design performance. Using this method, the cycle designer would not be aware that other potential heat exchanger designs might yield better

[1] It is usual that one of the hA terms yields a much higher thermal resistance, thus having a stronger (dominant) influence on the overall UA than the other (secondary) fluid. Which the dominant fluid is depends on the particular heat exchanger and on the operating conditions.

overall cycle performance.

The last method *e)* is able to capture changes in UA from off-design conditions, though it does not allow for fine grain adjustment of fluid-side dominance in the heat exchanger and thus would not allow the full range of off-design scenarios of a given heat exchanger to be explored. The method suffers from taking into account the properties of the (heat-exchange) dominant fluid only through the $\left(\frac{F_{d,off}}{F_{d,on}}\right)$ term (where d stands for dominant). This assumption could be acceptable for heat exchangers where one side is clearly dominant, for instance if one fluid changes phase, but it is not appropriate otherwise.

In order to overcome the aforedescribed limitations, a novel methodology named *Conductance Ratio Method* has been developed in collaboration with the Southwest Research Institute (USA) and Alfa-Laval (Korea). This methodology, presented at the sCO_2 Symposium 2016 [221] and ASME Turbo Expo 2017 [246], enables the calculation of the off-design performance of a heat exchanger without needing to know its geometry (nor to draft one for the calculations). Also, it is valid for variable thermodynamic properties and it accounts for changes in the operating conditions of the hot and cold fluids independently without requiring one of the fluids to be dominant over the other. As suggested by the name, the method is based on the conductance ratio, Eq.(5.12), where the term $(hA)^*$ defines how the on-design UA term is split into its constituent parts with the assumption that the contribution of the conductive resistance across the heat exchanger walls is negligible.

$$(hA)^* = \frac{hA_{hot}}{hA_{cold}} \tag{5.12}$$

There are two main advantages of this method:

1. Specifying a value of $(hA)^*$ suffices to determine the off-design performance of a heat exchanger, without needing to provide the detailed or even a draft geometry of the heat exchanger.
2. It follows that changing the value of $(hA)^*$ changes the off-design performance of the heat exchanger. This is another interesting features of the method as it enables the comparison of heat exchangers which have the same on-design (rated) performance but different off-design performances.

The *Conductance Ratio* method is comprised of two basic steps performed once the duty of the heat exchanger is known and the HX is divided into a series of divisions with equal enthalpy change. For each division k, the on-design $hA_{hot,k}$ and $hA_{cold,k}$ terms are calculated from the overall UA_k term and the given $(hA)^*$ value. Then, in off-design, the constituent $hA_{hot,k}$ and $hA_{cold,k}$ terms from the on-design analysis are scaled and a new overall $UA_{off,k}$ term for each division is calculated. All of the individual $UA_{off,k}$ terms are then used in an iterative manner to calculate the off-design performance of the heat exchanger. The entire methodology is summarized in the flowchart diagram of Figure 5.3.

5.3.1 On-Design Performance

The on-design performance calculation is initiated by defining the inlet and outlet conditions on both sides of the heat exchanger, the pressure drop on each side of the heat exchanger, the $(hA)^*$ value, and the number of divisions k as shown in Figure 5.3. The number of divisions is

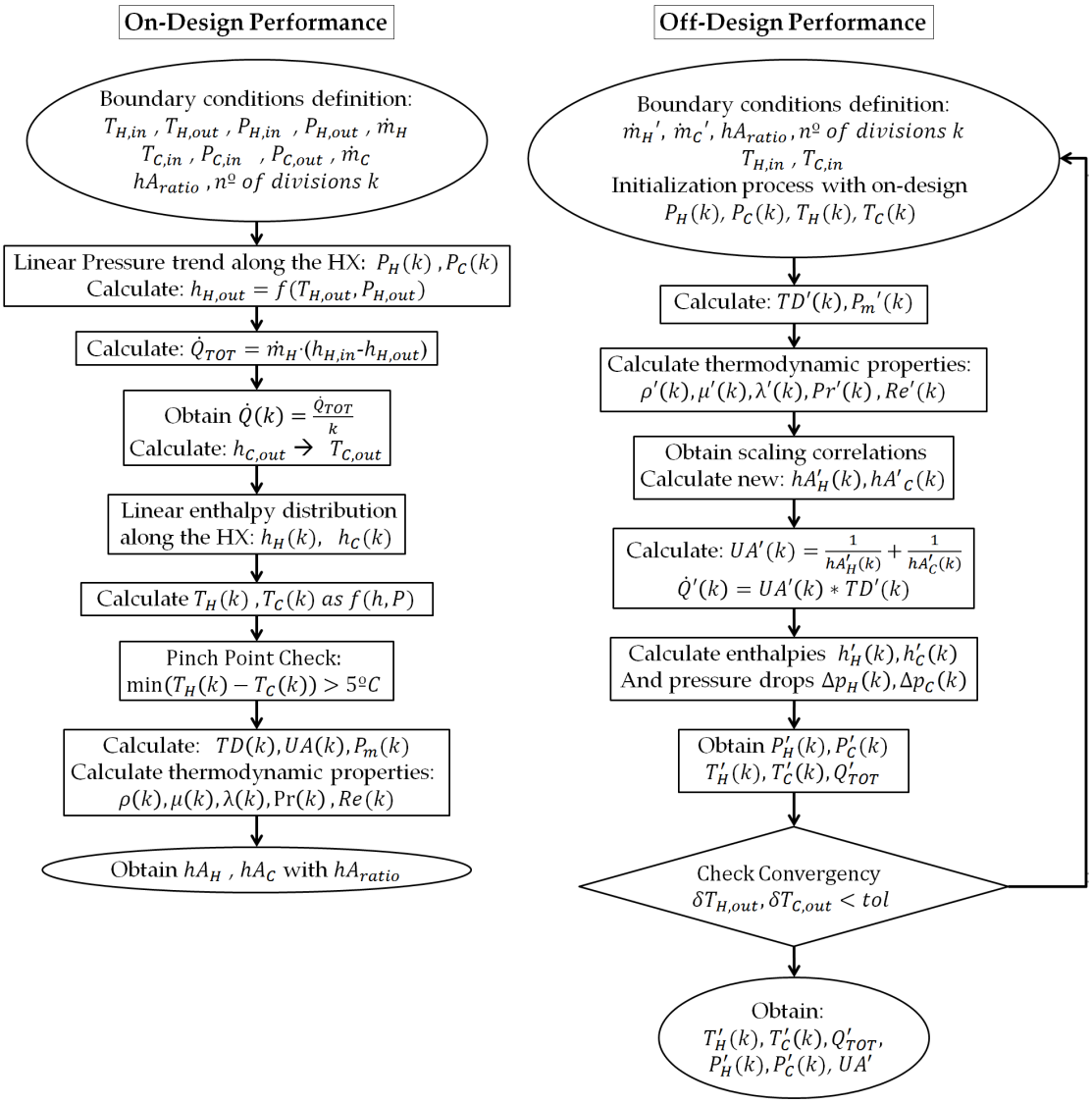

Figure 5.3: Flowchart of the *Conductance Ratio Method*. It is noted that the $(hA)^*$ term is named "hA_{ratio}" on this chart.

arbitrary though one must ensure that the temperature change across each division is small enough for the constant properties assumption to be reasonable [10].

Assuming that enthalpy and pressure change linearly along the heat exchanger allows the temperature distributions on both sides of the heat exchanger to be calculated. From these, the UA_k terms are calculated with Eq.(5.9). With the calculated UA_k, the last step is to calculate the on-design values of $hA_{hot,k}$ and $hA_{cold,k}$ using Eqs.(5.12) and (5.8) and assuming negligible wall resistance.

5.3.2 Off-Design Performance

Analyzing the off-design performance of the heat exchanger requires a new set of boundary conditions and a different iterative methodology. This is shown in Figure 5.3 where the terms with superscript " $'$ " are those differing from the on-design analysis. When off-design operation corresponds to a different mass flow rate on at least one side of the heat exchanger, the computation is initialized with the on-design pressure and temperature distributions but different mass flow on one or both sides of the heat exchanger. When off-design is due to a new inlet temperature to either side of the unit, a similar approach is employed. Starting with the on-design temperature and pressure distribution, the thermodynamic properties are obtained along with a new TD term in each division. With these, the scaling correlations defined in Eqs.(5.13-5.14) are applied to the division hA terms to reflect the change in operating conditions. Note that Eq.(5.14) is actually an evolution of Eq.(5.13), obtained through a simplification of the Reynolds term with the assumption of constant length scale.

$$hA_{off} = hA_{on} * \left[\frac{\lambda_{off}}{\lambda_{on}}\right] * \left[\frac{Re_{off}}{Re_{on}}\right]^{x} * \left[\frac{Pr_{off}}{Pr_{on}}\right]^{y} \tag{5.13}$$

$$hA_{off} = hA_{on} * \left[\frac{\lambda_{off}}{\lambda_{on}}\right] * \left[\frac{\dot{m}_{off}/\mu_{off}}{\dot{m}_{on}/\mu_{on}}\right]^{x} * \left[\frac{Pr_{off}}{Pr_{on}}\right]^{y} \tag{5.14}$$

The values x and y in Eqs.(5.13-5.14) can be defined for the hot and cold sides separately, thus adapting to the many correlations for Nusselt number available in literature; for instance, unless otherwise noted, the exponents in this paper have been set to those used by the Dittus-Boelter correlation to calculate the Nusselt number of turbulent flow in a circular pipe [10]. The new hA terms are calculated separately for the hot and cold sides, yielding new estimates of UA_k and $\dot{Q}_k$ when combined with the off-design value of the division TD.

With this updated division duty, the downstream enthalpy of both the hot and cold sides can be computed. The pressure drops of the new mass flows are obtained using the scaling correlation defined in Eq.(5.15), which yields the downstream pressure distribution.

$$\Delta P_{off} = \Delta P_{on} * \frac{\dot{m}^2_{off}/\rho_{off}}{\dot{m}^2_{on}/\rho_{on}} \tag{5.15}$$

Local temperatures in each subdivision are finally computed from the distribution of pressure and enthalpy. At this point, the first iteration is complete and another one begins with the updated downstream pressures and temperatures. The iterative process terminates once the changes in the outlet temperatures between subsequent iterations fall below a certain tolerance.

5.3.3 Method Validation

In order to validate the *Conductance Ratio Method*, it was compared against three different sets of heat exchanger off-design data: i) experimental data from an sCO_2/water heat exchanger tested by Bechtel Marine Propulsion Corporation (BMPC), ii) experimental data from Alfa-Laval for a nitrogen-nitrogen heat exchanger and iii) model data from Alfa Laval for sCO_2/water and sCO_2/sCO_2 heat exchangers. In the following section, only the results obtained from the comparison with the model data from Alfa-Laval are provided, in order to increase the readability of the chapter. Nevertheless, the verification against the experimental data are given in all detail in another work by the author [246].

Alfa-Laval Model Data - sCO_2/water

The model used by Alfa-Laval is regularly used to design and rate heat exchangers and as such contains the physical dimensions of the heat exchanger being modeled. The design operating conditions of this heat exchanger are shown in Table 5.1.

	Hot	Cold
Fluid	sCO2	Water
Inlet Temperature [°C]	170	20
Inlet Pressure [bara]	100	15
Pressure Drop [kPa]	96	89
Outlet Temperature [°C]	50	60
mass flow [kg/hr]	250,000	317,944

Table 5.1: Data provided by Alfa-Laval for a sCO_2-water cooler.

The off-design performance of this heat exchanger was calculated using the Alfa-Laval model at various different mass flow rates on either side of the exchanger. Two sets of data were created. In the first set, the sCO_2 mass flow rate was held constant and the water mass flow rate was varied from 100% to 60% of the design value. In the second set, the water mass flow rate was held constant and the sCO_2 mass flow rate was varied from 100% to 60% of the design value. The model results along with the results from the *Conductance Ratio Method* are shown in Figure 5.4(a). For these data, an $(hA)^*$ of 1/9 was used as it provided the best match to the data provided by Alfa-Laval.

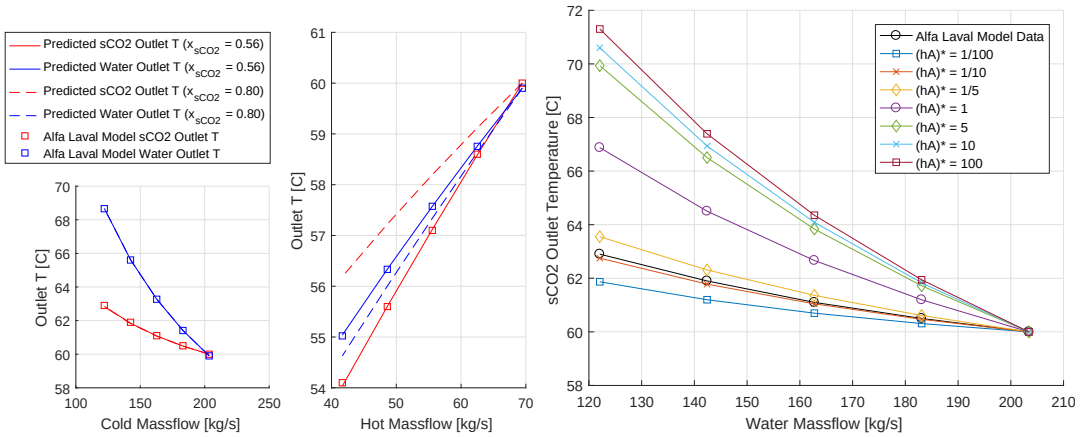

(a) Comparison between the outlet temperatures predicted by the *Conductance Ratio Method* and the data provided by Alfa-Laval at different sCO_2 and water mass flow rates. For these data, $(hA)^*$ was set to 1/9.

(b) Comparison between the outlet sCO_2 temperatures predicted bythe *Conductance Ratio Method* and the data provided by Alfa-Laval at different water mass flow rates.

Figure 5.4: Verification of the *Conductance Ratio Method* against data provided by Alfa-Laval for a sCO_2/water heat exchanger.

As shown in Figure 5.4, the *Re* scaling parameter, x in Eq.(5.13), for the sCO_2 side of the heat exchanger must be set to 0.56 in order to match the Alfa-Laval data consistently across the

entire operating range since a single $(hA)^*$ value providing a good match for both the sCO_2 and water mass flow variation cases is not found. It is nevertheless interesting that this change in *Re* scaling parameter does not affect the results in the water mass flow variation cases. This is because, in these cases, the mass flow on the sCO_2 side of the heat exchanger does not vary and thus the associated *Re* remains nearly constant, hence unaffected by a change in scaling parameter. The need for this adjustment comes from the specific sCO_2 side geometry used in the Alfa-Laval model which stems from the PCHE architecture used.

Figure 5.4(b) shows the effect of $(hA)^*$ on the outlet temperature of sCO_2 predicted by the *Conductance Ratio Method* at different values of $(hA)^*$ and as a function of water mass flow rate. This is also shown for the lowest water mass flow rate case in Figure 5.5(a) and the predicted duty for this case is shown in Figure 5.5(b). While only one single value of $(hA)^*$ match the results provided by Alfa-Laval, these results prove that heat exchangers having the same rated performance can lead to largely different off-design behaviors depending on the value of $(hA)^*$. This stresses the importance of geometry on heat exchanger performance across the entire operating range.

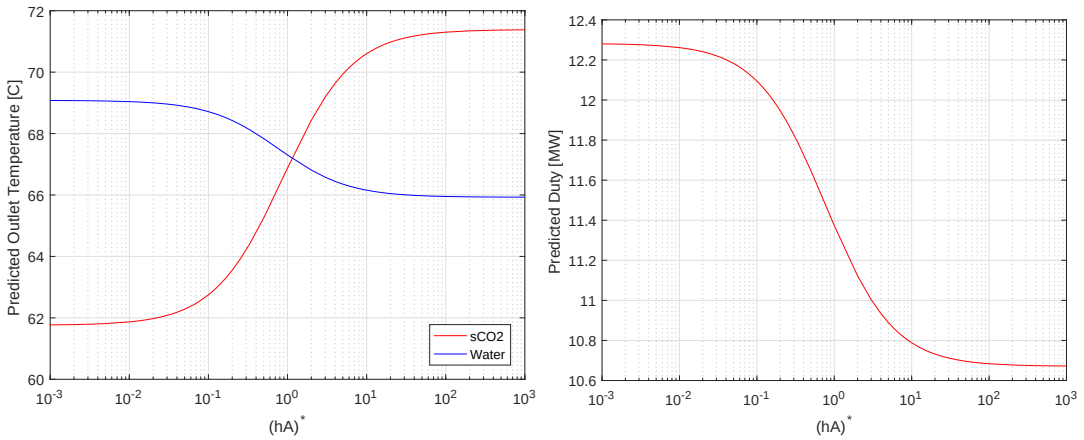

(a) Outlet temperature of sCO_2 predicted by the *Conductance Ratio Method* as a function of $(hA)^*$. Results are for the lowest sCO_2 mass flow rate case.

(b) Overall heat exchanger duty predicted by the *Conductance Ratio Method* as a function of $(hA)^*$ and for the lowest sCO_2 mass flow rate.

Figure 5.5: Performance predicted by the *Conductance Ratio Method* for the Alfa-Laval and BMPC sCO2/water coolers.

A comparison between the Alfa-Laval model data and the experimental data from BMPC, presented in [246], provides additional information about the *Conductance Ratio Method*. Both of these data-sets correspond to sCO_2 coolers using water on the cold side, but whilst the BMPC's HX is of the shell and tube type, Alfa-Laval's equipment is a PCHE. This different architecture brings about a very large difference in off-design performance; thus, whereas both heat exchangers exhibit the same outlet temperature variation pattern in response to changes in $(hA)^*$, the BMPC heat exchanger is best modeled with an $(hA)^*$ of 8 while the Alfa-Laval heat exchanger is best modeled with an $(hA)^*$ of 1/9.

This large range of $(hA)^*$ encompasses almost all of the performance variations due to $(hA)^*$ in both data-sets. This suggests that, even for the same application, a wide range of potential

values of $(hA)^*$ is possible by taking into account different heat exchanger architectures only. It should also be noted that neither of these heat exchangers were designed with a specific $(hA)^*$ in mind. Therefore, future research is needed to quantify the range of reasonable values of $(hA)^*$ for different heat exchanger types and applications as well as strategies for controlling $(hA)^*$ when designing a heat exchanger in order to achieve the best performance across the entire operating range.

Alfa-Laval Model Data - sCO_2/sCO_2

As a further comparison, an additional validation of the *Conductance Ratio Method* against data provided by Alfa-Laval of a sCO_2-to-sCO_2 heat exchanger is performed. The design operating conditions of this heat exchanger are shown in Table 5.2.

	Hot	Cold
Fluid	sCO2	sCO2
Inlet Temperature [C]	170	70
Inlet Pressure [bara]	96	200
Pressure Drop [bara]	1	1
Outlet Temperature [C]	80	150.47
mass flow [kg/hr]	273600	191520

Table 5.2: On-design operation conditions from Alfa Laval.

For off-design operation, this heat exchanger was modeled at different mass flow rates, hot inlet temperatures and cold inlet temperatures. These results along with the estimates of the *Conductance Ratio Method* are shown in Figure 5.6 exhibiting a very good match. Unfortunately, even though the off-design conditions included mass flow variations, since the heat exchanger being modeled is a recuperator, the variation was the same on both sides of the heat exchanger. Due to this, the results were not very sensitive to $(hA)^*$.

5.4 Acceleration of off-design performance calculation: Active Subspaces Methodology

Another important factor to take into account when predicting the off-design performance of heat exchangers is the computational time that is needed to perform these calculations, due to the complexity and iterative nature of the corresponding models. In fact, considering the *Partial Cooling* configuration, five nested iteration loops are needed to control the fundamental parameters of the cycle in order to assess the off-design conditions at a specific load (turbine inlet and outlet pressures, inlet temperatures to the LT and HT recuperators and split flow factor), plus two additional loops to control the inlet temperatures to compressors C1 and C2, see Figure 5.9 later. With respect to the *Allam* cycle, only three nested cycles are need, due to the presence of just one recuperator and the lack of split fraction valve, plus three additional loops to control the inlet temperatures to compressors and pump. This procedure, as said, must be repeated for each partial load of interest, what increases the computational cost of the code exponentially. It seems therefore evident that optimizing the off-design prediction model results to be fundamental in order to to limit the calculation time to reasonable values.

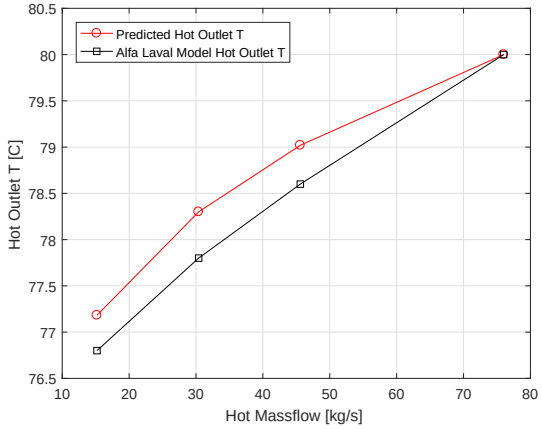

(a) Hot side outlet temperatures for different mass flow rates.

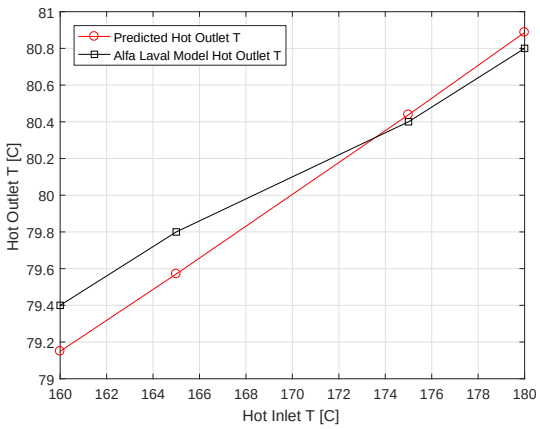

(b) Hot side outlet temperatures for different hot inlet temperatures.

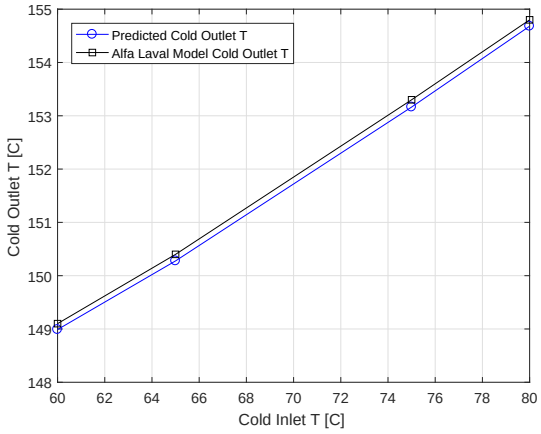

(c) Cold side outlet temperatures for different cold inlet temperatures.

Figure 5.6: Verification of the *Conductance Ratio Method* against model data provided by Alfa-Laval for a sCO_2/sCO_2 heat exchanger, considering hot side outlet temperatures against hot side mass flow or inlet temperature and cold side outlet temperature against inlet temperature.

If the part-load performance of turbomachinery is quite easy and fast to predict thanks to the creation of dedicated performance maps, the same cannot be said for heat exchangers. For this reason, a deeper discussion about their off-design models is worth.

Figure 5.7 presents the overall structure of the HX performance model for both on-design and off-design conditions. This is complemented by Table 5.3 showing a comparison between the results obtained with the PCHE design code and the *Conductance Ration Method* for on-design conditions. For the comparison, the *(hA)** values have been set those provided by the PCHE design code, which are consistent with the results shown in [246]. The large potential of the *Conductance Ratio Method* becomes evident as it is capable of obtaining results within a very small deviation from the complete PCHE design code (always smaller than 0.15%) but in a significantly faster way, saving between 80 and 97% of the calculation time.

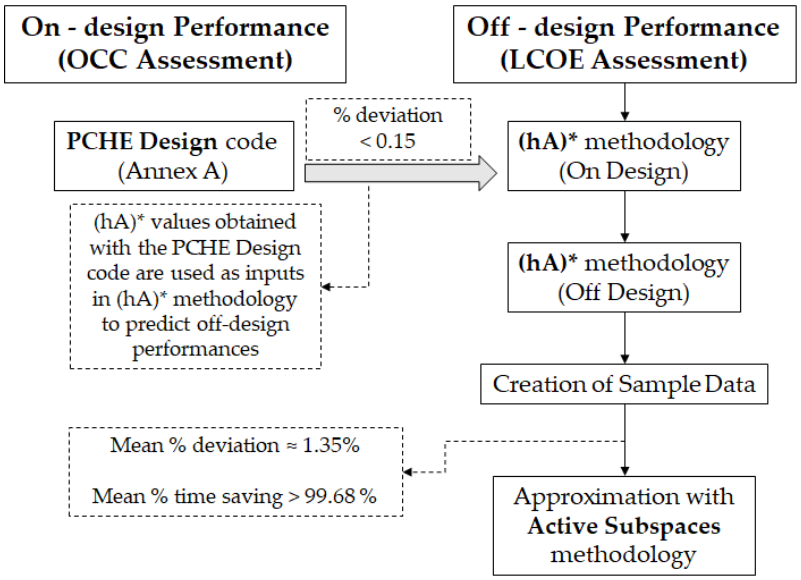

Figure 5.7: Overall Structure of the PCHE performance model, for both on and off-design conditions. Percentages refer to the values provided in Tables 5.3 and 5.4.

HX	T_{PCHE} [°C]	T_{CRM} [°C]	T PD [%]	Time$_{PCHE}$ [s]	Time$_{CRM}$ [s]	Time PD [%]	(hA)*
	Partial Cooling cycle						
Cooler 1	300.07	299.96	0.0356	7.3761	1.0611	85.614	0.1861
Cooler 2	300.00	299.96	0.0120	17.608	0.9951	94.349	0.2305
LT Rec	462.70	461.98	0.1554	0.9125	0.1916	79.005	0.8854
HT Rec	728.01	727.79	0.0294	1.7369	0.1869	89.237	0.8906
Heater	1023.2	1023.1	0.0098	5.5913	0.1513	97.295	1.2991
	Allam cycle						
Cooler 1	300.002	299.961	0.0137	7.1185	1.0346	85.466	0.1693
Cooler 2	300.095	299.961	0.0448	6.3894	1.0116	84.167	0,2169
Cooler 3	300.002	299.961	0.0137	24.317	1.0977	95.486	0.3133
LT Rec	584.522	584.178	0.0589	1.3994	0.2913	79.185	0.7472
Heater	1023.20	1023.10	0.0098	2.5516	0.1745	93.163	1.2947

Table 5.3: Comparison between the results obtained with the PCHE design code and the *Conductance Ratio Method* for both cycles. Percentage deviations on the cold side outlet temperature and calculation time are taken as figures of merit.

Nevertheless, the *Conductance Ratio Method* is still computationally burdensome when calculating off-design performance due to the large number of nested loops required, in particular those controlling compressor inlet temperature. For this reason, the author decided to apply the *Active Subspaces* (AS) methodology to the results obtained with the *Conductance Ratio Method* in order to explore significant computational time reductions. The former is a purely algebraical methodology capable of producing reduced-order models identifying fundamental directions (active variables driving the solution) in the parameter space of a given model's input data, previously collected in a matrix, through a combination of the eigenvalues and eigenvectors of the latter. This matrix is composed by an mxn submatrix and a q vector

(object function), where m stands for the total number of cases considered (similar to a set of different boundary conditions) and n is the number of independent variables describing the problem considered. The overall matrix is the actual input to *Active Subspaces* method which finally provides a reduced-order approximation of all the sample data input, which is a correlation dependent on two or more *active variables*. The latter variables are obtained as a combination of the eigenvalues of the input matrix, in the fundamental directions indicated by the eigenvectors. A complete explanation of this methodology is provided in the originally work of Constantine [265], and it has been already presented in sCO_2 literature by Bahamonde et al. for an optimal mean-line design code of unconventional turbomachinery [266]. As a matter of fact, the author of this thesis would like to acknowledge Dr. Bahamonde for kindly introducing him to the *Active Subspaces* methodology whilst in a short visiting research stay at TU Delft (The Netherlands).

In the present study of PCHEs, the independent variables are inlet temperatures and pressures and mass flow rates of both fluids while the objective function is the heat duty. A flow chart of this method is provided in Figure 5.8.

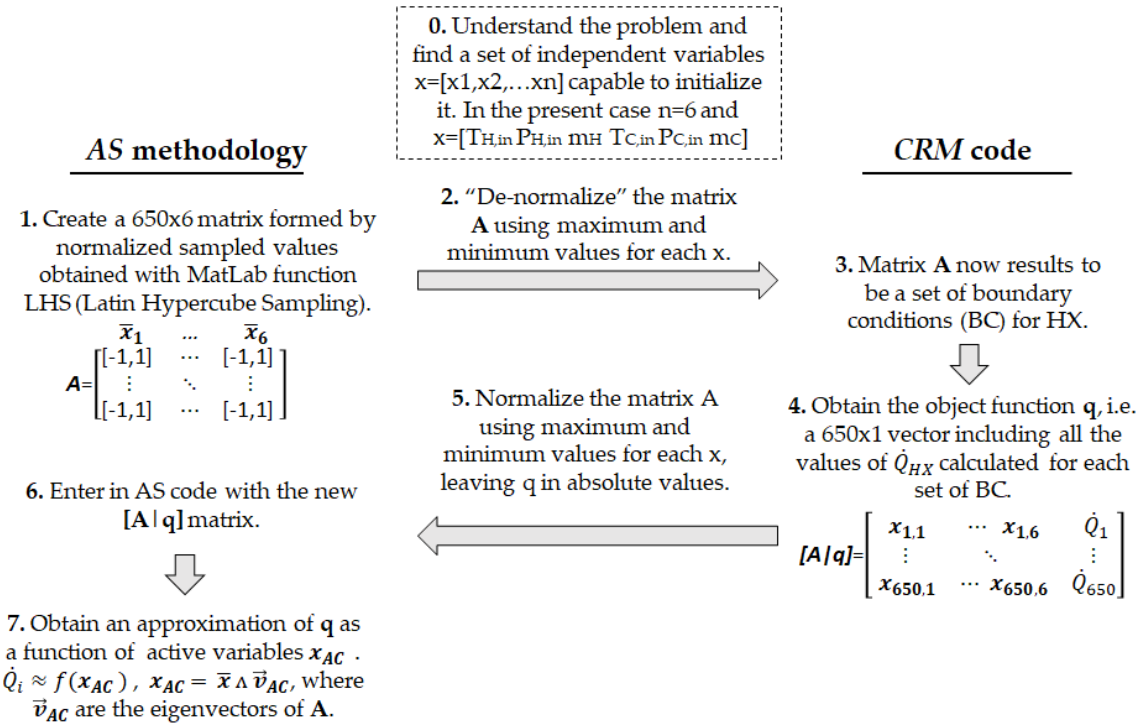

Figure 5.8: Flowchart of the *Active Subspaces* methodology employed to approximate the *Conductance Ratio Method* for the off-design performance prediction of heat exchangers.

A sampled and normalized 650x6 matrix is obtained with the MatLab Latin hypercube sampling function, containing only numbers between -1 and 1; such values are then transformed to absolute values and this requires that minimum and maximum values of all six input parameters are defined and that the corresponding heat duties are calculated with the standard *Conductance Ratio Method*. These absolute values are then normalized and centered (i.e., expressed in the range [-1,1]), creating the object function vector and completing the input

for the *Active Subspaces* methodology. Table 5.4 provides a comparison between using the *Conductance Ratio Method* only and using the *Active Subspaces* methodology, considering the first iteration at 99% load. For heaters and recuperators, the time reported corresponds to a single calculation, whereas for the coolers the time to solve the entire iterative loop is indicated.

HX	$\dot{Q}_{CRM}$ [ºC]	$\dot{Q}_{AS}$ [ºC]	$\Delta\dot{Q}$ [%]	Time$_{CRM}$ [s]	Time$_{AS}$ [s]	ΔTime [%]
	Partial Cooling cycle					
Cooler 1	17.955	18.252	1.653	141.433	5.875e-3	99.996
Cooler 2	30.936	31.039	0.335	902.627	0.0942	99.989
LT Rec	35.436	36.032	1.682	45.994	6.1e-4	99.999
HT	92.321	91.0724	1.353	49.499	6.71e-4	99.999
Heater	99.129	98.0612	1.078	45.689	7.23e-4	99.998
	Allam cycle					
Cooler 1	15.646	15.429	1.390	38.079	0.120	99.684
Cooler 2	11.228	11.113	1.028	50.643	0.184	99.636
Cooler 3	35.514	34.891	1.755	75.929	2.661	96.495
LT Rec	77.496	76.194	1.680	23.827	6.01e-4	99.997
Heater	112.79	111.55	1.1028	24.013	6.46e-4	99.997

Table 5.4: Comparison between the *Conductance Ratio Method* and the *Active Subspaces* methodology for both cycles. Percentage deviations in heat duty and calculation time are taken as figures of merit.

It is evident that the *Active Subspaces* methodology enables a drastic reduction in the computational cost of the code. Calculation times differ by more than four orders of magnitude, with an acceptable percentage deviation of around 1%. Moreover, this becomes even more impressive if a complete global iteration is considered, Table 5.5. For instance, considering the 97.5% load case for the *Allam* cycle, the code based on the *Conductance Ratio Method* completes the calculation in 56945 seconds (almost 16 hours) whereas it takes only 11.38 seconds if the *Active Subspaces* methodology is used. Therefore, the latter is capable of enabling a 99.98% reduction in computational cost, with a percentage deviation in terms of η_{th} of only 0.37%.

Cycle	$\eta_{th,CRM}$ [%]	$\eta_{th,AS}$ [%]	$\Delta\eta_{th}$ [%]	Time$_{CRM}$ [s]	Time$_{AS}$ [s]	ΔTime [%]
Allam	50.94	50.68	0.515	41302	21.56	99.95
Partial Cooling	45.06	44.89	0.369	56945	11.38	99.98

Table 5.5: Comparison between the *Conductance Ratio Method* and the *Active Subspaces* methodology for both cycles at 97.5% load. Percentage deviations in thermal efficiency and calculation time are taken as figures of merit.

5.5 Partial Load Control Strategies

Even if only a few studies of load control of sCO_2 power cycles have been published in literature, it is widely accepted that these systems can be considered similar to closed-cycle gas turbine

in as far as control strategies are concerned [83]. For this reason, three different strategies are considered in this work:

- **Inventory**: this strategy is based on the variation of the circulating mass flow in the power cycle. Load is reduced by bleeding sCO_2 off the high-pressure section of the cycle. This fluid is sent to storage in high-pressure tanks and, when the load must be increased, it is re-injected back into the low-pressure section of the cycle. This layout reduces the pumping power needed to manage the control system.
- **By-pass**: this strategy is based on reducing the mass flow rate through the turbine, hence reducing the power produced, but not in the remaining components of the cycle. Typically, sCO_2 is directed from the compressor or recuperator outlet to the recuperator or cooler inlet, thus bypassing the heater and turbine.
- **Temperature**: in this strategy, the mass flow rate of sCO_2 is kept constant while the turbine inlet temperature decrease as the heat input to the cycle is reduced.

These strategies bring about largely different effects on power cycle performance, and they are characterized by different operational ranges. Usually, the *inventory* strategy achieves very good thermal performance (small reduction of η_{th}) but narrow operational range, limited by the cost of the corresponding tank (whose size increases dramatically if large maneuverability is sought). Using the turbine *by-pass* brings about a penalty on thermal efficiency, even when operating close to the design point, but exhibits a fairly wide range of operation. Finally, the strategy based on variable operating *temperature* shows the worst performance.

Regarding the response time of the power block, *by-pass* is the fastest and most agile strategy, followed by turbine inlet *temperature* control. On the other hand, *inventory* control is very slow and exhibits a high inertia. Nevertheless, it is noted that this work does not look into the dynamics of plant control and hence these features are provided here from a qualitative standpoint only.

Figure 5.9 provides a graphical representation of the *Allam* and *Partial Cooling* cycle layouts and of the additional elements needed to implement the control strategies introduced before.

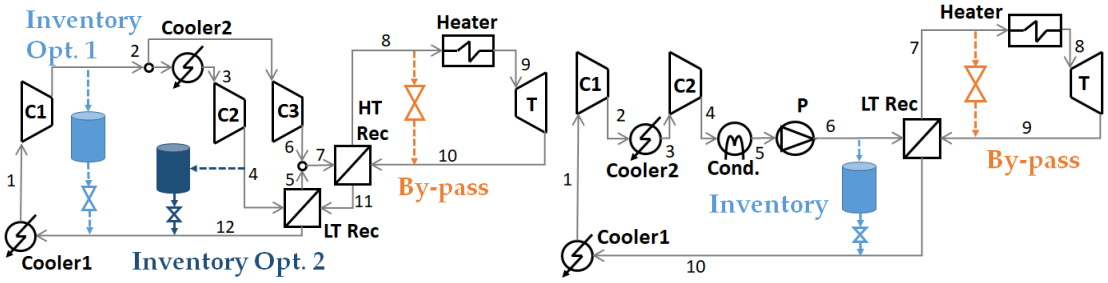

(a) *Partial Cooling.* (b) *Allam.*

Figure 5.9: Graphical representation of cycle layouts and the additional elements needed to implement the control strategies considered.

In the *Allam* cycle, the *Inventory* tank is located between the pump outlet (point 6) and the recuperator outlet (point 9), whereas two different options are considered in the *Partial*

Cooling layout, Figure 5.10. On the one hand, the tank could be situated between the outlet from the first compressor (point 2) and the outlet from the LT recuperator (point 12). Such layout would require a larger and more expensive tank since the pressure level is limited to 9 MPa and therefore the density of the sCO_2 is significantly lower. This is shown in Figure 5.10 where the density values of option 1 are four times lower than those of option 2 (or *Allam* case), with a four times larger bled volumetric flow. On the other hand, the tank could also be located between the outlet from the second compressor (point 4) and the outlet from the LT recuperator (point 12). This option would enable a smaller and cheaper inventory system, but it would probably lead to a longer cycle response time. In fact, the tank would be situated downstream of the flow-split valve, hence reducing a portion of the total sCO_2 stream only. The possibility to connect the cold side outlet of the LT recuperator with hot side inlet (point 7 to 11) is not considered due to the low density which would inevitably increase the size and cost of the inventory system.

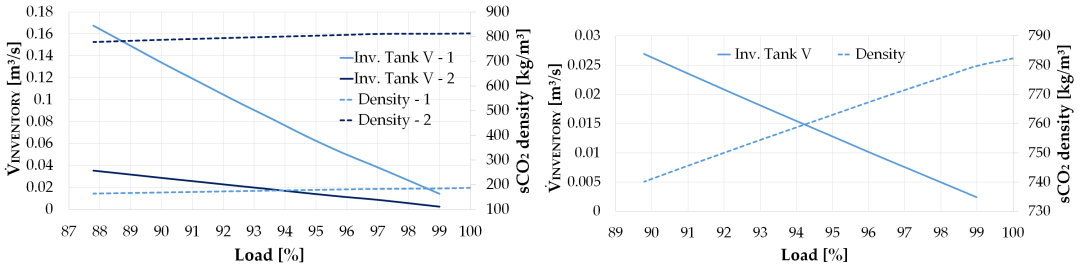

(a) *Partial Cooling.* (b) *Allam.*

Figure 5.10: Volumetric flow and density of the sCO_2 stream extracted (bled) from the cycle when *Inventory* control is employed. Bleeding point is shown in Figure 5.9.

Reducing the circulating mass flow rate in the cycle leads to lower minimum cycle pressures according to Eqs.(5.4,5.6), while the maximum pressure of the cycle and the mass flow rate are linked by Eq.(5.2). This also reduces the outlet pressure from the turbine, which has negative effect on the low-pressure section, limiting the operational range enabled by this control strategy. This is thoroughly described in the next sections of the chapter.

Regarding the *by-pass* strategy, the *by-pass* valve has been located between the inlet to the heater (point 7 for *Allam* cycle and 8 for *Partial Cooling* cycle) and the outlet from the turbine (point 9 and 10 respectively). With this layout, the mass flow circulating across the low-pressure side of the recuperator remains constant and the pressure drops incurred when adopting *inventory* control are significantly reduced, Eqs.(5.4,5.6). This enables a much wider operational range for both cycles, which can easily reduce turn-down (minimum stable load) to 50%., for which load the reduced mass flow circulating through the heater and turbine is obtained with Eq.(5.2). It is worth noting that, although this strategy enables a wide operational range, the *Allam* cycle is able to operate at loads lower than 60% only if the inlet temperature to the pump is increased by 2°C so as to avoid numerical problems due to the close vicinity of the critical point. Similar issues have already been discussed in literature by Wright et al. regarding the operation of the sCO_2 test loop at SANDIA [78], and by Carstens in his doctoral thesis where the control strategy of a *Recompression* cycle is analyzed [77]. In the latter work, Carstens concludes that compressor inlet temperature must be increased to 34°C in order to enable operation at intermediate to low loads, and defines the best control strategy based on

this temperature rise. Nevertheless, in this work, it has been decided to avoid this temperature rise in order to prevent the detrimental effect on the thermal efficiency of the cycle. Instead, other existing solutions allowing to maintain the operating conditions at compressor inlet temperature close to the rated value have been considered. Such is the case of the concept formulated in the Scarabeus project, which is currently under development in Europe by a consortium participated by the University of Seville. In this project, novel sCO_2 blends are used to enable low compressibility at high temperatures, thus retaining the supercritical-like features of the working fluid at the inlet to the compression station [48].

The *Temperature* control strategy is based on modifying turbine inlet temperature while the circulation mass flow rate of sCO_2 in the cycle is kept constant. The maximum cycle pressure is once again obtained with Eq.(5.2), which also allows to calculate the resulting TIT. In the iterative loop, in fact, turbine inlet density is directly related to TIP and TIT is therefore calculated as a combination of the two with the *CoolProp* library. This strategy leads to a quick reduction of thermal efficiency and its operational range is normally narrower than when using *By-pass* control.

With regard to the *Partial Cooling* cycle, it is worth highlighting another assumption made to predict off-design performance. In the previous chapters, the split-fraction factor α has been optimized to maximize cycle efficiency η_{th} at different pressures or temperatures. Nevertheless, in those cases, the mass flow circulating through the installation was similarly adapted to match the new cycle requirements. On the contrary, considering the control strategies mentioned above, only *Inventory* is based on a proportional reduction of mass flow whereas the other two schemes keep this at the rated value (note that the *by-pass* scheme modifies the mass flow circulating through the heater and turbine only and hence it does not affect the split-fraction). In this work, partial load conditions based on α modifications were tried for the three strategies, but this produced satisfactory results for *Inventory* control only. *By-pass* and *Temperature* schemes, in fact, presented extremely narrow operational range, limited by the abnormal behavior of the compressors. On the contrary, when keeping α constant at the rated (design) value), these two control schemes strategies enabled a wider operating range with acceptable part-load efficiency. This is just the opposite behavior to that observed for the *Inventory* scheme, for which the cycle was not able to operate with a constant α.

Therefore, the results provided in the next section are obtained for a constant α for the *by-pass* and *temperature* control strategies whereas this parameter takes different values depending on temperature and pressure for *Inventory*.

5.6 Effects of the control strategies on cycle and turbomachinery performances

In order to compare the results obtained for the different control strategies, a series of figures of merit are taken into account. Regarding thermal performance, 1^{st} Law efficiency, turbine inlet temperature, sCO_2 mass flow rate, turbomachinery inlet pressure and power output are chosen. For the analysis of turbomachinery, the three corrected parameters discussed in Section 5.2.1 are considered along with the pressure ratio and total-to-total efficiency.

In order to facilitate the comparison between control strategies, the results are provided in relative terms with respect to the rated (design) conditions. Absolute values are presented later in Section 5.7 for the best control strategy, which happens to be a combination between *Inventory* and *By-pass*.

5.6.1 Partial load analysis of the *Partial Cooling* cycle

Figures 5.11 to 5.13 show the trends of the aforementioned relative parameters against percentage load. A clear difference in the operational range of the three control strategies is visible. The *Partial Cooling* cycle is able to operate down to 86% load using *Inventory* control and maintaining the rated compressor inlet temperature. Lower loads would also be possible, but this would require higher compressor inlet temperatures that would drastically reduce cycle efficiency; for this reason, operating the cycle with lower loads based on this control scheme has not been considered . *By-pass* control is by far the most flexible option, ensuring 50% turn-downs, followed by *Temperature* control which operates stably down to 55% load.

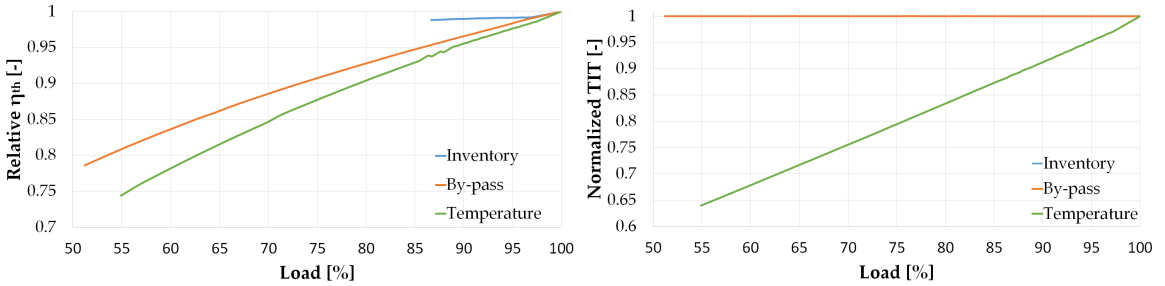

(a) Relative thermal efficiency of the *Partial Cooling* cycle at partial load.

(b) Relative turbine inlet temperature (*TIT*) of the *Partial Cooling* cycle at partial load. Lines corresponding to *Inventory* and *Bypass* merge on a single line.

Figure 5.11: Partial load performance of the *Partial Cooling* cycle (part 1). The three different control strategies are considered.

The narrower operating range of *Inventory* is due to the significant drop in cycle minimum pressure caused by the mass flow reduction that is typical of this strategy. This is confirmed by Figures 5.12(a), where sCO_2 mass flow rate experiences a 12% reduction, and 5.12(b), where the compressor inlet pressure exhibits a similar trend. On the contrary, it is worth noting that *Temperature* control leads to exactly the same compressor inlet pressure percentage reduction at 55% load, while the *By-pass* scheme shows an almost horizontal trend of this parameter; this is due to the constant mass flow rate in the low pressure side of the recuperators, as shown by the orange dotted line in Figure 5.12(a)(see also Eq.(5.4)).
As expected, the *Inventory* scheme provides very good performance at partial load, close to the rated values, while the other two strategies bring about a significant performance decay. *Temperature* control, in particular, presents a 7% drop of η_{th} at 85% load, 2% lower than the *By-pass* and 6% than *Inventory*. Regarding turbine inlet temperature, controlling *temperature* obviously leads to a significant reduction in this parameter, Figure 5.11(b), and this is the main reason why η_{th} drops significantly.
Trends of turbine and compressor power are provided in Figures 5.13. The results when using *Inventory* and *By-pass* control are very similar. This is because both strategies bring

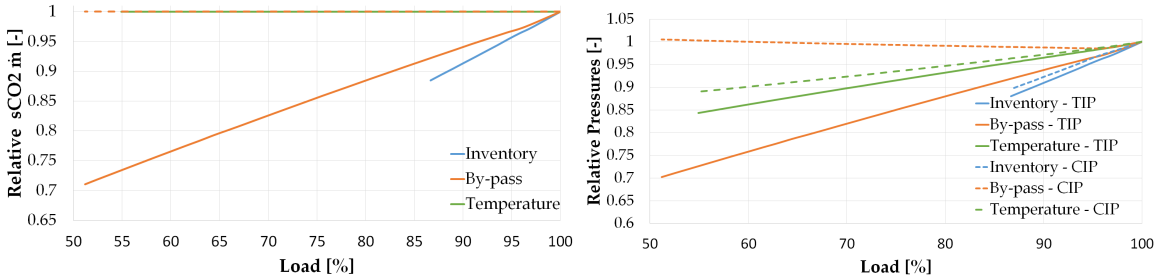

(a) Relative sCO_2 mass flow rate of the *Partial Cooling* cycle at partial load.

(b) Relative pressure of the *Partial Cooling* cycle at partial load.

Figure 5.12: Partial load performance of the *Partial Cooling* cycle (part 2). The three different control strategies are considered.

about a similar reduction in the mass flow circulating through the turbine and minimum cycle pressure. This results in a lower power consumption of the compression process, given that the compressors are progressively shifting towards the condensation dome. Regarding *Temperature* control, the lower slope in Figure 5.13(a) is due to the fact that the constant mass flow partly compensates for the significant drop in turbine inlet temperature, whereas only very small variations in compression power are observed.

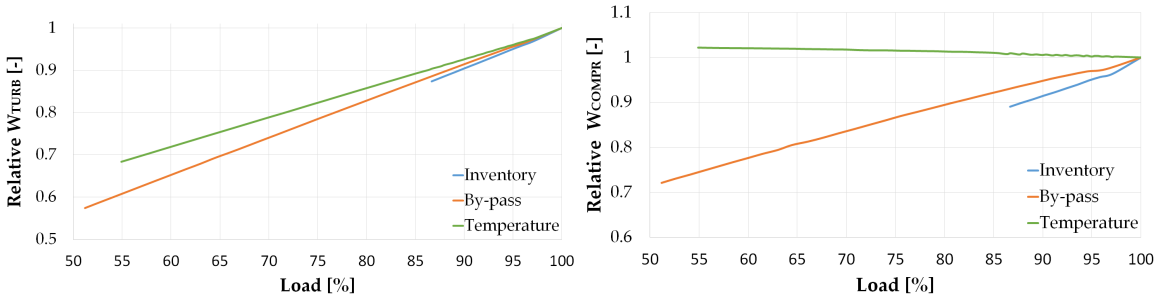

(a) Relative gross turbine power of the *Partial Cooling* cycle at partial load. The line corresponding to *Inventory* controlat partial load.
merges with that of the *By-pass* scheme almost entirely.

(b) Relative compressor power of the *Partial Cooling* cycle

Figure 5.13: Partial load performance of the *Partial Cooling* cycle (part 3). The three different control strategies are considered.

With regard to recuperators partial load performances, Fig. 5.14 presents the relative deviations of LT and HT recuperator efficiencies. It can be observed that *Inventory* strategy leads to very small deviations (around 1%), while *Temperature* and *By-pass* controls conduct respectively to a maximum 5% rise in LT Rec and 9% drop in HT Rec. Nevertheless, such deviations are still completely affordable for a good operation of the power cycle and do not result to be detrimental to its partial load performance.

Figure 5.15 presents the results obtained for compressor C2 which is shown in the layout in figure 5.9. This is the most representative compressor in the cycle, as well as the compressor

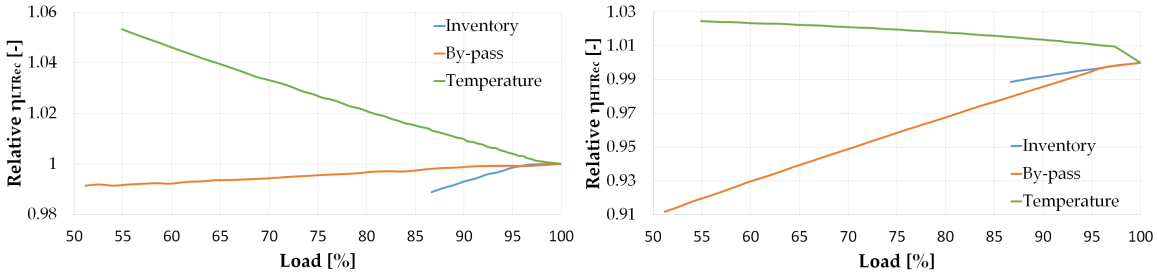

(a) Low-temperature recuperator efficiency of the *Partial Cooling* cycle at partial load.

(b) High-temperature recuperator efficiency of the *Partial Cooling* cycle at partial load.

Figure 5.14: High and low-temperature recuperator efficiency of the *Partial Cooling* cycle at partial load. The three different control strategies are considered.

whose operation turns out more difficult to control due to the proximity of the critical point, and thus it is decided to discuss the performance of this equipment only. The entire set of results obtained for the other two compressors is provided in Annex B.

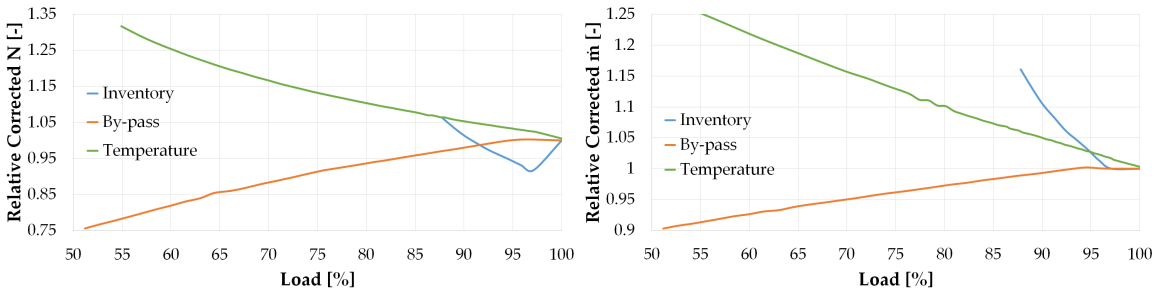

(a) Relative corrected shaft speed N_{corr}.

(b) Relative corrected mass flow rate $\dot{m}_{corr}$.

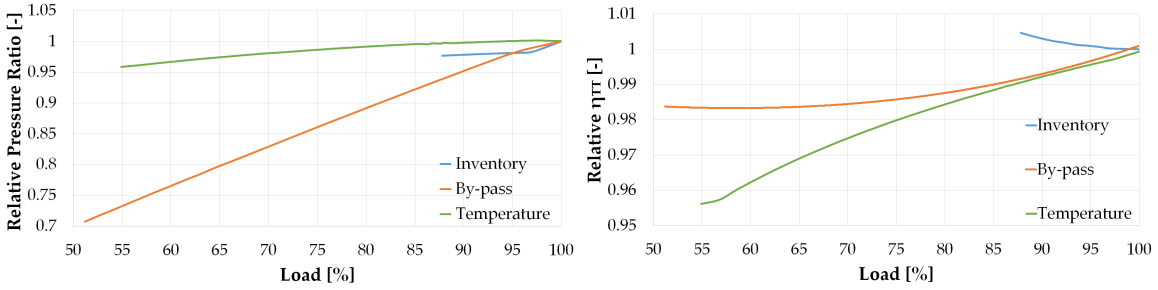

(c) Relative pressure ratio PR.

(d) Relative total-to-total efficiency η_{TT}.

Figure 5.15: Partial load performance of compressor C2 in the *Partial Cooling* cycle. The three different control strategies are considered.

Generally speaking, the *By-pass* control scheme leads to large variations of the main performance parameters, for instance 30% change of N_{corr} and PR as shown in Figure 5.15(a) and (c) respectively, mostly due to the also very wide operational range. *Temperature* control exhibits similar variations but in this case, these are somewhat mirrored to *By-pass* for N_{corr} and $\dot{m}_{corr}$, explaining the trend observed in Figure 5.15(c). Finally, *Inventory* control leads to smaller relative variations due to the narrow operating range.

The compressor performance maps for the three different control strategies are provided in Figure 5.16, showing pressure ratio as a function of m_{corr}. The arrows indicate the path followed by the compressor when operating at reduced load. It is observed that the *By-pass* scheme presents the opposite trend to the other strategies, showing a decreasing rather than increasing corrected mass flow rate for decreasing loads. This is due to an increase in sCO_2 density at compressor inlet, caused by the progressive approach to the condensation dome whilst the absolute mass flow rate and sound speed remain constant, see Eq.(5.1). Nevertheless, in spite of this trend, a surge margin is always respected to ensure that the compressor does not enter the unstable region to the left of the surge line.

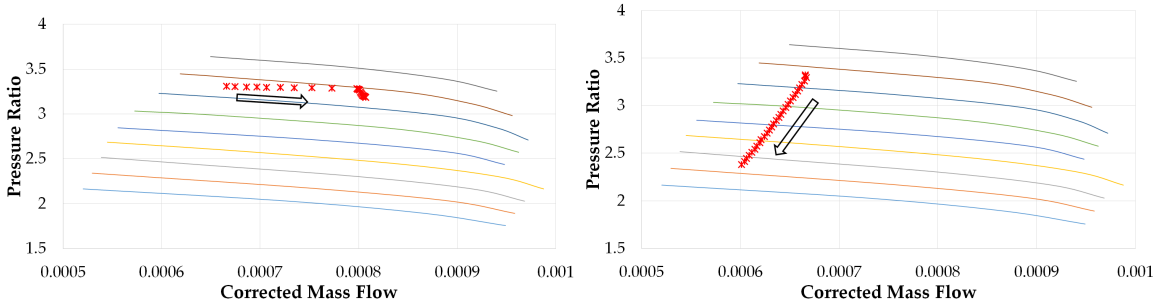

(a) Excursion of compressor C2 in the *Partial Cooling* cycle when operating at partial load. *Inventory* control.

(b) Excursion of compressor C2 in the *Partial Cooling* cycle when operating at partial load. *By-pass* control.

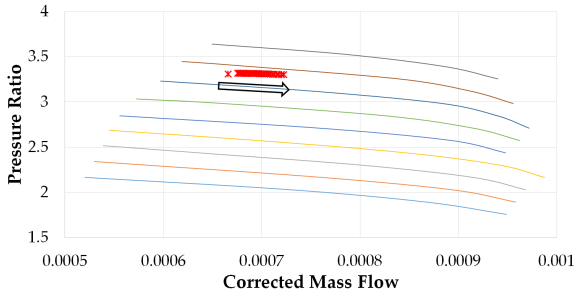

(c) Excursion of compressor C2 in the *Partial Cooling* cycle when operating at partial load. *Temperature* control.

Figure 5.16: Partial load performance of compressor C2 in the *Partial Cooling* cycle for the three control strategies considered.

5.6.2 Partial load analysis of the *Allam* cycle

Figures 5.17 to 5.22 show the same results as in the previous section but applied to the part-load performance of the *Allam* cycle. They are very similar to the results obtained for the *Partial Cooling* cycle; hence, only the main differences are highlighted here.

The first interesting feature is the reduction of the operational ranges of all the strategies. *Inventory* is able to reduce load down to 90% only, given that the design inlet pressure of the pump is set to 8 and not 9 MPa (the latter being the inlet pressure to compressor C2 in the *Partial Cooling* cycle). This implies that the compression process takes place closer to the critical point, with a narrower margin from the saturation line. Also, for the *Allam* cycle, it is not possible to reduce load further by increasing pump inlet temperature as it was the case for

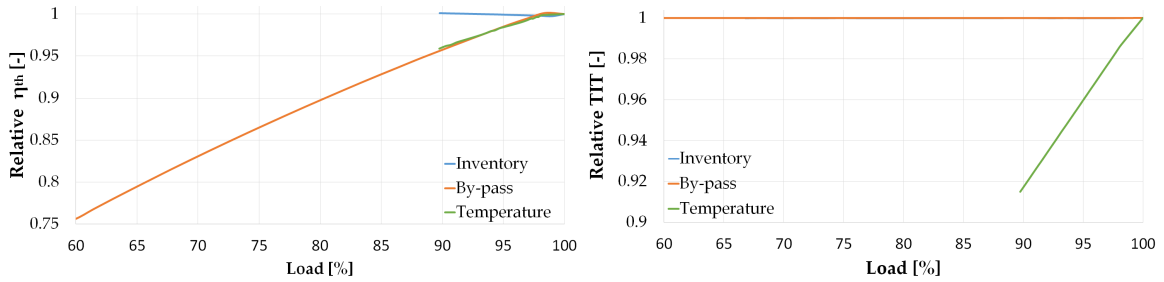

(a) Relative thermal efficiency of the *Allam* cycle at partial load.

(b) Relative turbine inlet temperature (*TIT*) of the *Allam* cyle at partial load. Lines corresponding to *Inventory* and *Bypass* merge on a single line.

Figure 5.17: Partial load performance of the *Allam* cycle (part 1). The three different control strategies are considered.

the *Partial Cooling* layout as this would bring about compressor-like operating conditions of this equipment.

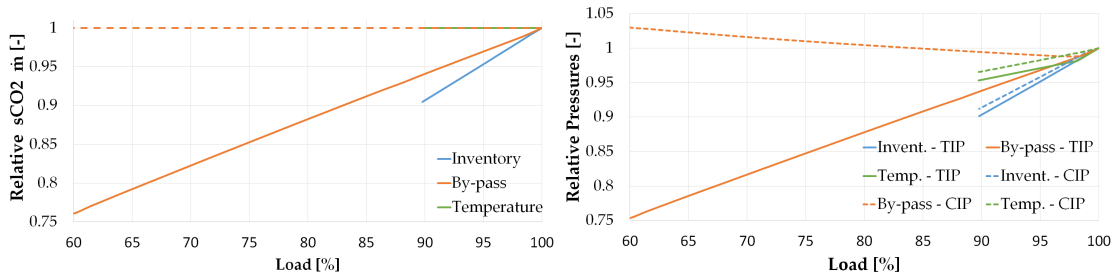

(a) Relative sCO_2 mass flow rate of the *Allam* cycle at partial load.

(b) Relative pressure of the *Allam* cycle at partial load.

Figure 5.18: Partial load performance of the *Allam* cycle (part 2). The three different control strategies are considered.

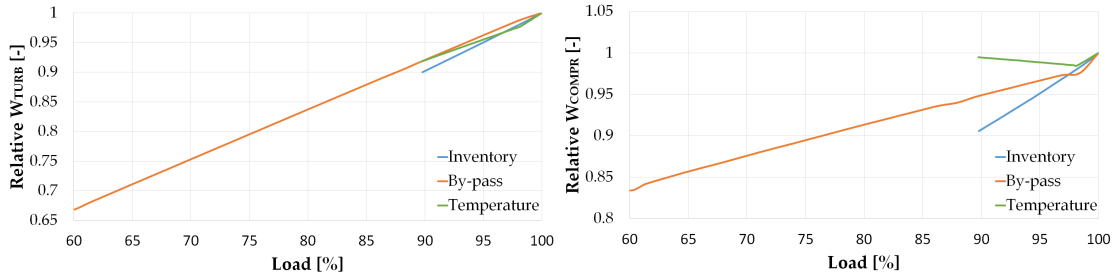

(a) Relative gross turbine power of the*Allam* cycle at partial load.

(b) Relative compressor power of the *Allam* cycle at partial load.

Figure 5.19: Partial load performance of the *Allam* cycle (part 3). The three different control strategies are considered.

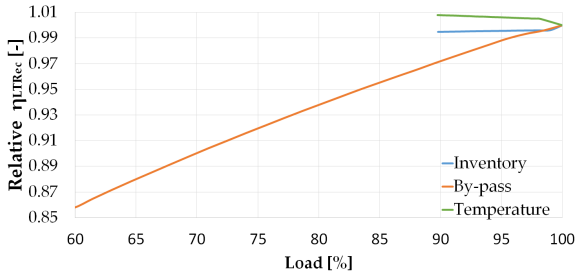

Figure 5.20: Recuperator efficiency of the *Allam* cycle at partial load. The three different control strategies are considered.

Regarding *By-pass* and *Temperature* control, their turn-down is now limited to 60% and 90% respectively given that further load reductions would require increasing pump inlet temperature by a little margin to ensure stable inlet conditions; nevertheless, as in the *Partial Cooling* cycle before, the author decided to not consider this modification in order to provide more coherent and consistent trends. Finally, it is to note that *Temperature* control enables the largest load reduction which makes the *Allam* cycle the only layout which could be operated just with this control strategy. It can also be stated that the *Allam* cycle exhibits worse part-load performance than the *Partial Cooling* layout when using *By-pass* control, Figure 5.17(a).

No further differences between Figures 5.17 to 5.20 and Figures 5.11 to 5.14 are worth noting.

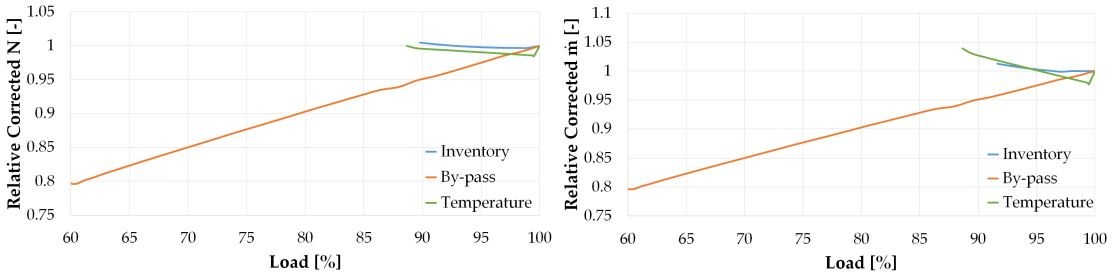

(a) Relative corrected shaft speed N_{corr}.

(b) Relative corrected mass flow rate $\dot{m}_{corr}$.

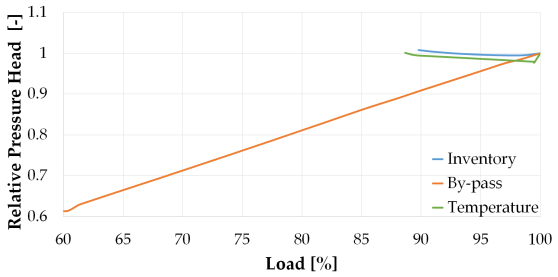

(c) Relative head.

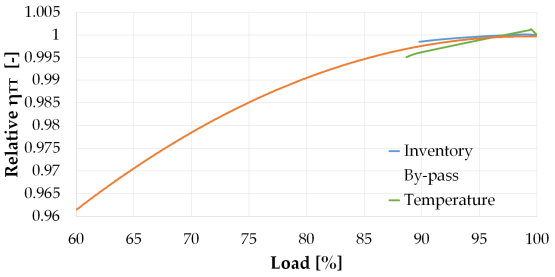

(d) Relative total-to-total efficiency η_{TT}.

Figure 5.21: Partial load performance of the pump in the *Allam* cycle. The three different control strategies are considered.

Regarding the compression process, the pump in the Allam cycle is subjected to very rigid

operating conditions given the close vicinity to the critical point. This was already the case for the compressors in the *Partial Cooling* cycle. Indeed, comparing Figures 5.21 and 5.15, the following observations can be made. Firstly, the *By-pass* control presents very similar trends but with larger deviations in terms of pressure ratio and corrected mass flow rate (some 13 % higher than in *Partial Cooling* cycle at 60% load). Secondly, with respect to the other two control strategies, very small deviations can be observed for the entire set of parameters, basically due to their largely limited operating range.

The performance maps in Figure 5.22 show similar plots to Figure 5.16. Nevertheless, it is worth noting that the pump in the *Allam* cycle increases the pressure of all the working fluid whereas compressor C2 in the *Partial Cooling* cycle works with a fraction of the mass flow rate only. Therefore, the large $\dot{m}_{corr}$ variation observed in Figure 5.21(b) is not found in Figure 5.22(b).

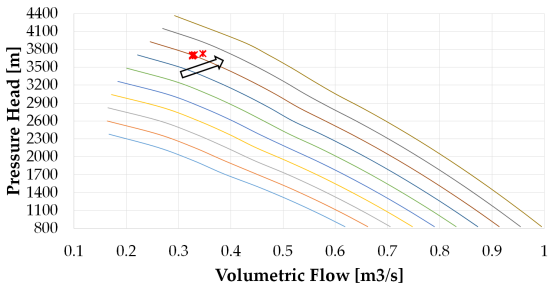

(a) Excursion of the pump in the *Allam* cycle when operating at partial load. *Inventory* control.

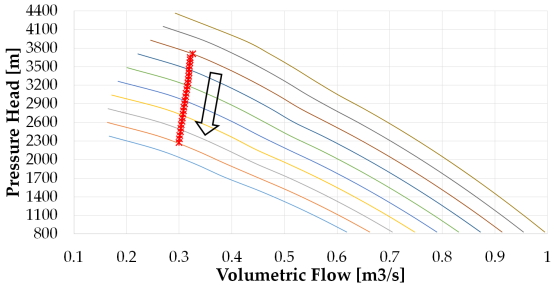

(b) Excursion of the pump in the *Allam* cycle when operating at partial load. *By-pass* control.

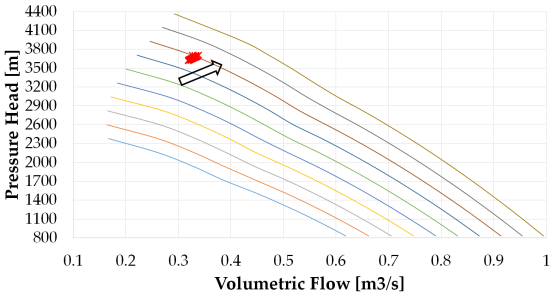

(c) Excursion of the pump in the *Allam* cycle when operating at partial load. *Temperature* control.

Figure 5.22: Partial load performance of the pump in the *Allam* cycle for the three control strategies considered.

5.7 Best Control Strategy

Once the individual control strategies have been studied in the *Partial Cooling* and *Allam* cycles, the best overall control strategy is discussed in this section. Such *optimum* strategy results from a combination of *inventory* at high load and *By-pass* at intermediate and low loads, at least in as far as thermal performance is concerned. In this regard, it is worth noting that the discussion in this section does not take economics into account, which will be assessed in

a later section devoted to LCoE analysis.

Figure 5.23 provides the total pressure vs. specific enthalpy diagram of the *Partial Cooling* cycle at partial load. The blue solid line represents the rated (design) conditions (100% load) whereas the blue dotted line corresponds to the 90% load case using *Inventory* control. At 86% load the control strategy is changed to *By-pass*, which is indicated by the orange color of the dashed lines (same colors as in Figures 5.11 to 5.21). Compressor C3 is represented for 100% and 50% load, to improve the readability of the plot.

Inventory control brings about larger variations of compressor inlet pressure, as discussed in Figure 5.12(b), and this parameter falls significantly even at 90% load. The utilization of *By-pass* control at lower loads keeps compressor inlet pressure approximately constant, explaining why the inlet conditions to the compressor shift south-east and also the trend shown in Figure 5.24(d).

Moreover, Figure 5.24(a) also confirms that the *Partial Cooling* cycle presents a 10% η_{th} drop with respect to the rated value at 50% load, while turbine power decreases from 70 to 40 MWe. This is also shown on the right hand side of Figure 5.23, where the enthalpy change available at the turbine is reduced progressively.

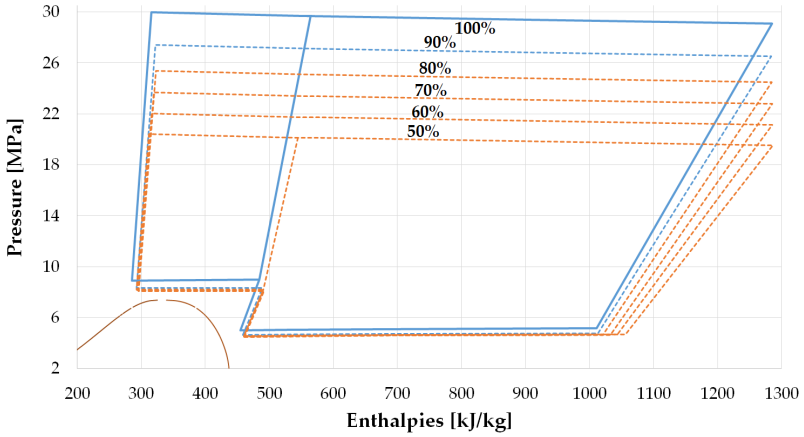

Figure 5.23: Pressure-enthalpy diagram of the *Partial Cooling* cycle at partial load. Blue and orange lines correspond to *Inventory* and *By-pass* control respectively.

Figure 5.25 provides the total pressure vs. specific enthalpy diagram of the *Allam* cycle at partial load where the switch from *Inventory* to *By-pass* control takes place at about 90%, see Figure 5.26(b). It is observed that the minimum cycle pressure remains almost constant because the rated inlet conditions to the pump are so close to the saturation line that there is virtually no margin for further shift leftwards when operating the cycle part-load. Actually, compressor inlet pressure increases slightly when *By-pass* control is employed, exceeding the rated value at loads lower than 80%, as from Figure 5.18(b).

As it was the case for the *Partial Cooling* cycle, the *Allam* cycle experiences a 10% thermal efficiency drop (η_{th}) accompanied by a 30 MW lower turbine gross output W_{TURB} at 60%

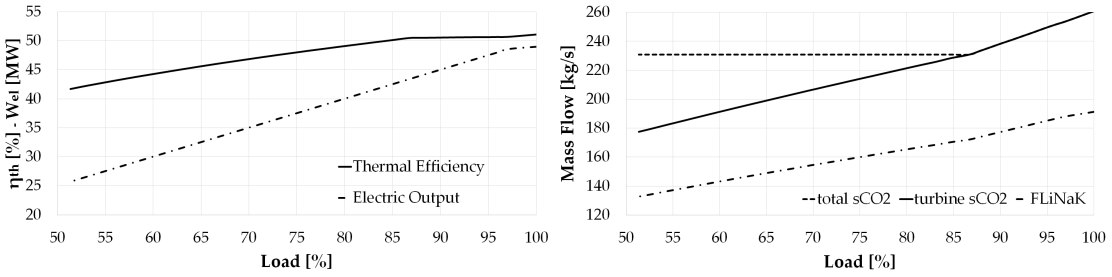

(a) Part-load thermal efficiency of the *Partial Cooling* cycle.

(b) Mass flow rates of sCO_2 and FLiNaK for the *Partial Cooling* cycle at part-load.

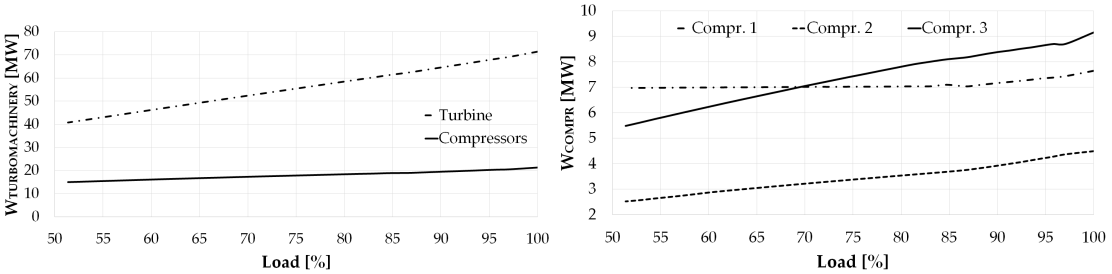

(c) Part-load turbine and compressor power of the *Partial Cooling* cycle.

(d) Breakdown of compressor power consumption for the *Partial Cooling* cycle at part-load.

Figure 5.24: Performance parameters of the *Partial Cooling* cycle at partial load. A combination of*Inventory* and *By-pass* control is considered.

load. On the contrary, the operating characteristics of the compression section are different, showing that the pump (which is equivalent to compressor C2 in the *Partial Cooling* layout) has the largest power consumption at higher loads. This is the opposite to Figure 5.24(d) where compressor C3 exhibits the largest power consumption followed by C1. This is, again, due to the parallel compression process of the *Partial Cooling* cycle. Also, the fact that the pump provides most of the pressure rise in the *Allam* cycle explains the dissimilar consumption of shaft power of this equipment and compressors C1 and C2.

Another interesting feature of Figure 5.26(b) is the dissimilar mass flow rates of sCO_2 and molten salts in the *Partial Cooling* cycle whereas these two streams have similar mass flow rates in the *Allam* cycle. Moreover, this difference in the *Partial Cooling* cycle increases at loads lower than 80%. Generally speaking, the *Partial Cooling* cycle requires a 25% higher sCO_2 mass flow rate than the *Allam* cycle, with 15% lower mass flow of molten salts. This is mostly due to the higher thermal efficiency of the *Partial Cooling* cycle for a similar temperature rise across the heater.

Regarding the off-design performance of recuperators, Figure 5.27 provides the effectiveness of these equipment for both the *Allam* and *Partial Cooling* cycles. Generally speaking, the latter presents better part-load performance, characterized by higher than 85% effectiveness regardless of the operating conditions. The low-temperature recuperator shows significantly lower η_{HX} if compared than the high-temperature recuperator, especially at high loads where the efficiency only reaches 88%. This circumstance is a well known characteristic in literature

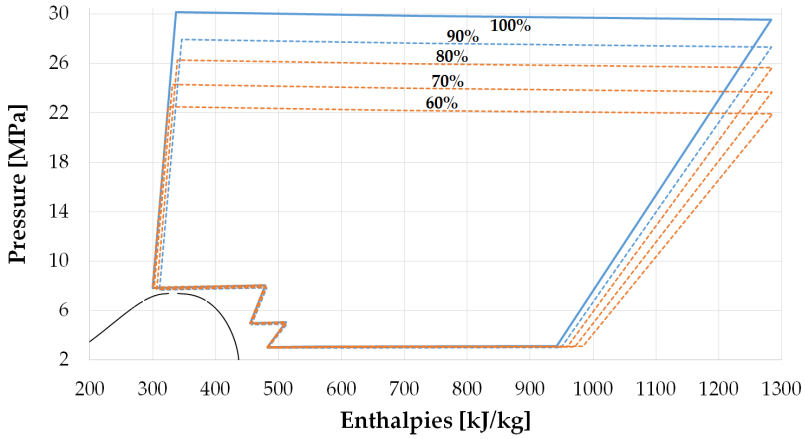

Figure 5.25: Pressure-enthalpy diagram of the *Allam* cycle at partial load. Blue and orange lines correspond to *Inventory* and *By-pass* control respectively.

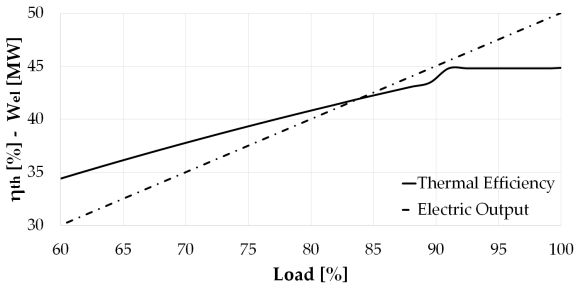

(a) Part-load thermal efficiency of the *Allam* cycle.

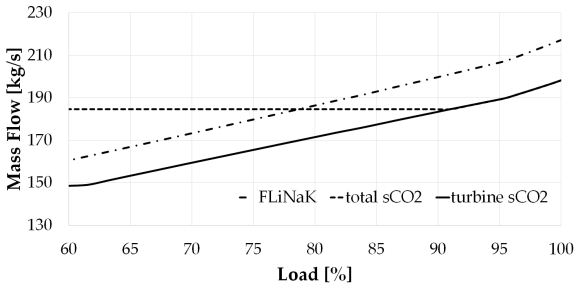

(b) Mass flor rates of sCO_2 and FLiNaK for the *Allam* cycle at part-load.

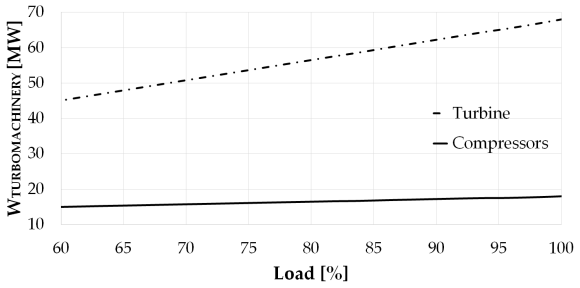

(c) Part-load turbine and compressor power of the *Allam* cycle.

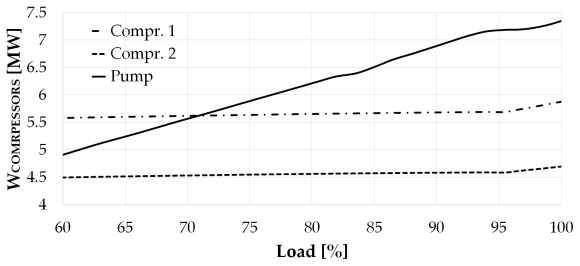

(d) Breakdown of compressor power consumption for the *Allam* cycle at part-load.

Figure 5.26: Performance parameters of the *Allam* cycle at partial load. A combination of*Inventory* and *By-pass* control is considered.

specific to sCO_2 which is brought about by the very close vicinity to the critical point, hence with larger property changes triggering internal pinch point problems. In practice, this is compensated for by the different mass flow rates on each side of the heat exchanger [38, 67]. Interestingly, the high temperature recuperator in the *Partial Cooling* cycle and the recuperator in the *Allam* cycle exhibit similar behavior.

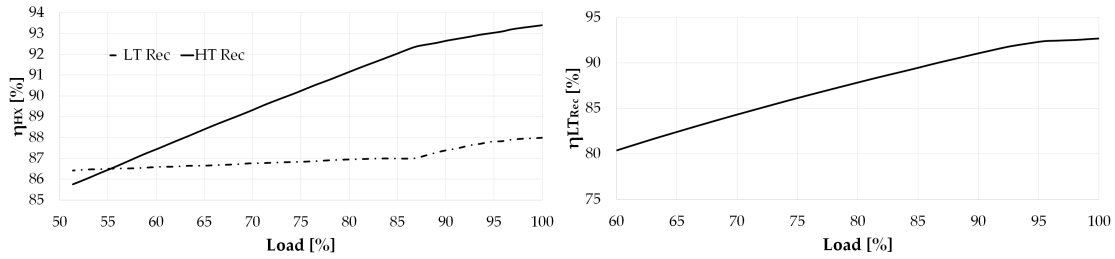

(a) Performance of the recuperators in the *Partial Cooling* cycle at part-load.

(b) Performance of the recuperators in the *Allam* cycle at part-load.

Figure 5.27: Performance of the recuperators in the *Partial Cooling* and *Allam* cycles at part load using the best load-control strategy.

Figure 5.28 shows the off-design performance of compressor C2 in the *Partial Cooling* cycle and the pump in the *Allam* cycle, along with their running lines overlayed on the corresponding performance maps.

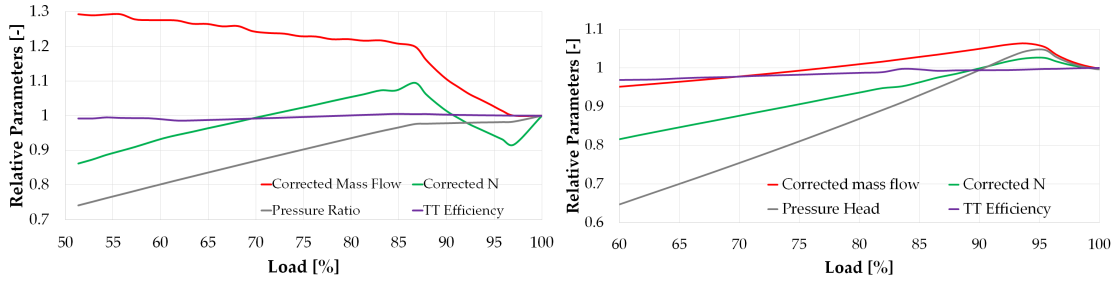

(a) Part-load performance of compressor C2 in the *Partial Cooling* cycle.

(b) Part-load performance of the pump in the *Allam* cycle.

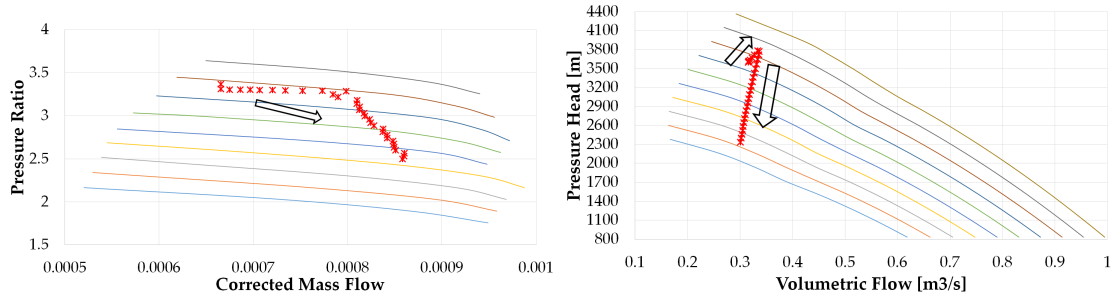

(c) Running line of compressor C2 in the *Partial Cooling* cycle.

(d) Running line of the pump in the *Allam* cycle.

Figure 5.28: Part-load performance of compressor C2 in the *Partial Cooling* cycle and of the pump in the *Allam* cycle when using the best control strategy.

The trends of the relative parameters are consistent with those observed in Figures 5.15 and 5.21, as they are actually a combination of the performance using *Inventory* and *By-pass* control independently. The same can be said for the part-load performance of the pump in the *Allam* cycle, Figure 5.28(d). On the other hand, Figure 5.28(c) shows a different scenario to that resulting from the mere combination of Figures 5.16(a) and (b). The progressive increase

in $\dot{m}_{corr}$ when using *By-pass* control, confirmed by the red line in Figure 5.28(a), differs from the decreasing trend presented in Figures 5.16(b) and 5.15(b). This is because of the different initial conditions of the cycle when shifting to *By-pass* control under the *Best Control Strategy*, especially in terms of circulating mass flow, pressure and flow distribution.

5.8 Assessment of the Levelized Cost of Electricity (LCoE)

Once the off-design performances of the sCO_2 cycles considered have been obtained, the Levelized Cost of Electricity of a Concentrating Solar Power plant using them CSP plant incorporating them can finally be calculated. To this end, the author has relied on the system Advisor Model SAM developed by the National Renewable Energy Laboratory of the United States Department of Energy since this is widely accepted by the scientific community and already employed in sCO_2 technology cost estimations [76, 237]. SAM allows to model several types of renewable energy systems, and includes an integrated cost-estimation and financial analysis tool capable of fully analyzing the real feasibility of the power plant under analysis.

The first part of this section described how the part-load performance of the *Allam* and *Partial Cooling* cycles are integrated in SAM's calculation process. Then, a 50 MWe CSP plant is modeled, employing these two power cycles and considering two different locations and four different combinations of financial parameters and dispatch control models. Finally, the results so obtained are compared with a commercial CSP facility using a steam turbine power block.

5.8.1 Integration of Partial Load Performance into SAM

Once the *CSP power tower molten salt - single owner* option is selected in SAM, the user is able to edit an long list of parameters regarding both the thermodynamic and financial models of the power plant. Nevertheless, in order to not increase the length of this section unnecessarily, only the sections actively used to integrate the original part-load results into the software will be reported here; the remaining parameters used in the simulations are listed in the corresponding Annex D.

Figure 5.29 shows the main interface of SAM with the corresponding subsections. The site is first selected from the NREL National Solar Radiation Database in *Location and Resource*. For each location, SAM provides information about weather and solar radiation, which critically affect the annual production of energy. Gross output at generator terminals and gross-to-net conversion efficiency are set in the *System Design* section along with cycle thermal efficiency, design point DNI (Direct Normal Irradiation) and hot and cold temperatures of the molten salts.

The input parameters defining the solar field in the Regarding *Heliostat Field* section are left to their default values and hence a simple optimization of field geometry according to the parameters set in the previous interface is performed. The type and composition of the molten salt (or Heat Transfer Fluid considered) is selected in the *Tower and Receiver* menu, where either commercial solar salts ($NaNO_3KNO_3$) or FLiNaK can be selected. The latter is the same molten salt employed by the in-house models developed by the author and it is therefore selected for this LCoE assessment.

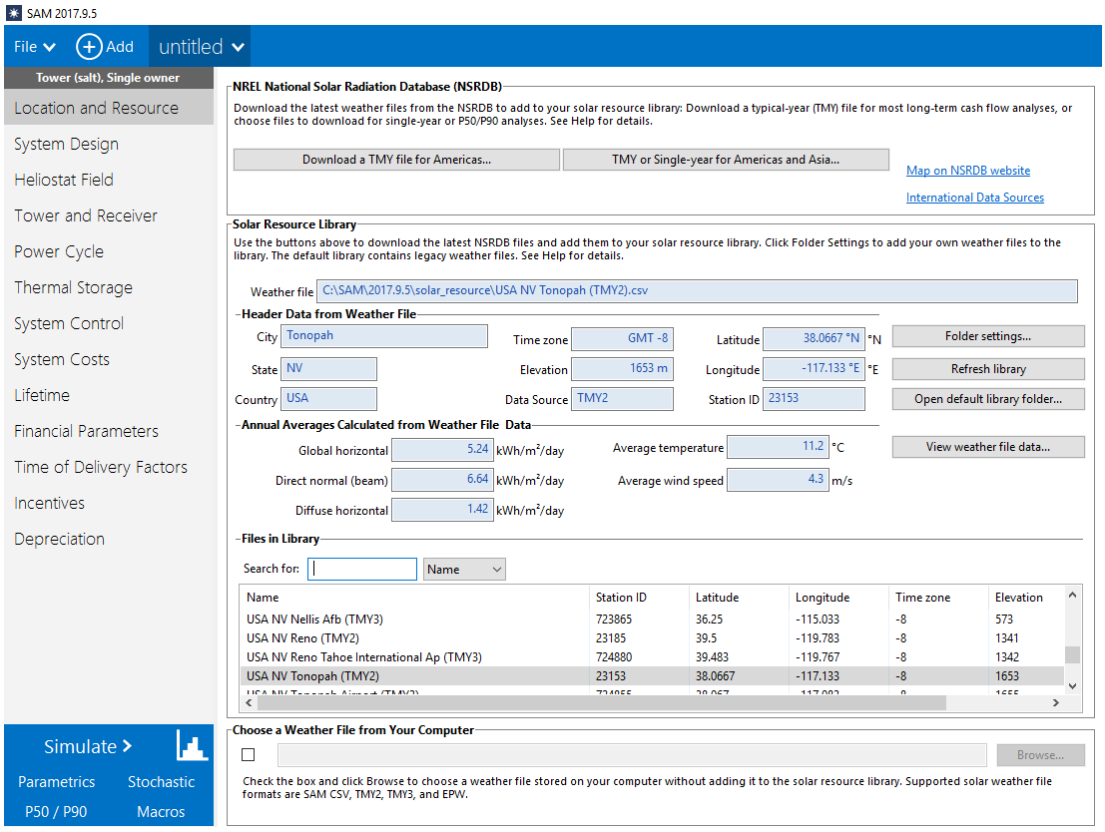

Figure 5.29: Main interface of the System Advisor Model software.

The *Power Cycle* menu is, as expected, the most important section in the integration process. The user can select a standard Rankine cycle, a Supercritical Carbon Dioxide Cycle or a *User Defined* cycle, the latter of which also requires that off-design performance be provided. This last option is adopted in this work and it is where the integration between SAM and author's in-house codes actually takes place. It is worth remarking that *Supercritical Carbon Dioxide Cycle* allows to modify a very limited number of cycle parameters only, since only the *Recompression* cycle can be modeled by default.

In this section, shown in Figure 5.30, some general design parameters such as design ambient temperature or type of cooling system (and others listed in the corresponding Annex D). Additionally, the user must provide the following information:

- **MOD1-Performance as a function of HTF temperature**: three values of normalized molten salt mass flow rates are considered (0.2, 1 and 1.05) and, for each of them, the part-load performance of the power cycle for variable molten salt (hot) temperature is obtained. The rated hot temperature of the molten salt is 770ºC and this parameter is varied between 700 and 800ºC.
- **MOD2-Performance as a function of HTF mass flow rate**: three values of ambient temperature are considered (5, 15 and 40 ºC) and, for each of the, the part-load performance of the power cycles for variable mass flow rate of molten salts is obtained. The operational range of the latter is the same as in MOD1; i.e., between 20% and 105% of the

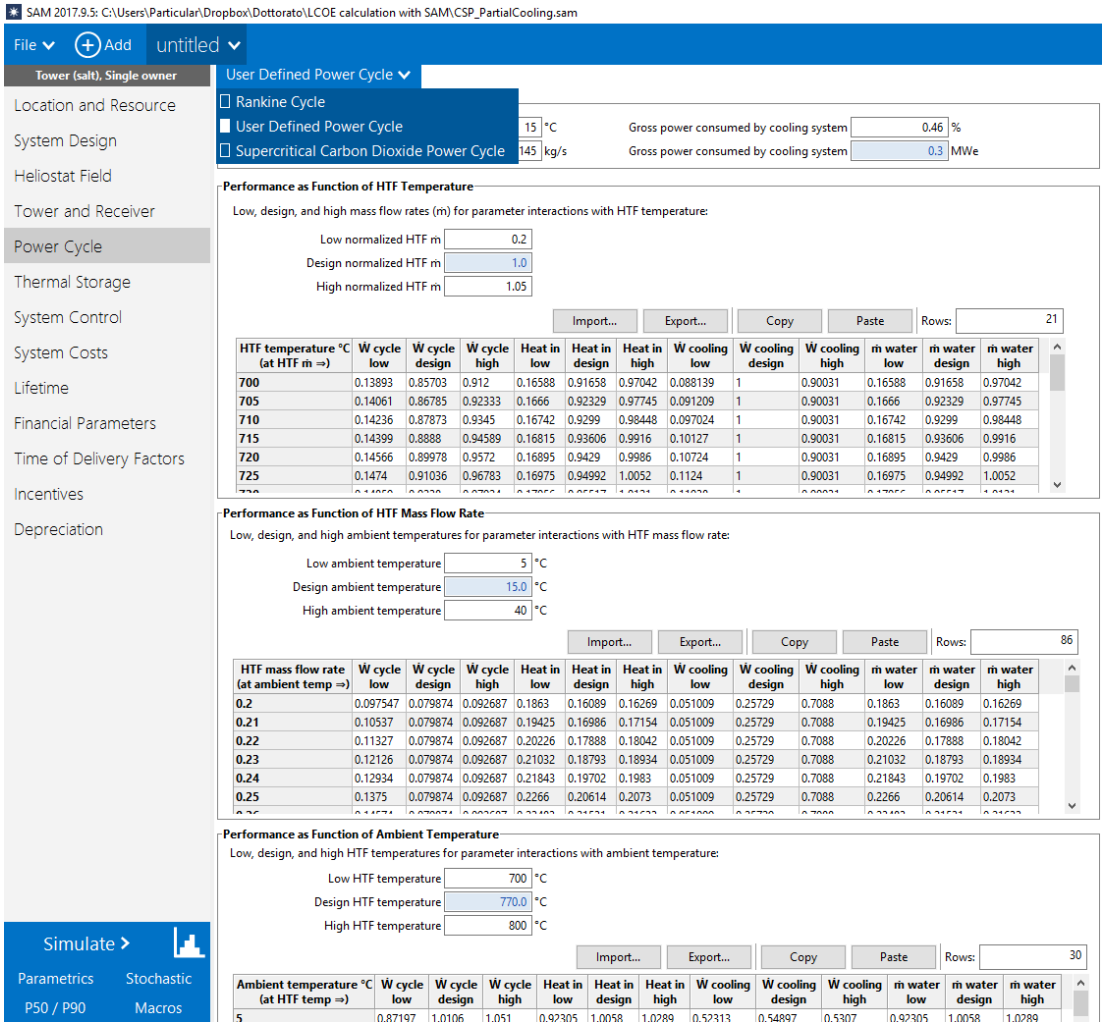

Figure 5.30: *Power Cycle* menu in SAM. *User Defined Power cycle* is selected.

rated FLiNaK mass flow rate.

- **MOD3-Performance as a function of ambient temperature**: in this last section, three molten salt (hot) temperatures are considered: 700, 770 and 800 ºC. For each of them, the part-load performance of the power cycles for varying ambient temperature is obtained. Ambient temperature is varied between 5 and 40ºC.

The part-load parameters to be specified are net electric output of the cycle ($\dot{W}_{cycle}$), heat addition to the cycle (Q_{in}) and power consumption ($\dot{W}_{cooling}$) and water mass flow rate ($\dot{m}_{w,cooling}$) of the cooling system. These parameters, which must be normalized with respect to their rated values, are obtained for the so-called *best control strategy*. Additionally, in order to produce comparable results to a Rankine cycle modeled by SAM (with a minimum stable load of 20%), the results presented previously are extended as follows. *By-pass* control is used to reduce the minimum stable load down to 35% load and 40% for the *Partial Cooling* and *Allam* cycles respectively, thanks to a compressor inlet temperature increase if necessary. For lower loads, and for the sake of simplicity, the performance trend-lines are extrapolated. This

assumption, though apparently simplistic, relies on the large uncertainty that remains in how such a complex power cycle could be operated at such low loads. As already stated before, such topic would constitute a doctoral work in itself and, hence, it is not approached here.

5.8.2 Dispatch Control and Financial Model

The energy dispatch model is specified in the *System Control* menu, as observed in Figure 5.29, while the remaining parameters of the financial model are set in the in *Financial Parameters* and *Time of Delivery Factors* menus. These models are of capital importance for a correct LCoE assessment since they affect both thermal performance and economic feasibility of the plant strongly, see Section 5.8.4 later. A complete and detailed analysis of these models goes beyond the scope of this research, due to its complexity and computational cost, and a thorough optimization of *Dispatch Control* and the *Financial Model* could, in fact, be considered for a follow-on research. Nevertheless, in order to improve the quality of the results and to have a sense of the impact of these settings on the LCoE obtained, the author has performed the thermo-economic analysis of the CSP plant for two different sets of dispatch and financial parameters, combined in four different cases as shown in Table 5.6.

	Financial Model	Dispatch Control
Case1	SAM Default	SAM Default
Case2	SAM Default	SunShot Vision Study
Case3	SunShot Vision Study	SAM Default
Case4	SunShot Vision Study	SunShot Vision Study

Table 5.6: Cases showing different combinations of Dispatch Control and Financial Models.

These two sets are the default values of SAM, automatically defined by the software for a commercial CSP power plant based on steam turbines, and those provided by the SunShot Vision Study, specifically proposed for a SCO_2 power cycle in the frame of the SunShot Programme [76].

The dispatch control model defines the operating schedule of the thermal energy storage system and power block; i.e., how the former is charged/discharged providing energy to the latter, which eventually converts it to electricity, in order to fit the available daily and annual solar radiation available. The user defines nine different turbine output fractions, on a monthly-hourly base, and the software automatically scales the cycle heat input relative to the rated value for the corresponding time-of-delivery period. Figure 5.31 provides a graphical representation of this control method, for both the SAM Default and SunShot Vision cases.
It is worth noting that this dispatch control does not substitute the control strategies described earlier, given that part-load operation is inevitable over the year due to unpredictable loss of solar radiation or to plant start-up and stand-by periods, but it merely defines an overall schedule of plant operation. For the default SAM dispatch control, the turbine works at full load whenever possible, except in summer when a 5% over charge during the central hours of the day characterized by the highest solar irradiation. For the SunShot Vision case, the load is reduced during winter in order to enable longer operating hours while maintaining the rated conditions during spring and summer.
Regarding the financial model, the auxiliary financial parameters summarized in Table 5.7 are

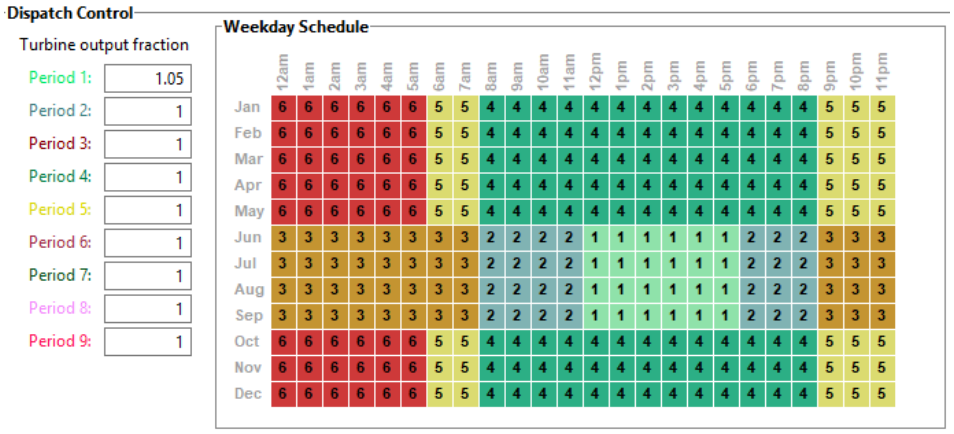

(a) Default dispatch control of SAM.

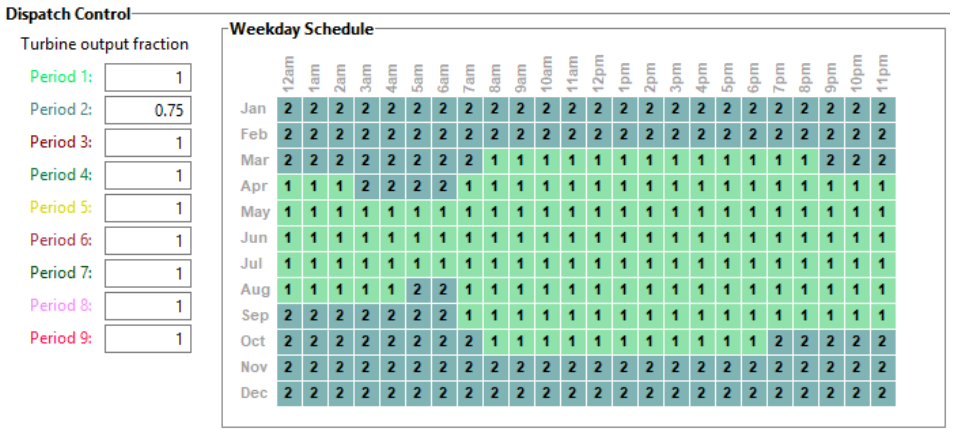

(b) Dispatch control scheme for the SunShot Vision case [76].

Figure 5.31: Different dispatch controls used for LCoE assessment.

added to the *Specify IRR target* menu. With this option, the user is specifies a target *Internal Rate of Return* and the year on which this is achieved, while the software automatically finds the *Purchase Price Allocation* (PPA) required to meet this target taking into account the other financial parameters specifically defined. The PPA price is actually another difference between SAM and Sunshot, in particular with regard to the *Time-of-delivery* factors (TOD) shown in Figure 5.32. If this option is selected, SAM multiplies the PPA bid price by the TOD factor to calculate the energy price in the corresponding hour. TOD factors and periods employed in both SAM's default and Sunshot Vision Study model are provided in Figure 5.32 and Table 5.8.

Finally, for the *System Cost* section, the default costs provided by SAM are used, except for the Thermal Energy Storage system and the power block, for which the values obtained with the in-house codes presented in Chapter 4 are employed. These estimates are provided in Table 5.9, where a comparison between the three cycles is shown.

	SAM Default	SunShot Vision Study
IRR target [%]	11	15
IRR target Year	20	30
Analysis period [years]	25	35
Inflation rate [%]	2.5	3
Nominal Discount rate [%]	8.14	8.66
Loan Percent of total capital cost [%]	50	60
Loan Duration [years]	18	15
Loan Annual interest rate [%]	7	7.1

Table 5.7: Financial parameters employed in the SAM's default and SunShot Vision cases. The parameters that are not reported here are set to the values used by SAM's default model in Table 5.6, and they are provided in the corresponding Annex D.

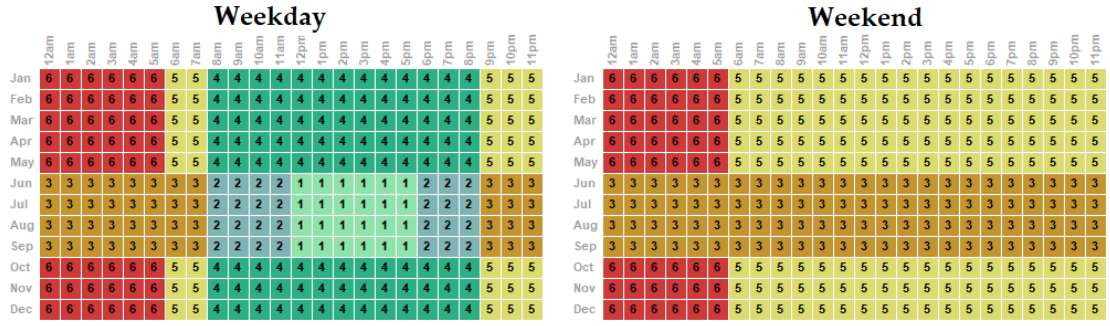

(a) SAM's default Time-of-Delivery factors.

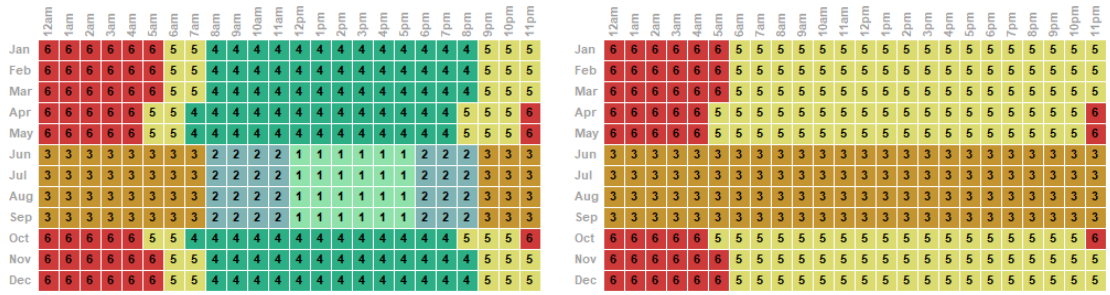

(b) Delivery factors of the SunShot Vision Study case [76].

Figure 5.32: Different Time-of-Delivery factors used for LCoE assessment.

Financial Model	Period 1	Period 2	Period 3	Period 4	Period 5	Period 6
SAM Default	2.064	1.2	1	1.1	0.8	0.7
SunShot Vision Study	3.28	1.28	0.67	1.02	0.82	0.65

Table 5.8: Different Time-of-Delivery factors employed by SAM's Default and SunShot Vision Study's financial models.

5.8.3 Plant Location and Specifications of the Power Cycles

Tonopah and Las Vegas, both in Nevada (USA), are the sites of choice for the assessment of LCoE. These are selected for their close proximity to *Crescent Dunes* [267], home to one of the

Cycle	ηth [%]	TIT [ºC]	Molten Salt	$T_{SALT,min}$-$T_{SALT,max}$ [ºC]	PB Cost [$/kWe]	TES Cost [$/kWht]
Allam	45.06	750	FLiNaK	480 - 770	460.1	62.77
Partial Cooling	51.10	750	FLiNaK	480 - 770	887.2	55.52
Rankine (steam)	41.20	550	$N_aNO_3KNO_3$	290 - 574	1100	24.00

Table 5.9: Different power cycles specifications employed in SAM for LCOE Assessment.

largest commercial CSP plant with Thermal Energy Storage worldwide. These two locations have similar ambient and radiation characteristics, suitable for the design conditions of sCO_2 power cycles taken into account in this work, see Table 5.9. These boundary conditions are also similar to those used in the thermo-economic analysis presented in Chapters 3 and 4.

A rated Direct Normal Irradiance (DNI) of 850 W/m^2 is considered in order to adapt the CSP plant to the mean solar radiation conditions of both locations, Figure 5.33, whilst the design ambient temperature is set to 15ºC (the same as in Chapter 4). Regarding ambient conditions, SAM allows to specify temperature but not relative humidity which is of uttermost importance if evaporative cooling is considered. Therefore, in the in-house models, this value is set to match that of the location under consideration, as obtained from SAM weather database directly. This is shown in Figure 5.33.

In addition to the *Allam* and *Partial Cooling* cycles, a standard Rankine steam cycle is included in the LCoE assessment, in order to have a benchmark for the innovative power cycles proposed in this work. For this cycle, the main parameters and performance specifications are summarized in Table 5.9, with further specifications provided in the corresponding Annex D. Common parameters used for these three cycles are DNI, set to 850 W/m^2, Solar Multiple, set to 2.4, and TES capacity, set to 10 hours at full capacity.
It is to note that the costs of power block and TES for the *Allam* and *Partial Cooling* cycles obtained in Chapter 4 are also provided in Table 5.9, along SAM's default values used in the steam cycle. Although the cost of the power blocks for the sCO_2 cycles may look significantly lower than that of the steam cycle, this do not differ largely from other values already published in literature [76].

5.8.4 Overall Anaysis of LCoE

The results provided by SAM for the three CSP power plants described before, and for the four possible cases, are presented in Figures 5.34 and 5.35. Five figures of merit are taken into account, two of them related to thermal performance and two financial:

- Performance:
  - Yield E_{year}, [GWh]: this is the annual production of electricity of the power plant.
  - Capacity Factor CF, [%]: ratio from the system's annual production of electricity in the first year of operation to the theoretical energy production should the system run at the rated capacity the entire year. This is a measure of the electricity that the system would be able to produce if it were operated at its nominal capacity for every hour of the year, and it can be significantly affected by plant location and operation of the Thermal Energy Storage system.

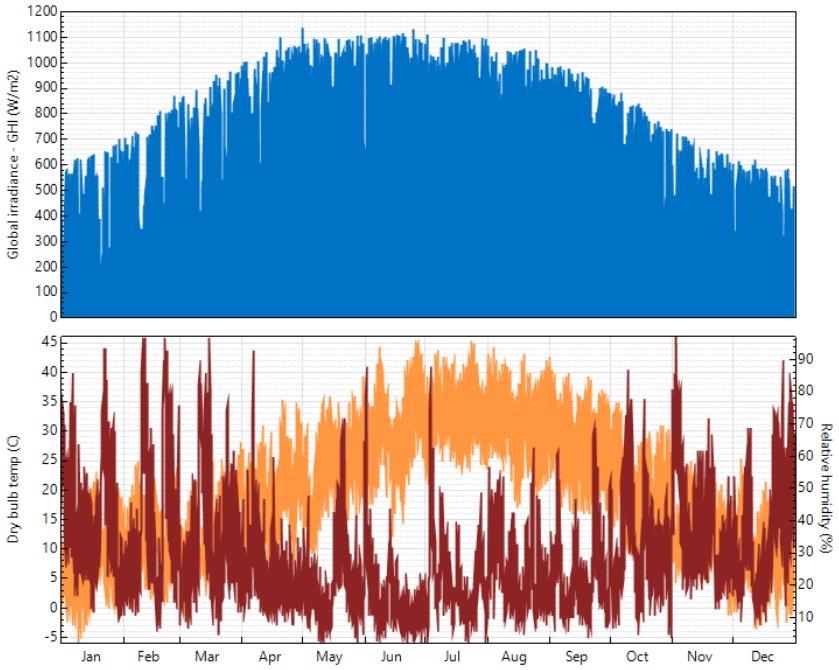

(a) Ambient conditions in Las Vegas, NV.

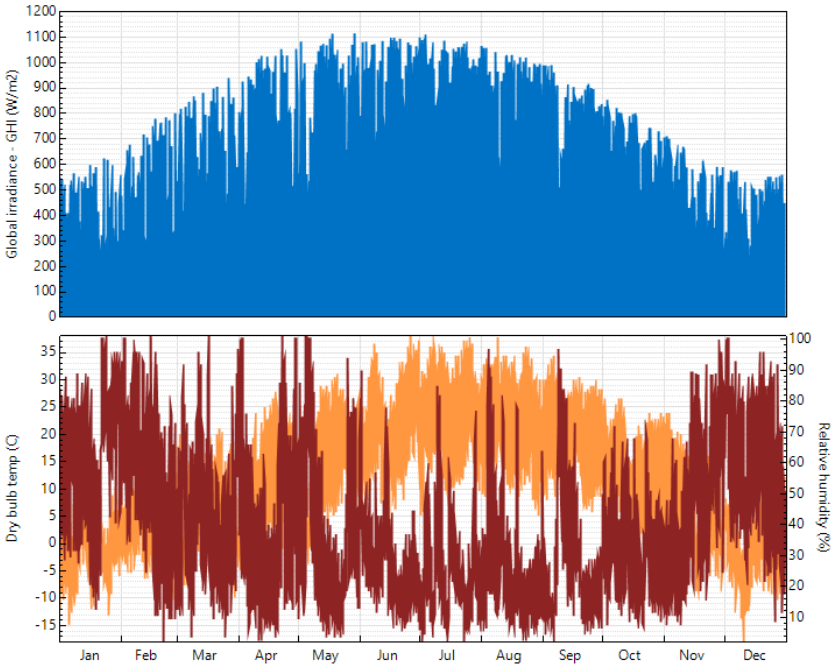

(b) Ambient conditions in Tonopah, NV.

Figure 5.33: Ambient conditions in the reference locations.

- Financial:
  - Levelized Cost Of Energy $LCoE$ [¢/kWh]: a measure of the total project life cycle costs relative to the total production of energy throughout the entire life of the

project.

- Net Present Value NPV [$]: discounted (present) value of the net cash inflow.
- Internal Rate of Return IRR, [%]: the nominal discount rate that would yield null NPV for the PPA financial models. As said, the *Specify IRR Target* option is selected in the present study and, therefore, this parameter is "fixed" by the financial model employed in each analysis. Hence, the only conclusion that can be drawn regarding this parameter is whether or not the value is achieved by the project itself. Eventually, it turns out that all the CSP plants considered manage to achieve the target IRR whose value is specified in Table 5.7.

The first observation in Figures 5.34 and 5.35 is that Las Vegas enable better performance than Tonopah for both thermal and financial performance, mostly due to the higher average DNI. It is also worth noting that SAM's default dispatch control (Case 1 and Case 3 in Figures 5.34(a) and (b)) yields larger annual production of electricity E_{year} and higher capacity factors CF for the steam power plant than those corresponding to the SunShot Vision Study, regardless of the site. The opposite situation is observed in sCO_2 power plants using an *Allam* cycle, for which a mirrored behavior is obtained, whilst the sCO_2 plant based on the *Partial Cooling* cycle seems to be insensitive to the dispatch control mode. Some conclusions can be drawn from the analysis.

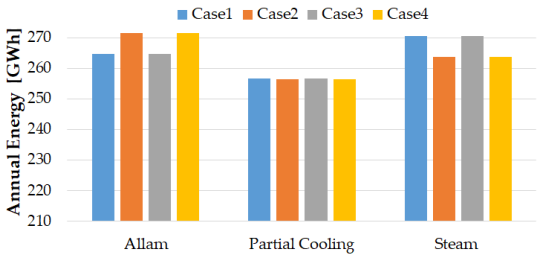

(a) Annual yield of the first year, Las Vegas (NV).

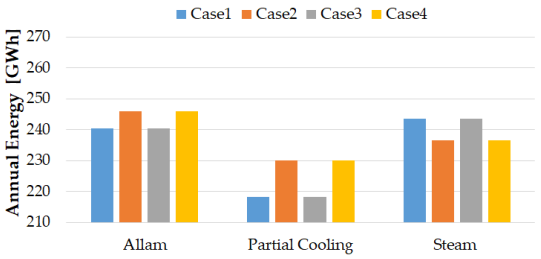

(b) Annual yield of the first year, Tonopah (NV).

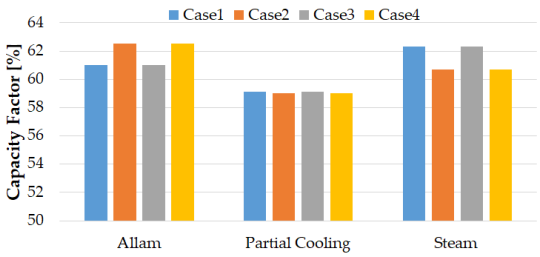

(c) Capacity factor for a CSP located in Las Vegas (NV).

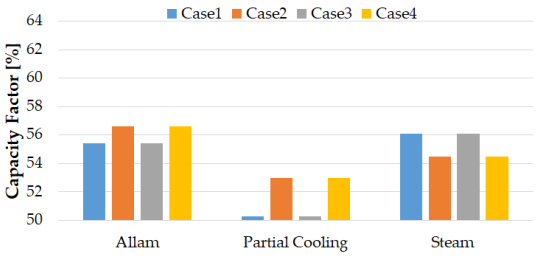

(d) Capacity Factor for a CSP located in Tonopah (NV).

Figure 5.34: Annual yield and capacity factor for the three power cycles and two locations considered. Case designation can be found in Table 5.6.

Annual yield E_{year} and capacity factor CF show very similar trends and, for a given power cycle, they are strongly dependent on dispatch control and location but fairly insensitive to the financial model. Cases 1 and 3, in fact, present almost identical performance metrics, and the same can be said for Cases 2 and 4. A CSP plant based on the *Allam* cycle in Las Vegas yields 10% higher yield and capacity factor than if it were located in Tonopah; the difference

would increase to about 12.5% if a *Partial Cooling* sCO_2 or a steam cycle were used. Regarding dispatch control, the SunShot Vision Study setting yields 3% higher E_{year} and CF when using the *Allam* cycle whereas a 3% drop in these parameters must be expected when considering a steam-turbine CSP plant. This can be explained by the fact that SAM's Default and SunShot Vision Study's dispatch control modes are specifically designed for steam and sCO_2 power cycles respectively.
Regarding the financial model employed in the SunShot Vision Study, it always leads to better financial results than SAM's, providing higher NPV and lower $LCoE$ for a given location, Figure 5.35.

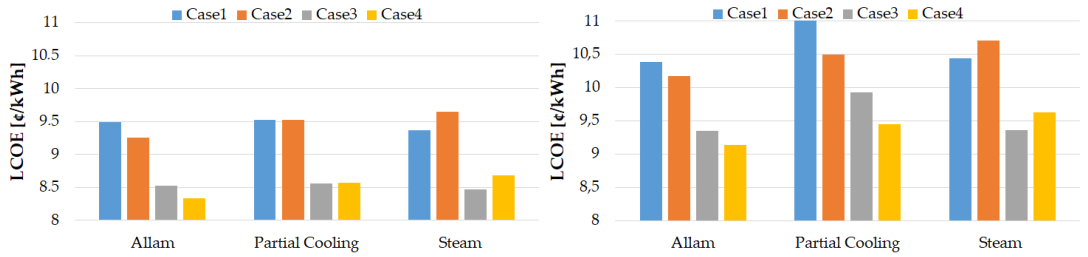

(a) Levelized Cost of Energy for a CSP located in Las Vegas (NV).

(b) Levelized Cost of Energy for a CSP located in Tonopah (NV).

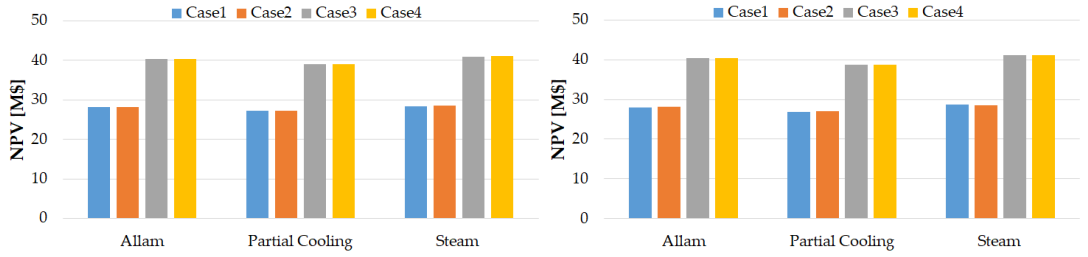

(c) Net Present Value of a CSP located in Las Vegas (NV).

(d) Net Present Value of a CSP located in Tonopah (NV).

Figure 5.35: Levelized Cost of Energy and Net Present Value of the three different cycles and four combinations of financial/control settings. Two locations in Nevada are considered: Las Vegas and Tonopah.

This is mostly due to the longer lifetime and higher IRR considered, even if the former model presents a larger debt fraction, set to 60% (versus 50% for SAM's default case) of the total capital cost. It is also observed that NPV depends on the financial model only inasmuch as only minimum deviations are seen between different locations, cycles or dispatch control systems. On the other hand, $LCoE$ happens to be strongly affected by all the factors considered so far. In particular, the following observations can be made:

- Las Vegas yields lower $LCoE$, even if some $LCoE$s obtained with the SunShot Vision Study case considering the *Allam* cycle in Tonopah are comparable to those obtained by SAM in Las Vegas, regardless of the cycle used.
- The trend followed by $LCoE$ is approximately symmetrical with respect to the performance metric (CF and E_{year}) and balanced by the financial model. Higher CF usually come with lower $LCoE$ but, if the two options with the lowest CF are considered -*Partial Cooling* cycle located in Tonopah for Cases 1 and 2-, it is found that Case 1 always yields

the highest $LCoE$ whereas the SunShot model can compensate for the CF effect in Case 3.

- If the same financial model is considered (Cases 1 and 2, Cases 3 and 4), the lowest $LCoE$s are achieved by plants presenting better performance metrics (higher CF and E_{year}), as observed in Figures 5.35(a) and (b) and 5.34(a) and (b). Based on this, increasing the capacity factor of a plant (and therefore its annual yield) is confirmed to be of capital importance to increase the feasibility of sCO_2-based CSP plants.

Based on the results presented, it is difficult to ascertain which the best power cycle is, given that they all yield similar Levelized Cost of Energy. Indeed, it is observed that the three power cycles yield very similar $LCoE$, most of them in the order of 8.5/9.5 ¢/kWh (see Figure 5.35(a) and (b)), and most of these small differences lie within the uncertainty incurred by all the assumptions made throughout this doctoral dissertation. In spite of this uncertainty, a global comparison can be made, defining the possible range of $LCoE$ values obtained for the three different cycles. This is shown in Figure 5.36.

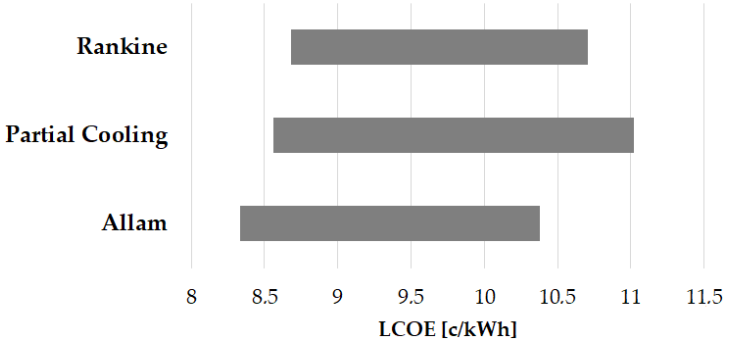

Figure 5.36: Range of $LCoE$ for CSP plants based on different power cycles.

The comparison in Figure 5.36 reveals that the lowest cost of electricity ($LCoE$) is obtained for the best combination of the *Allam* cycle (8.33 ¢/kWh), while the worst case based on the *Partial Cooling* cycle yields the highest $LCoE$ (11.02 ¢/kWh). The $LCoE$ range of plants based on steam turbines falls entirely within the values covered by the other cycles. The lack of a clear, unambiguous conclusion about the optimum CSP plant concept is a conclusion in itself. As a matter of fact, this result confirms the large potential of sCO_2 power cycles for CSP applications, which must be considered as a solid alternative to the standard steam Rankine cycle approach. Moreover, even if the results obtained are still far from the 6 ¢/kWh target set by the SunShot program, it must not be forgotten that the values of $LCoE$ presented in this document are estimates based on deliberately conservative assumptions. Therefore, it may be the case that mid-term CSP plants employing *Allam* and *Partial Cooling* cycles are able to achieve $LCoE$s lower than those obtained in this research and closer to the SunShot objective.

Further to the considerations made in the preceding paragraph, some works in literature already declare $LCoE$s in the order of 6 ¢/kWh for a sCO_2 plant based on the *Recompression* cycle and a set of more optimistic assumptions in terms of capital cost estimates [76]. This is certainly in contrast with the ample discussion in Chapter 4 which showed that, in spite of its great popularity, the *Recompression* cycle does not provide the best thermo-economic

performance.

As a wrap up, it is concluded that more accurate part-load models and integration schemes in SAM or equivalent software will prove that either the *Allam* or *Partial Cooling* cycle layouts have the potential to make a strong case for the next generation of CSP plants based on sCO_2 power cycles, enabling the ambitious objectives targeted by the SunShot Program.

5.9 Conclusions

The general methodology to estimate part-load performance of the *Allam* and *Partial Cooling* sCO_2 power cycles has been presented in this chapter, with the aim to assess the corresponding Levelized Cost of Energy $LCoE$. To achieve this objective, off-design prediction models for all the major equipment of the power block have been developed, in particular compressors and heat exchangers.

Regarding the heat exchangers, Printed Circuit Heat Exchangers in particular, a novel methodology based on the definition of a constant conductance ratio for on and off-design conditions has been presented and discussed, along with a methodology aimed to drastically reduce the computational cost of calculating the off-design performance of heat exchangers. This last method, based on the definition of a reduced order model employing the *Active Subspaces* methodology, results to be extremely interesting and efficient, and capable of reducing the computational cost of predicting part-load performance by up to a 99.98% whilst maintaining high accuracy.

Three different load control schemes have been considered: *Inventory*, *By-pass* and *Turbine Inlet Temperature* (or, simply, *Temperature*). A combination between the two former strategies is found to yield the best results, leading to good off-design cycle performance without detrimental effects on compressor operation. The thermal efficiency of the *Partial Cooling* cycle, starting at approximately 51% in rated conditions, remains at values higher than 50% down to 85% load. Below this load, thermal efficiency decreases when *By-pass* control is employed, showing values around 42% at a 50% load. The *Allam* cycle exhibits a more pronounced transition between *Inventory* and *By-pass* schemes. Thermal efficiency remains close to the rated value (45%) down to 90% load, where it experiences a 2.5% decrease due to the control strategy transition; below this, η_{th} decreases to 35% at 60% load. Considering heat exchanger efficiency, η_{HX}, the recuperators in the *Partial Cooling* cycle show efficiencies higher than 86% always, even at 50% of the load; on the contrary, the recuperator in the *Allam* cycle presents lower efficiency, in the order of 80% at 60% load.

With respect to the Levelized Cost of Energy, the System Advisor Model has been employed to calculate $LCoE$ at two different locations (Las Vegas and Tonopah, in Nevada) and two different sets of dispatch control schemes and financial parameters. In the most favourable cases, the *Partial Cooling* and *Allam* cycles provide an LCoE of 8.56 ¢/kWh and 8.33 ¢/kWh respectively, along with a Capacity Factor of around 59% and 62.5%. On the contrary, in the worst case scenarios, the LCoE of the *Partial Cooling* cycle increases to 11 ¢/kWh, with a CF slightly higher than 50%, while the values of the *Allam* cycle are 10.38¢/kWh and 55.4% respectively.

The results obtained for the CSP plants employing *Allam* and *Partial Cooling* sCO_2 cycles are compared with a reference plant based on a state-of-the-art steam Rankine cycle. The main finding is that both sCO_2 cycles have the potential to yield $LCoE$s comparable to those of the reference CSP plant, or even lower. Taking into account the conservative approach employed throughout the present work, especially in terms of economic estimations, this comes to confirm that sCO_2 poer cycles are an interesting alternative to enhance the competitiveness of CSP-STE plants in the mid to long term, even if tey do not seem to enable the drastic cost reductions claimed by some authors.

6 Conclusions

This thesis has presented a systematic approach, based on a thorough thermo-economic analysis, to selecting sCO_2 power cycles for Concentrated Solar Power applications with the aim to assess their actual potential to yield lower cost of electricity than state-of-the-art CSP plants based on steam turbines. This final chapter provides a closure to this work by presenting a critical review of the various assumptions and the methodology applied in the research, and by summarizing the main findings of it.

6.1 Critical review of assumptions and methodology

Assessing a trustworthy and thorough feasibility analysis of CSP plants employing sCO_2 power blocks is very challenging, mostly due to the low TRL of sCO_2 technology and to the scarcity of reliable cost-related information, especially for turbomachines. Furthermore, the comparison between several cycle configurations, characterized by different thermodynamic features and required boundary conditions, brings in additional complexity to the problem under analysis.

In consequence, a series of assumptions have been made throughout the present dissertation, in order to reduce the complexity of the problem down to a manageable level. In this section, these assumptions are revisited with the aim to assess the reliability of the results provided by the thesis, highlighting both the principal positive features and also the main flaws.

First of all, considering a single value of compressor inlet temperature may be regarded as an oversimplification. The value of 32ºC taken into account results to be only slightly higher than the supercritical point, and it could be argued that higher temperatures would be preferred in order to avoid strongly variable sCO_2 thermophysical properties. Nevertheless, the choice was pondered and considered reliable for the next reasons. On the one hand, 32ºC is well-established value in specific sCO_2 power cycle literature and does not undermine the validity of the results. Property databases like *Refprop* and *Coolprop* provide good approximations at temperatures 1ºC above the supercritical value, and considering higher temperatures would only lead to worse cycle thermal performances. On the other hand, looking into the future, 32ºC results would be suitable if sCO_2 blends were used in lieu of pure sCO_2 as this temperature would enable condensation of the working fluid and, hence, better thermal performance of the cycle. This is currently under research in the SCARABEUS project, funded by the European Commission under the H2020 programme and developed by an European consortium participated by the University of Seville.

Considering the thermodynamic comparison presented in Chapter 3, the efficiency of turbomachinery as calculated with lumped-volume models can be considered reliable, as well as the one-dimensional model employed for the heat exchangers, due to the fact that both are intended for on-design calculations only. Regarding the former equipment, a constant polytropic efficiency has been chosen, whose values can be considered consistent with the information available in literature. Moreover, the selection of polytropic instead of isentropic efficiency allows to better capture the influence of the very different pressure/temperature ratios of the cycles considered in the comparison. Along the same lines, the selection of the twelve cycles considered in Chapter 3 is deemed reliable, since it is the result of a thorough review of the state-of-the-art of sCO_2 technology provided in Chapter 2.

The PCHE design code employed in Chapter 4 is based on well-known and verified references, improved with the most recent thermal correlations presented in literature. Similarly, the *Conductance Ratio Method*, the original off-design performance model presented in Chapter 5, has been extensively proven against experimental data provided by manufacturers and users and also found in literature. On the contrary, the compressor performance maps used in this chapter might need a further check in the future, owing mostly to the low TRL of this technology and the lack of truly reliable information available in literature. Nevertheless, the maps obtained with *AxStream* and employed in Chapter 5 are still a good compromise and, therefore, constitute a suitable solution for the present dissertation. Finally, regarding the part-load performance of sCO_2 cycles, standard control strategies usually applied in closed cycle gas turbine applications are employed, along with the widely used software SAM.

As far as the economic analysis is concerned, the cost estimation process is inherently more uncertain than the design process. For this reason, the simplifying assumptions have to be made with even more care, in particular given the low TRL of sCO_2 technologies. This is why the economic analysis includes a thorough assessment of the effect of uncertainty.

Regarding the solar sub-system, solar field and tower are not strongly affected by the utilization of sCO_2, and the cost estimation provided by SAM can be considered satisfactory. The same can not be said for the solar receiver, this being the reason why two in-house correlations have been developed in order to improve the trustworthiness of the estimates and to take into account the higher receiver temperature required by the sCO_2 power cycle and the difference in heat capacity between FLiNaK and the standard solar salt. Finally, the in-house model employed for the Thermal Energy Storage system can be considered reliable since it has been validated against experimental data and modified to incorporate FLiNaK as HTF both thermodynamically and economically.

Similarly, the cost estimation of the Printed Circuit Heat Exchanger can be considered reliable given that it is based on the verified PCHE design code discussed earlier. Due to the lack of reliable cost data for sCO_2 turbomachinery, standard cost estimates for air compressors and centrifugal pumps are employed. This assumption does not undermine the validity of the cost estimation function inasmuch as the contribution of compressor and pump to the total installed cost is small compared to other power block equipment, and almost negligible in the context of the solar sub-system. Regarding sCO_2 turbine instead, this is expected to be less costly than steam turbines of similar output due to the lower footprint brought about by the

lower specific volume of the working fluid and the lower pressure ratio of the working cycle. For this reason, a series of correlations have been created in order to adjust the approximated cost estimation obtained with commercial software *Thermoflex* for state-of-the-art subcritical and supercritical steam turbines. Finally, the contributions of the Cooling Tower, Balance of Plant and other minor equipment to the total installed cost can be considered reliable since these are calculated with *Thermoflex* or directly obtained from well-known references found in literature.

With all this in mind, it is confirmed that the cost estimation methodology employed in this thesis is based on well-established guidelines, adjusted with dedicated correlations developed by the author and capable to take into account the different temperatures and Heat Transfer Fluids employed in both the solar subsystem and the power block. It is acknowledged though that a different approach could have been used and this is certainly an aspect worth looking into in further research carried out at the Department of Energy Engineering of the University of Seville.

6.2 Overall and specific conclusions

A number of questions were put forward at the beginning of this research, regarding the actual feasibility of a Concentrated Solar Power plant employing sCO_2 power cycle technology. Tentative answers to these questions, based on the findings of this research, are reported below:

- *For an actual power cycle, above which temperature do sCO_2 power cycles yield better thermodynamic performance than state-of-the-art steam cycles? Is this temperature achievable by the current or foreseen receiver technology?*
  A preliminary answer to this question was initially provided in Chapter 1, following Angelino's statement that sCO_2 power cycles are more efficient than Rankine steam cycles at turbine inlet temperatures higher than 600-650ºC. This assumption was then confirmed by the results presented in Chapter 3, showing that the thermal efficiency of a sCO_2 cycle achieves 55% at 770ºC turbine inlet temperature, which is almost 15 percentage points higher than contemporary steam cycles. Nevertheless, from a practical point of view, sCO_2 cycles presenting lower η_{th} (in the order of 50%) but higher temperature rise across the solar receiver were found to be more interesting in order to reduce installation costs, providing a better compromise between thermodynamic and economic features. It is worth noting that such values of thermal efficiency are still significantly higher than those enabled by steam cycles.
  With respect to the feasibility of achieving this temperature, it was not possible to provide a final answer to this question given that this impacts the design of the solar receiver dramatically, and this assessment was out of the scope of the thesis. Nevertheless, similar temperatures have already been considered in literature, and private communications with Abengoa Solar confirm that this value is achievable in a short-term future.
- *Even at a temperature range for which sCO_2 power cycles exhibit a clear thermodynamic advantage over contemporary steam technology, will they enable lower installation costs than state-of-the-art CSP plants based on steam turbines?*
  In the economic analysis presented in Chapter 4, sCO_2 cycles are proven to enable installation costs lower than 6000 $/kW with a 100% probability, and this value goes

down to roughly 5650 if an 85% confidence interval is considered. The latter value turns out to be lower than a state-of-the-art CSP plant, which is in the order of 5800$/kW [25]. Therefore, since the cost estimation methodology makes use of conservative assumptions, these results are deemed to demonstrate that sCO_2 power cycles have the potential to yield lower installations costs than steam powre plants.

- *Will sCO_2 power cycles enable a significant reduction of the LCoE of a CSP plant, making this technology competitive against steam-driven CSP and even gas or steam turbines run on fossil fuels? In particular, will sCO_2 power cycles enable the 6 ¢/kWh target cost of energy pursued by the Sunshot Programme [37]?*
  Considering the results obtained in Chapter 5, no clear answer can be provided for this question. On the one hand, sCO_2 cycles were found to enable Levelized Costs of Electricity between 8.3 and 11 ¢/kWh, depending on the location and dispatch control strategy considered. Such values are comparable to those of typical steam-driven CSP (even lower), but they are still higher than those enabled by combined cycle power plants running on natural gas. Nevertheless, in spite of the fact that the target cost pursued by the Sunshot Programme was not actually achieved, the competitiveness of this technology is still confirmed. In fact, it is worth noting that the results obtained by the present thesis probably overestimate sCO_2 installation costs and, therefore, LCoE. Moreover, significant uncertainty is still present when it comes to the cost estimation methodology of sCO_2 power cycle technology and part-load operation. Future research activities are therefore mandatory to demonstrate the actual potential of sCO_2 power cycles applied to CSP, but it can still be stated that the results presented in this thesis put this technology forward as a very interesting option, capable of enabling lower installation costs and LCoE than state-of-the-art CSP plants.

Regarding some more specific conclusions obtained throughout this dissertation, a good definition of maximum cycle temperature and pressure was found to be particularly important to enhance the thermal performance of the cycle. As discussed previously, a turbine inlet temperature of 750ºC is chosen, as a good compromise between high thermal efficiency and technical feasibility. On the other hand, maximum cycle pressures in the order of 30 MPa are found particularly interesting both thermodynamically and economically.
Moreover, the thesis confirms that combining thermodynamic and thermo-economic features of each cycle is vital when selecting the best cycle configuration. In Chapter 3, in fact, the *Recompression+IC+RH* and *Partial Cooling+RH* cycles were found to be the best options providing extremely good thermodynamic performance, with very high thermal efficiency and specific work (55% and 225 kJ/kg at 750ºC turbine inlet temperature). Nevertheless, in the economic comparison presented in Chapter 4, the temperature rise across the solar receiver was found to drastically affect installation costs. A low value of ΔT_{solar}, typical of largely recuperative cycles with high η_{th}, leads to much larger receiver and TES costs, which can triple the values obtained with higher temperature changes across the receiver. As a consequence, the *Partial Cooling* and *Allam* cycles were found to be the best configurations from a thermo-economic point of view, providing a very good compromise between economic and thermodynamic features and leading to thermal efficiencies and installation costs in the order of 50% and 5900 $/kW respectively.

Finally, regarding the part-load operation analysis presented in Chapter 5, the Levelized Cost of Electricity was seen to depend strongly on location, dispatch control strategy and financial

parameters. The *Allam* cycle yields the lowest value (8.33 ¢/kWh) in the best combination of these parameters and a whereas LCoE increases to 10.4 ¢/kWh if the least favorable combination is adopted. On the other hand, the *Partial Cooling* cycle yielded LCoE between 8.6 and 11 ¢/kWh. Therefore, no single conclusion about which the best cycle layout is could be achieved. Also, both sCO_2 cycles seem capable to provide LCoE values comparable to, or even lower than, Rankine steam cycles and this confirms that sCO_2 technology is interesting for CSP plants in the mid-term.

6.3 Future research activities

As it is always the case when wrapping up a long research work, one realizes the considerable number of things he would have wanted to add or study in more detail to further improve the reliability of his research, or to merely satisfy the curiosity that often arises spontaneously. Nevertheless, it would be impossible, and certainly not very appropriate, to dwell too much in this section, which could itself reach the extension of a short scientific report. Therefore, I would limit this section to suggesting some areas that, in my humble opinion, deserve further attention and should be investigated more deeply by further researchers:

- *Cost estimation methodology*: as said earlier in this chapter, cost estimation may be considered as the part of this thesis that is most strongly affected by uncertainty. The original correlations developed by the author and applied to existing databases and the incorporation of uncertainty assessment were aimed at overcoming this issue, but a more accurate analysis is certainly needed, particularly as the sCO_2 scientific and industrial communities develop more actual installations.
- *Off-design and part-load operation*: similarly, the analysis of off-design operation can be improved in future works, and this may be done following these suggested pathways: i) improving the design code of sCO_2 compressors previously developed at the Thermal Power Group of the University of Seville, including an off-design performance prediction tool and enabling the creation of performance maps; ii) if sCO_2 power cycles are to still be studied with SAM in the future, a deeper study of dispatch control and strategy should be done; iii) also, a tool capable of modeling the off-design performance of the solar sub-system could be developed and then integrated with sCO_2 power cycles employed in the power block; iv) finally, a deeper study of control strategies and their effect on the off-design performance of sCO_2 power cycles could be undertaken, developing a dynamic model and evaluating the response time of the different strategies.
- *Minimum cycle temperature of sCO_2 cycles*: as previously said in this chapter, the inherent problems caused by unstable sCO_2 thermo-physical properties in the vicinity of the supercritical point can be overcome completely by blending sCO_2 with other chemical compounds, shifting the pseudo-supercritical point of the mixture to a higher temperatures and enabling condensation of the working fluid at a higher temperature (hence using a pump in lieu of a compressor). This research is currently being developed by a consortium participated by the Thermal Power Group of the University of Seville through the H2020 programme of the European Commission.
- *Solar receiver design*: the solar receiver is the most critical equipment in the entire plant due to the challenging operating conditions and to the impact on overall plant performance. Therefore, deeper research regarding its thermal and mechanical design is highly recommended, and this is indeed an interesting topic for future developments.

A PCHE Design Code

This Annex describes the PCHE design code used to obtain the volume and mass of sCO_2 power cycles heat exchangers, in order to include them in the economic analysis in Chapter 4. The author does not claim any novelty in the present in-house code, since it is based on other works already published in sCO_2-specific literature. Nevertheless, this is a very important part of the thesis, since it allows to complete the economic comparison between the different sCO_2 cycles considered, and hence emphasis is put on verifying the code in order to ensure its the validity. In this regard, the newest correlations for wavy channels are employed, and a detailed thermal stress analysis is incorporated into the original code proposed in [246], in order to improve the results obtained and to make the code sensitive to operating pressures.

In the first part of this Annex, a flow chart of the entire design code is presented, discussing its thermal fundamentals and providing a draft geometry of the PCHE. Then, the thermal correlations used for the different fluids are reported (sCO_2, FLiNaK and water), along with the mechanical stress analysis.

A.1 Overall structure and thermodynamic principles

The in-house PCHE design code is based on the work by Gavic [268], which is in turn developed considering the handbook by Nellis and Klein [10].

The design process of the PCHEs begins with the complete definition of the cross sectional area of the heat exchanger, as shown in Figure A.1. A semicircular cross-sectional channel area is considered, with a diameter of 3 mm and channel pitch and plate thickness dependent on the mechanical stress analysis. Approximated values of these two parameters are 3.5 and 2 mm respectively. Both straight or zig-zag channels can be modeled by the in-house code.

Considering the control volume in Figure A.1(b), this is formed by four channels. The wall that separates the hot and cold channels is the plate of the heat exchanger whereas the vertical walls divide two adjoin channels on the cold or the hot sides. The number of channels in the cross sectional area depends on the height and width of the heat exchanger and on the specifications of the channel. The width and height of each PCHE are guessed at the beginning of the design process and then iterated until the target efficiency and pressure drops are achieved. Their mathematical formulation is provided in Eq.(A.1), where H and W are height and width of the cross sectional area taken into account, while $N_{ch,ver}$ and $N_{ch,hor}$ represent the number of vertical and horizontal channels. The total number of channels ($N_{ch,tot}$) is

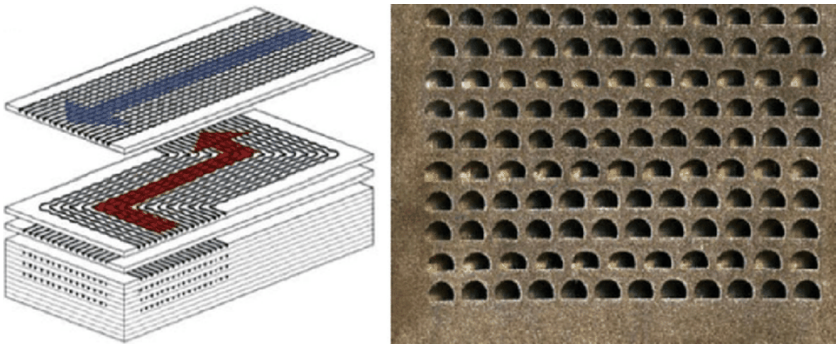

(a) Counter-flow Printed Circuit Heat Exchanger [9].

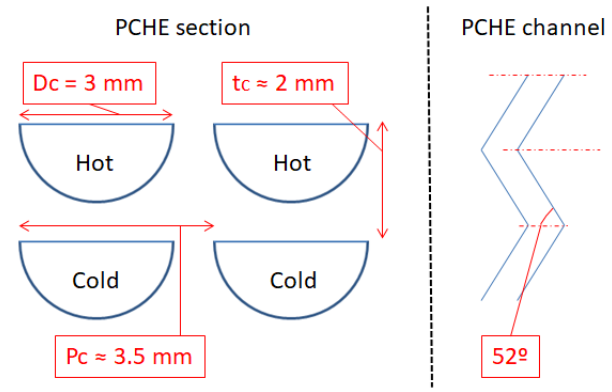

(b) Cross section of the counter-flow PCHE considered in the in-house model.

Figure A.1: Cross-sectional area of the counter-flow PCHE: actual heat exchanger and model.

obtained multiplying these two values.

$$H = N_{ch,ver} * t_c + (t_c + \frac{D_c}{2}); \qquad W = N_{ch,hor} \cdot (P_c) + p_c; \qquad (p_c = P_c - D_c) \tag{A.1}$$

The ϵ-NTU methodology cannot be applied directly to sCO_2 heat exchangers or to any other heat exchanger where fluid properties on one of the sides are not constant. This problem is nevertheless solved by dividing the heat exchanger into a number of subdivisions to produce an equivalent series arrangement of smaller heat exchangers each one of which fulfills this requirement [10]. The resulting temperature and pressure gradients in each subdivision turn out to be significantly smaller, hence bringing about negligible variations of the thermo-physical properties of the fluids and enabling the application of the ϵ-NTU methodology.

In order to apply this method, it is assumed that each sub-heat exchanger has the same duty (total heat exchange), as shown in Figure A.2 and Eq.(A.2):

$$\dot{Q}_i = \frac{\dot{Q}_{tot}}{N} \qquad for \quad i = 1...N \tag{A.2}$$

The total heat duty of the heat exchanger is calculated from the application of energy conservation to the results of the thermodynamic analysis, originally calculated assuming a target

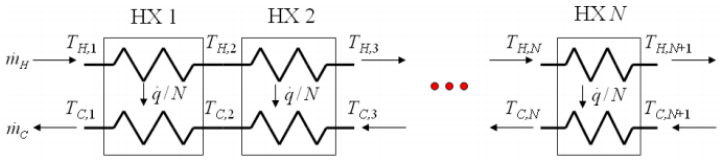

Figure A.2: Sub-HX model with counter-flow configuration [10].

effectiveness of the heat transfer equipment. Then, this duty is evenly distributed amongst all the internal divisions. Once $\dot{Q}_i$ (particular heat duty) is known, it is possible to calculate the effectiveness, number of transfer units and overall heat transfer coefficient of each sub-HX, using Eqs.(A.3-A.5). All the symbols in these equations are reported in the Nomenclature.

$$\epsilon_i = \frac{\dot{Q}_i}{\dot{C}_{min,i} \cdot (T_{H,i} - T_{C,i+1})} \qquad for \quad i = 1...N \tag{A.3}$$

$$NTU_i = \frac{1}{1 - \dot{C}_i^*} \cdot \ln \frac{1 - \epsilon_i \cdot \dot{C}_i^*}{1 - \epsilon_i} \qquad with \quad \dot{C}_i^* = \frac{\dot{C}_{min,i}}{\dot{C}_{max,i}} \qquad for \quad i = 1...N \tag{A.4}$$

$$UA_i = NTU \cdot \dot{C}_{min,i} \qquad for \quad i = 1...N \tag{A.5}$$

With the overall heat transfer coefficient UA_i, it is possible to obtain the required length of each subdivision i (ΔL_i, see Figure A.3) which ensures that the corresponding heat duty $\dot{Q}_i$ is achieved.

Figure A.3 shows the five different contributions to heat transfer within the heat exchanger taken into account in the present model: two convective thermal resistances (hot $R_{conv,H}$ and cold $R_{conv,C}$), conductive thermal resistance of the plate ($R_{cond,p}$) and contributions of the lateral walls, i.e. the walls that separate two neighbor channels. These last two conductive resistances are neglected given that the flow in adjacent hot or cold channels is considered to be at approximately the same temperature. The thermodynamic correlations available to calculate Nusselt number and friction factor are discussed in the next section.

Figure A.4 provides the flow-chart of the entire methodology.

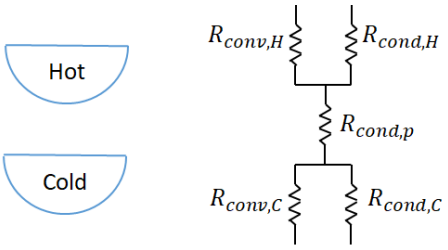

$$R_{conv,H} = \frac{1}{h_H A_H} \qquad for\ i = 1 \dots N$$

$$R_{cond,p} = \frac{2t_c}{k_{metal} A_{cond}} \qquad A_{cond,i} = \Delta L_i P_C$$

$$R_{conv,C} = \frac{1}{h_C Ac} \qquad A_{H,i} = A_{C,i} = \Delta L_i (D_C + {}^{\pi D_c}/_{2})$$

Figure A.3: Thermal resistance in a subdivision of a PCHE.

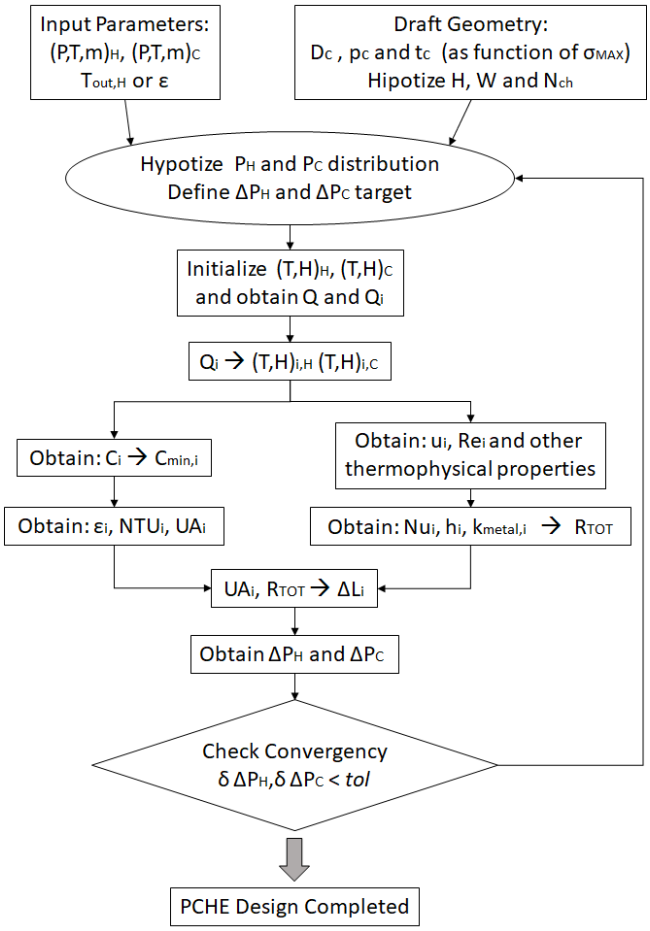

Figure A.4: Flow chart of the PCHE design.

A.2 Correlations

There are several heat transfer correlations available to calculate Nusselt number and friction factor depending on flow regime: laminar, transition or turbulent. In all cases, fully-developed thermal and hydrodynamic boundary layers are assumed given the aspect ratio of the channels: very long in comparison with channel diameter, enabling to neglect the effect of the entry region. It is also noted here that this assumption is conservative inasmuch as assuming fully developed flow yields a lower total heat transfer. In other words, the heat exchangers so calculated are slightly larger than they would otherwise be had the entry region been modeled in detail.

Straight Channels

If $3000 < Re_i < 5x10^6$:

$$f_{c,i} = (0.790 \cdot \ln(Re_i) - 1.64)^{-2} \tag{A.6}$$

$$Nu_{x,i} = \frac{(f_{c,i}/8) \cdot (Re_i - 1000) \cdot Pr_i}{1 + 12.7 \cdot (Pr_i^{2/3} - 1) \cdot \sqrt{f_{c,i}/8)}} \tag{A.7}$$

If $Re_i < 3000$:

$$f_{c,i} = \frac{15.78}{Re_i} \tag{A.8}$$

$$Nu_{x,i} = 4.089 + (\frac{\frac{f_{c,i}}{8} \cdot (5000 - 1000) \cdot Pr_i}{1 + 12.7 \cdot (Pr_i^{2/3} - 1) \cdot \sqrt{f_{c,i}/8)}} - 4.089) \cdot \frac{Re_i - 2300}{5000 - 2300} \tag{A.9}$$

These correlations, taken from [73], are valid for sCO_2, water and FLiNaK (molten salt). In the latter case, Eq.(A.9) is simplified and the resulting Nusselt has a constant value of 4.089.

Zig-Zag Channels

The correlations used for sCO_2 and water are provided here. Taken from [73], they apply to a zig-zag angle of 52° (see Figure A.1(b)) and are valid for Reynolds number in the range 3500-10000 and Prandtl numbers between 0.75 and 2.2.

$$f_{c,i} = 0.1924 \cdot Re_i^{0.091} \tag{A.10}$$

$$Nu_{x,i} = 0.1696 \cdot Re_i^{0.629} \cdot Pr_i^{0.317} \tag{A.11}$$

Regarding FLiNaK, the following correlations are used, once again obtained from [73], considering a zig-zag angle of 15° and laminar flow.

$$f_{c,i} = \frac{15.78 + 0.0487 \cdot Re_i^{0.84}}{Re_i} \tag{A.12}$$

$$Nu_{x,i} = 4.089 + 0.00497 \cdot Re_i^{0.95} \cdot Pr_i^{0.55} \tag{A.13}$$

Pressure drops

Regarding pressure drops across the PCHE, the approach found in Dostal's work is employed [67]. Eq.(A.14) is used to calculate primary friction losses through PCHE channels, while secondary pressure losses at inlet and outlet are obtained with Eq.(A.15).

$$\Delta P_{f,i} = \frac{f_{c,i} * \Delta L_i}{D_{hyd}} \rho_i \frac{u_i^2}{2}, \qquad where \quad D_{hyd} = \frac{4 \cdot Area}{Perimeter} = \frac{4 \cdot \frac{\pi D_c^2}{8}}{\frac{\pi \cdot D_c}{2} + D_c} \tag{A.14}$$

$$\Delta P_{inlet} = 0.5 \cdot \frac{\rho_{inlet} \cdot u_{inlet}^2}{2} \qquad \Delta P_{outlet} = 1 \cdot \frac{\rho_{outlet} \cdot u_{outlet}^2}{2} \tag{A.15}$$

A.3 Mechanical stress analysis

The analysis of mechanical stress is based on the work published by Yoon et al. at Idaho National Laboratory [13]. Fixing channel diameter and the maximum allowable mechanical stress of the material under consideration (σ_{MAX}, see Figure 4.7 in Chapter 4), channel pitch and plate thickness are strongly dependent on the pressure gradient between the hot and cold sides of the PCHE. These geometrical parameters are obtained with Eqs.(A.16,A.17) respectively. It is worth noting though that $P_{in,Pmax}$ and $P_{in,Pmin}$ can refer to either the hot or the cold side of the PCHE, depending on which heat exchanger is considered. For instance, in a recuperator, the cold side (generally the compressor outlet) is at a higher pressure than the hot side (turbine outlet), and the same applies to sCO_2/FLiNaK heaters. On the contrary, the sCO_2 side is at higher temperature and pressure in the coolers.

$$P_c = D_c \cdot \frac{1 + (P_{in,Pmax} - P_{in,Pmin})}{\sigma_{MAX}} \tag{A.16}$$

$$t_p = \frac{D_c}{2} \cdot \sqrt{\frac{\sigma_{MAX} - P_{in,Pmax}}{\sigma_{MAX} + 2 \cdot P_{in,Pmin} - P_{in,Pmax}}} \tag{A.17}$$

A.4 Verification of the code

Providing an exhaustive validation of the in-house PCHE design code is challenging due to the absolute lack of information published in literature. Therefore, in order to validate the design code of PCHEs, the recuperator of a standard *Allam* cycle is modeled and the results are compared with those obtained with the *CRM* methodology, already validated against experimental data from Alfa Laval in Chapter 5 and further in [246]. The main operating conditions, taken from [269], are summarized in Table A.1. It is worth noting that the working fluid is pure CO_2

in lieu of the gas mixture flowing in the *Allam* cycle. This enables easier property evaluation even if it brings about some deviations in the final results. The conclusions of the analysis regarding the validity of the scaling methodology should not be affected by this change, since both methods use pure sCO_2.

The default geometry considered in the application of the PCHE design code to the operating conditions in Table A.1 is slightly different from the one presented in Figure A.1(b) since a channel diameter of 2 mm is considered.

	T_{in} [°C]	$p_{in}[bar]$	T_{out} [°C]	$p_{out}[bar]$	$\dot{m}[kg/s]$
sCO2 (hot side)	776.9	30.86	102.9	30.05	290
sCO2 (cold side)	81.9	297.62	624.6	297.48	290

Table A.1: Operating conditions of the selected recuperator.

The off-design case studies are summarized in Table A.2 along with the outlet temperatures and pressures predicted by the scaling method. The inlet temperatures and pressures remain constant (boundary conditions) whilst the mass flow rates on both sides decrease from the rated value down to 25% of the design mass flow.

		PCHE Design Code				CRM Methodology			
$\dot{m_{CO2}}$ $[kg/s]$	Q $[kW]$	$T_{out,h}$ [°C]	$T_{out,c}$ [°C]	$p_{out,h}$ $[bar]$	$p_{out,c}$ $[bar]$	$T_{out,h}$ [°C]	$T_{out,c}$ [°C]	$p_{out,h}$ $[bar]$	$p_{out,c}$ $[bar]$
58.0	44599	102.9	624.6	30.05	297.48	102.9	624.5	30.05	297.48
55.1	42417	102.1	625.3	30.12	297.49	102.3	625.1	30.14	297.49
52.2	40230	101.3	625.9	30.19	297.50	101.6	625.7	30.21	297.51
49.3	38038	100.5	626.6	30.25	297.51	100.9	626.3	30.28	297.52
46.4	35841	99.6	627.3	30.31	297.51	100.2	626.9	30.35	297.53
43.5	33639	98.8	628.0	30.37	297.52	99.4	627.5	30.41	297.54
40.6	31432	98.0	628.7	30.42	297.53	98.6	628.2	30.48	297.55
37.7	29220	97.2	629.4	30.48	297.54	97.8	628.9	30.53	297.56
34.8	27002	96.4	630.0	30.53	297.55	96.9	629.6	30.58	297.57
31.9	24778	95.6	630.7	30.57	297.55	96.0	630.4	30.63	297.58
29.0	22549	94.9	631.3	30.61	297.56	95.1	631.2	30.67	297.59
26.1	20313	94.2	631.9	30.65	297.57	94.1	632.0	30.71	297.59
23.2	18071	93.6	632.4	30.69	297.58	93.0	632.9	30.74	297.60
20.3	15822	93.1	632.8	30.72	297.58	91.9	633.8	30.77	297.60
17.4	13565	93.0	632.9	30.75	297.59	90.7	634.8	30.79	297.61
14.5	11297	93.5	632.5	30.78	297.59	89.4	635.9	30.81	297.61

Table A.2: Operating conditions of the selected recuperator.

The outlet temperatures on both sides of the recuperator are presented graphically in Figures A.5(a) and (b) . A very good match between the PCHE model and the CRM methodology is observed for loads higher than 50%. The deviation is small for loads between 40% and 50% and, below 40%, there is an evident mismatch between both models. Since the PCHE design code in the present doctoral dissertation is meant only for on-design conditions, it can be considered verified by these results. Nevertheless, a discussion about the observed mismatch is reported here in order to provide a deeper insight into the thermal model of the PCHE.

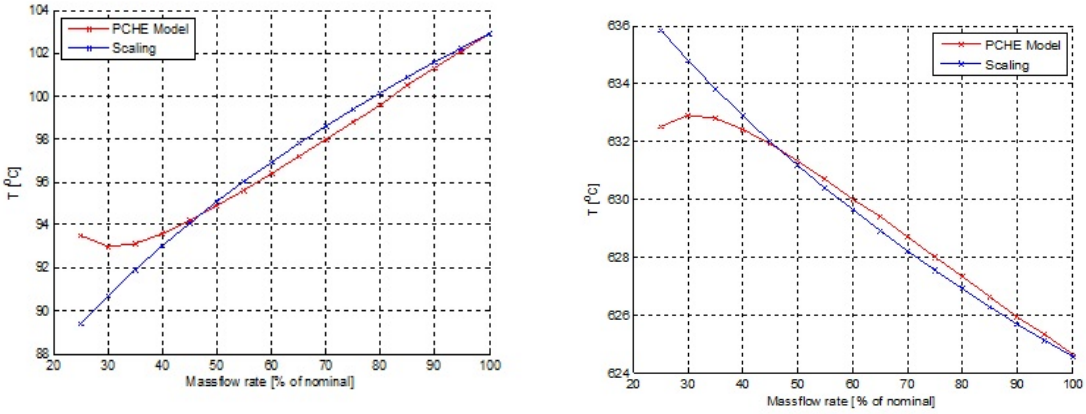

(a) Predicted outlet temperature on the hot (low pressure) side.

(b) Predicted outlet temperature on the hot (high pressure) side.

Figure A.5: Predicted outlet temperatures of the selected recuperator.

A closer look into the results of the PCHE model reveals that the root cause for the deviation observed at loads lower than 40% is that the flow becomes laminar. Indeed, at very low loads, the velocity of the flow decreases substantially and so does Reynolds number. At about 40% load, local Reynolds numbers decrease to values lower than 3000 which is the assumed critical value [10]. This is easily observed in Figure A.6 where Re on the hot and cold sides is plotted for 25% and 100% load.

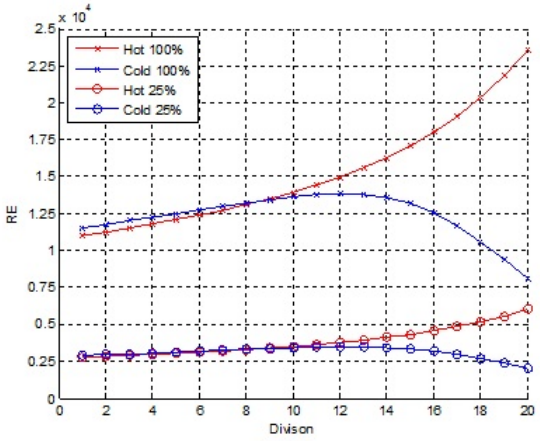

Figure A.6: Average Reynolds number on both sides as predicted by the PCHE model at various load settings. In this figure, the hot side of the heat exchanger flows from left to right while the cold side of the heat exchanger flows leftwards.

At full load, the Reynolds number is higher than 10^4 everywhere in the heat exchanger. Nevertheless, at 25% load, low values of Re in the entry regions of both sides bring about laminar flow locally, hence lower heat transfer coefficients (h) and higher thermal resistance ($1/hA$).

This hinders heat transfer locally and brings about a higher temperature gradient at both ends of the heat exchanger, as observed in Figures A.5(a) and (b). It should also be noted that the larger temperature difference at both ends of the equipment is not due to laminar flow on both sides but just to low heat transfer coefficients on one side. In other words, the pattern exhibited on both sides is an increasing *Re* from inlet to roughly 50% of the HX length and a later decrease to values below critical. These latter values are not likely to bring about laminar flow as the flow is also influenced by the upstream regime.

B Off-design performance of the Partial Cooling cycle

This Annex provides the results of the off-design performance of the *Partial Cooling* cycle that are not included in Chapter 5. Firstly, pressure-enthalpy and enthalpy-entropy diagrams are provided for each control strategy, representing compressor C3 only for the highest and lowest load to improve the readability of the plots. Secondly, the off-design performance of compressors C1 and C3 is presented.

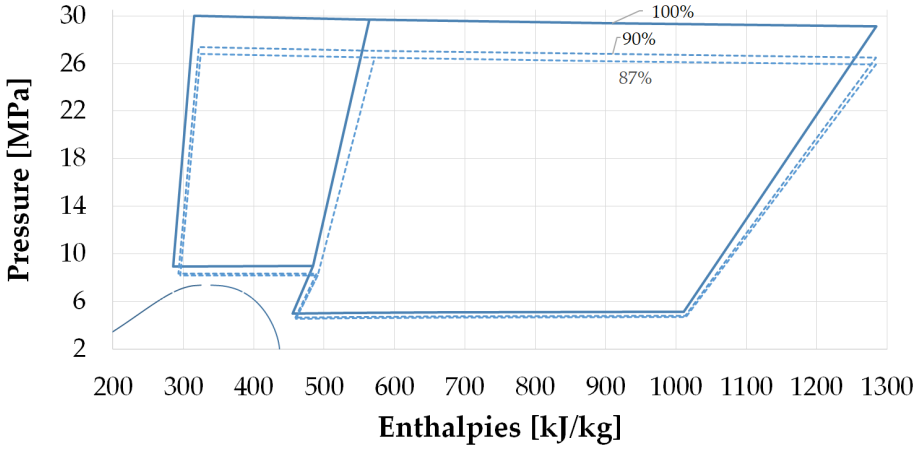

(a) Pressure-enthalpy diagram of the *Partial Cooling* cycle at partial load considering *Inventory* control strategy.

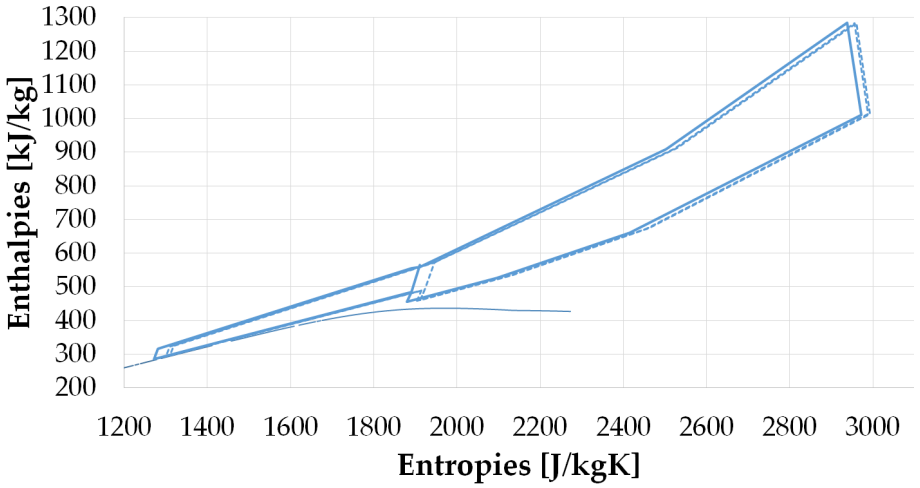

(b) Enthalpy-entropy diagram of the *Partial Cooling* cycle at partial load considering *Inventory* control strategy.

Figure B.1: Pressure-enthalpy and Enthalpy-entropy diagrams of the *Partial Cooling* cycle at partial load considering *Inventory* control strategy.

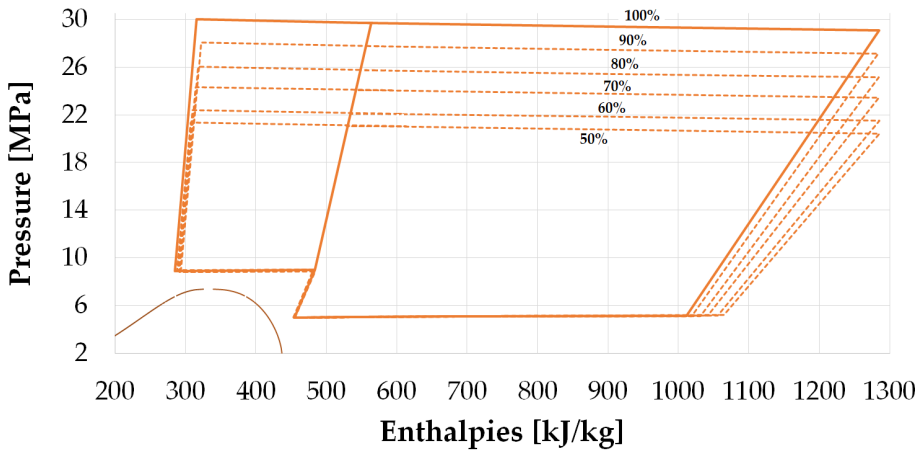

(a) Pressure-enthalpy diagram of the *Partial Cooling* cycle at partial load considering *By-pass* control strategy.

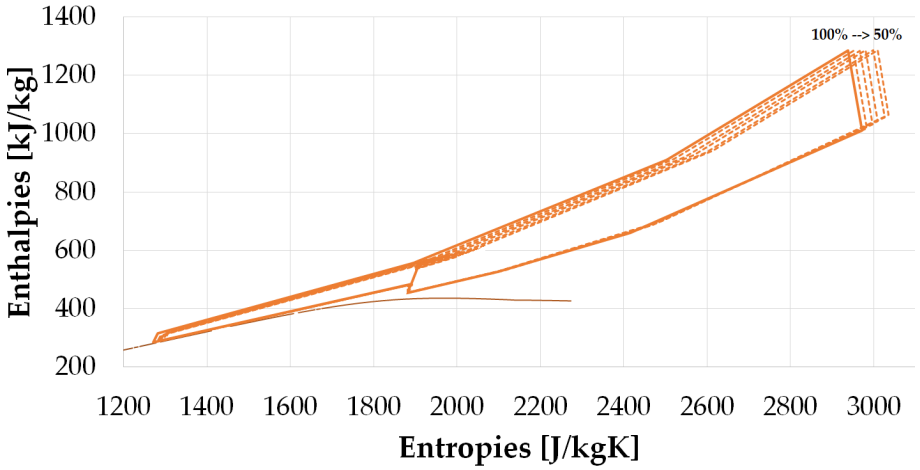

(b) Enthalpy-entropy diagram of the *Partial Cooling* cycle at partial load considering *By-pass* control strategy.

Figure B.2: Pressure-enthalpy and Enthalpy-entropy diagrams of the *Partial Cooling* cycle at partial load considering *By-pass* control strategy.

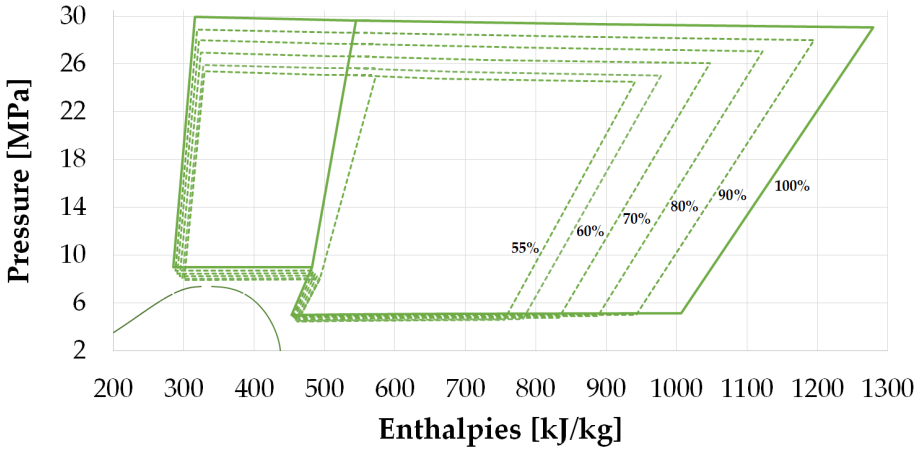

(a) Pressure-enthalpy diagram of the *Partial Cooling* cycle at partial load considering *Temperature* control strategy.

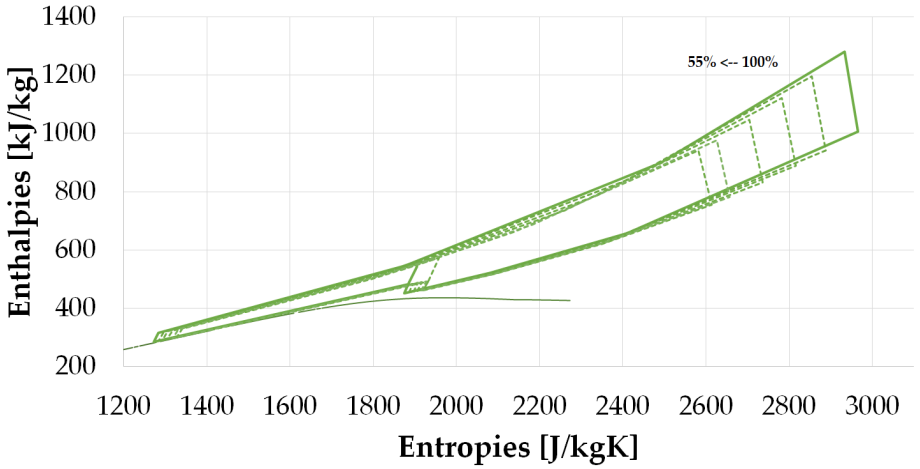

(b) Enthalpy-entropy diagram of the *Partial Cooling* cycle at partial load considering *Temperature* control strategy.

Figure B.3: Pressure-enthalpy and Enthalpy-entropy diagrams of the *Partial Cooling* cycle at partial load considering *Temperature* control strategy.

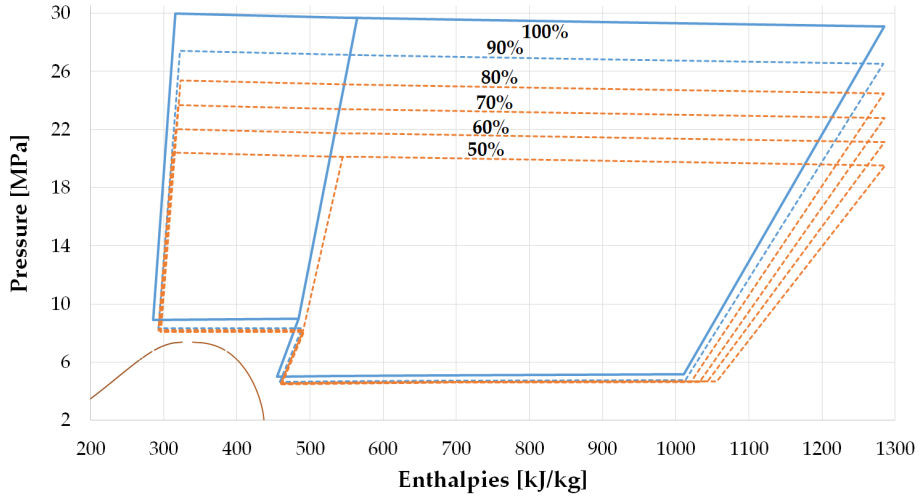

(a) Pressure-enthalpy diagram of the *Partial Cooling* cycle at partial load considering best control strategy.

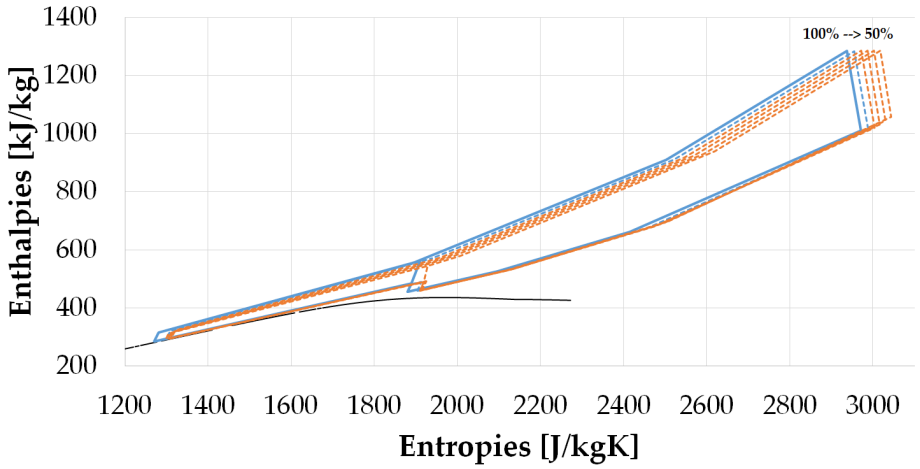

(b) Enthalpy-entropy diagram of the *Partial Cooling* cycle at partial load considering best control strategy.

Figure B.4: Pressure-enthalpy and Enthalpy-entropy diagrams of the *Partial Cooling* cycle at partial load considering the best control strategy, a combination of *Inventory* and *By-pass*.

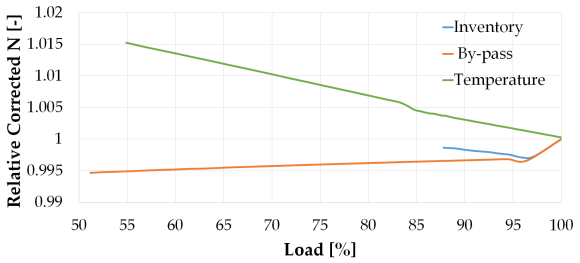

(a) Relative corrected shaft speed N_{corr}.

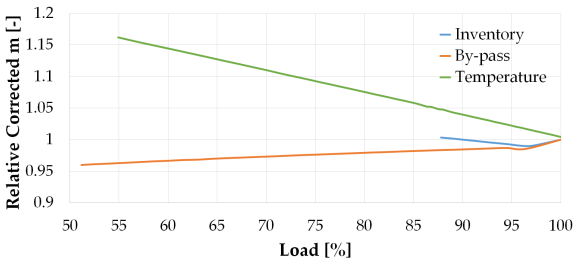

(b) Relative corrected mass flow rate $\dot{m}_{corr}$.

Figure B.5: Partial load performance of compressor C1 in the *Partial Cooling* cycle - part 1. The three different control strategies are considered.

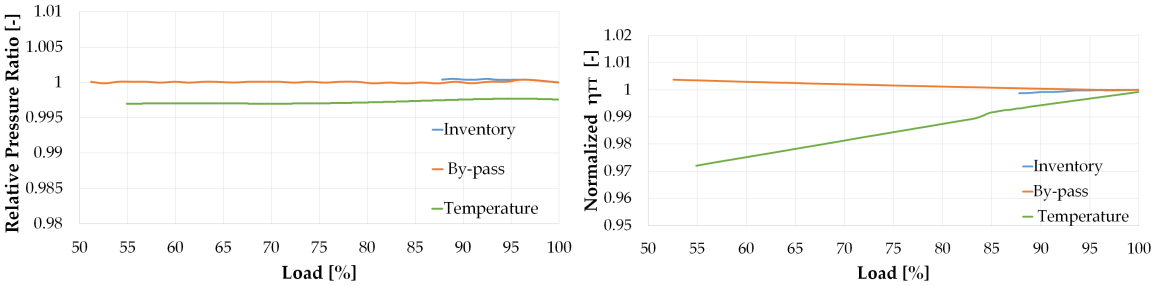

(a) Relative pressure ratio PR.

(b) Relative total-to-total efficiency η_{TT}.

Figure B.6: Partial load performance of compressor C1 in the *Partial Cooling* cycle - part 2. The three different control strategies are considered.

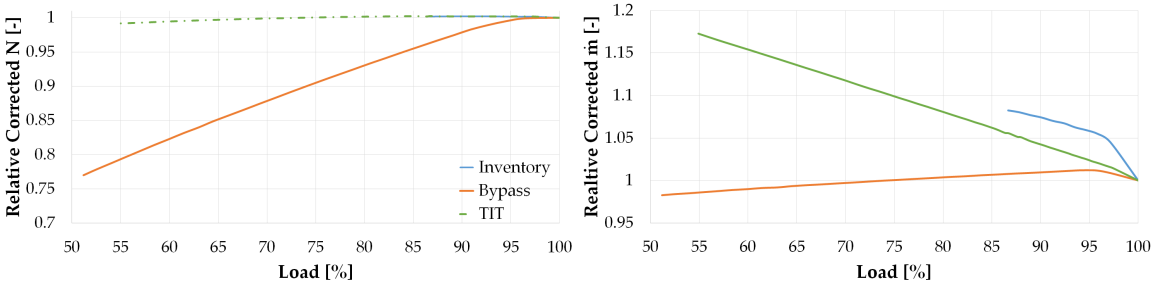

(a) Relative corrected shaft speed N_{corr}.

(b) Relative corrected mass flow rate $\dot{m}_{corr}$.

Figure B.7: Partial load performance of compressor C3 in the *Partial Cooling* cycle - part 1. The three different control strategies are considered.

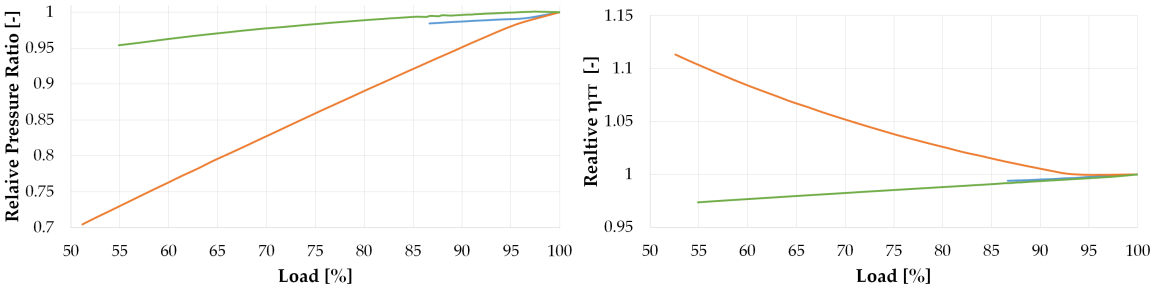

(a) Relative pressure ratio PR.

(b) Relative total-to-total efficiency η_{TT}.

Figure B.8: Partial load performance of compressor C3 in the *Partial Cooling* cycle - part 2. The three different control strategies are considered.

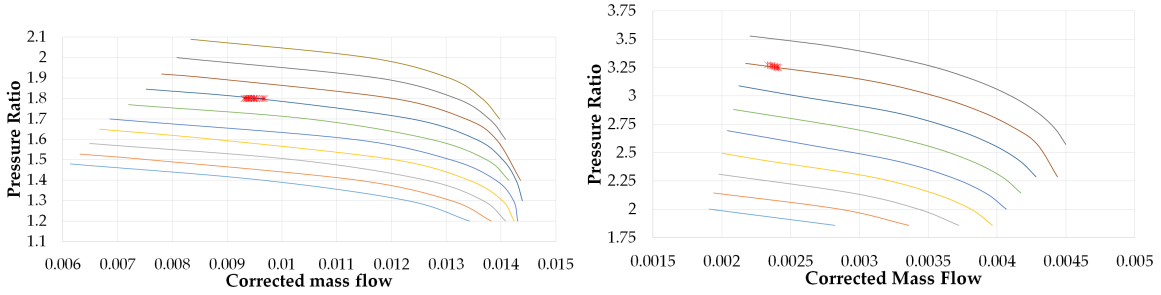

(a) Excursion of compressor C1 in the *Partial Cooling* cycle when operating at partial load. *Inventory* control.

(b) Excursion of compressor C3 in the *Partial Cooling* cycle when operating at partial load. *Inventory* control.

Figure B.9: Partial load performance of compressors C1 and C3 in the *Partial Cooling* cycle for *Inventory* control strategy.

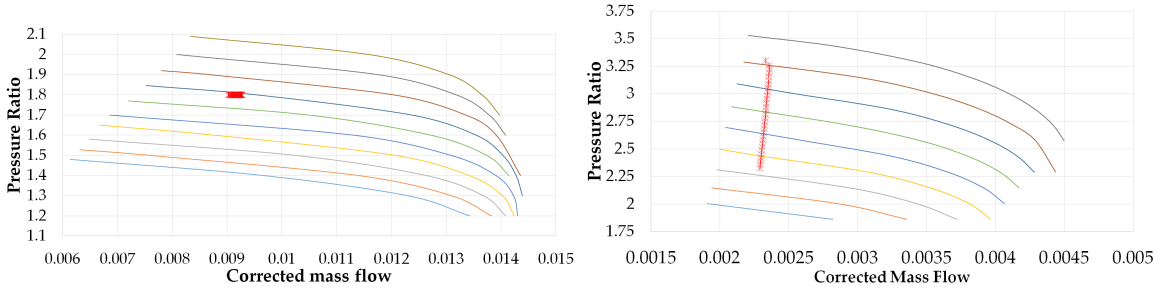

(a) Excursion of compressor C1 in the *Partial Cooling* cycle when operating at partial load. *By-pass* control.

(b) Excursion of compressor C3 in the *Partial Cooling* cycle when operating at partial load. *By-pass* control.

Figure B.10: Partial load performance of compressors C1 and C3 in the *Partial Cooling* cycle for *By-pass* control strategy.

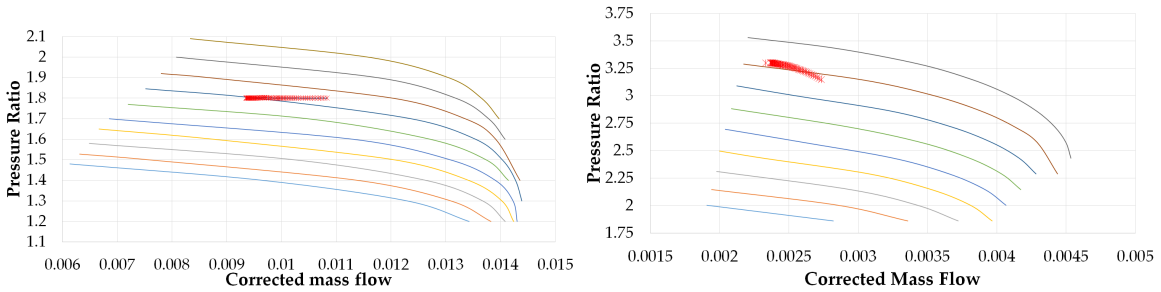

(a) Excursion of compressor C1 in the *Partial Cooling* cycle when operating at partial load. *Temperature* control.

(b) Excursion of compressor C3 in the *Partial Cooling* cycle when operating at partial load. *Temperature* control.

Figure B.11: Partial load performance of compressors C1 and C3 in the *Partial Cooling* cycle for *Temperature* control strategy.

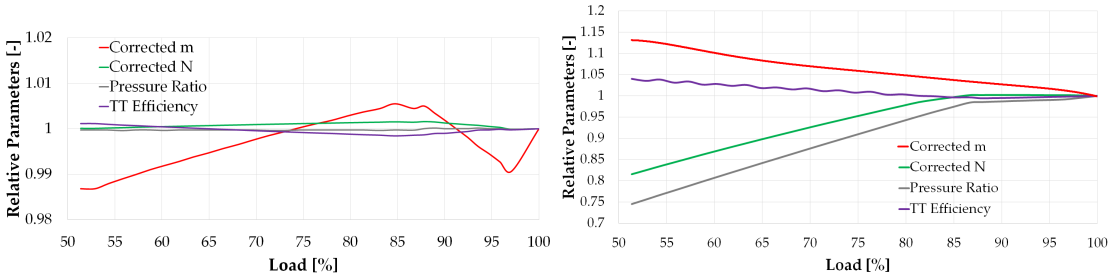

(a) Part-load performance of compressor C1 in the *Partial Cooling* cycle.

(b) Part-load performance of compressor C3 in the *Partial Cooling* cycle.

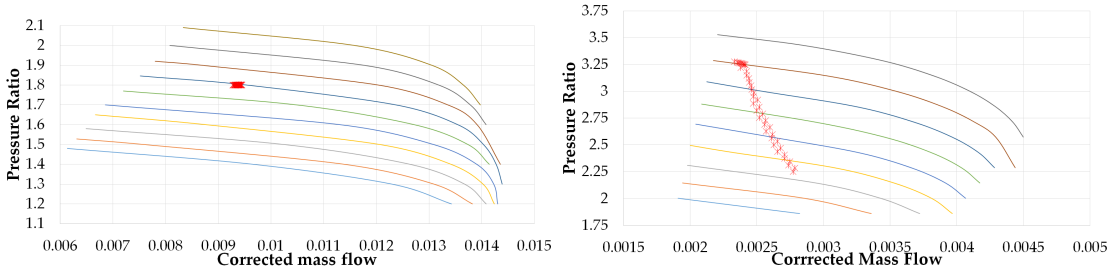

(c) Running line of compressor C1 in the *Partial Cooling* cycle.

(d) Running line of compressor C3 in the *Partial Cooling* cycle.

Figure B.12: Part-load performance of compressors C1 and C3 in the *Partial Cooling* cycle when using the best control strategy.

C Off-design performance of the Allam cycle

This Annex provides the results of the off-design performance of the *Allam* cycle that are not included in Chapter 5. Firstly, pressure-enthalpy and enthalpy-entropy diagrams are provided for each type of control strategy. Secondly, the off-design performance of compressors C1 and C2 is presented.

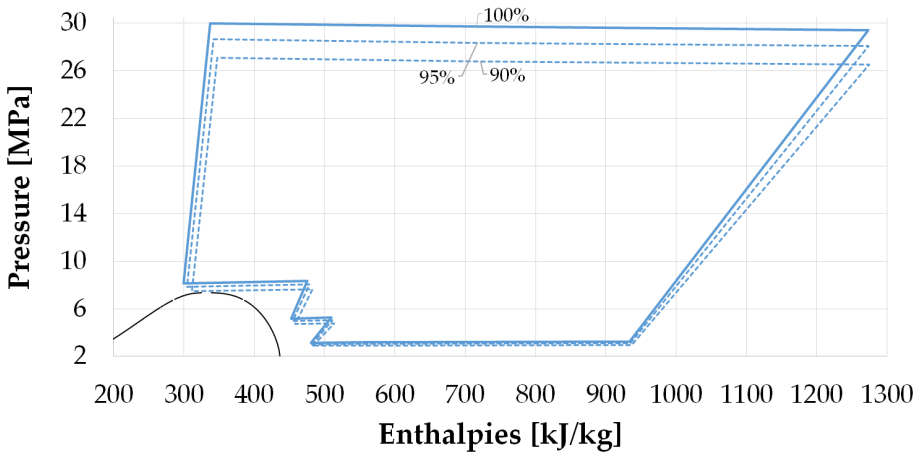

(a) Pressure-enthalpy diagram of the *Allam* cycle at partial load considering *Inventory* control strategy.

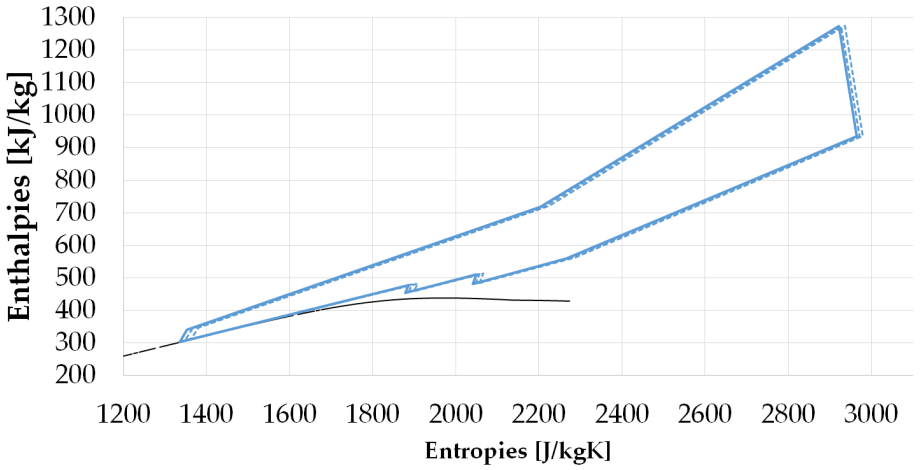

(b) Enthalpy-entropy diagram of the *Allam* cycle at partial load considering *Inventory* control strategy.

Figure C.1: Pressure-enthalpy and Enthalpy-entropy diagrams of the *Allam* cycle at partial load considering *Inventory* control strategy.

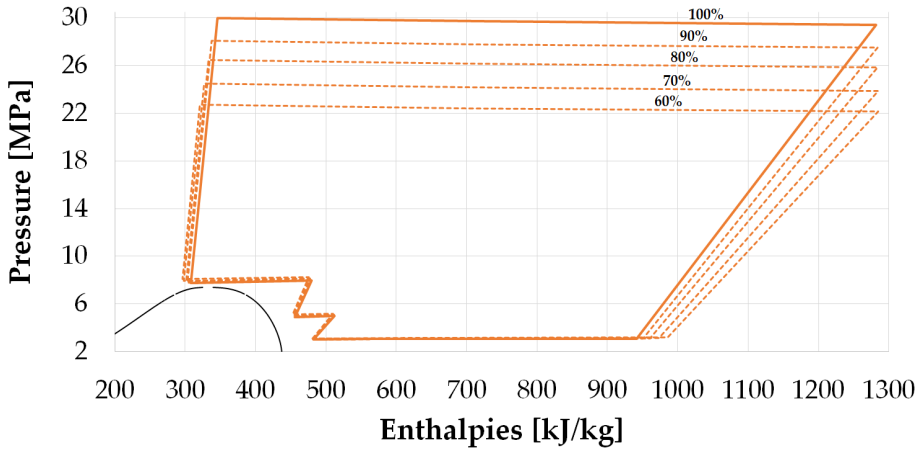

(a) Pressure-enthalpy diagram of the *Allam* cycle at partial load considering *By-pass* control strategy.

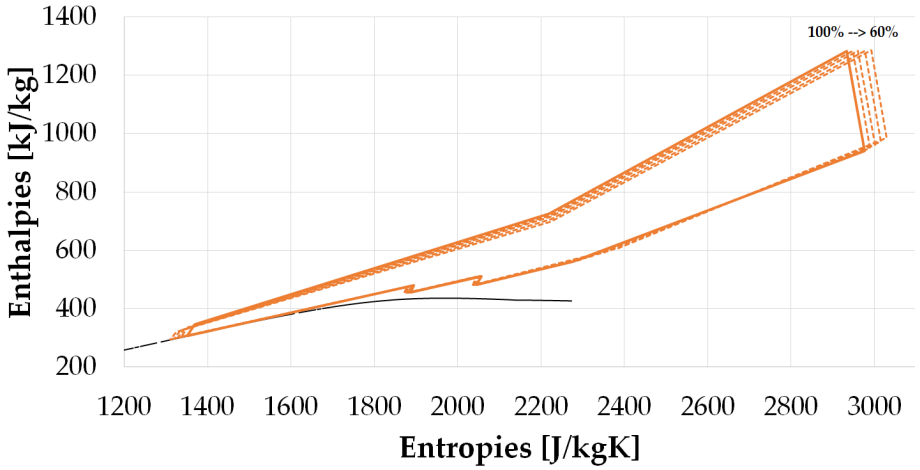

(b) Enthalpy-entropy diagram of the *Allam* cycle at partial load considering *By-pass* control strategy.

Figure C.2: Pressure-enthalpy and Enthalpy-entropy diagrams of the *Allam* cycle at partial load considering *By-pass* control strategy.

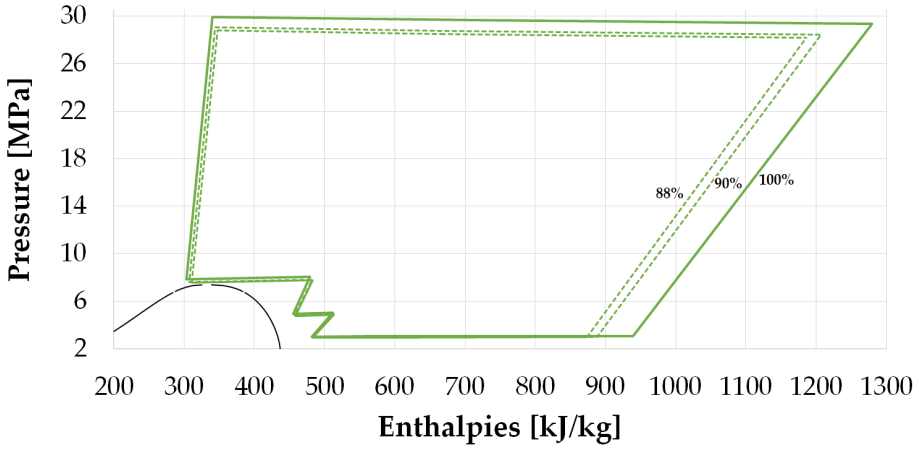

(a) Pressure-enthalpy diagram of the *Allam* cycle at partial load considering *Temperature* control strategy.

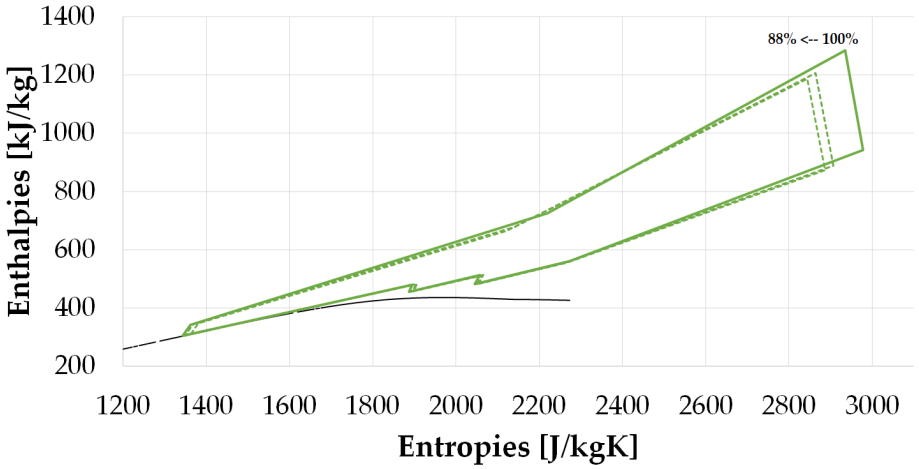

(b) Enthalpy-entropy diagram of the *Allam* cycle at partial load considering *Temperature* control strategy.

Figure C.3: Pressure-enthalpy and Enthalpy-entropy diagrams of the *Allam* cycle at partial load considering *Temperature* control strategy.

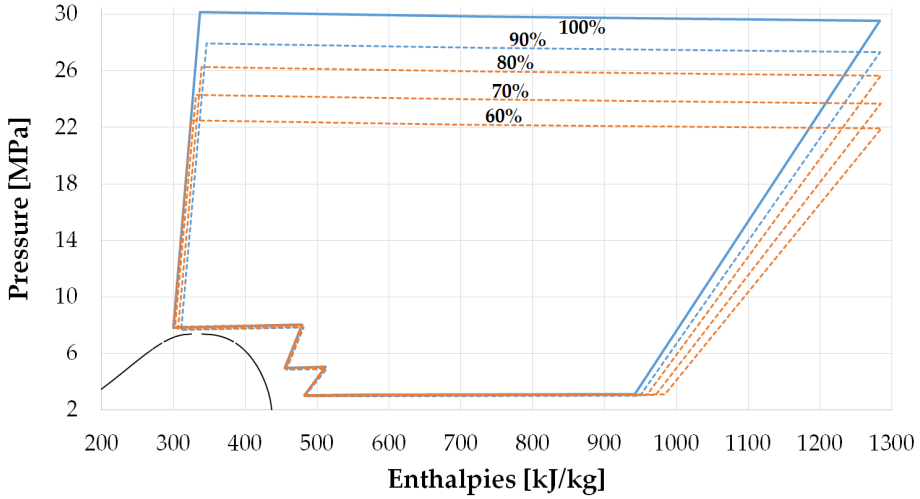

(a) Pressure-enthalpy diagram of the *Allam* cycle at partial load considering best control strategy.

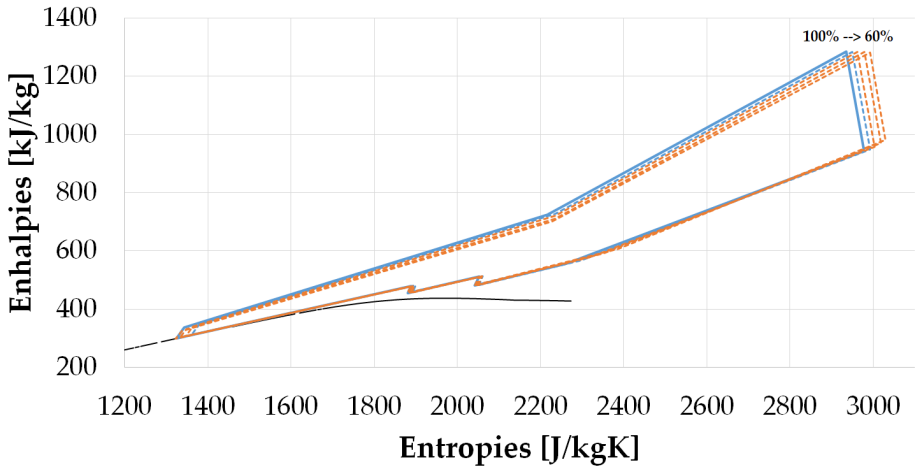

(b) Enthalpy-entropy diagram of the *Allam* cycle at partial load considering best control strategy.

Figure C.4: Pressure-enthalpy and Enthalpy-entropy diagrams of the *Allam* cycle at partial load considering best control strategy.

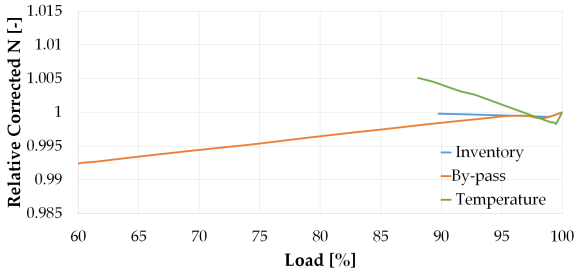

(a) Relative corrected shaft speed N_{corr}.

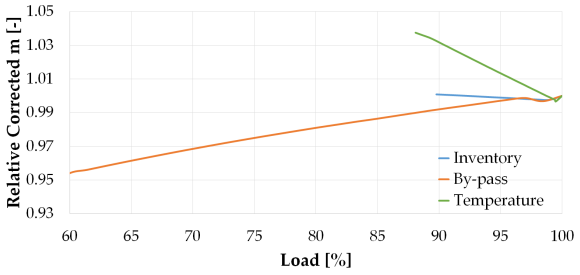

(b) Relative corrected mass flow rate $\dot{m}_{corr}$.

Figure C.5: Partial load performance of compressor C1 in the *Allam* cycle - part 1. The three different control strategies are considered.

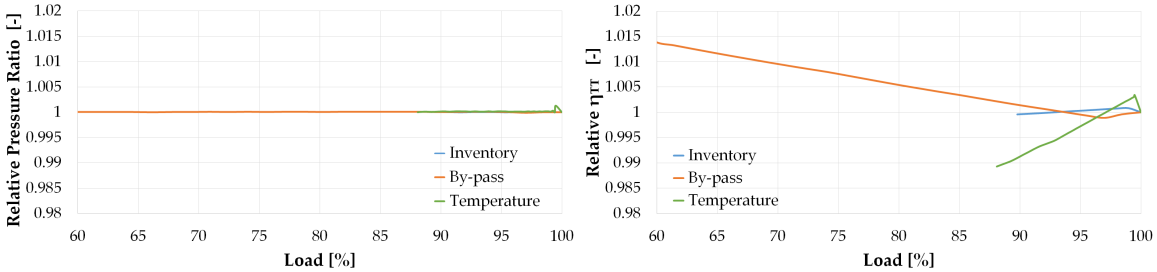

(a) Relative pressure ratio PR.

(b) Relative total-to-total efficiency η_{TT}.

Figure C.6: Partial load performance of compressor C1 in the *Allam* cycle - part 2. The three different control strategies are considered.

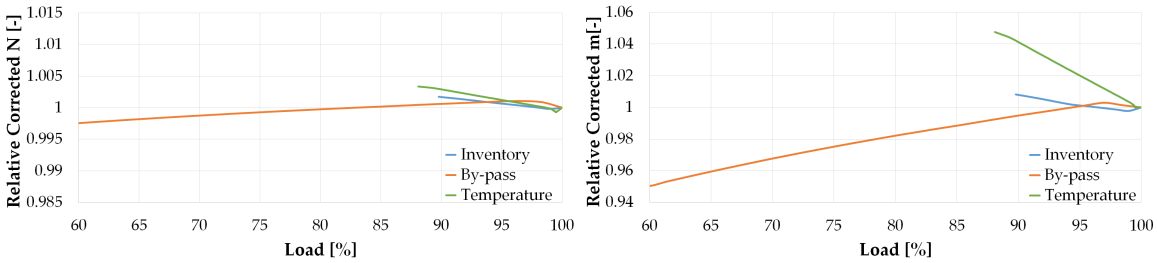

(a) Relative corrected shaft speed N_{corr}.

(b) Relative corrected mass flow rate $\dot{m}_{corr}$.

Figure C.7: Partial load performance of compressor C2 in the *Allam* cycle - part 1. The three different control strategies are considered.

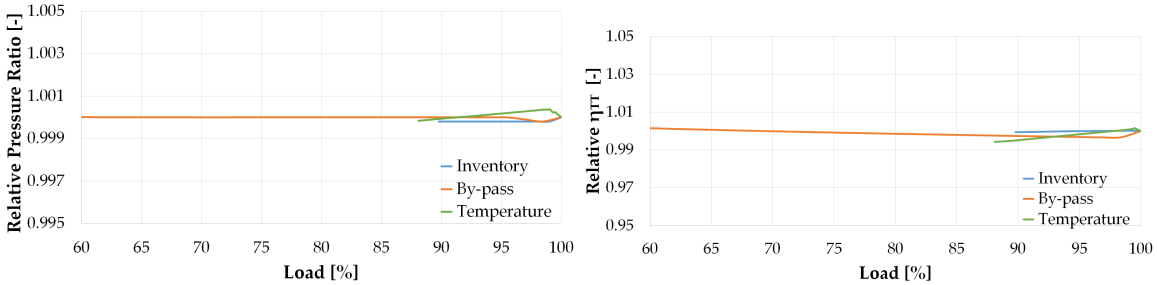

(a) Relative pressure ratio PR.

(b) Relative total-to-total efficiency η_{TT}.

Figure C.8: Partial load performance of compressor C2 in the *Allam* cycle - part 2. The three different control strategies are considered.

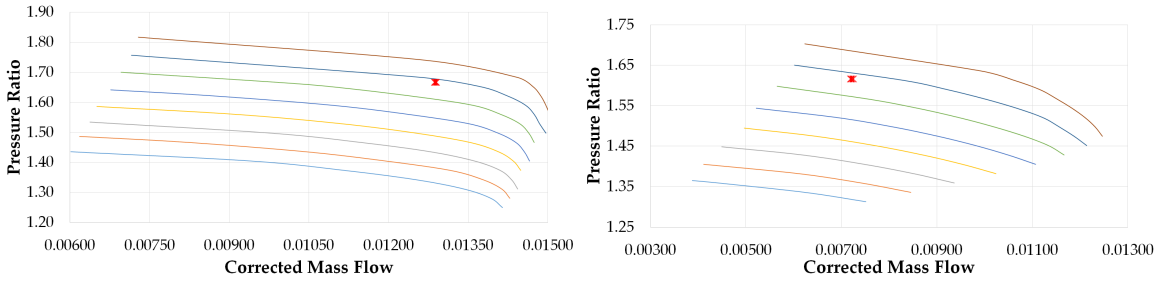

(a) Excursion of compressor C1 in the *Allam* cycle when operating at partial load. *Inventory* control.

(b) Excursion of compressor C2 in the *Allam* cycle when operating at partial load. *Inventory* control.

Figure C.9: Partial load performance of compressors C1 and C2 in the *Allam* cycle for *Inventory* control strategy.

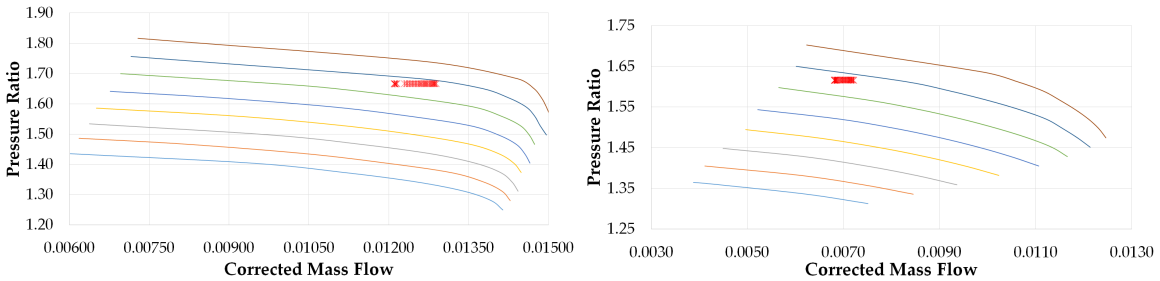

(a) Excursion of compressor C1 in the *Allam* cycle when operating at partial load. *By-pass* control.

(b) Excursion of compressor C2 in the *Allam* cycle when operating at partial load. *By-pass* control.

Figure C.10: Partial load performance of compressors C1 and C2 in the *Partial Cooling* cycle for *By-pass* control strategy.

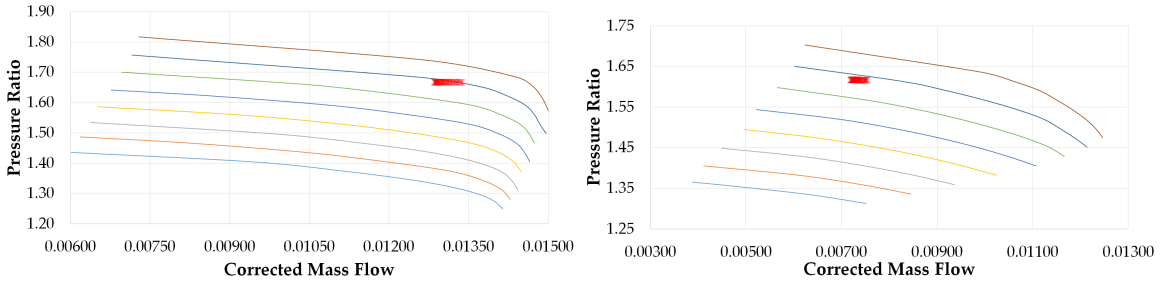

(a) Excursion of compressor C1 in the *Allam* cycle when operating at partial load. *Temperature* control.

(b) Excursion of compressor C2 in the *Allam* cycle when operating at partial load. *Temperature* control.

Figure C.11: Partial load performance of compressors C1 and C2 in the *Partial Cooling* cycle for *Temperature* control strategy.

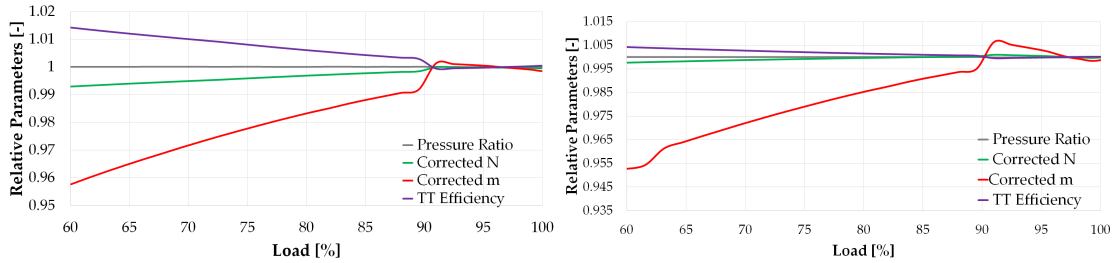

(a) Part-load performance of compressor C1 in the *Allam* cycle.

(b) Part-load performance of compressor C2 in the *Allam* cycle.

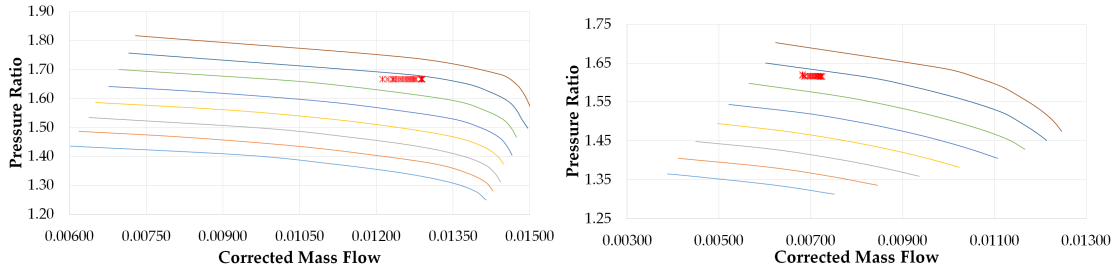

(c) Running line of compressor C1 in the *Allam* cycle.

(d) Running line of compressor C2 in the *Allam* cycle.

Figure C.12: Part-load performance of compressors C1 and C2 in the *Allam* cycle when using the best control strategy.

D SAM Input Parameters

This annex provides all the input parameters to the System Advisor Model that are not included in Section 5.8, with the aim to avoid increasing the length of the main report, hence improving readability.

The screenshots of the main menus are provided for a CSP plant located in Las Vegas, for the *Allam* cycle and employing the dispatch control and financial models setting of Case 1. This information is completed with a series of tables providing the input parameters that apply to the settings, cycles and locations.

Regard *System Control* and *Time of delivery factors*, no further information is discussed herein, since they are thoroughly discussed in Section 5.8.2. Similarly, no screenshots of the *Lifetime* menu are shown since, for all the cases considered, the degradation rate is set to null.

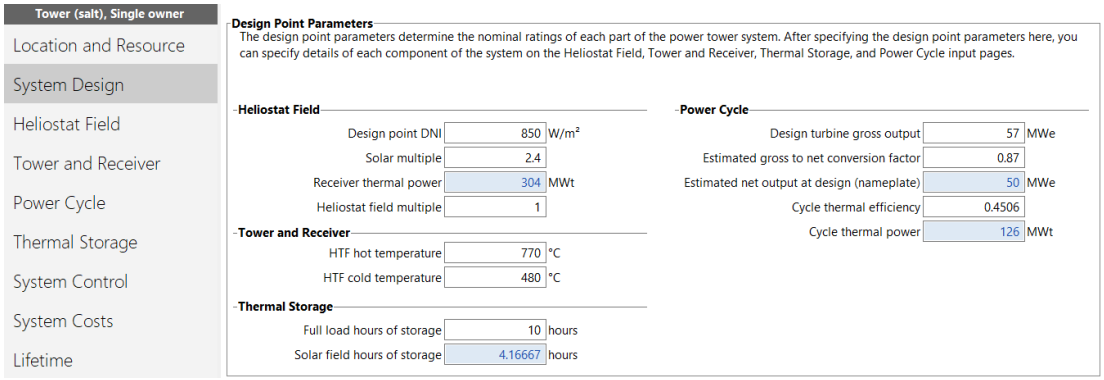

Figure D.1: *System Design* menu in SAM.

	Allam	*Partial Cooling*	*Rankine*
η_{th} [%]	45.06	51.10	41.20
Thermal Power [MWt]	126	112	138
Rec. Thermal Power [MWt]	304	268	332
$T_{HTF,Hot}$ [ºC]	770	770	574
$T_{HTF,Cold}$ [ºC]	480	480	290

Table D.1: *System Design* parameters for the three different cycles considered, see Figure D.1.

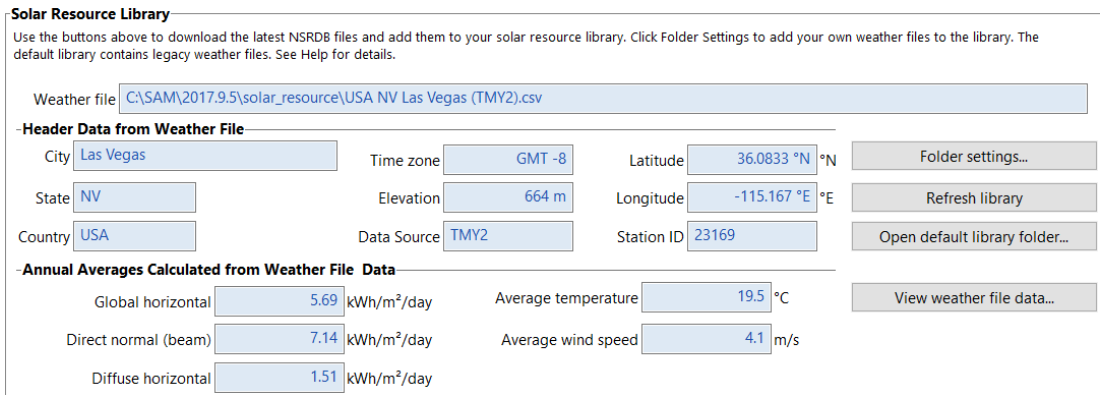

(a) Las Vegas.

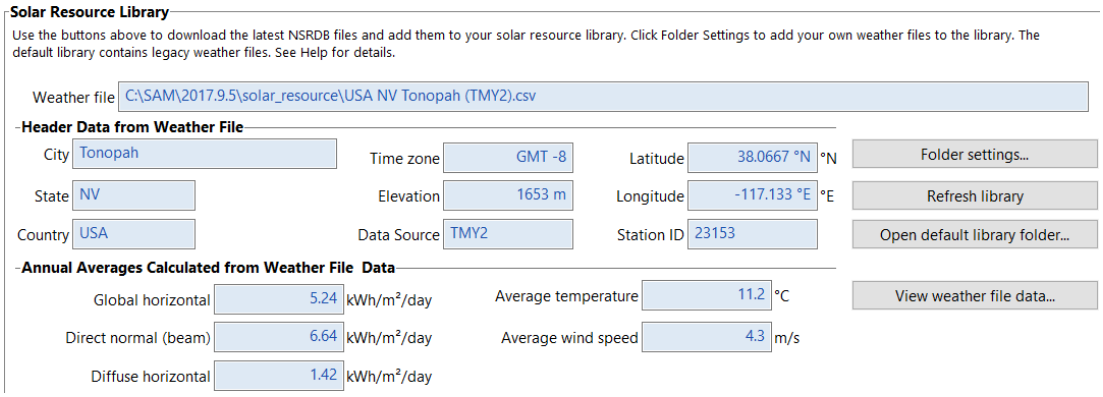

(b) Tonopah.

Figure D.2: *Location and Resource* menu in SAM.

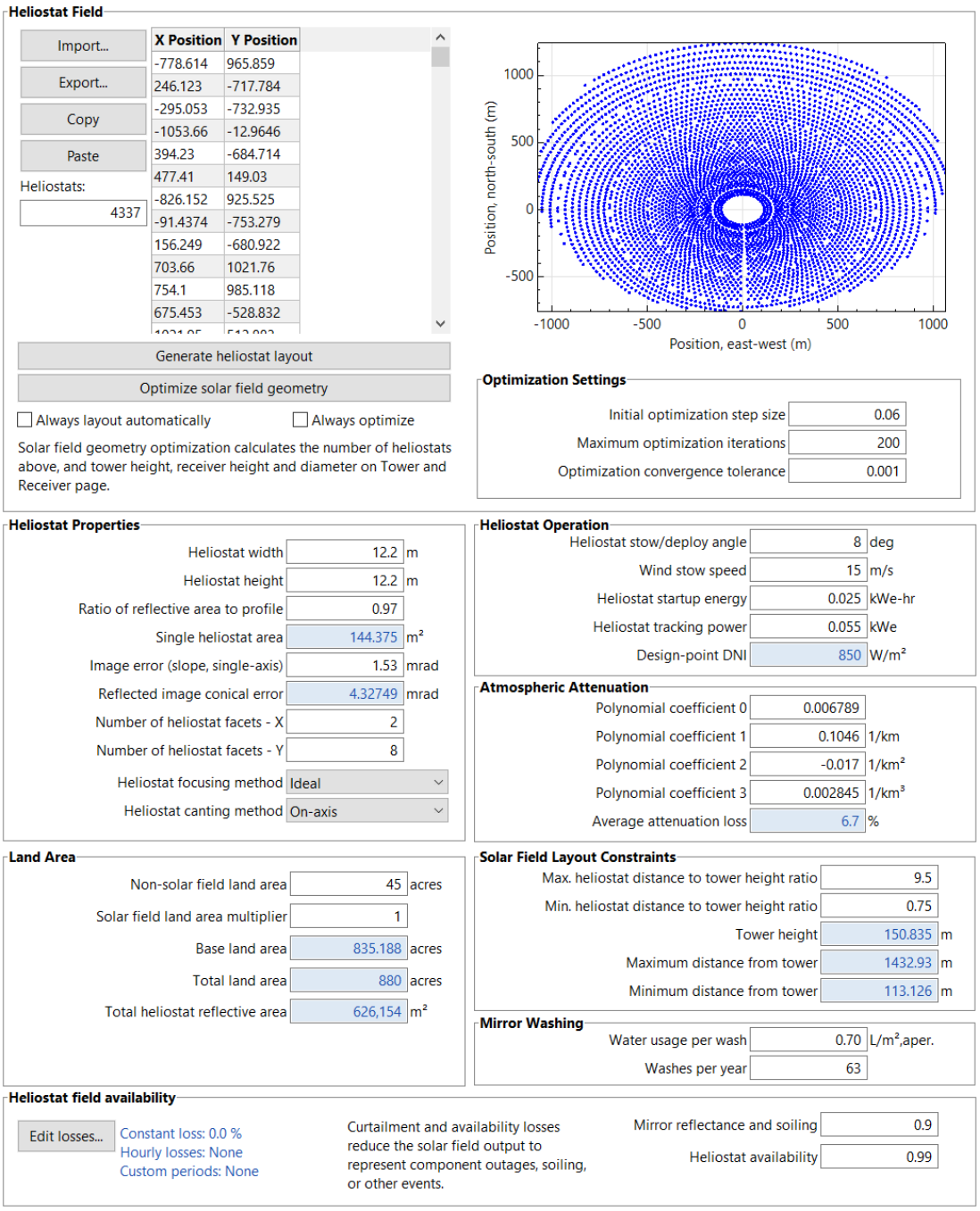

Figure D.3: *Heliostat Field* menu in SAM.

	Las Vegas			Tonopah		
	Allam	*Partial Cooling*	*Rankine*	*Allam*	*Partial Cooling*	*Rankine*
Nº Heliostats	4337	3768	4849	4398	3876	4782
Base land area [ac]	835.188	649.913	1024.06	902.065	802.2	958.359
Total land area [ac]	880	740	1069	947	847	1003
Total refl. area [m^2]	626154	544004	700073	634960	559597	690400
Tower height [m]	150.835	148.895	146.526	142.819	134.107	154.265
$L_{MAX,Tower}$ [m]	1432.93	1414.5	1392	1356.78	1274.01	1465.52
$L_{MIN,Tower}$ [m]	113.126	111.671	109.894	107.114	100.58	115.699

Table D.2: Parameters of the *Heliostat Field* for the three different cycles considered, see Figure D.3.

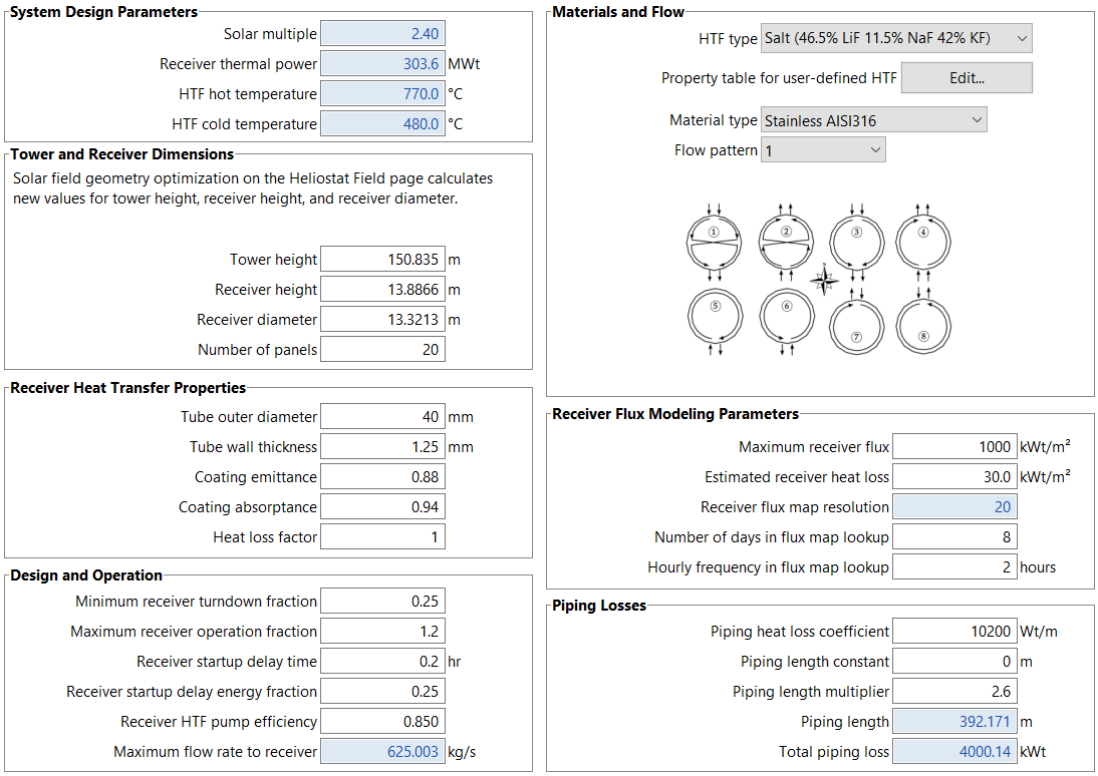

Figure D.4: *Tower and Receiver* menu in SAM.

	Las Vegas			Tonopah		
	Allam	*Partial Cooling*	*Rankine*	*Allam*	*Partial Cooling*	*Rankine*
Tower Height [m]	150.835	148.895	146.526	142.819	134.107	154.265
Rec. Height [m]	13.887	13.602	14.325	13.771	12.726	14.153
Rec. Diameter [m]	13.321	12.744	13.726	13.282	12.725	14.482
$\dot{m}_{MAX,Rec.}$ [kg/s]	625.003	551.128	931.217	625.003	551.128	931.217
Piping Length [m]	392.171	387.126	380.967	371.33	348.678	401.09
Tot. Piping Loss [kWt]	4000.14	3948.68	3885.87	3787.56	3556.51	4091.12

Table D.3: Parameters of the *Tower and Receiver* for the three different cycles considered, see Figure D.4.

	Allam	*Partial Cooling*	*Rankine*
Design $\dot{m}_{HTF}$ [kg/s]	217	191.4	323.3
$\dot{m}_{COOLING}$ [kg/s]	1457	1145	- [1]
$W_{COOLING}$ fraction [%]	0.58	0.46	-
$W_{COOLING}$ [MWe]	0.3	0.3	-

Table D.4: Parameters of the *Power Cycles* for the three different cycles considered, see Figure D.5.

	Allam	*Partial Cooling*	*Rankine*
TES Capacity [MWt-hr]	1265	1115.5	1383.5
Available V_{HTF} [m^3]	3766	3321	6436
$V_{StorageTank}$ [m^3]	3965	3496	6775
Tank Diameter [m]	15.9	14.9	20.8
Estimated Heat loss [MWt]	0.42	0.39	0.45

Table D.5: Parameters of the *Thermal Storage* system for the three different cycles considered, see Figure D.6.

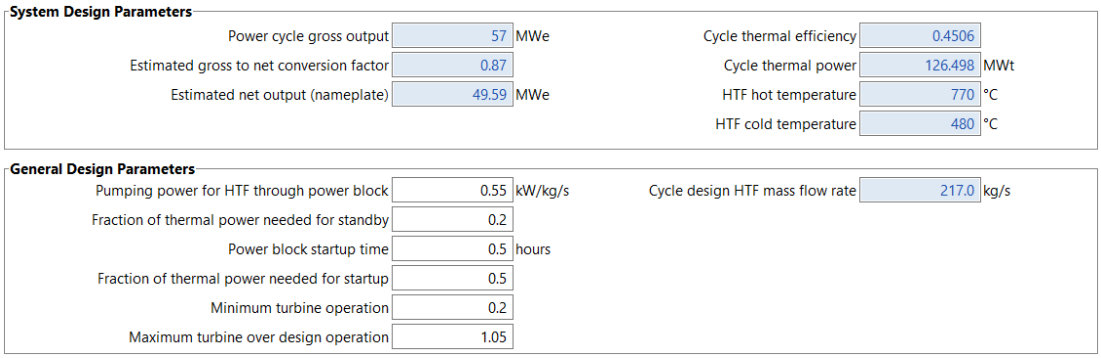

(a) User defined Power cycle.

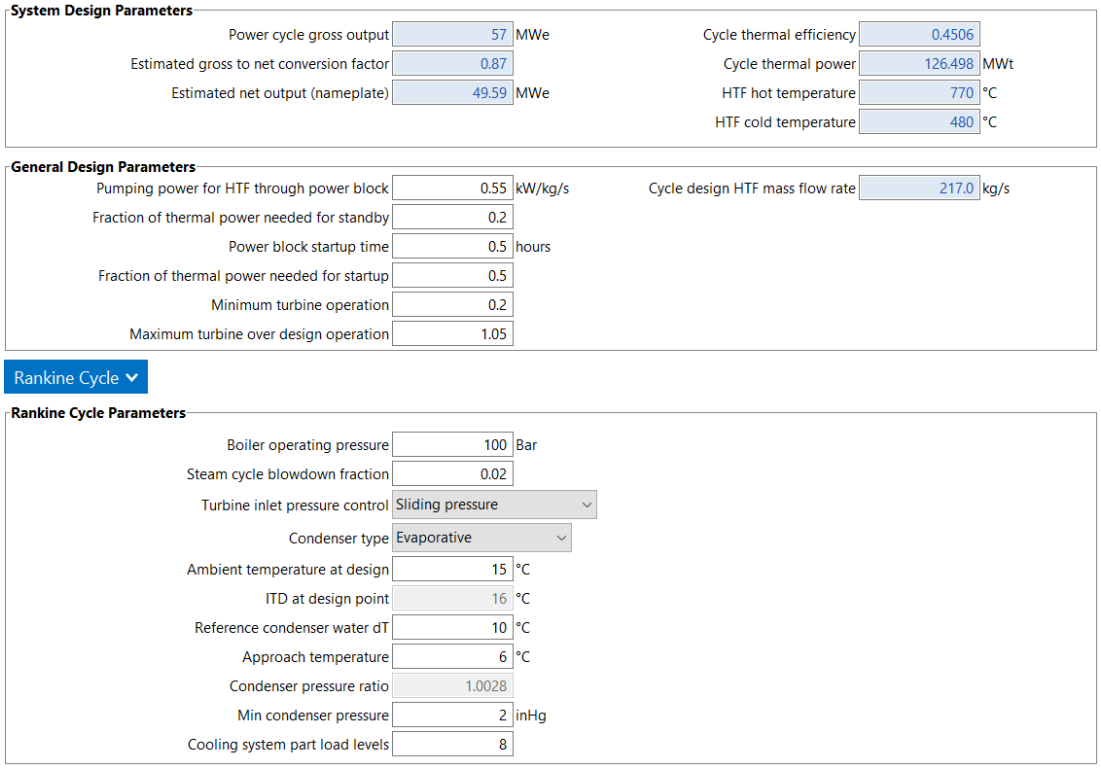

(b) Rankine Power cycle.

Figure D.5: Parameters of the *Power Cycle* in SAM.

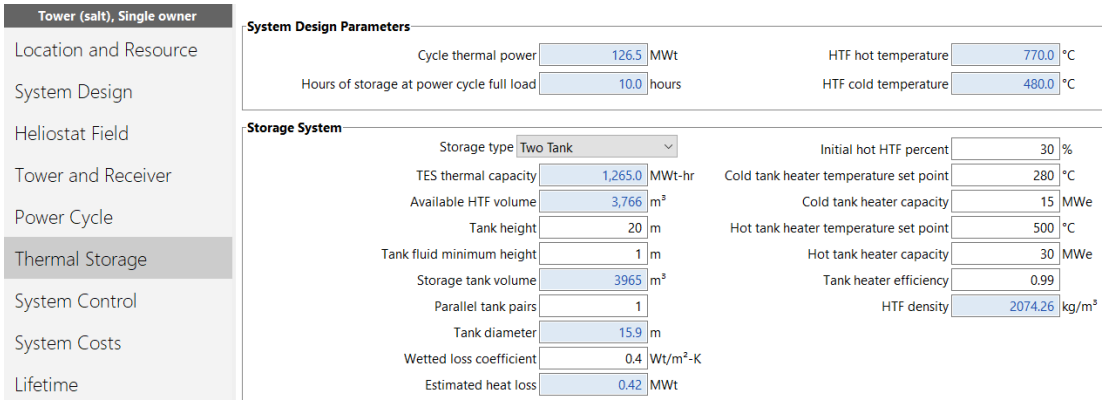

Figure D.6: *Thermal Storage* menu in SAM.

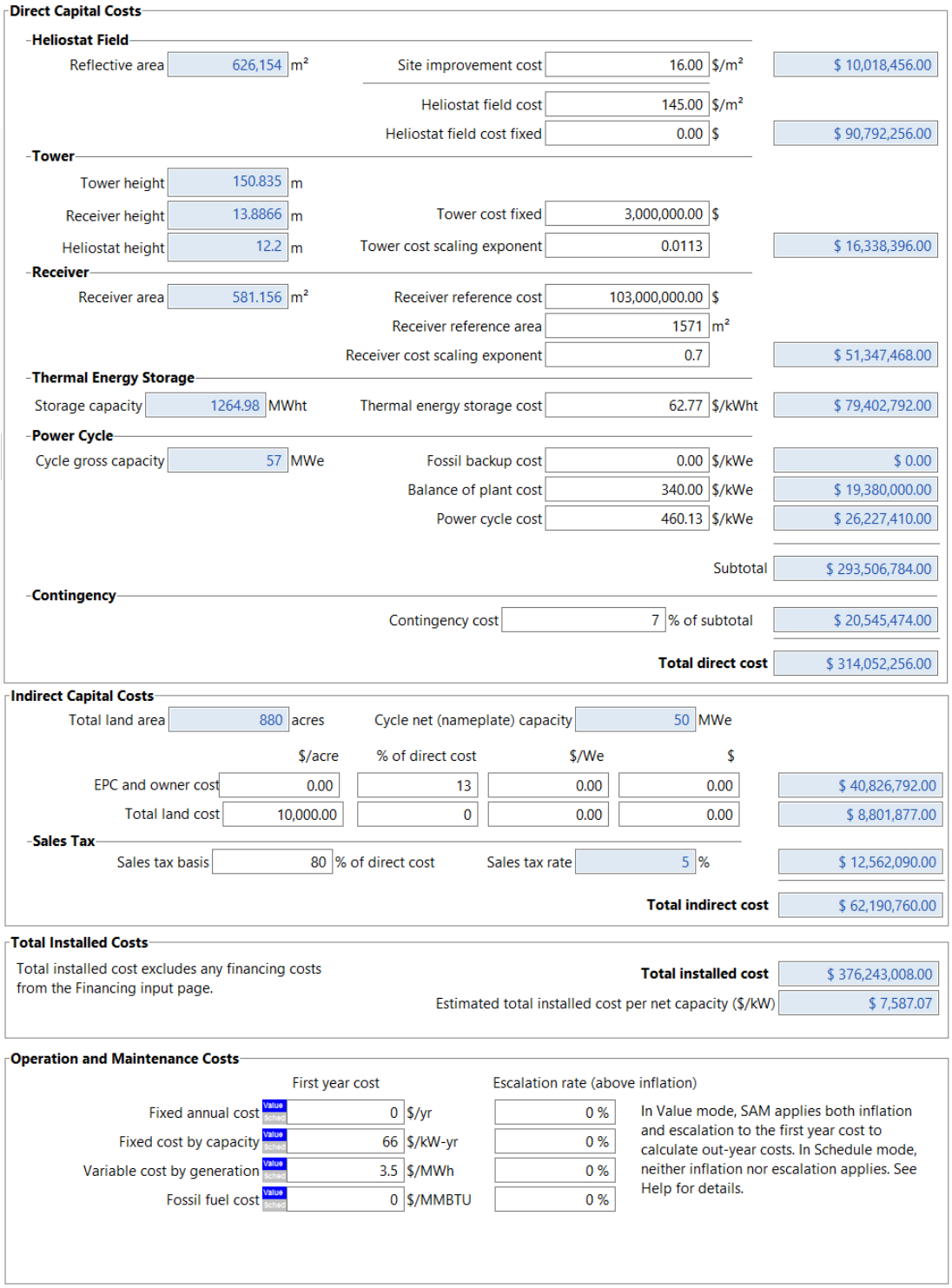

Figure D.7: *System Costs* menu in SAM.

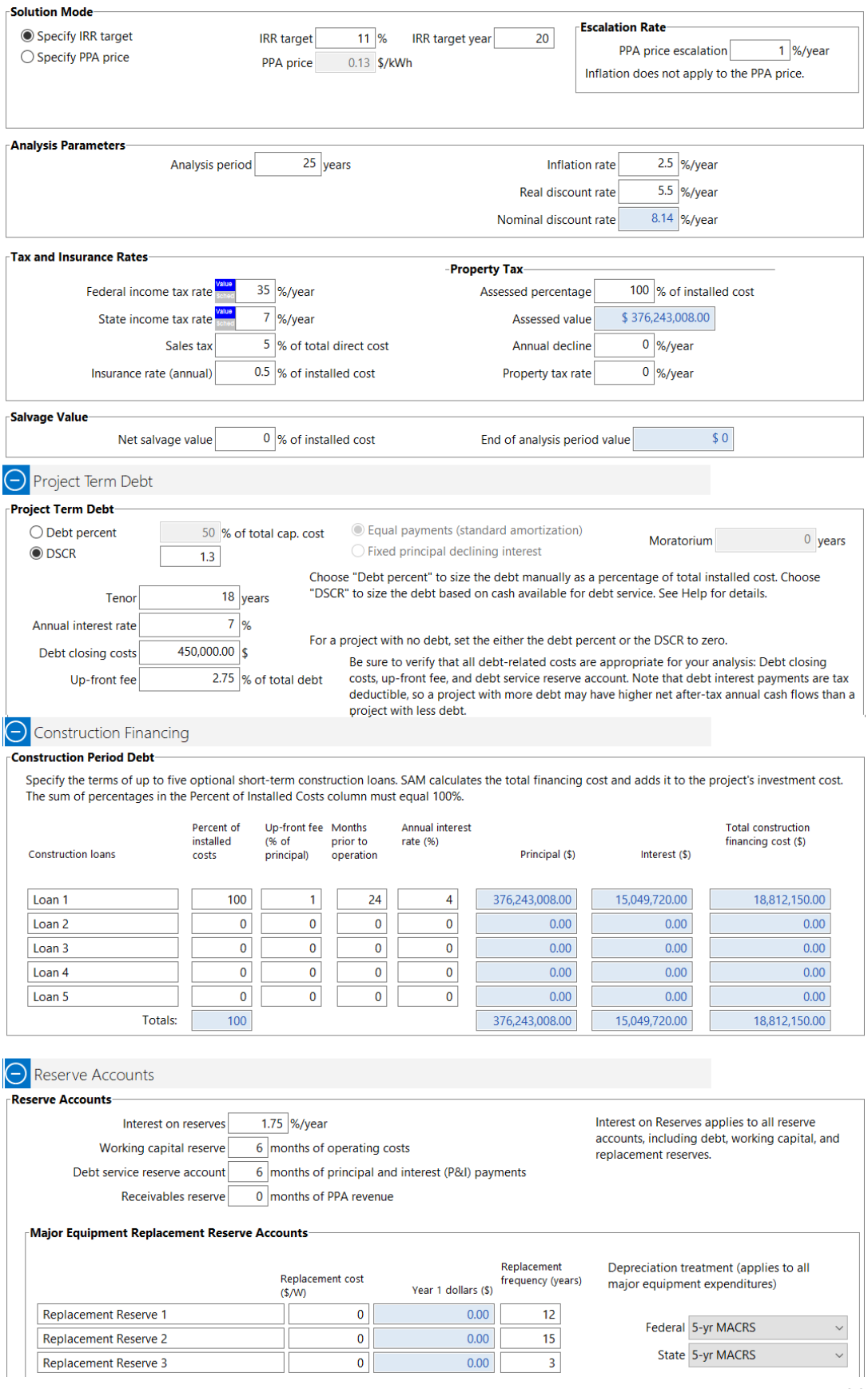

Figure D.8: *Financial Parameters* menu in SAM.

Figure D.9: *Incentives* menu in SAM.

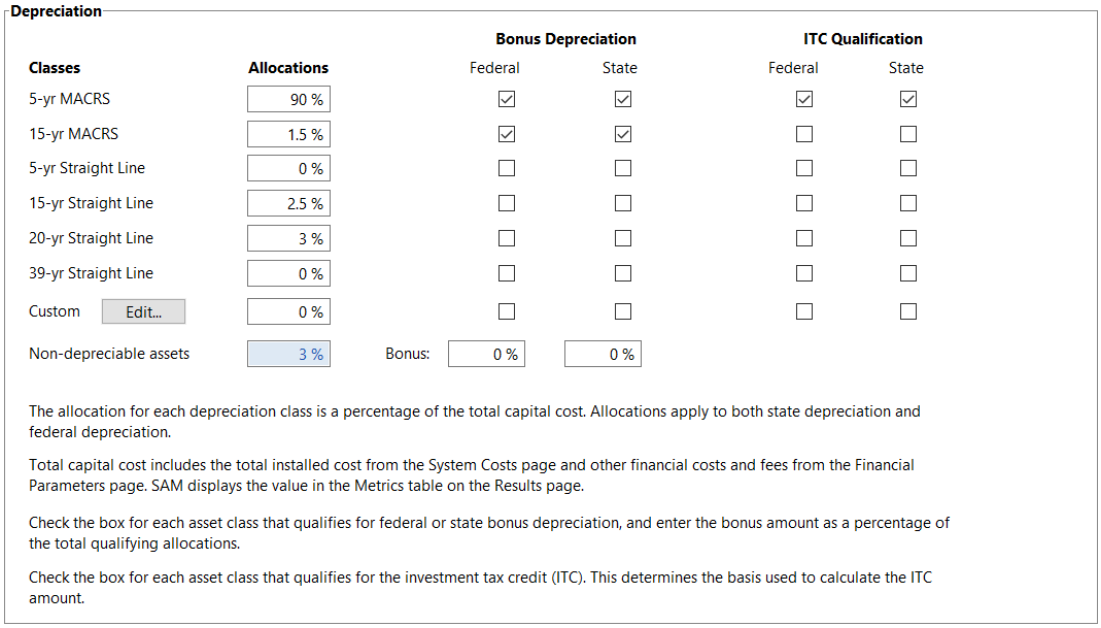

Figure D.10: *Depreciation* menu in SAM.

Bibliography

[1] Our World in Data - Research and interactive data visualizations to understand the world's largest problems. http://www.ourworldindata.org. Retrieved March 15^{th} 2019 .

[2] BP Statistical Review of World Energy. 2018., author=Bp, G., year=2018, institution=BP plc,. Technical report.

[3] L. Capuano. International Energy Outlook 2018 (ieo2018). *US Energy Information Administration (EIA): Washington, DC, USA*, 2018:21, 2018.

[4] S. Teske, S. Sawyer, O. Schäfer, T. Pregger, S. Simon, T. Naegler, S. Schmid, E.D. Özdemir, J. Pagenkopf, F. Kleiner, et al. Energy [r]evolution - a sustainable world energy outlook 2015. 2015.

[5] K. Vignarooban, X. Xu, A. Arvay, K. Hsu, and A.M. Kannan. Heat transfer fluids for concentrating solar power systems – a review. *Applied Energy*, 146:383–396, 2015.

[6] G. Angelino. Real gas effects in carbon dioxide cycles. In *ASME 1969 Gas Turbine Conference and Products Show*, Cleveland,OH, 1969.

[7] M.P. Boyce. *Gas turbine engineering handbook*. Elsevier, 2011.

[8] J. Dyreby, S. Klein, G. Nellis, and D. Reindl. Design Considerations for Supercritical Carbon Dioxide Brayton Cycles With Recompression. *Journal of Engineering for Gas Turbines and Power*, 136(10):101701, 2014.

[9] W.M. Kays and A.L. London. Compact heat exchangers. 1984.

[10] G. Nellis and S. Klein. *Heat Transfer*. Cambridge University Press, 2009.

[11] M. Kulhánek and V. Dostal. Thermodynamic analysis and comparison of supercritical carbon dioxide cycles. In *The 3^{rd} Supercritical CO_2 Power Cycles Symposium*, pages 24–25, Boulder, CO, 2011.

[12] E.G. Feher. The supercritical thermodynamic power cycle. *Energy Conversion and Management*, 8:85–90, 1968.

[13] S. Yoon, P. Sabharwall, and E. Kim. Analytical study on thermal and mechanical design of printed circuit heat exchanger. Technical report, Technical report, Idaho Nation Laboratory, Idaho Falls, 83415, 2013.

[14] B. Plumer and N. Popovich. The New York Times - Why half a degree of global warming is a big deal. https://www.nytimes.com/interactive/2018/10/07/climate/ipcc-report-half-degree.html. Published October 7, 2018. Retrieved March 15^{th} 2019 .

[15] J. Holder, N. Kommenda, and J. Watts. The Guardian - The three-degree world: the cities that will be drowned by global warming. https://www.theguardian.com/cities/ng-interactive/2017/nov/03/three-degree-world-cities-drowned-global-warming. PublishedNovember 3, 2017. Retrieved March 15^{th} 2019 .

[16] International Institute for Sustainable Development. https://www.iisd.org/topic/sustainable-development. Retrieved July 9^{th} 2019 .

[17] M.Z. Jacobson, M.A. Delucchi, M.A. Cameron, and B.A. Frew. Low-cost solution to the grid reliability problem with 100penetration of intermittent wind, water, and solar for all purposes. *Proceedings of the National Academy of Sciences*, 112:15060–15065, 2015.

[18] C.T.M. Clack, S.A. Qvist, J. Apt, M. Bazilian, A.R. Brandt, K. Caldeira, S.J. Davis, V. Diakov, M.A. Handschy, P.D.H. Hines, P. Jaramillo, D.M. Kammen, J.C.S. Long, A. Morgan, M.G. Reed, V. Sivaram, Tynan G.R. Sweeney, J. and, D.G. Victor, J.P. Weyant, and J.F. Whitacre. Evaluation of a proposal for reliable low-cost grid power with 100wind, water, and solar. *Proceedings of the National Academy of Sciences*, 114:6722–6727, 2017.

[19] Md. T. Islam, N. Huda, A.B. Abdullah, and R. Saidur. A comprehensive review of state-of-the-art concentrating solar power (csp) technologies: Current status and research trends. *Renewable and Sustainable Energy Reviews*, 91:987–1018, 2018.

[20] A. Aly, A. Bernardos, C.M. Fernandez-Peruchena, S.S. Jensen, and A.B. Pedersen. Is concentrated solar power (csp) a feasible option for sub-saharan africa?: Investigating the techno-economic feasibility of csp in tanzania. *Renewable Energy*, 135:1224–1240, 2019.

[21] Y. Jia, G. Alva, and G. Fang. Development and applications of photovoltaic–thermal systems: A review. *Renewable and Sustainable Energy Reviews*, 102:249–265, 2019.

[22] Torresol Energy - Reinventing Solar Power. http://torresolenergy.com/gemasolar/. Retrieved March 15^{th} 2019 .

[23] Masen - Ouarzazate Solar Power Station. http://www.masen.ma/fr/publications/rapports/noor-ouarzazate. Retrieved March 15^{th} 2019 .

[24] BrightSource Limitless. http://www.brightsourceenergy.com/ivanpah-solar-project.XJ3r6ZhKiUk. Retrieved March 15^{th} 2019 .

[25] M. Taylor, P. Ralon, and A. Ilas. The power to change: solar and wind cost reduction potential to 2025. *International Renewable Energy Agency (IRENA)*, 2016.

[26] V. Black. Cost and performance data for power generation technologies. *Prepared for the National Renewable Energy Laboratory*, 2012.

[27] November Lazard. Lazard's levelized cost of energy analysis–version 11.0, 2017.

[28] IEA. Renewables 2019: Market Analysis and Forecasts to 2024. Technical report, International Energy Agency, October 2019.

[29] A. Daabo, S. Mahmoud, and R. Al-Dadah. The optical efficiency of three different geometries of a small scale cavity receiver for concentrated solar applications. *Applied Energy*, 179:1081–1096, 2016.

[30] L. Teng and Y. Xuan. Design of a composite receiver for solar-driven supercritical CO_2 brayton cycle. *Journal of CO_2 Utilization*, 32:290–298, 2019.

[31] A. Calderón, A. Palacios, C. Barreneche, M. Segarra, C. Prieto, A. Rodriguez-Sanchez, and A.I. Fernández. High temperature systems using solid particles as tes and htf material: A review. *Applied Energy*, 213:100–111, 2018.

[32] W.Q. Wang, Y. Qiu, M.J. Li, F. Cao, and Z.B. Liu. Optical efficiency improvement of solar power tower by employing and optimizing novel fin-like receivers. *Energy Conversion and Management*, 184:219–234, 2019.

[33] M. Slootweg, K.J. Craig, and J.P. Meyer. A computational approach to simulate the optical and thermal performance of a novel complex geometry solar tower molten salt cavity receiver. *Solar Energy*, 187:13–29, 2019.

[34] F. Crespi, A. Toscani, P. Zani, D. Sánchez, and G. Manzolini. Effect of passing clouds on the dynamic performance of a csp tower receiver with molten salt heat storage. *Applied Energy*, 229:224–235, 2018.

[35] J.A. Duffie and W.A. Beckman. *Solar engineering of thermal processes.* John Wiley & Sons, 2013.

[36] K. Lovegrove and W. Stein. *Concentrating solar power technology: principles, developments and applications.* Elsevier, 2012.

[37] Office of energy efficiency $ renewable energy - the sunshot iniciative. https://www.energy.gov/eere/solar/sunshot-initiative. Retrieved March 15^{th} 2019 .

[38] G. Angelino. Carbon Dioxide Condensation Cycles for Power Production. *Journal of Engineering for Power*, 90(3):287–295, 1968.

[39] M. Bauer. Pathway to cost competitive Concentrated Solar Power via supercritical CO_2 power cycles. In *The 5^{th} Supercritical CO_2 Power Cycles Symposium*, San Antonio, TX, 2016.

[40] J.D. Osorio, R. Hovsapian, and J.C. Ordonez. Effect of multi-tank thermal energy storage, recuperator effectiveness, and solar receiver conductance on the performance of a concentrated solar supercritical co 2-based power plant operating under different seasonal conditions. *Energy*, 115:353–368, 2016.

[41] S. Wright, C. Davidson, and W. Scammell. Thermo-economic analysis of four sCO_2 waste heat recovery power cycle systems. In *The 5^{th} Supercritical CO_2 Power Cycles Symposium*, San Antonio, TX, 2016.

[42] T. Abram and S. Ion. Generation-IV nuclear power: A review of the state of the science. *Energy Policy*, 36(12):4323–4330, 2008.

[43] NET Power's clean energy demonstration plant, La Porte, Texas. https://www.power-technology.com/projects/net-powers-clean-energy-demonstration-plant-la-porte-texas/. Retrieved July 9^{th} 2019 .

[44] R. Dennis. US DOE advanced turbines program and future power systems. In *ASME Turbo Expo 2019: Turbine Technical Conference and Exposition*, Phoenix, AZ, 2019.

[45] Step Demo - The project. https://www.gti.energy/step-demo/step-demo-project/. Retrieved July 9^{th} 2019 .

[46] sCO_2 HeRo - The supercritical CO_2 HEat Removal system. http://www.sco2-hero.eu/. Retrieved July 9^{th} 2019 .

[47] sCO_2 Flex - supercritical CO_2 cycle for flexible & sustainable support to the electricity system. http://www.sco2-flex.eu/about/the-project/. Retrieved July 9^{th} 2019 .

[48] Supercritical CARbon dioxide/Alternative fluids Blends for Efficiency Upgrade of Solar power plants. https://cordis.europa.eu/project/rcn/221766/factsheet/en. Retrieved July 9^{th} 2019 .

[49] T. Conboy, J. Pasch, and D. Fleming. Control of a supercritical CO_2 recompression brayton cycle demonstration loop. In ASME, editor, *ASME Turbo Expo 2013: Turbine Technical Conference and Exposition*, San Antonio, TX, 2013.

[50] T. Conboy, S. Wright, J. Pasch, D. Fleming, G. Rochau, and R. Fuller. Performance Characteristics of an Operating Supercritical CO_2 Brayton Cycle. *Journal of Engineering for Gas Turbines and Power*, 134(11):111703, 2012.

[51] J. Pasch, T. Conboy, D. Fleming, M. Carlson, and G. Rochau. Steady State Supercritical Carbon Dioxide Recompression Closed Brayton Cycle Operating Point Comparison with Predictions. In ASME, editor, *ASME Turbo Expo 2014: Turbine Technical Conference and Exposition*, Dusseldorf, 2014.

[52] J. Pasch, M. Carlson, D. Fleming, and G. Rochau. Evaluation of Recent Data From the SANDIA National Laboratories Closed Brayton Cycle Testing. In ASME, editor, *Proceeding of ASME Turbo Expo 2016: Turbomachinery Technical Conference and Exposition*, Seoul, 2016.

[53] K.J. Kimball and E.M. Clementoni. Supercritical Carbon Dioxide Brayton Power Cycle Development Overview. In ASME, editor, *ASME Turbo Expo 2012: Turbine Technical Conference and Exposition*, Copenhaguen, 2012.

[54] E. M. Clementoni, T. L. Cox, and C. P. Sprague. Startup and Operation of a Supercritical Carbon Dioxide Brayton Cycle. In ASME, editor, *ASME Turbo Expo 2013: Turbine Technical Conference and Exposition*, San Antonio, TX, 2013.

[55] K. J. Kimball, K. D. Rahner, J. P. Nehrbauer, and E. M. Clementoni. Supercritical Carbon Dioxide Brayton Cycle Development Overview. In ASME, editor, *ASME Turbo Expo 2013: Turbine Technical Conference and Exposition*, San Antonio, TX, 2013.

[56] E. M. Clementoni and T. L. Cox. Steady State Power Operation of a Supercritical Carbon Dioxide Power Cycle. In ASME, editor, *ASME Turbo Expo 2014: Turbine Technical Conference and Exposition*, Dusseldorf, 2014.

[57] E.M. Clementoni, T. L Cox, and M.A. King. Off-nominal Component Performance in a Supercritical Carbon Dioxide Brayton Cycle. *Journal of Engineering for Gas Turbines and Power*, 138(1):011703, 2016.

[58] Y. Ahn, J. Lee, S. G. Kim, J.I. Lee, and J.E. Cha. The Design Study of Supercritical Carbon Dioxide Integral Experiment Loop. In ASME, editor, *ASME Turbo Expo 2013: Turbine Technical Conference and Exposition*, San Antonio, TX, 2013.

[59] J. Cho, H. Shin, H.S. Ra, G. Lee, C. Roh, B. Lee, and Y.J. Baik. Development of the Supercritical Carbon Dioxide Power Cycle Experimental Loop in KIER. In ASME, editor, *Proceeding of ASME Turbo Expo 2016: Turbomachinery Technical Conference and Exposition*, Seoul, 2016.

[60] M. Utamura, H. Hasuike, and T. Yamamoto. Demonstration Test Plan of Closed Cycle Gas Turbine with Super-Critical CO_2 as Working Fluid. In 5^{th} *Conference on Sustainable Development of Energy Water and Environment Systems*, pages 459–465, Dubrovnik, 2009.

[61] Y. Huang, J. Wang, J. Zang, and G. Liu. Research Activities on Supercritical Carbon Dioxide Power Conversion Technology in China. In ASME, editor, *ASME Turbo Expo 2014: Turbine Technical Conference and Exposition*, Dusseldorf, 2014.

[62] L. Vesely, V. Dostal, and P. Hajek. Design of Experimental Loop With Supercritical Carbon Dioxide. In ASME, editor, 22^{nd} *International Conference on Nuclear Engineering*, Prague, 2014.

[63] B. Twomey, A. Nagy, H. Russel, A. Rowlands, J. Czapla, R. Singh, C. A de M Ventura, and I. Jahn. The University of Queensland Refrigerant and Supercritical CO_2 Test Loop. In ASME, editor, *Proceeding of ASME Turbo Expo 2016: Turbomachinery Technical Conference and Exposition*, Seoul, 2016.

[64] M. Persichilli, T. Held, S. Hostler, E. Zdankiewicz, and D. Klapp. Transforming Waste Heat to Power Through Development of a CO_2-Based Power Cycle. *Electric Power Expo*, pages 10–12, 2011.

[65] A. Kacludis, S. Lyons, D. Nadav, and E. Zdankiewicz. Waste Heat to Power (WH2P) Applications Using a Supercritical CO_2-Based Power Cycle. *Power-Gen International*, pages 11–13, 2012.

[66] M. Persichilli, A. Kacludis, E. Zdankiewicz, and T. Held. Supercritical CO_2 Power Cycle Developments and Commercialization: Why sCO2 can Displace Steam. In PowerGen, editor, *Power-Gen India and Central Asia*, New Delhi, 2012.

[67] V. Dostal, M. Driscoll, and P. Hejzlar. *A supercritical carbon dioxide cycle for next generation nuclear reactors*. PhD thesis, Massachusetts Institute of Technology, 2004.

[68] R. Dennis. Overview of supercritical carbon dioxide based power cycles for stationary power generation. In *Proceedings of the 4th International Seminar on ORC Power Systems*, 2017.

[69] M.J. Driscoll. Supercritical CO_2 plant cost assessment. *Center for Advanced Nuclear Energy Systems, MIT Nuclear Engineering Department, Massachusetts Institute of Technology, Cambridge, MA, Report No. MIT-GFR-019*, 2004.

[70] J.J. De Barbadillo, B.A. Baker, and R. Gollihue. Nickel-base superalloys for advanced power systems–an alloy producer's perspective. In *Proceeding of the 4th Symposium on Heat Resistant Steels and Alloys for High Efficiency USC Power Plants, China*, 2011.

[71] S. Cich, J. Moore, A. Rimpel, and K. Hoopes. Supercritical CO_2 power cycle limits based on material cost. In *Fifth Supercritical CO_2 Power Cycles Symposium, San Atonio, TX, Mar*, pages 29–31, 2016.

[72] J.F. Hinze, G.F. Nellis, and M.H. Anderson. Cost comparison of printed circuit heat exchanger to low cost periodic flow regenerator for use as recuperator in a s-CO_2 brayton cycle. *Applied energy*, 208:1150–1161, 2017.

[73] I.H. Kim, X. Zhang, R. Christensen, and X. Sun. Design study and cost assessment of straight, zigzag, s-shape, and osf pches for a flinak–sCO_2 secondary heat exchanger in fhrs. *Annals of Nuclear Energy*, 94:129–137, 2016.

[74] N. Weiland, B. Lance, and S. Pidaparti. sCO_2 power cycle component cost correlations from doe data spanning multiple scales and applications (final). Technical report, Phoenix, AR, 2019.

[75] National Renewable Energy Laboratory, *Solar Advisor Model Reference Manual for CSP Trough Systems*, NREL (2009).

[76] J. Schmitt, J. Wilkes, T. Allison, J. Bennett, K. Wygant, and R. Pelton. Lowering the levelized cost of electricity of a concentrating solar power tower with a supercritical carbon dioxide power cycle. In *ASME Turbo Expo 2017: Turbomachinery Technical Conference and Exposition*, pages V009T38A028–V009T38A028. American Society of Mechanical Engineers, 2017.

[77] N.A. Carstens. *Control Strategies for Supercritical Carbon Dioxide Power Conversion Systems*. PhD thesis, Massachusetts Institute of Technology, 2007.

[78] S.A. Wright, R.F. Radel, M.E. Vernon, G.E. Rochau, and P.S. Pickard. Operation and analysis of a supercritical CO_2 brayton cycle. *Sandia Report, No. SAND2010-0171*, 2010.

[79] J.J. Dyreby, S.A. Klein, G.F. Nellis, and D.T. Reindl. Modeling off-design and part-load performance of supercritical carbon dioxide power cycles. In *ASME turbo expo 2013: turbine technical conference and exposition*, pages V008T34A014–V008T34A014. American Society of Mechanical Engineers, 2013.

[80] J.J. Dyreby, G.F. Nellis, S.A. Klein, and D.T. Reindl. Development of a flexible modeling tool for predicting optimal off-design performance of simple and recompression brayton cycles. In *The 4th International Symposium–Supercritical CO_2 Power Cycles*, pages 9–10, 2014.

[81] V.K. Avadhanula and T.J. Held. Transient modeling of a supercritical CO_2 power cycle and comparison with test data. In *ASME Turbo Expo 2017: Turbomachinery Technical Conference and Exposition*, pages V009T38A007–V009T38A007. American Society of Mechanical Engineers, 2017.

[82] C. Gao, P. Wu, J. Shan, and B. Zhang. Development of a transient analysis code for s-CO_2 power conversion system. In *The 6^{th} Supercritical CO_2 Power Cycles Symposium*, Pittsburgh, PA, 2018.

[83] A. Moisseytsev and J.J. Sienicki. Recent developments in s-CO_2 cycle dynamic modeling and analysis at anl. In *The 4th International Symposium–Supercritical CO_2 Power Cycles, Pittsburgh, Pennsylvania, USA,(September 9-10, 2014)*, 2014.

[84] E.M. Clementoni, T.L. Cox, and M.A. King. Response of a compact recuperator to thermal transients in a supercritical carbon dioxide brayton cycle. In *ASME Turbo Expo 2017: Turbomachinery Technical Conference and Exposition*, pages V009T38A002–V009T38A002. American Society of Mechanical Engineers, 2017.

[85] P. Mahapatra, S.E. Zitney, J. Albright, and E.A. Liese. Advanced regulatory control of a 10 mwe supercritical CO_2 recompression brayton cycle towards improving power ramp rates. In *The 6^{th} Supercritical CO_2 Power Cycles Symposium*, Pittsburgh, PA, 2018.

[86] J. Zhang, Z. Yang, and Y. Le Moullec. Dynamic modeling and transient analysis of a molten salt heated recompression supercritical CO_2 brayton cycle. In *The 6^{th} Supercritical CO_2 Power Cycles Symposium*, Pittsburgh, PA, 2018.

[87] S.A. Wright, C.S. Davidson, and C. Husa. Off-design performance modeling results for a supercritical CO_2 waste heat recovery power system. In *The 6^{th} Supercritical CO_2 Power Cycles Symposium*, Pittsburgh, PA, 2018.

[88] T.C. Allison, J.J. Moore, D. Hofer, M.D. Towler, and J. Thorp. Planning for successful transients and trips in a 1 mwe-scale high-temperature sCO_2 test loop. *Journal of Engineering for Gas Turbines and Power*, 141(6):061014, 2019.

[89] T. Sawyer. The Closed Cycle Gas Turbine, the Most Efficient Turbine Burning any Fuel. In ASME, editor, *International Gas Turbine Conference and Exhibit*, pages 1–5, Amsterdam, 1984.

[90] G. Sulzer. Verfahren zur erzeugung von arbeit aus warme. *Swiss Patent*, page 269599, 1950.

[91] E.G. Feher. Investigation of supercritical (feher) cycle. *Astropower Laboratory, Missile & Space Systems Division*, 1968.

[92] R.A. Strub and A.J. Frieder. High pressure indirect CO_2 closed-cycle gas turbines. In *Nuclear gas turbines*. 1970.

[93] J.C. Corman. Energy Conversion Alternatives Study (ECAS), General Electric Phase 1. Volume 1: Executive Summary. 1976.

[94] G. Kimzey. Development of a Brayton Bottoming Cycle Using Supercritical Carbon Dioxide as the Working Fluid. Technical report, EPRI project, 2012.

[95] P. Garg, P. Kumar, and K. Srinivasan. Supercritical carbon dioxide brayton cycle for concentrated solar power. *The Journal of Supercritical Fluids*, 76:54–60, 2013.

[96] T.M. Conboy and S.A. Wright. Experimental Investigation of the S-CO_2 Condensing Cycle. In *The 3rd Supercritical CO_2 Power Cycles Symposium*, Boulder, CO, 2011.

[97] A. Moisseytsev and J.J. Sienicki. Investigation of Alternative Layouts for the Supercritical Carbon Dioxide Brayton Cycle for a Sodium-Cooled Fast Reactor. *Journal of Engineering for Power*, 239(7):1362–1371, 2009.

[98] H.U. Frutschi. *Closed-Cycle gas turbines. Operating experience and future potential*. ASME Press, New York, 2005.

[99] M. Kulhanek and V. Dostal. Supercritical carbon dioxide cycles thermodynamic analysis and comparison. In *The 3rd Supercritical CO_2 Power Cycles Symposium*, pages 24–25, Boulder, CO, 2011.

[100] T. Neises and C. Turchi. A comparison of supercritical carbon dioxide power cycle configurations with an emphasis on CSP applications. *Energy Procedia*, 49:1187–1196, 2014.

[101] Y. Ahn, S.J. Bae, M. Kim, S.K. Cho, S. Baik, J.I. Lee, and J.E. Cha. Cycle layout studies of S-CO_2 cycle for the next generation nuclear system application. In *Transactions of the Korean Nuclear Society Autumn Meeting*, Pyeongchang, 2014.

[102] R. Chacartegui, D. Sanchez, F. Jimenez-Espadafor, A. Munoz, and T. Sanchez. Analysis of intermediate temperature combined cycles with a carbon dioxide topping cycle. In *ASME Turbo Expo 2008: Power for Land, Sea, and Air*, pages 673–680, Berlin, 2008. American Society of Mechanical Engineers.

[103] C.S. Turchi, Z. Ma, and J. Dyreby. Supercritical Carbon Dioxide Power Cycle Configurations for use in Concentrating Solar Power Systems. In *ASME Turbo Expo 2012: Turbine Technical Conference and Exposition*, pages 967–973, Copenhagen, 2012. American Society of Mechanical Engineers.

[104] D.V. Di Maio, A. Boccitto, and G. Caruso. Supercritical Carbon Dioxide Applications for Energy Conversion Systems. *Energy Procedia*, 82:819–824, 2015.

[105] G.A. Johnson, M.W. McDowell, G.M. O'Connor, C.G. Sonwane, and G. Subbaraman. Supercritical CO_2 Cycle Development at Pratt and Whitney Rocketdyne. In *ASME Turbo Expo 2012: Turbine Technical Conference and Exposition*, pages 1015–1024, Copenhagen, 2012. American Society of Mechanical Engineers.

[106] M.T. Dunham and B.D. Iverson. High-efficiency thermodynamic power cycles for concentrated solar power systems. *Renewable and Sustainable Energy Reviews*, 30:758–770, 2014.

[107] C. Wu, X. Yan, S. Wang, K. Bai, J. Di, S. Cheng, and J. Li. System optimisation and performance analysis of CO_2 transcritical power cycle for waste heat recovery. *Energy*, 100:391–400, 2016.

[108] R. Vásquez-Padilla, Y.C.S. Too, R. Benito, and W. Stein. Exergetic Analysis of Supercritical CO_2 Brayton Cycles Integrated with Solar Central Receivers. *Applied Energy*, 148:348–365, 2015.

[109] A. Nassar, L. Moroz, M. Burlaka, P. Pagur, and Y. Govoruschenko. Designing Supercritical CO_2 Power Plants Using an Integrated Design System. In *ASME 2014 Gas Turbine India Conference*, New Delhi, 2014. American Society of Mechanical Engineers.

[110] J. Sarkar. Review and future trends of supercritical CO_2 Rankine cycle for low-grade heat conversion. *Renewable and Sustainable Energy Reviews*, 48:434–451, 2015.

[111] V. Dostal and M. Kulhanek. Research on the Supercritical Carbon Dioxide Cycles in the Czech Republic. In *The 2^{nd} Supercritical CO_2 Power Cycles Symposium*, pages 29–30, Troy, NY, 2009.

[112] J.C. Bryant, H. Saari, and K. Zanganeh. An analysis and comparison of the simple and recompression supercritical CO_2 cycles. In *The 3^{rd} Supercritical CO_2 Power Cycles Symposium*, pages 24–25, Boulder, CO, 2011.

[113] Y. Ahn, S.J. Bae, M. Kim, S.K. Cho, S. Baik, J.I. Lee, and J.E. Cha. Review of supercritical CO_2 power cycle technology and current status of research and development. *Nuclear Engineering and Technology*, 47(6):647–661, 2015.

[114] C.S. Turchi, Z. Ma, and J. Dyreby. Supercritical CO_2 for application in concentrating solar power systems. In *The 2^{nd} Supercritical CO_2 Power Cycles Symposium*, pages 1–5, Troy, NY, 2009.

[115] T.W. Neises and C.S. Turchi. Supercritical CO_2 Power Cycles: Design Considerations for Concentrating Solar Power. In *The 4^{th} Supercritical CO_2 Power Cycles Symposium*, volume 2, pages 9–10, Pittsburgh, PA, 2014.

[116] C.S. Turchi, Z. Ma, T.W. Neises, and M.J. Wagner. Thermodynamic Study of Advanced Supercritical Carbon Dioxide Power Cycles for Concentrating Solar Power Systems. *Journal of Solar Energy Engineering*, 135(4):041007, 2013.

[117] H. Zhao, Q. Deng, W. Huang, and Z. Feng. Thermodynamic and Economic Analysis and Multi-Objective Optimization of Supercritical CO_2 Brayton Cycles. In *ASME Turbo Expo 2015: Turbine Technical Conference and Exposition*, Montreal, 2015. American Society of Mechanical Engineers.

[118] R. Chacartegui, J.M. Muñoz de Escalona, D. Sánchez, B. Monje, and T. Sánchez. Alternative cycles based on carbon dioxide for central receiver solar power plants. *Applied Thermal Engineering*, 31(5):872–879, 2011.

[119] G. Klemenic, S. Flegkas, A. Werner, M. Haider, and H. Leibinger. Comparison of conventional and CO_2 power generation cycles for waste heat recovery. In *The 5^{th} Supercritical CO_2 Power Cycles Symposium*, pages 1–15, San Antonio, TX, 2016.

[120] W.W. Shelton, N. Weiland, C. White, J. Plunkett, and D. Gray. Oxy-coal-fired circulating fluid bed combustion with a commercial utility-size supercritical CO_2 power cycle. In *The 5^{th} Supercritical CO_2 Power Cycles Symposium*, pages 1–18, San Antonio, TX, 2016.

[121] M. Mecheri and Y. Le Moullec. Supercritical CO_2 Brayton cycles for coal-fired power plants. *Energy*, 103:758–771, 2016.

[122] H.S. Pham, N. Alpy, J.H. Ferrasse, O. Boutin, J. Quenaut, M. Tothill, D. Haubensack, and M. Saez. Mapping of the thermodynamic performance of the supercritical co 2 cycle and optimisation for a small modular reactor and a sodium-cooled fast reactor. *Energy*, 87:412–424, 2015.

[123] L. Santini, C. Accornero, and A. Cioncolini. On the adoption of carbon dioxide thermodynamic cycles for nuclear power conversion: A case study applied to mochovce 3 nuclear power plant. *Applied Energy*, 181:446–463, 2016.

[124] H. Karig. Supercritical thermal power system using combustion gases for working fluid, June 5 1973. US Patent 3,736,745.

[125] Y. Chen, P. Lundqvist, A. Johansson, and P. Platell. A comparative study of the carbon dioxide transcritical power cycle compared with an organic Rankine cycle with R123 as working fluid in waste heat recovery. *Applied Thermal Engineering*, 26(17):2142–2147, 2006.

[126] E. Cayer, N. Galanis, M. Desilets, H. Nesreddine, and P. Roy. Analysis of a carbon dioxide transcritical power cycle using a low temperature source. *Applied Energy*, 86(7):1055–1063, 2009.

[127] Y. Song, J. Wang, Y. Dai, and E. Zhou. Thermodynamic analysis of a transcritical CO_2 power cycle driven by solar energy with liquified natural gas as its heat sink. *Applied energy*, 92:194–203, 2012.

[128] P. Garg, K. Srinivasan, P. Dutta, and P. Kumar. Comparison of co 2 and steam in transcritical rankine cycles for concentrated solar power. *Energy Procedia*, 49:1138–1146, 2014.

[129] R. Vásquez-Padilla, Y.C.S. Too, R. Benito, R. McNaughton, and W. Stein. Multi-objective thermodynamic optimisation of supercritical CO_2 brayton cycles integrated with solar central receivers. *International Journal of Sustainable Energy*, pages 1–20, 2016.

[130] T.J. Held. Hot day cycle, 2014. US Patent 8,783,034.

[131] R.J. Allam, M. Palmer, G.W. Brown, et al. System and method for high efficiency power generation using a carbon dioxide circulating working fluid, 2013. US Patent 8,596,075.

[132] R.J. Allam, J.E. Fetvedt, B.A. Forrest, and D.A. Freed. The Oxy-Fuel, Supercritical CO_2 Allam Cycle: New Cycle Developments to Produce Even Lower-Cost Electricity From Fossil Fuels Without Atmospheric Emissions. In *ASME Turbo Expo 2014: Turbine Technical Conference and Exposition*, Dusseldorf, 2014. American Society of Mechanical Engineers.

[133] J. Isles. Gearing up for a new supercritical CO_2 power cycle system. *Gas Turbine World*, November-December:14–18, 2014.

[134] X. Lu, B. Forrest, S. Martin, J. Fetvedt, M. McGroddy, and D. Freed. Integration and Optimization of Coal Gasification Systems with a Near-Zero Emissions Supercritical Carbon Dioxide Power Cycle. In ASME, editor, *Proceeding of ASME Turbo Expo 2016: Turbomachinery Technical Conference and Exposition*, Seoul, 2016.

[135] R. Scaccabarozzi, M. Gatti, and E. Martelli. Thermodynamic analysis and numerical optimization of the NET power oxy-combustion cycle. *Applied energy*, 178:505–526, 2016.

[136] Y. Muto, M. Aritomi, T. Ishizuka, and N. Watanabe. Comparison of Supercritical CO2 Gas Turbine Cycle and Brayton CO_2 Gas Turbine Cycle for Solar Thermal Power Plants. In *The 4^{th} Supercritical CO_2 Power Cycles Symposium*, Pittsburgh, PA, 2014.

[137] P.H. Mathieu and R. Nihart. Zero-emission MATIANT cycle. *Journal of Engineering for Gas Turbines and Power*, 121(1):116–120, 1999.

[138] P.H. Mathieu and R. Nihart. Sensitivity analysis of the MATIANT cycle. *Energy Conversion and Management*, 40(15):1687–1700, 1999.

[139] E. Iantovski and P.H. Mathieu. Highly efficient zero emission CO_2-based power plant. *Energy conversion and management*, 38:S141–S146, 1997.

[140] M. Purjam, K. Goudarzi, and M. Keshtgar. A New Supercritical Carbon Dioxide Brayton Cycle with High Efficiency. *Heat Transfer Asian Research*, 2016.

[141] E.I. Yantovski, K.N. Zvagolsky, and V.A. Gavrilenko. The COOPERATE-demo power cycle. *Energy conversion and management*, 36(6):861–864, 1995.

[142] E.I. Yantovski. Stack downward: Zero emission fuel-fired power plants concept. *Energy conversion and management*, 37(6):867–877, 1996.

[143] R. Vásquez-Padilla, Y.C.S. Too, R. Benito, R. McNaughton, and W. Stein. Thermodynamic feasibility of alternative supercritical CO_2 Brayton cycles integrated with an ejector. *Applied Energy*, 169:49–62, 2016.

[144] S.A. Wright, R.F. Radel, T.M. Conboy, and G.E. Rochau. Modeling and Experimental Results for Condensing Supercritical CO_2 Power Cycles - SAND2010-8840. Technical report, Sandia National Laboratories, Albuquerque,NM, 2011.

[145] C. White, W. Shelton, and R. Dennis. An assessment of supercritical CO_2 power cycles integrated with generic heat sources. In *The 4^{th} Supercritical CO_2 Power Cycles Symposium*, pages 1–24, Pittsburgh, PA, 2014.

[146] V.T. Cheang, R.A. Hedderwick, and C. McGregor. Benchmarking supercritical carbon dioxide cycles against steam Rankine cycles for Concentrated Solar Power. *Solar Energy*, 113:199–211, 2015.

[147] J.E. Cha, T.H. Lee, J.H. Eoh, S.H. Seong, S.O. Kim, D.E. Kim, M.H. Kim, T.W. Kim, and K.Y. Suh. Development of a supercritical CO_2 Brayton energy conversion system coupled with a sodium cooled fast reactor. *Nuclear Engineering and Technology*, 41(8):1025–1044, 2009.

[148] H.J. Yoon, Y. Ahn, J.I. Lee, and Y. Addad. Potential advantages of coupling supercritical CO_2 Brayton cycle to water cooled small and medium size reactor. *Nuclear Engineering and Design*, 245:223–232, 2012.

[149] A. McClung, K. Brun, and J. Delimont. Comparison of Supercritical Carbon Dioxide Cycles for Oxy-Combustion. In *ASME Turbo Expo 2015: Turbine Technical Conference and Exposition*, Montreal, 2015. American Society of Mechanical Engineers.

[150] I.P. Serrano Remón, J.I. Linares Hurtado, A. Cantizano González, and B.Y. Moratilla Soria. Enhanced arrangement for recuperators in supercritical CO_2 Brayton power cycle for energy conversion in fusion reactors. *Fusion Engineering and Design*, 89:1909–1912, 2014.

[151] A.R. Ludington. *Tools for supercritical carbon dioxide cycle analysis and the cycle's applicability to sodium fast reactors*. PhD thesis, Massachusetts Institute of Technology, 2009.

[152] W.S. Jeong, J.I. Lee, and Y.H. Jeong. Potential improvements of supercritical recompression CO_2 Brayton cycle by mixing other gases for power conversion system of a SFR. *Nuclear Engineering and Design*, 241(6):2128–2137, 2011.

[153] Y. Ahn and J.I. Lee. Study of various Brayton cycle designs for small modular sodium-cooled fast reactor. *Nuclear Engineering and Design*, 276:128–141, 2014.

[154] R. PVásquez-Padilla, R. Benito, and W. Stein. An Exergy Analysis of Recompression Supercritical CO_2 Cycles With and Without Reheating. *Energy Procedia*, 69:1181–1191, 2015.

[155] J. Dyreby, M. Anderson, and B. Beihoff. Integration of a 10 MWe Supercritical Carbon Dioxide Power Cycle into an Existing Cogeneration Power Plant. In *The 5^{th} Supercritical CO_2 Power Cycles Symposium*, San Antonio, TX, 2016.

[156] M.A. Reyes-Belmonte, A. Sebastián, M. Romero, and J. González-Aguilar. Optimization of a recompression supercritical carbon dioxide cycle for an innovative central receiver solar power plant. *Energy*, 112:17–27, 2016.

[157] B.D. Iverson, T.M. Conboy, J.J. Pasch, and A.M. Kruizenga. Supercritical CO_2 Brayton cycles for solar-thermal energy. *Applied Energy*, 111:957–970, 2013.

[158] M. Atif and F.A. Al-Sulaiman. Energy and exergy analyses of solar tower power plant driven supercritical carbon dioxide recompression cycles for six different locations. *Renewable and Sustainable Energy Reviews*, 68:153–167, 2017.

[159] I.P. Serrano, J.I. Linares, A. Cantizano, and B.Y. Moratilla. A Novel Supercritical CO_2 Power Cycle for Energy Conversion in Fusion Power Plants. *Fusion Science and Technology*, 64(3):483–487, 2013.

[160] J.I. Linares, A. Cantizano, B.Y. Moratilla, V. Martín-Palacios, and L. Batet. Supercritical CO_2 Brayton power cycles for DEMO (demonstration power plant) fusion reactor based on dual coolant lithium lead blanket. *Energy*, 98:271–283, 2016.

[161] A. McClung, K. Brun, and L. Chordia. Technical and Economic Evaluation of Supercritical Oxy-combustion for Power Generation. In *The 4^{th} Supercritical CO_2 Power Cycles Symposium*, pages 1–24, Pittsburgh, PA, 2014.

[162] V. Dostal and J. Dostal. Supercritical CO_2 Regeneration Bypass-Cycle - Comparison to Traditional Layouts. In *The 3^{rd} Supercritical CO_2 Power Cycles Symposium*, pages 1–5, Boulder, CO, 2011.

[163] J.I. Linares, L.E. Herranz, I. Fernández, A. Cantizano, and B.Y. Moratilla. Supercritical CO_2 Brayton power cycles for DEMO fusion reactor based on helium cooled lithium lead blanket. *Applied Thermal Engineering*, 76:123–133, 2015.

[164] R. Vásquez-Padilla, Y.C.S. Too, A. Beath, R. McNaughton, and W. Stein. Effect of pressure drop and reheating on thermal and exergetic performance of supercritical carbon dioxide brayton cycles integrated with a solar central receiver. *Journal of Solar Energy Engineering*, 137(5):051012, 2015.

[165] G.D. Perez-Pichel, J.I. Linares, L.E. Herranz, and B.Y. Moratilla. Thermal analysis of supercritical CO_2 power cycles: Assessment of their suitability to the forthcoming sodium fast reactors. *Nuclear Engineering and Design*, 250:23–34, 2012.

[166] A. Schroder and M. Turner. Mapping the design space of a supercritical carbon dioxide power cycle. In *38^{th} AIAA Dayton - Cincinnati Aerospace Science Symposium*, 2013.

[167] A.U. Schroder. *A Study of Power Cycles Using Supercritical Carbon Dioxide as the Working Fluid*. PhD thesis, University of Cincinnati, 2016.

[168] N. Zhang and N. Lior. A novel near-zero CO_2 emission thermal cycle with LNG cryogenic exergy utilization. *Energy*, 31(10):1666–1679, 2006.

[169] H. Tuo. Parametric analysis of a reheat carbon dioxide transcritical power cycle using a low temperature heat source. In *2nd International Conference on Environmental Engineering and Applications, IPCBEE*, volume 17, Shangai, 2011.

[170] X. Li, H. Huang, and W. Zhao. A supercritical or transcritical Rankine cycle with ejector using low-grade heat. *Energy Conversion and Management*, 78:551–558, 2014.

[171] J. Gatewood, J. Moore, M. Nored, K. Brun, and V. Iyengar. The Texas Cryogenic Oxy-fuel Cycle (TCO): A Novel Approach to Power Generation with CO_2 Options. In *ASME Turbo Expo 2012: Turbine Technical Conference and Exposition*, pages 1007–1014, Copenhagen, 2012. American Society of Mechanical Engineers.

[172] R. Fuller, J. Preuss, and J. Noall. Turbomachinery for Supercritical Carbon Dioxide Cycles. In *ASME Turbo Expo 2012: Turbine Technical Conference and Exposition*, Copenhagen, 2012.

[173] M. Utamura. Thermodynamic Analysis of Part-Flow Cycle Supercritical CO_2 Gas Turbines. *Journal of Engineering for Gas Turbines and Power*, 132(11), 2010.

[174] G. Manente and A. Lazzaretto. Innovative biomass to power conversion systems based on cascaded supercritical CO_2 brayton cycles. *Biomass and Bioenergy*, 69:155–168, 2014.

[175] H.U. Frutschi. Process for operation of a gas turbine plant, February 3 2004. US Patent 6,684,643 B2.

[176] B. Stankovic. Brayton or Brayton-Rankine Combined Cycle With Hot-Gas Recirculation and Inverse Mixing Ejector. In *ASME Turbo Expo 2002: Power for Land, Sea, and Air*, pages 571–580, Amsterdam, 2002. American Society of Mechanical Engineers.

[177] G. Johnson and M. McDowell. Issues associated with coupling supercritical CO_2 power cycles to nuclear, solar and fossil fuel heat sources. In *The 2nd Supercritical CO_2 Power Cycles Symposium*, pages 29–30, Troy, NY, 2009.

[178] R. Kehlhofer, F. Hannemann, F. Stirniman, and B. Rukes. *Combined-Cycle Gas & Steam Power Plants*. Pennwell Corp, 2009.

[179] S.M. Besarati and D.Y. Goswami. Analysis of Avdanced Supercritical Carbon Dioxide Power Cycles With a Bottoming Cycle for Concentrating Solar Power Applications. *Journal of Solar Energy Engineering*, 136(1):010904, 2014.

[180] X. Wang, J. Wang, P. Zhao, and Y. Dai. Thermodynamic Comparison and Optimization of Supercritical CO_2 Brayton Cycles with a Bottoming Transcritical CO_2 Cycle. *Journal of Energy Engineering*, page 04015028, 2015.

[181] X. Wang, Y. Wu, J. Wang, Y. Dai, and D. Xie. Thermo-economic analysis of a recompression supercritical CO_2 cycle combined with a transcritical CO_2 cycle. In *ASME Turbo Expo 2015: Turbine Technical Conference and Exposition*, Montreal, 2015. American Society of Mechanical Engineers.

[182] H. Zhang, S. Shao, H. Zhao, and Z. Feng. Thermodynamic analysis of a SCO_2 part-flow cycle combined with an organic Rankine cycle with liquefied natural gas as heat sink. In *ASME Turbo Expo 2014: Turbine Technical Conference and Exposition*, Dusseldorf, 2014. American Society of Mechanical Engineers.

[183] X. Wang and Y. Dai. Exergoeconomic analysis of utilizing the transcritical CO_2 cycle and the ORC for a recompression supercritical CO2 cycle waste heat recovery: A comparative study. *Applied Energy*, 170:193–207, 2016.

[184] A.D. Akbari and S.M. Mahmoudi. Thermoeconomic analysis & optimization of the combined supercritical CO_2 (carbon dioxide) recompression brayton/organic rankine cycle. *Energy*, 78:501–512, 2014.

[185] A. Tahmasebipour, A. Seddighi, and M. Ashjaee. Conceptual design of a super-critical CO_2 brayton cycle based on stack waste heat recovery for Shazand power plant in Iran. *Energy Equipment and Systems*, 2(1):95–101, 2014.

[186] G. Shu, L. Shi, H. Tian, S. Deng, X. Li, and L. Chang. Configurations selection maps of CO_2-based transcritical Rankine cycle (CTRC) for thermal energy management of engine waste heat. *Applied Energy*, 2016.

[187] J.Y. Heo, Y. Ahn, and J.I. Lee. A Study of s-$CO_2$2 Power Cycle for Waste Heat Recovery Using Isothermal Compressor. In ASME, editor, *Proceeding of ASME Turbo Expo 2016: Turbomachinery Technical Conference and Exposition*, Seoul, 2016.

[188] L. Moroz, M. Burlaka, O. Rudenko, and C. Joly. Evaluation of Gas Turbine Exhaust Heat Recovery Utilizing Composite Supercritical CO_2 Cycle. In *Proceedings of International Gas Turbine Congress*, pages 109–115, Tokyo, 2015.

[189] H.T. Walnum, P. Nekså, L.O. Nord, and T. Andresen. Modelling and simulation of CO_2 (carbon dioxide) bottoming cycles for offshore oil and gas installations at design and off-design conditions. *Energy*, 59:513–520, 2013.

[190] M.S. Kim, Y. Ahn, B. Kim, and J.I. Lee. Study on the supercritical CO_2 power cycles for landfill gas firing gas turbine bottoming cycle. *Energy*, 111:893–909, 2016.

[191] D. Sánchez, R. Chacartegui, F. Jiménez-Espadafor, and T. Sánchez. A New Concept for High Temperature Fuel Cell Hybrid Systems Using Supercritical Carbon Dioxide. *Journal of Fuel Cell Science and Technology*, 6(2):021306, 2009.

[192] D. Sanchez, J.M. Muñoz de Escalona, R. Chacartegui, A. Muñoz, and T. Sanchez. A comparison between molten carbonate fuel cells based hybrid systems using air and supercritical carbon dioxide Brayton cycles with state of the art technology. *Journal of Power Sources*, 196(9):4347–4354, 2011.

[193] A. Baronci, G. Messina, S.J. McPhail, and A. Moreno. Numerical investigation of a MCFC (Molten Carbonate Fuel Cell) system hybridized with a supercritical CO_2 Brayton cycle and compared with a bottoming Organic Rankine Cycle. *Energy*, 93:1063–1073, 2015.

[194] S.J. Bae, Y. Ahn, J. Lee, and J.I. Lee. Hybrid System of Supercritical Carbon Dioxide Brayton Cycle and Carbon Dioxide Rankine Cycle Combined Fuel Cell. In *ASME Turbo Expo 2014: Turbine Technical Conference and Exposition*, Dusseldorf, 2014. American Society of Mechanical Engineers.

[195] S.J. Bae, Y. Ahn, J. Lee, and J.I. Lee. Various supercritical carbon dioxide cycle layouts study for molten carbonate fuel cell application. *Journal of Power Sources*, 270:608–618, 2014.

[196] S.K. Cho, M. Kim, S. Baik, Y. Ahn, and J.I. Lee. Investigation of the Bottoming Cycle for High Efficiency Combined Cycle Gas Turbine System With Supercritical Carbon Dioxide Power Cycle. In *ASME Turbo Expo 2015: Turbine Technical Conference and Exposition*, Montreal, 2015. American Society of Mechanical Engineers.

[197] P. Huck, S. Freund, M. Lehar, and M. Peter. Performance comparison of supercritical CO_2 versus steam bottoming cycles for gas turbine combined cycle applications. In *The 5^{th} Supercritical CO_2 Power Cycles Symposium*, pages 1–14, San Antonio, TX, 2016.

[198] D.S. Stapp. A Novel sCO$_2$ Primary Cycle for Air-Combustible Fuels. In *The 4th Supercritical CO$_2$ Power Cycles Symposium*, pages 1–10, Pittsburgh, PA, 2014.

[199] G.S. Martínez, D. Sánchez, F. Crespi, and G. Gavagnin. A global approach to assessing the potential of combined cycles using supercritical technology. In *The 1st Global Power and Propulsion Forum*, pages 1–8, Zurich, CH, 2017.

[200] Y. Kim, D. Shin, S. Lee, and D. Favrat. Isothermal transcritical CO$_2$ cycles with TES (thermal energy storage) for electricity storage. *Energy*, 49:484–501, 2013.

[201] Y.M. Kim, C.G. Kim, and D. Favrat. Transcritical or supercritical CO$_2$ cycles using both low-and high-temperature heat sources. *Energy*, 43(1):402–415, 2012.

[202] P. Vinnemeier, M. Wirsum, D. Malpiece, and R. Bove. Integration of Pumped-Heat-Electricity-Storage into Water/Steam Cycles of Thermal Power Plants. In *The 5th Supercritical CO$_2$ Power Cycles Symposium*, pages 1–14, San Antonio, TX, 2016.

[203] V. Aga, E. Conte, R. Carroni, B. Burcker, and M. Ramond. Supercritical CO$_2$-based Heat Pump Cycle for Electrical Energy Storage for Utility Scale Dispatchable Renewable Energy Power Plants. In *The 5th Supercritical CO$_2$ Power Cycles Symposium*, pages 1–16, San Antonio, TX, 2016.

[204] M. Morandin, M. Mercangöz, J. Hemrle, F. Maréchal, and D. Favrat. Thermoeconomic design optimization of a thermo-electric energy storage system based on transcritical CO$_2$ cycles. *Energy*, 58:571–587, 2013.

[205] Y. Chen and P.G. Lundqvist. Carbon dioxide cooling and power combined cycle for mobile applications. In *7th IIR-Gustav Lorentzen Conference on Natural Working Fluids*, Trondheim, Norway, 2006.

[206] Y. Chen, P.G. Lundqvist, and P. Platell. Theoretical research of carbon dioxide power cycle application in automobile industry to reduce vehicle's fuel consumption. *Applied Thermal Engineering*, 25(14):2041–2053, 2005.

[207] O.V. Combs. *An investigation of the supercritical CO$_2$ cycle (Feher cycle) for shipboard application.* PhD thesis, Massachusetts Institute of Technology, 1977.

[208] A. Agresta, A. Ingenito, R. Andriani, and F. Gamma. Feasibility Study of a Supercritical Cycle as a Waste Heat Recovery System. In *ASME 2013 International Mechanical Engineering Congress and Exposition*, San Antonio,TX, 2013. American Society of Mechanical Engineers.

[209] S. Hou, W. Zhang, Z. Zeng, and J. Ji. Supercritical CO$_2$ Cycle System Optimization of Marine Diesel Engine Waste Heat Recovey. In *International Conference on Advances in Energy, Environment and Chemical Engineering*, Changsha, 2015.

[210] L. Moroz, M. Burlaka, and O. Rudenko. Study of a Supercritical CO$_2$ Power Cycle Application in a Cogeneration Power Plant. In *The 5th Supercritical CO$_2$ Power Cycles Symposium*, San Antonio, TX, 2014.

[211] Y. Chen, W. Pridasawas, and P.G. Lundqvist. Dynamic simulation of a solar-driven carbon dioxide transcritical power system for small scale combined heat and power production. *Solar Energy*, 84(7):1103–1110, 2010.

[212] A. Kouta, F. Al-Sulaiman, M. Atif, and S.B. Marshad. Entropy, exergy, and cost analyses of solar driven cogeneration systems using supercritical CO_2 Brayton cycles and MEE-TVC desalination system. *Energy Conversion and Management*, 115:253–264, 2016.

[213] X. Zhang, H. Yamaguchi, D. Uneno, K. Fujima, M. Enomoto, and N. Sawada. Analysis of a novel solar energy-powered Rankine cycle for combined power and heat generation using supercritical carbon dioxide. *Renewable Energy*, 31(12):1839–1854, 2006.

[214] B.S. Higgins and C.M. Oldenburg. Process Modeling of a Closed-Loop sCO_2 Geothermal Power Cycle. In *The 5^{th} Supercritical CO_2 Power Cycles Symposium*, pages 1–12, San Antonio, TX, 2016.

[215] Y. Chen, P.G. Lundqvist, and W. Pridasawas. Theoretical Study of a Carbon Dioxide Double Loop System. In *International Congress of Refrigeration*, Beijing, 2007.

[216] X. Zhang, H. Yamaguchi, and Y. Cao. Hydrogen production from solar energy powered supercritical cycle using carbon dioxide. *International Journal of Hydrogen Energy*, 35(10):4925–4932, 2010.

[217] Z. Zhang, L. Tong, and X. Wang. Thermodynamic analysis of double-stage compression transcritical CO_2 refrigeration cycles with an expander. *Entropy*, 17(4):2544–2555, 2015.

[218] M. Yari, A.S. Mehr, and S.M.S. Mahmoudi. Thermodynamic analysis and optimization of a novel dual-evaporator system powered by electrical and solar energy sources. *Energy*, 61:646–656, 2013.

[219] D.G. Wilson. *The Design of High-Efficiency Turbomachinery and Gas Turbines*.

[220] Coolprop. http://www.coolprop.org/. Retrieved April 15^{th} 2019 .

[221] K. Hoopes, D. Sánchez, and F Crespi. A New Method for Modelling Off-Design Performance of sCO_2 Heat Exchangers Without Specifying Detailed Geometry. In *The 5^{th} Supercritical CO_2 Power Cycles Symposium*, San Antonio, TX, 2016.

[222] J. Xia, J. Wang, G. Zhang, J. Lou, P. Zhao, and Y. Dai. Thermo-economic analysis and comparative study of transcritical power cycles using CO_2-based mixtures as working fluids. *Applied Thermal Engineering*, 144:31–44, 2018.

[223] C.J. Sánchez and A.K. da Silva. Technical and environmental analysis of transcritical rankine cycles operating with numerous CO_2 mixtures. *Energy*, 142:180–190, 2018.

[224] G. Manzolini, M. Binotti, D. Bonalumi, C. Invernizzi, and P. Iora. CO_2 mixtures as innovative working fluid in power cycles applied to solar plants. techno-economic assessment. *Solar Energy*, 181:530–544, 2019.

[225] G.J. Silvestri. Eddystone Station, 325 MW Generating Unit, A Brief History, 2003.

[226] A.F. Armor. Ultrasupercritical Steam Turbines: Design and Materials Issues for the Next Generation, 2002.

[227] C.F. McDonald. Recuperator considerations for future higher efficiency microturbines. *Applied Thermal Engineering*, 23(12):1463–1487, 2003.

[228] M. Binotti, M. Astolfi, S. Campanari, G. Manzolini, and P. Silva. Preliminary assessment of sCO_2 cycles for power generation in csp solar tower plants. *Applied energy*, 204:1007–1017, 2017.

[229] K. Wang, Y. He, and H. Zhu. Integration Between Supercritical CO_2 Brayton Cycles and Molten Salt Solar Power Towers: A Review and A Comprehensive Comparison of Different Cycle Layouts. *Applied Energy*, 195:819–836, 2017.

[230] M. Martín and D. Sánchez. A Detailed Techno-Economic Analysis of Gas Turbines Applied to CSP Power Plants with Central Receiver. In *ASME Turbo Expo 2018: Turbomachinery Technical Conference and Exposition*, Lillestrøm, 2018. American Society of Mechanical Engineers.

[231] D. Kearney, B. Kelly, R. Cable, N. Potrovitza, U. Herrmann, P. Nava, R. Mahoney, J. Pacheco, D. Blake, and H. Price. Overview on use of a molten salt htf in a trough solar field. In *NREL Parabolic Trough Thermal Energy Storage Workshop*, 2003.

[232] S. Yoon and P. Sabharwall. Parametric study on maximum transportable distance and cost for thermal energy transportation using various coolants. *Progress in Nuclear Energy*, 74:110–119, 2014.

[233] R.R. Romatoski and L.W. Hu. Fluoride Salt Coolant Properties for Nuclear Reactor Applications: A Review. *Annals of Nuclear Energy*, 109:635–647, 2017.

[234] B.D. Kelly. Advanced thermal storage for central receivers with supercritical coolants. Technical report, Abengoa Solar Inc., 2010.

[235] D.F. Williams, L.M. Toth, K.T. Clarno, et al. *Assessment of Candidate Molten Salt Coolants for the Advanced High Temperature Reactor (AHTR)*. United States. Department of Energy, 2006.

[236] C.K. Ho and G.J. Kolb. Incorporating Uncertainty into Probabilistic Performance Models of Concentrating Solar Power Plants. *Journal of Solar Energy Engineering*, 132(3):031012, 2010.

[237] C. Ho, M. Mehos, C. Turchi, and M. Wagner. Probabilistic Analysis of Power Tower Systems to Achieve Sunshot Goals. *Energy Procedia*, 49:1410–1419, 2014.

[238] J.M. Rodríguez, D. Sánchez, G.S. Martínez, B. El Ghali, and B. Ikken. Techno-Economic Assessment of Thermal Energy Storage Solutions for a 1MWe CSP-ORC Power Plant. *Solar Energy*, 140:206–218, 2016.

[239] W.M. Vatavuk. Updating the ce plant cost index. *Chemical Engineering*, 109(1):62–70, 2002.

[240] M.S. Peters, K.D. Timmerhaus, R.E. West, K. Timmerhaus, and R. West. *Plant design and economics for chemical engineers*, volume 4. McGraw-Hill New York, 1968.

[241] Global construction cost yearbook. Technical report, Compass International Consultants Inc., 2015.

[242] Q. Li, G. Flamant, X. Yuan, P. Neveu, and L. Luo. Compact heat exchangers: A review and future applications for a new generation of high temperature solar receivers. *Renewable and Sustainable Energy Reviews*, 15(9):4855–4875, 2011.

[243] Heatric - meggit - enabling the extraordinary:to fly to power to live. https://www.heatric.com/. Retrieved May 14^{th} 2019 .

[244] Vpe Diffusion Bonded Microchannel Heat Exchanger. http://www.vpei.com/diffusion-bonded-microchannel-heat-exchangers/. Retrieved May 14^{th} 2019 .

[245] Alfa laval. https://www.alfalaval.es/. Retrieved May 14^{th} 2019 .

[246] F. Crespi, G. Gavagnin, D. Sánchez, and G.S. Martínez. The Conductance Ratio Method for Off-Design Heat Exchanger Modeling and its Impact on an sCO_2 Recompression Cycle. In *ASME Turbo Expo 2017: Turbomachinery Technical Conference and Exposition*, page V009T38A025, Charlotte, NC, 2017. American Society of Mechanical Engineers.

[247] Cis Inspector, 30/11/2018, https://www.cis-inspector.com/asme-code-calculation-allowable-stresses-high-alloy.html.

[248] Special Metals, 30/11/2018, http://www.specialmetals.com/assets/smc/documents/alloys/inconel/inco alloy-617.pdf.

[249] J.R. Couper, W.R. Penney, and J.R. Fair. *Chemical Process Equipment-Selection and Design (Revised 2nd Edition)*. Gulf Professional Publishing, 2009.

[250] Thermoflow Inc., 2 Willow St., Suite 100, Southborough, MA 01745-1020, USA , http://www.thermoflow.com.

[251] F. Crespi, G. Gavagnin, D. Sánchez, and G.S. Martínez. Analysis of the Thermodynamic Potential of Supercritical Carbon Dioxide Cycles: A Systematic Approach. *Journal of Engineering for Gas Turbines and Power*, 140(5):051701, 2017.

[252] G. Gavagnin, D. Sánchez, G.S. Martínez, J.M. Rodríguez, and A. Muñoz. Cost Analysis of Solar Thermal Power Generators Based on Parabolic Dish and Micro Gas Turbine: Manufacturing, Transportation and Installation. *Applied Energy*, 194:108–122, 2017.

[253] F. Crespi, D. Sánchez, J.M. Rodríguez, and G. Gavagnin. Fundamental Thermo-Economic Approach to Selecting sCO_2 Power Cycles for CSP Applications. *Energy Procedia*, 129:963–970, 2017.

[254] Various. Cost and Performance Data for Power Generation Technologies. Technical report, Black & Veatch for the National Renewable Energy Laboratory, Cambridge, MA, 2012.

[255] Various. The Power to Change: Solar and Wind Cost Reduction Potential to 2025. Technical report, IRENA, Abu Dhabi, United Arab Emirates, 2016.

[256] Y. Muto, N. Watanabe, M. Aritomi, and T. Ishizuka. Partial load characteristics of the supercritical CO_2 gas turbine system for the solar thermal power system with the na-al-CO_2 heat exchanger. In *The 6^{th} Supercritical CO_2 Power Cycles Symposium*, Pittsburgh, PA, 2018.

[257] Nicholas A Cumpsty. *Compressor aerodynamics*. Number BOOK. Longman Scientific & Technical, 1989.

[258] T. Sánchez Lencero, A. Muñoz Blanco, and F.J. Jiménez Espadafor. *Turbomáquinas térmicas*. Síntesis, 2004.

[259] Softinway incortporated: Axstream software platform. http://www.softinway.com/en/software/. Retrieved July 15^{th} 2019 .

[260] Nicolás Del Pozo. Design and Off-Design Performance of of Supercritical CO_2 Compressors (in Spanish.

[261] K.C. Cotton. *Evaluating and Improving Steam Turbine Performance: Includes Cogeneration and Combined Cycles*. Cotton Fact Incorporated, 1998.

[262] J.M. Muñoz de Escalona Pavón. Estudio del potencial de los motores de combustió externa de fluido no condensable integrados en sistemas híbridos con pilas de combustible de carbonatos fundidos.

[263] V. Ganapathy. *Industrial boilers and heat recovery steam generators: design, applications, and calculations*. CRC Press, 2002.

[264] V. Ganapathy. *Steam generators and waste heat boilers: for process and plant engineers*. CRC Press, 2014.

[265] P.G. Constantine. *Active subspaces: Emerging ideas for dimension reduction in parameter studies*, volume 2. SIAM, 2015.

[266] S. Bahamonde, M. Pini, C. De Servi, and P. Colonna. Active subspaces for the optimal meanline design of unconventional turbomachinery. *Applied Thermal Engineering*, 127:1108–1118, 2017.

[267] Crescent dunes: Csp power plant from solar reserve - solar energy with integrated storage. https://www.solarreserve.com/en/global-projects/csp/crescent-dunes/. Retrieved July 15^{th} 2019 .

[268] D.J. Gavic. *Investigation of water, air, and hybrid cooling for supercritical carbon dioxide Brayton cycles*. PhD thesis, University of Wisconsin–Madison, 2013.

[269] R.J. Allam, M.R. Palmer, G.W. Brown, J. Fetvedt, D. Freed, H. Nomoto, M. Itoh, N. Okita, and C. Jones. High efficiency and low cost of electricity generation from fossil fuels while eliminating atmospheric emissions, including carbon dioxide. *Energy Procedia*, 37:1135–1149, 2013.